UNIVERSITAT AUTONOMA DE BARCELONA

Institut de Física d'Altes Energies

Doctoral Thesis

Measurement of the gamma-ray opacity of the Universe with the MAGIC telescopes

Author:
Adiv González Muñoz

Supervisor:
Dr. Abelardo Moralejo Olaizola

Tutor:
Dr. Enrique Fernández Sánchez

A thesis submitted in fulfilment of the requirements for the degree of Doctor of Philosophy in the

Departament de Física

2015, Barcelona

Contents

Introduction

Only the most energetic phenomena in the Universe are capable to produce the most energetic form of light: the gamma rays. This form of radiation, produced in places that can be as far as thousands of millions of light years form us, can travel unimpeded to be detected at Earth. The detection of these gamma rays, with resolution in energy, has brought us information about the energetic processes that produce them. However, not all gamma rays heading to Earth complete the travel. Some of them interact with another form of radiation that fill the intergalactic space: the extragalactic background light (EBL). This background radiation is supplied by all the processes capable to produce electromagnetic radiation in the Universe. Therefore, the EBL contains information no only about the amount of light accumulated in the history of the Universe, but also about how it has been produced. For the gamma-ray astronomy, the correct determination of the EBL is of prime importance, since it is only after the observed energy spectrum from an extragalactic source is corrected for the absorption caused by the EBL, that the intrinsic spectrum of the source could be determined. However, this corrections could also reveal anomalies in the spectra, that could lead, among other things, to the discovery of the theoretical axion-like particle.

In this work the observations and the results of the data analysis from four active galactic nuclei are presented: 1ES 1011+496, Markarian 421, 1ES 0229+200 and 1ES 0647+250. The observations at very-high energy were performed by the Cherenkov Telescope MAGIC. Special emphasis has been placed into two of these sources, 1ES 1011+496 and Markarian 421, which were observed in flaring states of extraordinary nature. These two observations were very fortunate from the point of view of EBL studies. The effect of the EBL is more pronounced the more distant is the source and the more energetic are the observed gamma rays form the source. 1ES 1011+496 is located at a distance at which the redshift is $z = 0.212$ and the observed energy spectrum from its flaring event could be reconstructed at energies at which the EBL has a sizable effect on it. Markarian 421, on the other hand, is much closer (redshift $z = 0.031$), however, its flaring event had such enormous output of very-high energy gamma rays that its spectrum could been reconstructed at energies where the EBL start to have a significant impact on it. Using a likelihood maximization method, the gamma-ray opacity caused by the EBL was measured using data from these two flares.

This Thesis has been arranged as follows:

- **Chapter 1** introduces a general overview of the processes taking place in the production and propagation of the cosmic gamma rays. Also a description of the main characteristics of the active galactic nuclei is provided. This chapter contains also a review of the EBL and the theoretical aspects of its interaction with the gamma rays. At the end of the chapter, the interaction of the axion-like particles with the gamma rays and the EBL is briefly described.

- **Chapter 2** is where the MAGIC telescopes are described. This chapter includes the general aspects of the Imaging Atmospheric Cherenkov technique, the description of the main components of the telescopes and how the data analysis is performed.
- **Chapter 3** is devoted to the observations and the data analysis from the extraordinary flares of 1ES 1011+496 and Markarian 421. A brief review of previous observations of both sources, in which the MAGIC telescopes have participated, is included.
- **Chapter 4** presents the central results of this work, which are the measurements of the gamma-ray opacity using the data from 1ES 1011+496 and Markarian 421. A comprehensive description of the likelihood maximization technique is included and also a brief review of EBL measurements from observations of very-high energy gamma rays.
- **Chapter 5** provides the results from the observations of 1ES 0229+200 and 1ES 0647+250. Also a study about the possible detection of the axion-like particle, based in a particular model, is included.

A summary of the main results from this work are presented in the Conclusions.

Chapter 1

Origin and propagation in the intergalactic medium of cosmic gamma rays

1.1 Gamma rays

The gamma rays are produced in non thermal processes that either include nuclear reactions or the acceleration of subatomic particles to high energies. These processes occurs in a variety of astrophysical objects in our galaxy, the Milky Way, as well as in other galaxies. The measurement of the flux and energy of gamma rays coming from those objects gives information of the processes that produce them, which in turn, gives information of the inner workings of the source.

The observation of gamma rays from extragalactic objects also gives information of the intervening space between the source and the Earth. The enormous voids between galaxies are filled with the light produced by all the stars in the Universe, and the re-emission of this light by interstellar dust. Also contributing to this light are thermal processes produced by gravitational fields, e. g. in the surroundings of a Black Hole. This light is called the Extragalactic Background Light (EBL) and one way to study it is by measuring the effect that it has upon the flux of gamma rays from a distant source.

In this chapter I will outline the basic processes that produce gamma rays, followed by a description of the largest class of astrophysical objects where extragalactic gamma rays are generated: the Active Galactic Nuclei (AGN). A description of the EBL and how it interacts with gamma rays will be provided. The chapter will conclude with a recount of possible anomalies in the propagation of gamma rays that might originate from the coupling of photons to hypothetical particles.

1.1.1 The electromagnetic spectrum

The EBL and the gamma rays are electromagnetic (EM) radiation, although they differ in the origin and energy range.

The energy E of the photons (the quanta of light) is connected to the frequency ν and the wavelength λ through the relations:

$$E = h\nu = \frac{hc}{\lambda} \quad , \tag{1.1}$$

where c is the speed of light in the vacuum ($\sim 3 \times 10^8$ m/s) and h the Planck constant (4.136×10^{-15} eV s). In high energy physics, the preferred unit of energy for the photons is the electron volt (1 eV = 1.602^{-19} J), defined as the energy acquired by an electron when it crosses a region with an electric potential difference of 1 volt. Throughout this work this unit will be widely used.

Going from the lowest energy to the highest energy, the electromagnetic spectrum is divided in the following regions or bands [Longair, 1999]:

Region	Energy range (eV) (order of magnitude)	Wavelenght (m) (order of magnitude)
Radio waves	10^{-15} - 10^{-6}	10^{8} - 1
Microwaves	10^{-6} - 10^{-3}	1 - 10^{-3}
Far infrared	$\sim 10^{-3}$	10^{-3} - 10^{-4}
Mid infrared	$\sim 10^{-2}$	10^{-4} - 10^{-5}
Near infrared	$\sim 10^{-1}$	10^{-5} - 10^{-6}
Visible	1.7 - 3.2	7.5×10^{-7} - 3.9×10^{-7}
Ultraviolet	10 - 10^{2}	10^{-7} - 10^{-8}
Soft X-rays	10^{2} - 10^{4}	10^{-8} - 10^{-10}
Hard X-rays	10^{4} - 10^{5}	10^{-10} - 10^{-11}
Gamma-rays	$> 10^{5}$	$< 10^{-11}$

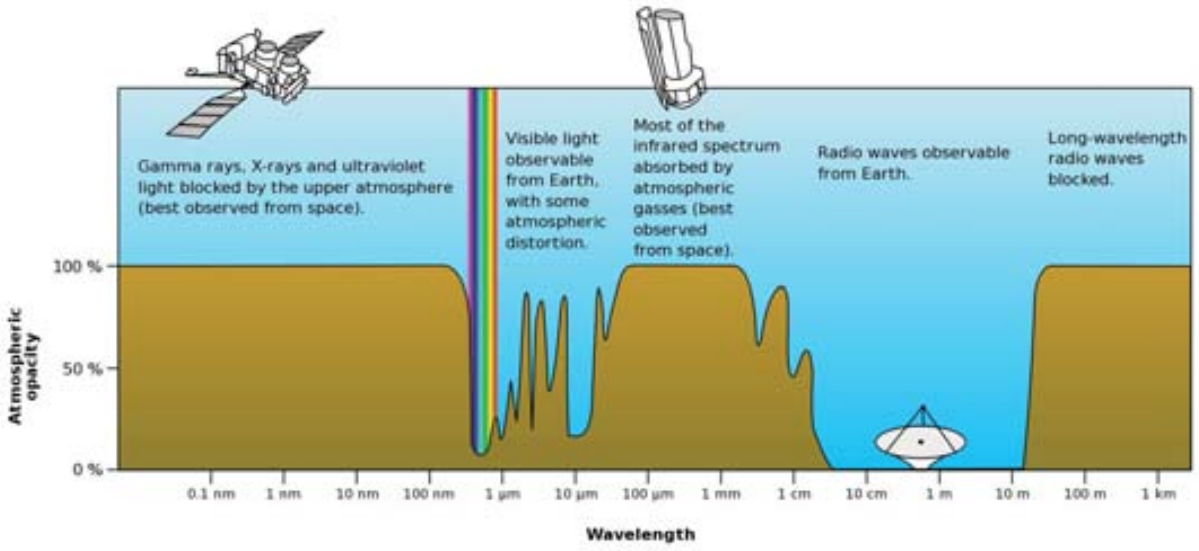

FIGURE 1.1: Atmospheric electromagnetic opacity. Image from NASA

Radio waves are used in telecommunications and also are widely used in astronomy, since most of the universe is transparent to these wavelengths. Several astronomical objects emit radiation in radio waves. Some radio emission can be associated with thermal radiation of hot electrons

from ionized hydrogen. But in most radio sources the emission comes from sychrotron radiation (see section 1.1.2). Microwaves are also used in telecommunications but their importance to astronomy is that they are the carriers of one of the most relevant phenomena in the Universe, the Cosmic Microwave Background (CMB). The CMB is the cool remnant of the equilibrium radiation spectrum formed when the early Universe became transparent. The infrared light is generated in processes that involve the excitation of molecules, like the ones present in clouds of interstellar dust. These clouds absorb light from stars, getting heated in the process and then emitting at longer wavelengths. This radiation has a very relevant contribution to the EBL, as will be described later. The visible band, as the name says, is the region of the EM spectrum that can be detected with the human eye. Most of the stars have their peak emissions at wavelengths in the visible band, therefore also making a sizeable contribution to the EBL. Stars also have emission in the ultraviolet band, coming from regions of very high temperature in their surfaces. Phenomena of even higher temperature will emit X-rays, like the coronas of stars or accretion disks around very massive objects, like black holes, present at the center of AGNs. Finally, in the most energetic part of the EM spectrum are the gamma rays. Only the most energetic phenomena in the Universe are capable of producing gamma rays, either by nuclear reactions or through the acceleration to very high energies of charged particles which subsequently produce the high energy photons through one of several processes described in the next section.

The atmosphere of the Earth is transparent to EM radiation only in certain bands. It is transparent to visible light and radio waves, but is opaque to ultraviolet and shorter wavelengths, including the gamma rays. The only way to detect directly the gamma rays coming from outer space is to place detectors in satellites. But indirect observation of those gamma rays is possible from ground. That will be explained in Chapter 3, when the MAGIC telescopes will be described.

1.1.2 Production mechanisms of gamma-rays

From the point of view of gamma ray astronomy, the most relevant production mechanisms, briefly described, are (see e.g. Aharonian 2004, Grupen 2005, and Ghisellini 2012):

Bremsstrahlung

A charged particle which is deflected (accelerated) in the Coulomb field of a charge (ions or atomic nuclei) emits bremsstrahlung photons. The energy spectrum of the emitted photons depends on the shape of the initial energy spectrum of electrons. In the particular case of electrons having an initial power-law spectrum $Q(\epsilon_e) \propto \epsilon_e^{-\Gamma}$, the cooled steady-state spectrum is also a power-law, $N(\epsilon_e) \propto \epsilon_e^{-\Gamma}$, which implies that the produced gamma-rays have a power-law spectrum as well. In the relativistic case, the steady-state electron spectrum becomes flatter, $N(\epsilon_e) \propto \epsilon_e^{-\Gamma+1}$, producing gamma-rays with power-law index $\Gamma - 1$. In environments where the bremsstrahlung is in competition with other energy loss processes, the steady-state electron spectrum becomes steeper, $N(\epsilon_e) \propto \epsilon_e^{-\Gamma-1}$, then, the bremsstrahlung gamma-rays emerge with photon index $\Gamma + 1$.

Synchrotron radiation

If a charged particle is moving in a magnetic field, it is subjected to centripetal acceleration. As for another acceleration processes, the charge will emit photons. The emitted photons are called synchrotron radiation. The energies of the synchrotron photons are generally much less than the energy of parent electrons. However, in extreme environments, e.g. in pulsar magnetospheres or in magnetized accretion disks, the production of high energy

gamma rays is possible. The differential energy spectra of gamma rays due to synchrotron radiation depends mainly on a single parameter $\chi_0 = \epsilon_0 B/B_{cr}$, where ϵ_0 is the initial energy of the electron, B the magnetic field and B_{cr} the critical value for the magnetic field ($\approx 4.4 \times 10^{13}$ G) relevant to quantum effects. At $\chi_0 \ll 1$, the gamma-ray spectra are very steep, but at large values, $\chi_0 \geq 1$, gamma rays are characterized by a flat distribution.

Inverse Compton scattering

In the Compton scattering, energetic photons transfer part of their energy to free electrons in a collision, thereby losing certain amount of energy. The Inverse Compton (IC) scattering is the process in which relativistic electrons interact with low energy photons transferring energy to them, hence producing gamma rays. The IC is a very relevant process in astrophysics and is widely used in models to explain the gamma rays coming from a wide range of very energetic environments, e.g. supernova remnants, pulsars or AGNs. For the description of the IC there are two regimes, that are called the *Thomson* and the *Klein-Nishina* regimes (see Fig. 1.2). In the Thomson regime, seeing the interaction from the frame of reference with the electron at rest, the energy of the photon is smaller than $m_e c^2$, with m_e being the electron mass. In the case of the Klein-Nishina regime, the photon energy is larger than $m_e c^2$ and quantum effects has to be taken into account. The energy losses in the two regimes have a quite a different dependence on the electron energy. In the Thomson regime the energy loss rate is proportional to ϵ_e^2, while in the Klein-Nishina regime it is almost energy independent. This implies that in the first case the electron spectrum becomes steeper, whereas the Compton losses in the Klein-Nishina regime make the electron spectrum harder. For a power-law distribution of electrons, $dN_e/d\epsilon_e \propto \epsilon_e^{-\Gamma}$, where N_e is the electron population, the resulting gamma-ray spectrum in the nonrelativistic regime has a power-law form with photon index $\alpha = (\Gamma + 1)/2$. In the ultrarelativistic regime the γ-ray spectrum is noticeably steeper, with a photon index $\alpha = (\Gamma + 1)$.

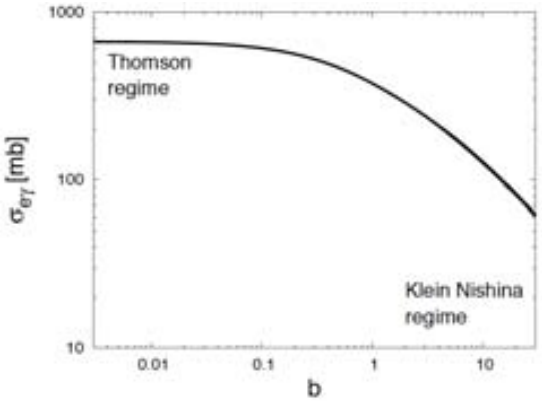

FIGURE 1.2: Cross-section for inverse Compton interactions with an isotropic photon distribution as a function of the squared center-of-mass energy in the collisions in units of $(m_e c^2)^2$, quantity referred as b (from [Aharonian and Taylor, 2010]).

π^0 decay

Relativistic protons and nuclei produce high energy gamma-rays in inelastic collisions with ambient gas due to the production and decay of secondary pions, kaons and hyperons. The neutral π^0-mesons provide the main channel of conversion of the kinetic energy of protons to high energy gamma rays since their main decay channel is $\pi^0 \rightarrow 2\gamma$. The energy threshold of protons for the production of π^0-mesons is $E_{th} = 2m_\pi c^2(1 + m_\pi/4m_p)$, where m_π and m_p are the masses of the π^0-meson and the proton, respectively. At high energies

all three types of π-mesons ($\pi^{\pm}$, π^0) are produced with comparable probabilities. The gamma-ray spectrum from the decaying π^0 depends on the spectrum of the parent protons. If the parent protons have a energy spectrum described by a power-law, the π^0-decay gamma rays will also have a energy spectrum described by a power-law. However, these gamma rays will have a distinct feature in their spectrum: a maximum at $E_\gamma = m_\pi c^2/2$, independent of the energy distribution of π^0 mesons, and consequently of the parent protons. The decay of charged pions leads to ν_e and ν_μ neutrinos with spectra quite similar to the spectrum of the accompanying π^0-decay gamma rays.

1.2 Active Galactic Nuclei

An Active Galactic Nucleus (AGN) is an object capable of generating extreme luminosity, that in some cases is 10^4 times the luminosity of the host galaxy, in a very compact region (probably $\ll 1$ pc^3, compared, for example, to the volume of the Milky Way that is of the order of 10^{12} pc^3) [Krolik, 1999] . The radiation from this region can emerge over an extraordinarily broad range of frequencies. The most widely accepted theory is that AGNs are powered by accretion onto supermassive black holes (10^5-10^{10} $M_\odot$).

For the description of the spectral properties of the AGN and other astrophysical objects, a clarification on the used units is required. The specific flux (F_ν of F_λ) is the rate at which energy arrives per unit area per unit frequency ν or unit wavelength λ. The standard unit for F_ν is the Jansky, 10^{-23} erg cm^{-2} s^{-1} Hz^{-1}. However, in high-energy astronomy, where photon-counting devices prevail, the customary measured quantity is dF/dE ($= F_\nu/(h\epsilon)$), the rate at which photons arrive per unit area per unit energy ϵ. Additionally, a compact way to talk about a certain range in wavelength is the "band", which generally means a span in the logarithm of the wavelength. For example, the term *infrared*, generally refers to a range in wavelength from ~ 1 to ~ 100 μ. Therefore, the most convenient quantity for describing which band is most important in terms of energetics is the spectral energy distribution (SED) $\nu F_\nu = dF/d\log\nu = dF/d\log\lambda = \lambda F_\lambda$. This unit is also written as $E^2 \times dF/dE$.

There is not a unique way to describe an AGN, since not all AGNs share the same characteristics, but we can list the observable phenomena we can use to find them. Following Krolik [1999] these observable phenomena are:

- **Very small angular size**. For AGNs that are near enough to Earth, so the brightness of the host galaxy can be seen, the nucleus often appears to be a bright point in optical images. But this contrast in luminosity between the nucleus and its host galaxy depends strongly on the wavelength. For example, many AGNs have a much greater ratio of x-ray luminosity to optical than does any normal galaxy. For this reason, their x-ray images are essentially pure points.

- **High luminosity**. The characteristic luminosity of a field galaxy is $\sim 10^{44}$ $erg\ s^{-1}$ while AGN isotropic luminosities can range from $\sim 10^{42}$ to $\sim 10^{48}$ $erg\ s^{-1}$. However, the true output of an AGN can be modified by the presence of extremely thick dust extinction surrounding the nucleus. Also, the presence of a relativistic jet can distort the angular distribution of light, favoring those AGNs whose jet is pointing toward us, and making those that are beaming away from us not even detectable. Thus, the true luminosity can significantly differ assuming isotropic radiation or the presence of a jet.

- **Broad-band continuum emission**. A "broad-band" means a span in several decades in frequency. To put it in perspective, an ordinary galaxy can be approximated as a collection of stars and the emission of a star can be described, at zero-order, as the spectrum of a blackbody. The bulk of the emission of a black body is within a factor of three in frequency, so, for a collection of stars with different surface temperatures will emit most of their power within no more than one decade of frequency. On the other hand, an AGN usually has a SED that is flat from the mid-infrared to the hardest X-rays observed. For a particular subclass of AGN, the SED at 1GeV is at least as large as that in lower frequency bands, and there are a few examples of this subclass with an SED at 1 TeV greater than anywhere else in the electromagnetic spectrum.

- **Emission lines**. AGN emission lines are often very prominent in contrast to the spectra of most star and galaxies. Also, there is an interesting split in the line width distribution. In some objects, many of the lines have broad wings extending from the line center, whereas in others, the lines are much narrower.

- **Variability**. Most AGNs can be seen to have a variability in the optical band of ∼10%, over timescales of few years. However, the variability tends to increase at shorter wavelengths. Any statement about variability is strongly dependent on the timescale in question. AGNs for the most part vary with no special timescales. In consequence, the amplitude of variability for AGNs is not straightforward to measure. For a small subset of AGNs, the blazars (see section 1.2.1), the variation is more prominent. Such variability is also very strongly correlated with three other properties: strong polarization, compact radio structure and strong high-energy gamma-ray emission.

- **Polarization**. Most AGNs are weakly polarized, but just enough more strongly for their polarization distribution to be statistically distinguishable from that of regular galaxies. The light from stars is linearly polarized by ~ 0.5 % due to interstellar dust transmission polarization. In comparison, blazars are much more strongly polarized, often $\sim$ 10 % in linear polarization. The detection of this polarization will depend on the wavelength observed.

- **Radio Emission**. From the earliest radio astronomical observations it was discovered that many bright radio sources come in the form of double lobes with a galaxy located halfway between them. Many of the known AGNs are strong radio emitters and since radio astronomical techniques are quite developed, a great deal is known about the phenomenology of that emission.

1.2.1 Classification

The main division among the AGNs is set by the fraction of the total power that they emit in the radio band. The AGNs with a relatively strong radio emission (although it accounts for less than the 1% of the bolometric luminosity) are called *radio-loud*. AGNs with almost no emission in radio are called *radio-quiet*. The majority of AGNs are part of the second group.

Based on the characteristics of their optical and ultraviolet spectra, AGNs can also be separated into three broad types [Urry and Padovani, 1995] :

- Those with bright continua and broad emission lines are known as Type 1 AGNs. In the radio-quiet group, these include the Seyfert 1 galaxies, which have relatively low-luminosities, and the higher-luminosity radio-quiet quasars (QSO) (see figure 1.3) .

- Type 2 AGNs have weak continua and only narrow emission lines. They can be radio-loud or radio-quiet. Radio-quiet Type 2 AGNs include Seyfert 2 galaxies at low luminosities, as well as the narrow-emission-line X-ray galaxies. Radio-loud Type 2 AGNs, often called Narrow-Line Radio Galaxies (NLRG), include two distinct morphological types: the low-luminosity Fanaroff-Riley (FR) type I radio galaxies, which have often-symmetric radio jets whose intensity falls away from the nucleus, and the high-luminosity FR type II radio galaxies, which have more highly collimated jets leading to well-defined lobes with prominent hot spots.

- A small number of AGNs have very unusual spectral characteristics, possibly related to a small angle of the emission jet to the line of sight (see figure 1.4 (b)). These include the BL Lacertae (BL Lac) objects, which are radio-loud AGNs that lack strong emission or absorption features. There are no known radio-quiet BL Lacs. A subset of Type 1 quasars, including those defined variously as Optically Violently Variable (OVV) quasars, Highly Polarized Quasars (HPQ), Core-Dominated Quasars (CDQ) or Flat Spectrum Radio Quasars (FSRQ) show characteristics that point to fact that they are all more or less the same thing. Collectively, BL Lacs and FSRQ are called blazars.

1.2.2 Unified scheme

The AGN classification described in the previous section is based in what is called the "unified scheme" proposed by Urry and Padovani [1995]. This scheme starts with the prevailing picture of the physical structure of an AGN, illustrated in Fig. 1.4 (a). The enormous gravitational pull of a supermassive black hole at the center is the ultimate source of the AGN luminosity. The matter falls into the gravitational well forming an accretion disk losing momentum trough

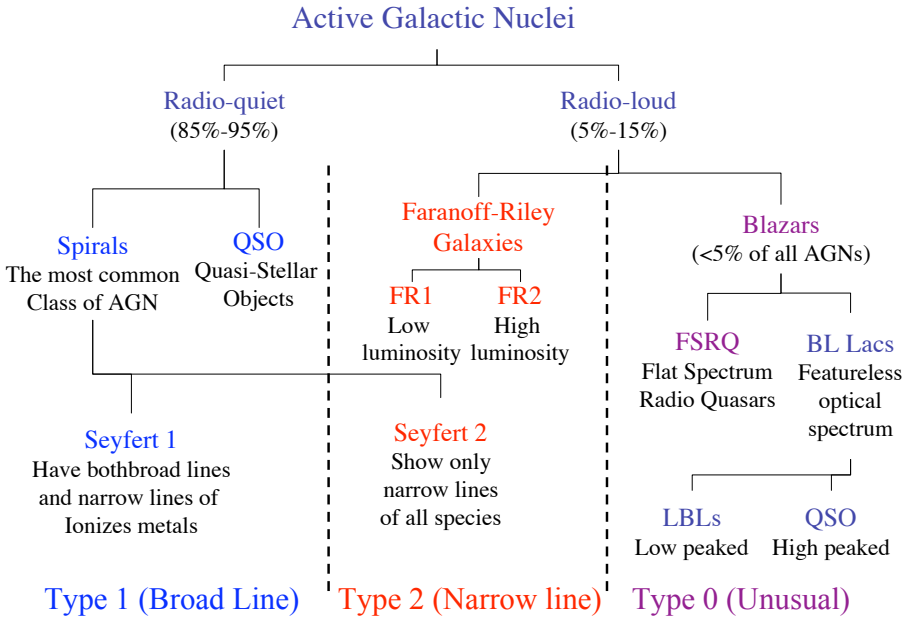

FIGURE 1.3: AGN classification scheme. Based on Urry and Padovani 1995

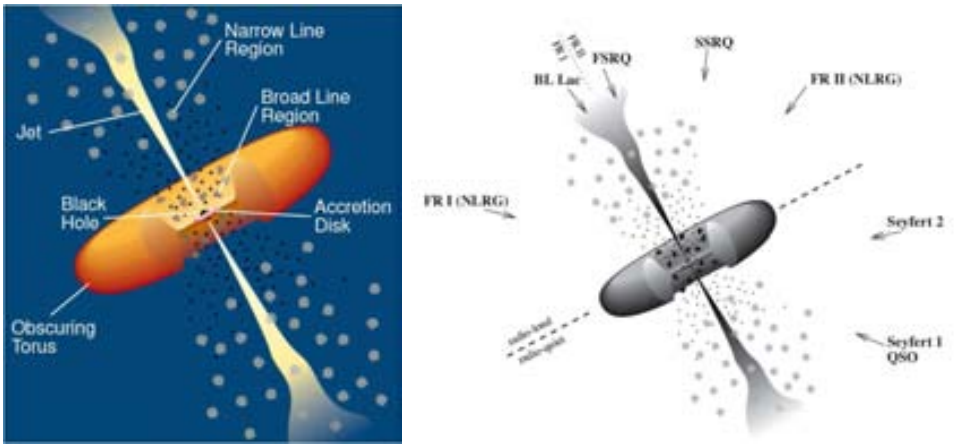

(a) The most characteristic regions of an AGN

(b) Classification of an AGN depending on the viewing angle with respect of the observer's line of sight

FIGURE 1.4: Schematic view of an AGN according to the unified model, from [Urry and Padovani, 1995]

viscous and turbulent processes. Strong optical and ultraviolet emission lines are produced in clouds of gas moving rapidly in the potential of the black hole, the so-called "broad-line clouds". The optical and ultraviolet radiation is obscured along some lines of sight by a torus or warped disk of gas and dust well outside the accretion disk and broad-line region. Beyond the torus, slower moving clouds of gas produce emission lines with narrower widths. Outflows of energetic particles occur along the poles of the disk or torus, escaping and forming collimated radio-emitting jets and sometimes giant radio sources when the host galaxy is an elliptical, but forming only very weak radio sources when the host is a gas-rich spiral. The plasma in the jets, at least on the smallest scales, streams outward at very high velocities, beaming radiation relativistically in the forward direction. This relativistic jets, when close to the line of sight, can be detected as gamma-ray emitters at very high energies ($\sim$ TeV).

Wether AGNs are classified Type 1 or Type 2 depends on obscuration of the luminous nucleus, and wether a radio-loud AGNs is a blazar or a radio galaxy depends on the alignment of the relativistic jet with the line of sight (see figure 1.4 (b)). The cause of the first kind on anisotropy, may be explained by the presence of obscuring material in the central regions of many AGN. This material, probably dust, prevents infrared through ultraviolet light from penetrating some lines of sight. This dust may be distributed in a torus or in a warped disk. The most direct evidence of the presence of this torus or disk is from spectropolarimetry of Type 2 objects. Some fraction of the light from these objects is highly polarized. The polarization plane is perpendicular to the radio jet axis, as expected if a Type 1 nucleus is at least partially obscured by a thick wall of gas and dust whose axis coincides with the radio jet axis [Urry and Padovani, 1995]. The second kind of anisotropy appears as a consequence of a relativistic effect. When an emitting plasma has a bulk relativistic motion relative to a fixed observer, it emission is beamed in the forward direction (in the fixed frame). An observer located in or near the path of such plasma sees much more intense emission than if the same plasma were at rest. Time scales for variability are also shorter. The rapid variations, high polarization, and high luminosities that characterize blazars can be explained by strong relativistic beaming. The evidence to support this idea came from the observations of blazars at high energy. In several of these blazars, the

gamma-ray flux is highly variable. This rapid variability leads to the argument that the gamma rays must be relativistically beamed. In order for gamma rays to escape the source, the optical depth to pair production must be of order unity or less. This means that the *compactness*, which a dimensionless parameter that represents source luminosity divided by its dimension, must be less than about 40 at the threshold for pair production. From observations of blazars, like 3C 279 and PKS 0528+134, values for the compactness of 5000 to 15000 are inferred, well in excess of the optical depth limit. The fact that is possible to observe gamma rays from these sources means that the true gamma-ray luminosity, $\mathscr{L}$, must be much smaller than observed and the true dimension much larger. Relativistic beaming can solve this since it has the effect that $L_{obs} = \delta^4 \mathscr{L}$, where δ is the Doppler beaming factor.

1.2.3 Emission models

If AGNs generated their energy solely by quiescent accretion of matter in thermodynamic equilibrium, the highest temperatures present there would be only $\sim 10^5$ K, that is barely enough to emit X-rays, not to mention gamma-rays. The detection of gamma-rays coming from AGNs points to the existence of relativistic particles inside of the jet. One way in which these particles can reach relativistic velocities is by repeated crossings of shock fronts, resulting in a first-order Fermi acceleration. This shocks could be generated very near an accreting black hole, where flows of highly supersonic material converge.

1.2.3.1 Leptonic models

The leptonic models of TeV blazars assume that both the X-ray and TeV emission components originate in the relativistic jets due to synchrotron and inverse Compton (IC) radiation of the same population of directly accelerated electrons. The target photons for the IC process are likely to be the synchrotron photons themselves (synchrotron-self-Compton, SSC) [Tavecchio et al., 1999].

The SSC model in its simplest form assumes a spherical emission region (a "blob") filled with an isotropic electron population and a randomly oriented magnetic field, moving towards the observer at relativistic velocities. The three basic model parameters are: the radius of the blob R, magnetic field B, and Doppler factor of the bulk motion $\delta = [\Gamma(1 - \beta \cos\theta)]^{-1}$. The observed variability time-scale t_{var} of a source gives information about the blob dimension R through the causality relation $R \leq c t_{var} \delta$.

The SSC model for blazars is able to reproduce the characteristic SED with two bumps observed in these objects. In a study by Fossati et al. [1998], they analyzed a large sample of BL Lacs and FSRQs and divided it into radio luminosity bins, and the luminosity in selected bands was averaged to form the SED representative of the blazars in each bin. The division into radio luminosity bins matched the division into bins of bolometric luminosity. All spectra could be described by two broad peaks, the first at mm/soft X-rays frequencies, the second in the MeV-GeV band. In the figure 1.5 can be seen what Fossati et al. named as the "blazar sequence": blazars with greater bolometric luminosity have "redder" SEDs (Low-energy peak BL Lacs, LBL), and the high-energy peak is more prominent. Blazars of lower bolometric luminosity have instead a "blue" SED (High-energy peak BL Lacs, HBL) with the two peaks having approximately the same luminosity. Thus, this sequence relates the shape of the SED with the bolometric observed luminosity. The simplicity of this scheme has made the blazar sequence a popular idea, although its validity has been debated [Nieppola et al., 2008, Padovani, 2007]. A

extended version of the blazar sequence was presented by Ghisellini and Tavecchio [2008] where additionally to the bolometric luminosity, the SED is linked to the mass of the black hole and the accretion rate.

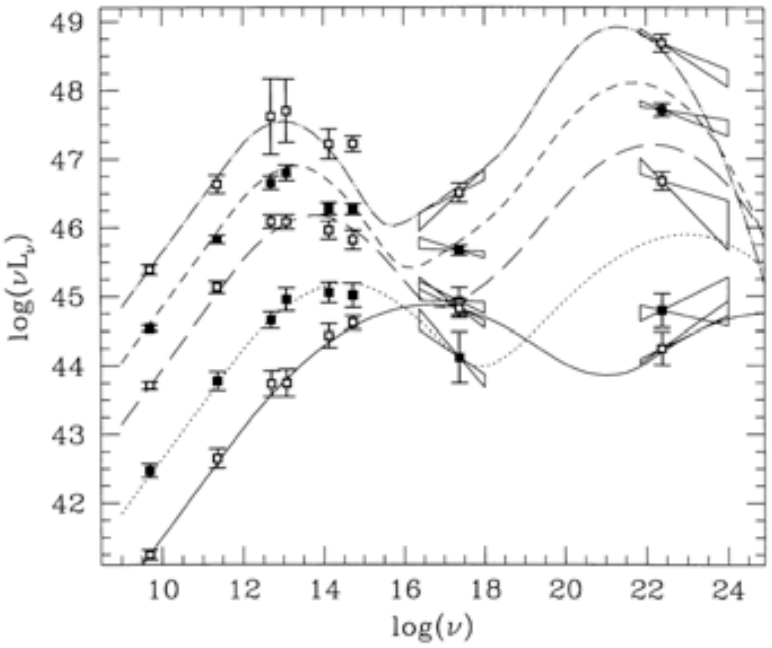

FIGURE 1.5: Average SEDs for 126 blazars sample binned according to radio luminosity irrespective of the original classification. The overlaid curves are analytic approximations described in Fossati et al. 1998.

Statistical particle acceleration mechanisms produce a power-law spectrum for electrons, however the cooling processes of the electrons make a spectral break. With the approximation that electrons are continuously injected into the blob in a time of the order of R/c, the energy spectrum in the blob is assumed to have a broken power-law spectrum [Takami, 2011],

$$\frac{\mathrm{d}n_e}{\mathrm{d}\gamma} = n_0 \gamma^{-s_1} \left(1 + \frac{\gamma}{\gamma_{br}}\right)^{s_1 - s_2} \quad (\gamma_{min} < \gamma < \gamma_{max}) \tag{1.2}$$

where n_0 and γ are the normalization factor of the number density of electrons and the Lorentz factor of electrons ($1/\sqrt{1-\beta^2}$), respectively. γ_{min} and γ_{max} are the minimum and the maximum values of the Lorentz factor, and γ_{br} is its value at the spectral break. s_1 and s_2 are the spectral indices below and above γ_{br}.

Following the model developed by H. Takami (2011), γ_{max} can be estimated by comparing the time-scale to accelerate electrons τ_{acc} and the shortest energy-loss time-scale, which in turn, is determined by comparing the energy density of magnetic field U_B, and the energy density of radiation U_{rad}. However, U_{rad} cannot be estimated before the calculation of the SED. So, it is assumed that $U_B > U_{rad}$, which means that the shortest time-scale is the energy-loss via synchrotron radiation τ_{syn}. Thus, γ_{max} can be estimated setting $\tau_{acc} = \tau_{syn}$, getting

$$\gamma_{max} = \left(\frac{6\pi e}{\theta_F \sigma_T B}\right)^{-1/2} , \tag{1.3}$$

where e is the charge of the electron, θ_F the diffusion coefficient from the acceleration mechanism, σ_T the cross-section of Thomson scattering and B the magnetic field strength.

The cooling of electrons via synchrotron radiation and IC scattering makes a power-law index steeper by 1, $s_2 = s_1 + 1$ above characteristic energy γ_{br}. With the assumption that accelerated electrons are continuously provided into the blob and since the electrons lose energy during their staying in the blob, this characteristic energy can be estimated by $\tau_{syn} < \tau_{esc}$, where τ_{esc} is the time-scale for electrons to escape from the blob. Under the assumption that electrons escape from the blob by the velocity of $c/3$, which corresponds to the velocity downstream fluid in a shock system under the strong shock limit of a relativistic shock, we have,

$$\gamma_{br} = \frac{2\pi m_e c^2}{\sigma_T R B^2} \quad , \tag{1.4}$$

with m_e being the electron mass. H. Takami's model in particular has five free parameters: $s_1(s_2)$, B, R, n_0 and δ is the Doppler factor of the blob [Takami, 2011].

1.2.3.2 Hadronic model

The mechanisms that accelerate particles to relativistic energies in the jets of AGNs are not exclusive to electrons, they can also act upon protons and nuclei [Mannheim, 1993]. However, the acceleration has to proceed at the maximum (theoretically possible) rate, otherwise they cannot offer efficient gamma-ray production mechanisms in the jets [Aharonian, 2004]. Protons reaching Lorentz factors in the range 10^9 - 10^{11} generate hard photons with energies from keV to TeV via inelastic proton-photon collisions and subsequent synchrotron cascade reprocessing:

$$p + \gamma \rightarrow \pi + X \quad , \tag{1.5}$$

where X are hadrons and the γ are synchrotron-photons from accelerated electrons [Mannheim et al., 1991].

The high energy photons from the decay $\pi^0 \rightarrow 2\gamma$ and also from $\pi^+ \rightarrow e^+ + \nu$ and $\pi^- \rightarrow e^- + \bar{\nu}$ (leading to synchrotron gamma-rays) can be pair-absorbed and those pairs will radiate a new generation of very energetic synchrotron photons. This proton-initiated cascade emission can dominate over SSC emission and bremsstrahlung even at X-ray frequencies, giving a more "flat" IC peak with respect of leptonic models.

In the previous lines, the production mechanisms of the gamma rays and how this mechanisms are present in the AGNs have been described, particularly in the case of the SSC models. These models have been proved to be a good approximation, explaining the differential energy spectrum of several observations of AGNs. This theoretical knowledge, as will be shown in Chapter 4, works as a basis to explore another phenomenon, related to the propagation of gamma rays through the Universe. As stated at the beginning of the chapter, VHE gamma rays from extragalactic sources interact with background photons, modifying the energy spectrum observed at Earth. These background photons are part of the extragalactic background light.

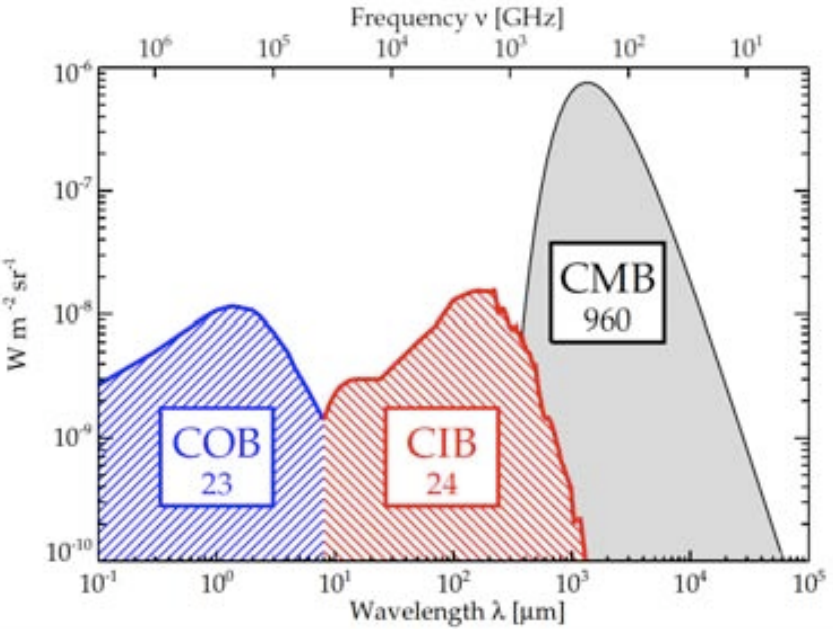

FIGURE 1.6: Schematic Spectral Energy Distribution of the most important (by intensity) backgrounds in the universe, and their approximate brightness in $nW\ m^2\ sr^{-1}$ written in the boxes (from Dole et al. [2006]).

1.3 The extragalactic background light

The extragalactic background light (EBL) is the diffuse radiation that came from the contribution of all the light emitted by stellar nucleosynthesis in the optical and near infrared (IR) and the IR radiation emitted by dust after absorbing the starlight. The fraction of the EBL that goes in wavelength (or frequency) from the UV to the near IR is called Cosmic Optical Background (COB) and the fraction going from the near IR to the far IR is called Cosmic Infrared Background (CIB) (see figure 1.6). Other contributions to this diffuse radiaton, like emission from AGN and quasars, are expected to produce no more than 5 to 20% of the total EBL density in the mid IR [Matute et al., 2006]. The SED of the electromagnetic radiation in the Universe is dominated by the Cosmic Microwave Background (CMB), being the EBL about 5% of the brightness of the CMB. The contributions to the EBL of the radio, UV, X-ray and gamma-ray extragalactic backgrounds are smaller by one to three orders of magnitude than the COB and CIB [Dole et al., 2006].

The study of the EBL provides key information to understand the evolution of the Universe. The intensity of the EBL is directly connected to the cosmic star formation rate and the stellar-mass density today [Madau and Pozzetti, 2000]. Additionally, most of the EBL intensity is supplied by massive stars that end their life as supernovae. Therefore, the total EBL intensity can be used to derive an estimate of the supernova rate and the resulting flux of supernova neutrinos [Beacom, 2010].

The EBL intensity is usually given in units of nW m^{-2} sr^{-1}. Its measurement can be done directly, a method that poses considerable challenges. It requires the removal of strong foreground emission from interplanetary dust particles (also know as zodiacal light) and from stellar and interstellar emission components from the Milky Way.

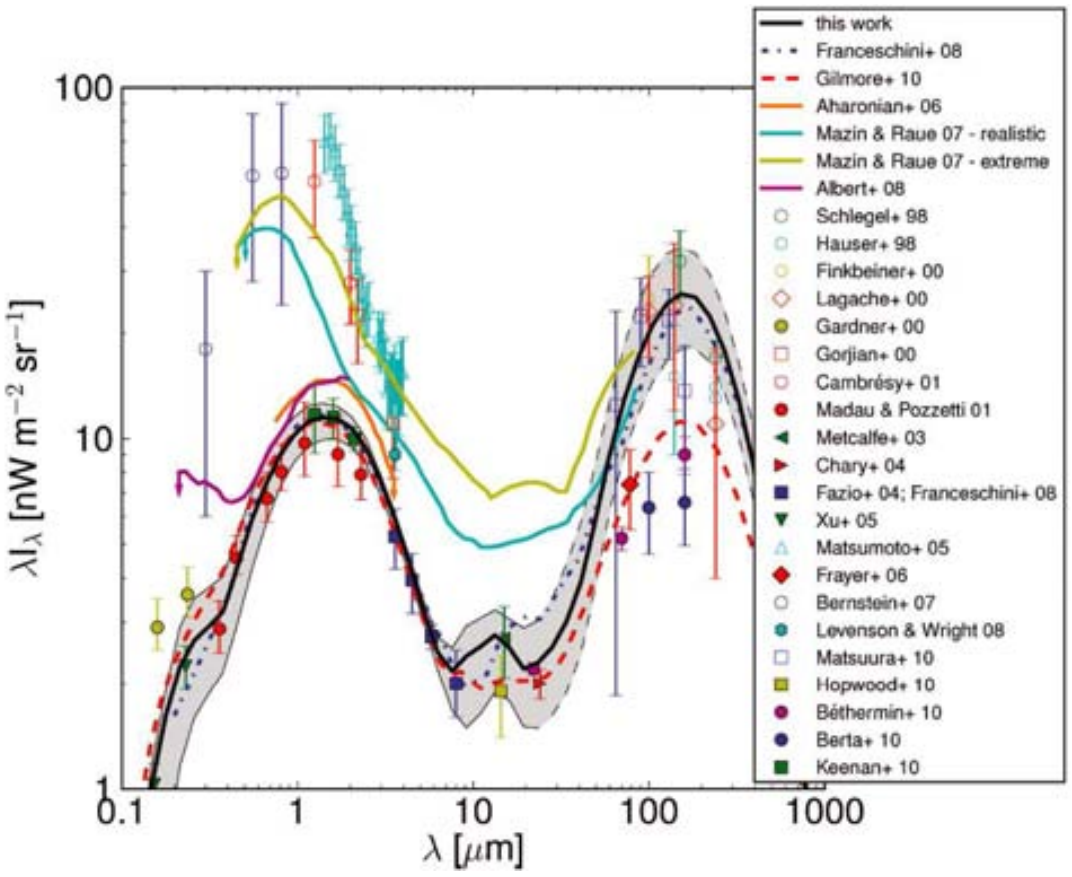

FIGURE 1.7: Measurements and models of the spectral energy distribution of the EBL. The solid black line is the EBL model by Domínguez et al. 2011. Empty symbols are direct measurements. Filled symbols are galaxy-counts data, considered lower limits. Coloured solid lines are upper limits from gamma-ray astronomy. Figure from Domínguez et al. [2011]

Strict lower limits to the EBL intensity have been obtained by adding up the light emitted by resolved galaxies. Using data from the *Hubble Space Telescope* (HST) and *COBE* satellite, limits to the COB has been obtained [Madau and Pozzetti, 2000]. For this measurements, they took a solid angle portion of the sky (50×50 arcsec^2) and count the galaxies within that field for different wavelength bands. From this counts the EBL was calculated integrating the emitted flux times the differential number counts down to the detection threshold. This measurements are lower limits since the low surface brightness regions of galaxies may be missed in the standard aperture photometry. Furthermore, a truly diffuse background will always remain undetected in such surveys.

For the CIB also direct measurements have been done by Dole et al. [2006] using data from the *Spitzer* Observatory. This measurements used a stacking analysis technique. Stacking of astronomical images of sources detected at one wavelength enhances their signal relative to the random background fluctuations at some other wavelength.

In Figure 1.7 a collection of measurements and limits to the EBL intensity, derived by the methods described above is presented. The figure shows that the EBL is poorly determined in the $\sim$5-6 μm wavelength region, where the foreground emission from the interplanetary dust is more prominent.

Several models have been proposed to estimate the intensity and spectral distribution of the EBL at redshift $z = 0$. Those models can be divided in four groups (see Dwek and Krennrich [2013] and the references therein):

Backward evolution models

These models start with the construction of a library of SEDs from galaxies in the local universe and then evolve them back in time in order to fit the observed number counts. The galaxies in such library should represent the range of observed galactic morphologies (spiral, elliptical, irregular) and activities (AGN, normal, starburst, mergers) in the local universe. The evolution of the spectral luminosity density, $L_\nu(\lambda, z)$, with the redshift can be inferred directly from observations if the redshift of the sources is known and their number counts are complete. it also can be modeled by evolving the relative number of the different type galaxies with redshift. Once the evolution of the spectral luminosity density with redshift is determined, the EBL is obtained by integrating $L_\nu(\lambda, z)$ over redshift. Recent examples of these models are by Stecker and Scully [2006], Franceschini et al. [2008], and Domínguez et al. [2011].

Forward evolution models

The starting point for these model is the determination of the redshift dependence of the cosmic star formation rate (CSFR). The calculation of the CSFR is complicated by extinction effect at UV and optical wavelengths, and by the implicit assumption that the IR luminosity is powered by stars and representative of the total bolometric luminosity of the galaxies. The most difficult part is determining the fraction of starlight that is absorbed by dust, and the spectrum of the reradiated IR emission. Population synthesis models, combined with simple radiative transfer calculation, can be used for determining the UV to radio SED of individual galaxies. An example of this kind of models is by Finke et al. [2010]

Cosmic chemical evolution models

These models treat the universe as a closed system in which all galaxies within a large comoving volume element are represented by their basic ingredients: stars, interstellar gas, metallicity, and radiation. Chemical evolution equations are used to follow the evolution of the average stellar, gaseous, and radiative contents in each comoving volume in a self consistent manner. Similar to forward evolution models, population synthesis models are used to calculate the stellar SED at each redshift.

Semi-analytical models

The approach of these models is based in the formation and evolution of galaxies in a cold dark matter Lambda dominated (ΛCDM) universe using the cosmological parameters derived from the 5-year *Wilkinson Microwave Anisotropy Probe* (WMAP5) observations as the initial conditions. The models then follow the growth and merging of dark matter halos, and the emergence of galaxies which form as baryonic matter falls into the potential wells of these halos. As in all EBL models, determination of the galaxies' SED is complicated by the detailed microscopic and large scale parameters needed to calculate the amount of starlight that is absorbed by dust, and the spectrum of the reradiated emission. Semi-analytical models are the most physically motivated models, and quite successful in reproducing a large number of observational constraints. An example of this kind of approach is by Gilmore et al. [2012].

1.3.1 Interaction of very high-energy gamma rays with the EBL

The EBL interacts with very-high energy (VHE) gamma rays from extragalactic sources producing electron-positron pairs ($\gamma + \gamma \rightarrow e^+ + e^-$). This interaction decreases the gamma-ray flux from these extragalactic sources (mainly AGNs) altering their observed energy spectra, and imposing a gamma-ray horizon. The attenuation of TeV gamma rays can be used to constrain the intensity and spectrum of the EBL, particularly in the $\sim 5 - 60\mu$m wavelength region, where direct measurements are greatly hampered by foreground emission from interplanetary dust [Dwek and Krennrich, 2005].

The cross section for the $\gamma + \gamma \rightarrow e^+ + e^-$ interaction of a gamma-ray photon of energy E_γ emitted from a source at redshift z with a background photon of energy ϵ is given by

$$\sigma_{\gamma\gamma} = \frac{3\sigma_T}{16}(1-\beta^2)\left[2\beta(\beta^2-2) + (3-\beta^4)\ln\left(\frac{1+\beta}{1-\beta}\right)\right], \tag{1.6a}$$

$$\beta \equiv \sqrt{1 - \frac{\epsilon_{th}}{\epsilon}}, \tag{1.6b}$$

$$\epsilon_{th}(E_\gamma, \mu) = \frac{2(m_e c^2)^2}{E_\gamma(1-\mu)} \quad , \tag{1.6c}$$

where $\sigma_T = 6.65 \times 10^{-25}$ cm^2 is the Thompson cross section, ϵ_{th} the threshold energy of the interaction, and $\mu \equiv \cos\theta$, where θ is the angle between the incident photons. The γ-γ cross section for the interaction with an isotropic distribution of background photons has a peak value of 1.70×10^{-25} cm^2 for $\beta = 0.70$, which correspond to energies for which the product $E_\gamma \epsilon \approx 4(m_e c^2)^2 \approx 1$ MeV^2, or $\lambda_\epsilon \approx 1.24 E_\gamma$ (TeV), where λ_ϵ is the wavelength of the background photon.

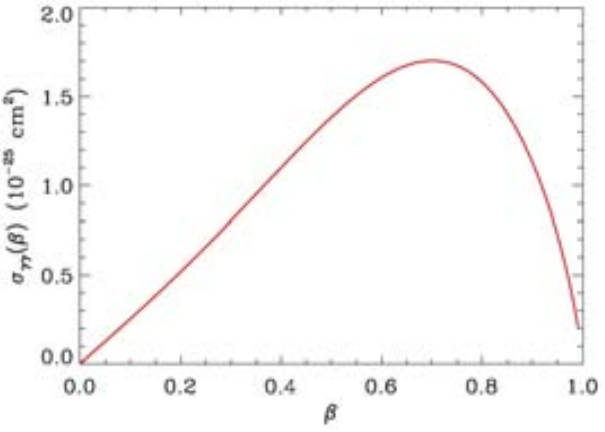

FIGURE 1.8: The cross section for the γ-γ interaction vs β, defined in Eq. 1.6b [Dwek and Krennrich, 2013].

The optical depth traversed by a photon observed at energy E_γ that was emitted by a source at redshift z is given by

$$\tau_\gamma(E_{\gamma,z}) = \int_0^z \left(\frac{dl}{dz'}\right) dz' \int_{-1}^{+1} d\mu \frac{1-\mu}{2} \int_{\epsilon'_{th}}^{\infty} d\epsilon' n_\epsilon(\epsilon', z') \sigma_{\gamma\gamma}(E'_\gamma, \epsilon', \mu), \tag{1.7}$$

where $n_\epsilon(\epsilon', z')d\epsilon'$ is the comoving number density of EBL photons with energies between ϵ' and $\epsilon' + d\epsilon'$ at redshift z', $\epsilon'_{th} = \epsilon_{th}(E'_\gamma, \mu)$, $E'_\gamma = E_\gamma(1+z')$, and where dl/dz is given by

$$\left(\frac{dl}{dz}\right) = c\left(\frac{dt}{dz}\right) = \frac{R_H}{(1+z)E(z)} \tag{1.8a}$$

$$E(z) \equiv \left\{(1+z)^2(\Omega_m z + 1) + z(2+z)[(1+z)^2\Omega_r - \Omega_\Lambda]\right\}^{1/2}, \tag{1.8b}$$

where Ω_m and Ω_r are, respectively, the matter and radiation energy density normalized to the critical density, $\Omega_\lambda = \lambda/3H_0^2$ is the dimensionless cosmological constant ($\Omega_m + \Omega_r + \Omega_\Lambda = 1$ in a flat universe), $R_H \equiv c/H_0$ is the Hubble radius, c is the speed of light, and H_0 is the Hubble constant. The comoving number density of EBL photons of energy ϵ at redshift z is given by

$$\epsilon^2 n_\epsilon(\epsilon, z) = \left(\frac{4\pi}{c}\right)\nu I_\nu(\nu, z) \tag{1.9a}$$

$$= \int_z^\infty \nu' L_{\nu'}(\nu', z')\left|\frac{dt}{dz'}\right|\frac{dz'}{1+z'} \quad , \tag{1.9b}$$

where $\epsilon = h\nu$, $\nu' = \nu(1+z')$, and $L_\nu(\nu', z')$ is the specific comoving luminosity density at frequency ν' and redshift z' [Dwek and Krennrich, 2005]. Thus, for a blazar located at redshift z with a intrinsic spectrum $(dF/dE)_{int}$, the observed spectrum $(dF/dE)_{obs}$ will be

$$\left(\frac{dF}{dE}\right)_{obs} = \exp[-\tau_{\gamma\gamma}(E, z)]\left(\frac{dF}{dE}\right)_{int} \quad , \tag{1.10}$$

Most of the EBL models available to the public, provide the optical depth τ values [e.g. Domínguez et al., 2011, Franceschini et al., 2008]. These values are used in the expression 1.10 in order to obtain the intrinsic spectrum of and observed source, a standard procedure in observations of extragalactic sources at very-high energies. Also, as will be explained in Chapter 4, the values of τ can be used as a template. Then, making reasonable assumptions about the intrinsic spectrum of the source, it is possible to derive limits to the EBL intensity scaling up or down the values of τ. However, these kind of approaches are based in the supposition that there is no mechanism in which the gamma rays could avoid the interaction with the EBL. Such mechanism has been proposed, although derived from a theoretical solution to a elementary particle physics problem. The particle responsible for that mechanism, is the axion-like particle.

1.4 Possible anomalies in the propagation of gamma-rays: axion-like particles

Axions were postulated as a consequence of the spontaneous breaking of the Peccei-Quinn symmetry proposed to solve the strong CP problem [Peccei and Quinn, 1977]. A generalization of these particles are the axion-like particles (ALPs), for which, unlike axions, the mass m_a and the coupling constant to the photons are not related to each other. An important property

of ALPs is that they are expected to convert into photons (and *vice versa*) in the presence of magnetic fields (Primakoff effect). This photon/ALP mixing is the main signature used in ALP searches in experiments like CAST [Collaboration, 2007] and ADMX [Collaboration, 2010]. The presence of ALPs could also affect the propagation of photos over cosmological distances, distorting the spectra of gamma-ray sources, such as AGNs, in the TeV range [de Angelis et al., 2007, Mirizzi et al., 2007].

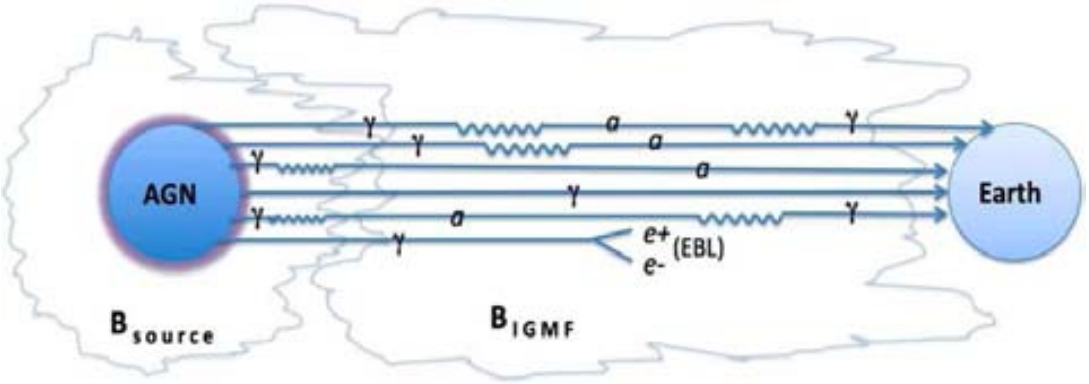

FIGURE 1.9: Photon/ALP conversions (crooked lines) that can occur in the emission from a cosmological source, γ and a symbols represent gamma-ray photons and ALPs respectively. The diagram collects the main physical scenarios that are identified inside the formalism followed by Sánchez-Conde et al. 2009. Each of them are schematically represented by a line that goes from the source to the Earth.

One scenario for the photon/ALP mixing effect for distant AGN was studied by Sánchez-Conde et al. 2009, in which the mixing takes place inside or near the gamma-ray emitter as well as in the intergalactic magnetic field (IGMF). In the artistic view in Fig. 1.9, the main physical cases that a photon may encounter in its travel from the source to the Earth are shown. From top to bottom: (1) the photon converts to an axion and back to photon in the IGMF, (2) the photon converts to an axion in the IGMF, (3) the photon converts to an axion at the source, which then does not interact with the EBL, therefore traveling unimpeded from the source to the Earth, (4) the photon travels unimpeded from the source to the Earth, (5) the photon converts to an axion at the source and back to photon in the IGMF, (6) the photon interacts with an EBL photon resulting in a pair production. The cases 1, 4, 5 allow for a recovery of the intrinsic photon yield, while the cases 2, 3 and 6 correspond to an attenuation of the intrinsic source flux.

The probability of a photon of energy E_γ to be converted into an ALP (and *vice versa*) can be written as [Hooper and Serpico, 2007]:

$$P_0 = \frac{1}{1 + (E_{crit}/E_\gamma)} \sin^2 \left[\frac{Bs}{2M} \sqrt{1 + (\frac{E_{crit}}{E_\gamma})^2} \right] \quad , \tag{1.11}$$

where s is the length of the domain where there is a roughly constant magnetic field B, and M is the inverse of the photon/axion coupling constant. A characteristic energy, E_{crit} is defined:

$$E_{crit} \equiv \frac{m^2 M}{B} \quad , \tag{1.12}$$

or in more convenient units:

$$E_{crit}(GeV) \equiv \frac{m_{\mu eV}^2 M_{11}}{0.4 B_G} \quad , \tag{1.13}$$

with the dimensionless quantities: $m_{\mu eV} \equiv m/\mu eV$, $M_{11} \equiv M/10^{11}$ GeV and $B_G \equiv$ B/Gauss; m is the effective mass of the ALP $m^2 \equiv |m_a^2 - \omega_{pl}^2|$, with $\omega_{pl} = 0.37 \times 10^{-4} \mu eV \sqrt{n_e/cm^{-3}}$ the plasma frequency and n_e the electron density. The measurements from CAST [Arik et al., 2011] gives the most stringent constraint currently for the range of ALP mass with a limit of $M_{11} \geq 0.114$ for ALP mass $m_a \leq 0.02$ eV.

The main effect produced by photon/ALP mixing in the source is an *attenuation* in the total expected intensity of the source just above a critical energy E_{crit}. As for the mixing in the IGMFs, despite the low magnetic field B, the photon/ALP conversion take place due to the large distances involved. In the model of Sánchez-Conde et al. [2009], it is assumed that the photon beam propagates over N domains of a given length. The modulus of the IGMF is the same in all of them, whereas its orientation changes randomly from one domain to the next, which in practice is also equivalent to a variation in the strength of the component of the magnetic field relevant to the photon/ALP mixing.

The EBL has an important role to be considered in the in the propagation of photons and ALP in the intergalactic medium, being its main effect an additional attenuation of the photon flux, as discussed in the previous section. Taking together the effect of the EBL and the photon/ALP conversion in the IGMF, can lead to an *attenuation* or an *enhancement* of the photon flux at Earth, depending on distance, magnetic fields and the EBL model considered. The enhancement in the flux is possible since ALPs travel without obstruction through the EBL, and a fraction of them can convert back into photons before reaching the Earth. The strength of the IGMF is expected to be many orders of magnitude weaker (∼nG) than that of the sources and its surroundings (∼G). Consequently, as described in Eq. 1.13, the energy at which photon/ALP conversion occurs in this case is many orders of magnitude larger than that at which conversion can occur in the source and its vicinity. Assuming a mid-value of B∼0.1 nG, and $M_{11} = 0.114$ (CAST lower limit), the effect could be observationally detectable by Imaging Atmospheric Cherenkov Telescopes (IACT) only if the ALP mass is of the order of 10^{-10} eV.

Following the formalism by Sánchez-Conde et al. [2009] the drop in the flux of gamma rays above E_{crit} is independent on the source, therefore, a property that, although difficult to measure in a single observation, it should be revealed stacking observations from several sources. However, it has been pointed out that because of the random nature of the intergalactic magnetic fields, the effect of photon/ALP mixing should be very different from one source to another [Burrage et al., 2009, Mirizzi and Montanino, 2009].

In section 5.3.1 we present a study based in the framework for the photon/ALP mixing from Sánchez-Conde et al. 2009 and in section 5.3.2, some hints of detection of ALPs under other frameworks.

Chapter 2

Detection of cosmic gamma rays

The atmosphere of the Earth is transparent to only a fraction of the electromagnetic (EM) spectrum. It is not just by accident that our eyes evolved adapted to the range of the EM spectrum where the Sun has it maximum output and in which the atmosphere is transparent. With that limitation, for the bigger part of the history of astronomy, all observations were done exclusively in the optical range. It was not until the twentieth century, with technology developments, mainly in electricity and electronics, that the observations of the Universe could be extended to other wavelengths. However, the astronomers were still limited only to wavelengths that could penetrate the atmosphere. The observation of shorter wavelengths, namely X-rays and gamma rays, had to wait until the arrival of the space era.

The direct detection of gamma rays with space-borne detectors is based in having an absorbing material where the gamma-ray energy is transferred to charged particles. In the case of a Compton telescope, as the name suggest, the energy of the gamma-ray is transferred to electrons in a Compton interaction and then the scattered photon transfers its remaining energy in a photoelectric interaction. In a pair-conversion telescope, like EGRET or Fermi-LAT [1], the gamma-ray transfer its energy producing pairs electron-positron. The production of the pairs is inside of a tracker, where the direction is determined, then the electron-positron pairs goes into a calorimeter, where the energy of the primary gamma-ray is estimated. An important factor for the capability of detecting gamma rays in a wide range of energy is the volume of the detector, not only because of the capacity to completely absorb the gamma rays, but also because of the rapid decrease in flux of them at higher energies. Being the space technology as expensive as it is, is not economically viable to place in orbit a very large detector, and this limits the energy range in which the gamma rays can be detected by space-born devices.

The very thing that impedes the direct detection of gamma rays at the surface of the Earth also provides the means to detect them at very high energy. The atmosphere works as a giant calorimeter. This chapter will be dedicated to the description of the technique used by the MAGIC telescopes to observe the cosmic gamma rays, the description of MAGIC itself and the processing of the data recorded by the telescopes.

[1] https://www-glast.stanford.edu/

2.1 Extensive air showers

An Extensive Air Shower (EAS) is initiated when a very energetic cosmic particle (usually called primary or parent particle) reaches the atmosphere producing a cascade of secondary particles. The EAS initiated by a gamma ray or by and electron (or positron) is usually called an "electromagnetic shower", whereas a EAS initiated by a proton or a heavier particle is called a "hadronic shower".

A couple of useful quantities to understand the propagation of particles through the atmosphere are the *radiation length* and the *interaction length*. The radiation length X_0 is defined as the average distance over which a electron loses all but $1/e$ of its energy due to bremsstrahlung. The interaction (or collision) length λ for hadrons is defined also in an analog way, only that the energy losses are due to collisions with atomic nuclei. The atmosphere has a depth corresponding to 27 radiations lengths, and 11 interaction lengths. This means that practically not a single primary particle arrives at sea level. Already at altitudes of 15 to 20 km primary cosmic particles interact with atomic nuclei of the air and initiate the EAS.

A schematic view of the transformation of primary cosmic rays in the atmosphere is shown in Fig. 2.1. Atomic nuclei constitute the largest fraction of primary cosmic rays, around 99%, and the remaining 1% are mostly electrons. This proportion is true for energies around tens of GeV. However, since the spectral of protons and electrons are different, when considering all energies, there is equal number of protons and electrons, otherwise the planet will be charged-up. From the proportion corresponding to nuclei, $\sim 90\%$ are protons, $\sim 9\%$ alpha particles and less than 1%, nuclei of heavier elements. The fractions of the primary nuclei are nearly constant over a energy range from tens of GeV to somewhat beyond 100 TeV [Beringer et al., 2012]. The flux of gamma rays is about 1000 times smaller than of the nuclei. The secondary particles most copiously produced are the pions. Kaons on the other hand are only produced with a probability of 10% compared to pions. Neutral pions initiate (via their decay $\pi^0 \rightarrow 2\gamma$) electromagnetic showers. The electromagnetic showers development is characterized by a shorter radiation length ($X_0 \approx \frac{1}{3}\lambda$ in air). This shower component is absorbed relatively easily and is therefore also named soft component. Charged pions and kaons can either initiate further interactions or decay [Grupen, 2005]. The leptonic decays of pions and kaons produce the penetrating muon and neutrino components ($\pi^+ \rightarrow \mu^+ + \nu_\mu$, $\pi^- \rightarrow \mu^- + \bar{\nu}_\mu$; $K^+ \rightarrow \mu^+ + \nu_\mu$, $K^- \rightarrow \mu^- + \bar{\nu}_\mu$). Muons can also decay and contribute via their decay to the soft component and neutrinos to the neutrino component ($\mu^+ \rightarrow e^+ + \nu_e + \bar{\nu}_\mu$, $\mu^- \rightarrow e^- + \bar{\nu}_e + \nu_{mu}$).

In an electromagnetic shower, if the primary gamma-ray has enough energy, it has a probability to interact with the Coulomb field around a nucleus producing a pair electron-positron. The high-energy electrons and positrons will produce more photons through bremsstrahlung and these photons, if their energy is still sufficiently high, will produce more pairs electron-positron. These two processes continue until the energy of the photons is below the threshold for pair production and the energy losses for the electrons through ionization start to dominate over the bremsstrahlung. The energy at which the energy loss rate through bremsstrahlung and ionization are equal is called *critical energy* E_c. For electromagnetic showers, the critical energy is $E_c \approx 84$ MeV.

Apart from their longitudinal development, the electromagnetic and hadronic components of a shower also spread out laterally in the atmosphere. The lateral spread is essentially caused by the transferred transverse momenta in hadronic interactions and multiple scattering of low-energy shower particles. This spread will prove to be very useful to distinguish a hadronic shower from an electromagnetic one. A electromagnetic shower is more slender and approximately symmetric

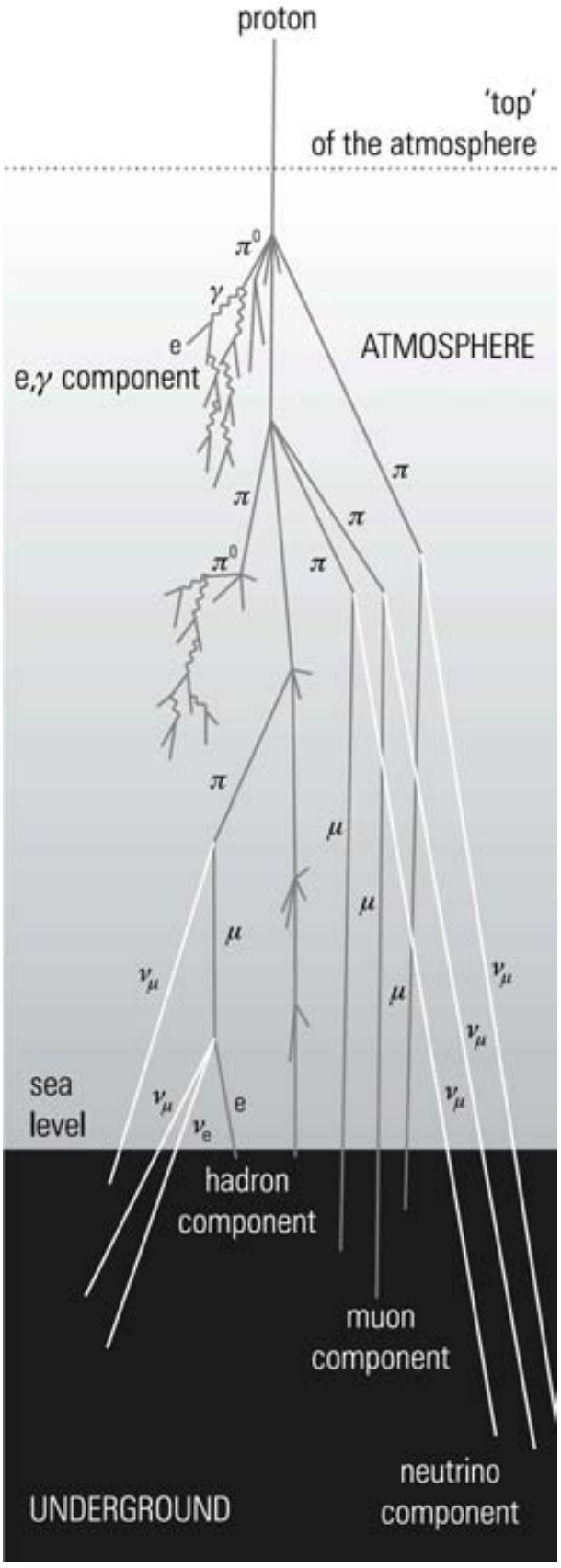

FIGURE 2.1: Transformation of primary cosmic rays in the atmosphere [Grupen, 2005].

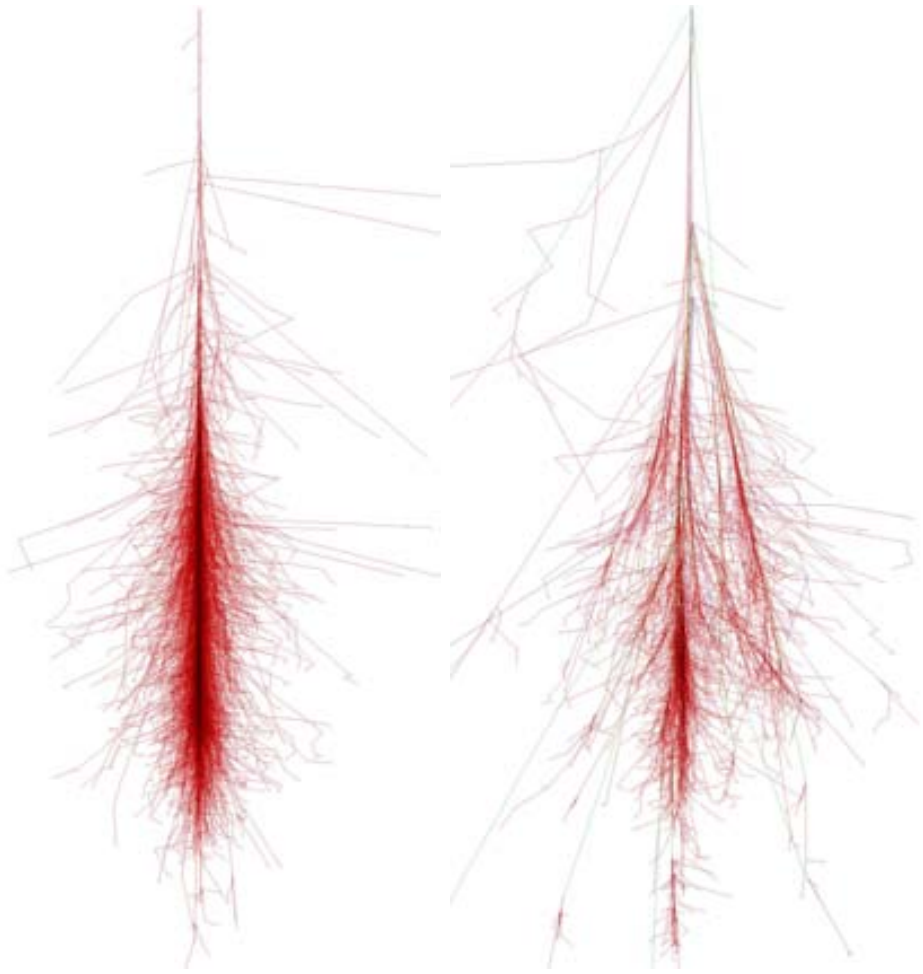

(a) 100 GeV photon (b) 100 GeV proton

FIGURE 2.2: Comparison of the development of electromagnetic and hadronic showers in the atmosphere. In red are the electrons, positrons and gammas, green the muons and blue the hadrons. From [Schmidt]

with respect to the direction of the primary, compared to a hadronic shower. Figure 2.2 shows a comparison between the two kinds of showers for simulated 100 GeV photons and 100 GeV protons in the atmosphere.

For a very-high energy primary gamma-ray, the relativistic electrons and positrons produced in the shower will follow essentially the direction of the original incident photon and if their speed is greater than the speed of light in the atmosphere, they will emit Cherenkov light.

2.1.1 The Cherenkov effect

When a fast charged particle travels through a medium at a constant velocity v, grater than the velocity of light in that medium, it emits *Cherenkov radiation*. The emission of Cherenkov radiation is a cooperative phenomenon involving a large number of atoms of the medium whose electrons are accelerated by the fields of the passing particle and so emit radiation. The wavefronts emitted in different points of the particle's trajectory can sum coherently [Jackson, 1975].

A simple geometric picture of the process can be seen considering the fields of the fast particle in the dielectric medium with refractive index n, as a function of time. The velocity of the particle is v and the velocity of light in the medium is c/n, being c the speed of light in the vacuum. Fig. 2.3 shows a succession of spherical field wavelets for $v > c/n$. The wavelets interfere constructively to form a "shock" front or wake behind the particle. The normal to the wake makes an angle θ_C with the velocity direction, where

$$\cos\theta_C = \frac{c}{vn} = \frac{1}{\beta n} \tag{2.1}$$

with $\beta = v/c$. An observer at rest sees a wavefront moving in the direction of θ_C.

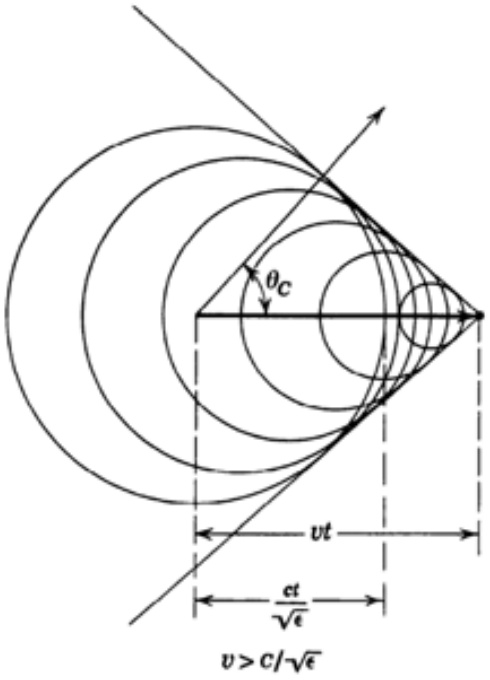

FIGURE 2.3: Emission of Cherenkov radiation by a charged particle traversing a medium with a velocity exceeding the velocity of light in that medium [Jackson, 1975].

The threshold velocity for the particle to produce Cherenkov light is given by $\beta_{min} = 1/n$. Therefore, the energy threshold for a particle with mass m_0 is:

$$E_{th} = \frac{m_0 c^2}{\sqrt{1-\beta_{min}^2}} = \frac{m_0 c^2}{\sqrt{1-n^{-2}}}. \tag{2.2}$$

The Cherenkov radiation is useful for the detection of very-high energy gamma rays when they enter to the atmosphere. The high energy gamma-ray initiates an electromagnetic shower and the electron-positron pairs created acquire velocities greater than the speed of light in air. These electrons and positrons radiate optical Cherenkov radiation which can be detected by light detectors at ground level.

The number of photons produced per unit path length of a particle with charge Ze and per unit of photon wavelength λ is [Beringer, 2012]

$$\frac{d^2N}{dxd\lambda} = \frac{2\pi\alpha Z^2}{\lambda^2}\left(1 - \frac{1}{\beta^2 n^2(\lambda)}\right) \tag{2.3}$$

where α is the fine structure constant $\alpha = 7.297 \times 10^{-3}$. The $1/\lambda^2$ dependency means that most of the Cherenkov photons will be emitted at short wavelengths, from the ultraviolet down to the visible region.

The atmospheric Cherenkov light emission from a single particle forms a forward cone with an opening angle $\theta \approx 1^\circ$ that increases downwards. This emission off Cherenkov light produced by the secondary particles in the electromagnetic shower will produce a compact, homogeneous distribution of photons on the ground usually called the "light pool". For a vertical electromagnetic shower, the light pool is circular, centered on the shower core. Fig. 2.4 shows the lateral distribution of Cherenkov photons for a 100 GeV gamma-ray induced shower and a 400 GeV proton-induced shower. The refractive index of the atmosphere has a value very close to 1 (1.000293 at 0° and 1 atm of pressure), which means that the Cherenkov light emitted by the particles in the shower travels almost at the same velocity of these particles. This constrains the duration of the Cherenkov light flash to a few nanoseconds (see Fig. 2.5)

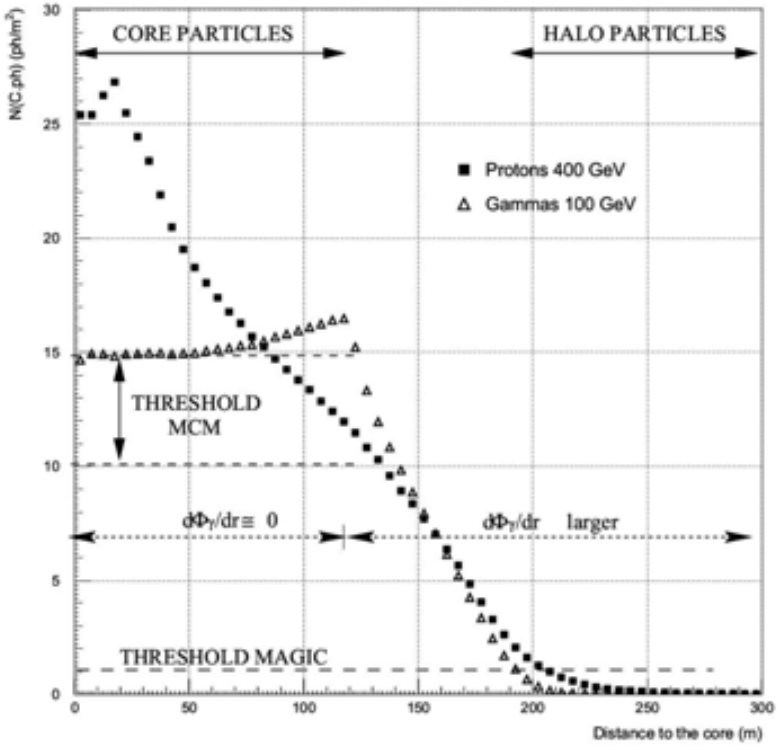

FIGURE 2.4: Lateral distribution of Cherenkov photons at an altitude of 2200 for a 100 GeV gamma-ray induced shower (white triangles) and a 400 GeV proton-induced shower (black squares). The segmented line in the bottom part of the plot indicates the projected threshold for MAGIC. The MCM threshold is for a MAGIC-like telescope with a diameter of 10 m. The gamma-ray flux radial gradient $d\Phi_{\gamma/dr}$ shows an abrupt change at $\sim$ 120 m. From [Barrio, 1998b]

The Cherenkov light in its travel to ground is subject to attenuation processes. The main ones are the molecular (Rayleigh) scattering, aerosol (Mie) scattering and ozone absorption (see Fig. 2.6). The Rayleigh scattering results from the electric polarizability of particles (molecules or atoms) whose size is much smaller than the wavelength of light. This particles, being exited by the light, radiate in the same frequency. The Rayleigh scattering cross section depends

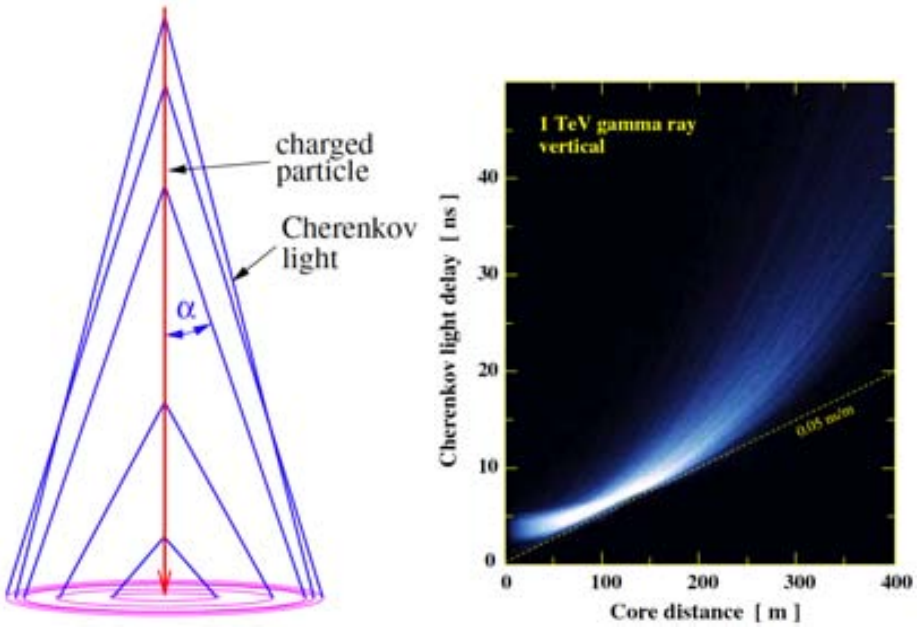

(a) Cherenkov light emitted by a downward-moving particle in the atmosphere

(b) Distribution of arrival time and core distance of Cherenkov photons from a 1 TeV γ-ray-shower

FIGURE 2.5: Cherenkov light emission by EAS particles. From [Völk and Bernlöhr, 2009]

on the wavelength as λ^{-4} which means that the shorter wavelengths (as Cherenkov light) are scattered more strongly than longer wavelengths. Mie scattering in the atmosphere occurs when the particles are the same size as the wavelengths being scattered. Aerosols are mainly limited to the *boundary layer* of typically 1-2.5 km thickness above the surrounding terrain where the diurnal variation and the dependence on ground material and wind speed is the largest. Ozone is an important absorber for light with wavelengths below 340 nm with a maximal absorption around the 250 nm, through the process $O_3 + \gamma \rightarrow O_2 + O$. The ozone in the atmosphere is concentrated in the ozone layer (20 to 30 km above sea level) but is also present at ground level [Bernlöhr, 2000].

2.2 The Imaging Atmospheric Cherenkov Technique

Conceptually, an Imaging Atmospheric Cherenkov Telescope (IACT) has two basic components, a *mirror*, where the Cherenkov photons are collected and reflected into a *camera*, positioned in the telescope focal plane. Since the flash of Cherenkov light last just a few nanoseconds, the camera needs very fast detectors in order to integrate the signal without adding too much noise from unwanted background light. This is usually accomplished using Photomultiplier Tubes (PMTs) in a matrix array where the Cherenkov photons are measured, and from which a pixelated image of the shower can be extracted.

The beginnings of the IACTs goes back to 1948, when P. M. S. Blackett predicted that relativistic cosmic particles passing the atmosphere should produce Cherenkov light [Blackett, 1948]. In

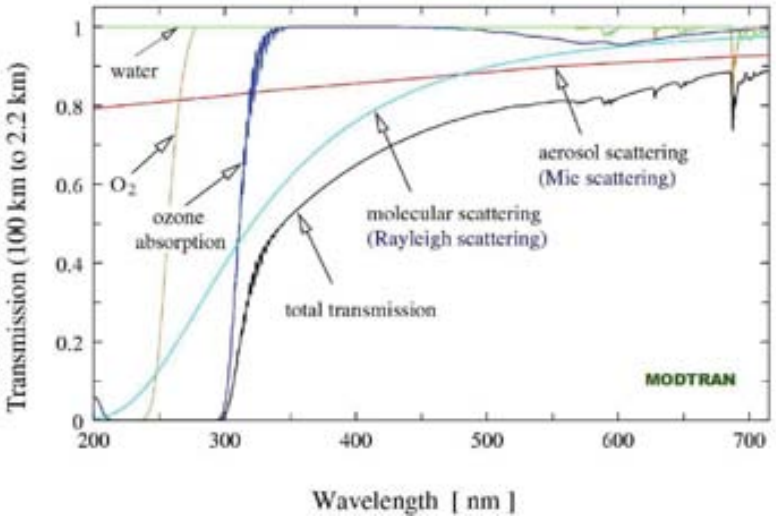

FIGURE 2.6: Direct transmission of light from space along a vertical path to an altitude of 2.2 km, as calculated with MODTRAN [Bernlöhr, 2000].

1953, B. Galbraith and J. V. Jelley made the first detection of Cherenkov light from air showers [Galbraith and Jelley, 1953]. The first setup consisted in a search-ligh mirror viewed by a photomultiplier, shielded from stray light with a garbage can. A more refined setup used larger mirrors and replacing the single PMT by a few arranged in the focal plane. These first detectors could not discriminate between hadronic and electromagnetic showers. The observers tried to identify sources by just a change in the counting rate pointing their telescopes to the sources and later, for the same exposure time, slightly off the source, however no detection was achieved. In 1968, a large 10 m telescope was completed at the Fred Lawrence Whipple Observatory in Arizona, USA. The telescope along the years implemented several upgrades, including the use of an *imaging camera*, proposed by T. C. Weekes and K. E. Turver in 1977 [Weekes and Turver, 1977] and built until 1987. With this camera and the introduction of a gamma/hadron separation method based on the calculation of image moments [Hillas, 1985], the Whipple collaboration, in 1989, published the first convincing observation of gamma-ray emissions from Crab Nebula [Weekes et al., 1989]. A extended historical review can be found in, e. g., Lorenz and Wagner [2012].

The Cherenkov photons, coming from different parts of the shower, will reach the pixels located in different regions of the camera depending on the angle between the telescope axis and the incoming photon direction. The mirror of a IACT can be parabolic or spherical (Davies-Cotton optics). In the case of a parabolic mirror, the photons coming with a certain angle β with respect to the telescope axis are focused in a certain point on the focal plane, at a distance ρ from the focal point (see Fig. 2.7). Using a coordinate system fixed in the focal plane, the focused position (ρ) can be calculated from the incoming direction of the photon (β) by the formula:

$$\rho = \sin(\beta) \cdot f \simeq \beta \cdot f \tag{2.4}$$

where f is the focal distance of the paraboloid. The approximation $\sin(\beta) \simeq \beta$ is applied for small angles. For IACTs, the field of view is small (less than 4°), therefore the approximation is justified. Thus, the distance from the focal point (camera center) varies linearly with the

incident angle. In other words, there is a univocal relation between illuminated pixels in the camera and the (almost) parallel beams of Cherenkov photons coming from the shower.

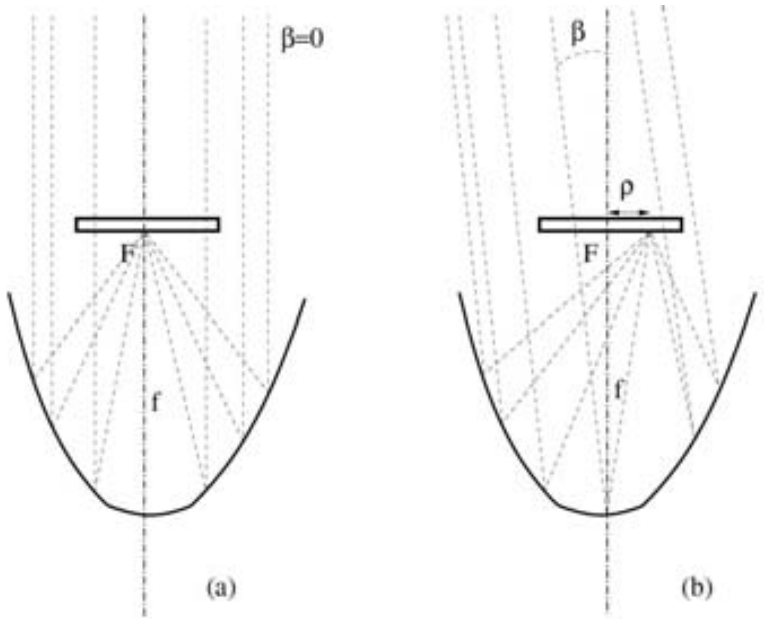

FIGURE 2.7: Image formation scheme in a parabolic reflector. If the photon beam is parallel to the parabola axis ($\beta = 0$) the photons are concentrated in the central part of the camera, located in the focal plane (a). It the photon beam is slightly inclined (an angle β), the photons are reflected into a different area of the camera (b).

Fig. 2.8 shows a schematic view of the principle of the imaging technique, where different regions of the shower form and image in the camera.The different number of secondary particles producing the Cherenkov light at different altitudes is reflected in the longitudinal structure of the recorded Cherenkov image. The image have also a transversal width that is correlated with the real width of the shower.

The major axis in the ellipse points approximately to the direction of the primary gamma-ray or particle that initiated the shower. In the case of a stereoscopic system, when a shower is recorded by at least two cameras, the triangulation allows the direction of the primary gamma-ray to be reconstructed with a better precision, as well as the impact point and the shower maximum (see Fig. 2.9). The only case when the triangulation is not possible from the images of two cameras, is when the major axes of both images are almost parallel. This may happen when the shower is in the plane defined by the centers of the telescopes mirrors and the axes of the telescopes. Having multiple Cherenkov telescopes has the additional advantage that the background signal is suppressed more efficiently by means of a coincidence trigger.

An IACT, just as any other optical astronomical instrument, has to be installed in a place with a light contamination as low as possible. However, even in optimal weather conditions, some background light will be present. These sources of unwanted light are known as Night Sky Background (NSB), and the main ones are: stars, airglow, zodiacal light, man-made artificial light and moonlight.

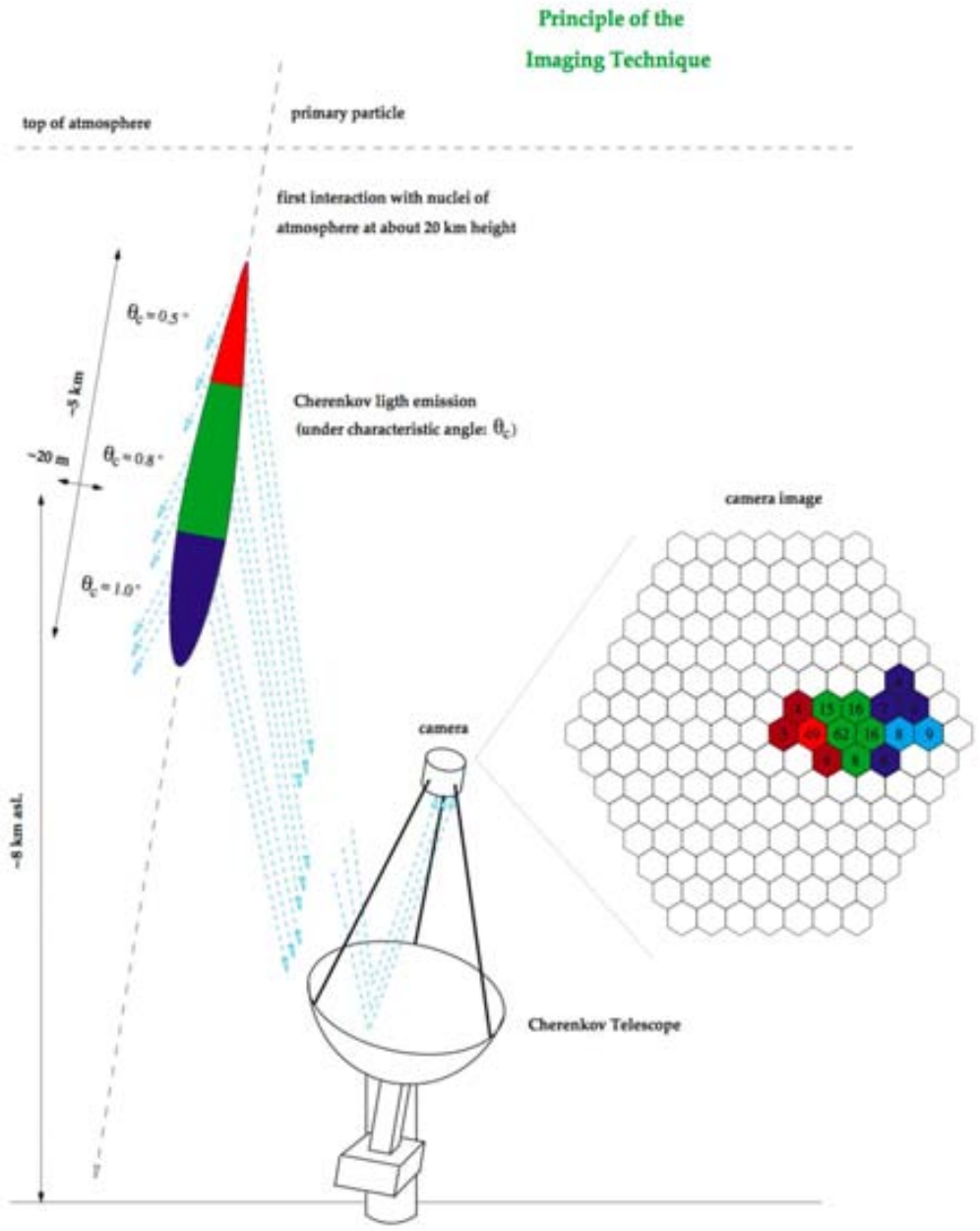

FIGURE 2.8: Image formation scheme in the camera of a Cherenkov telescope. The values are refer to a 1 TeV gamma-induced shower. The blue part is the image *head* whereas the red part is the image *tail*. The numbers in the pixels are a measurement of the light collected in the PMTs (Figure courtesy of Tescaro [2010]).

2.2.1 Basic image reconstruction

As pointed out in the previous section, the imaging technique is based in the information that can be extracted from the images recorded by the cameras. Once the image is cleaned (an algorithm to select the pixels whose signal is likely dominated by Cherenkov light from the shower, see section 2.4.0.2), it can be characterized by a set of parameters used in the analysis to recover information of the primary particle, which include its direction, energy and its nature, that is, if the shower is hadronic or electromagnetic. The basic image parameters are called

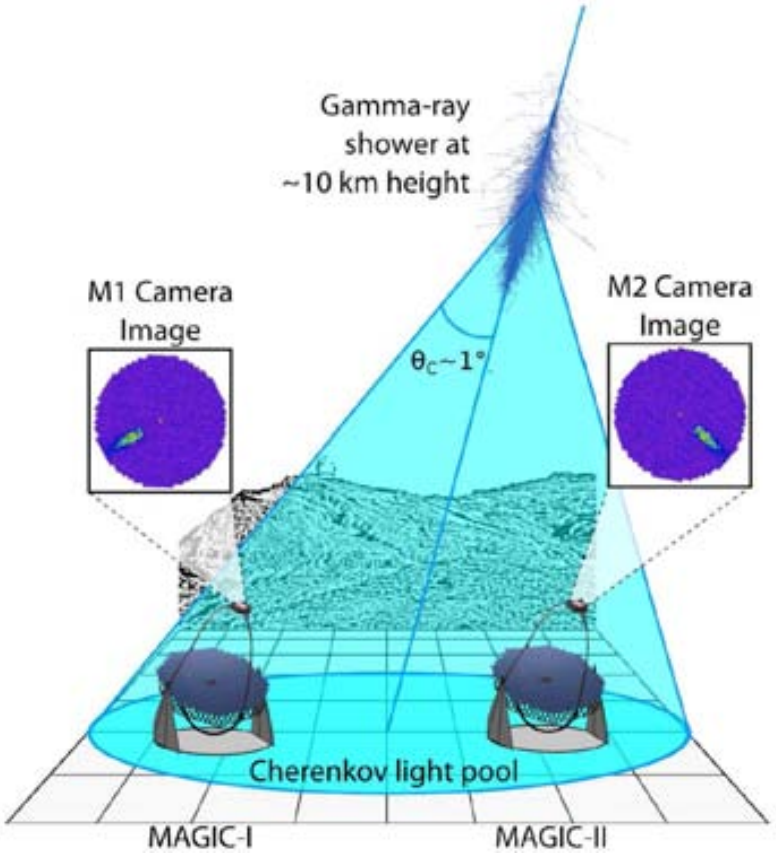

FIGURE 2.9: Stereo Cherenkov observation: two telescope collect Cherenkov light from the same shower; the shower axis and the arrival direction of the primary gamma-ray is reconstructed from the orientation and position of the shower image in the two cameras, since the telescope pointing direction is known (Figure courtesy of Giavitto [2013]).

Hillas parameters [Hillas, 1985]. A graphical description of the image parameters can be seen in Fig. 2.10. For the particular case of the standard MAGIC analysis, the parameters are:

- **SIZE** Total number of photo-electrons collected in the shower image, defined as:

$$\textbf{SIZE} = \sum_{i=1}^{k} N_i \tag{2.5}$$

  This parameter, for a fixed zenith angle of observation and *impact parameter* value (distance of the shower axis to the telescope axis), and primary particle type (gamma rays) is roughly proportional to the energy.

- **LENGTH** Second order moment of the light distribution on the camera, computed along the major axis of the shower ellipse.

- **WIDTH** Second order moment of the light distribution on the camera, computed along the minor axis of the shower ellipse.

- **DIST** Distance between the image centroid and the source position in the camera. This is correlated to the impact parameter of the shower.

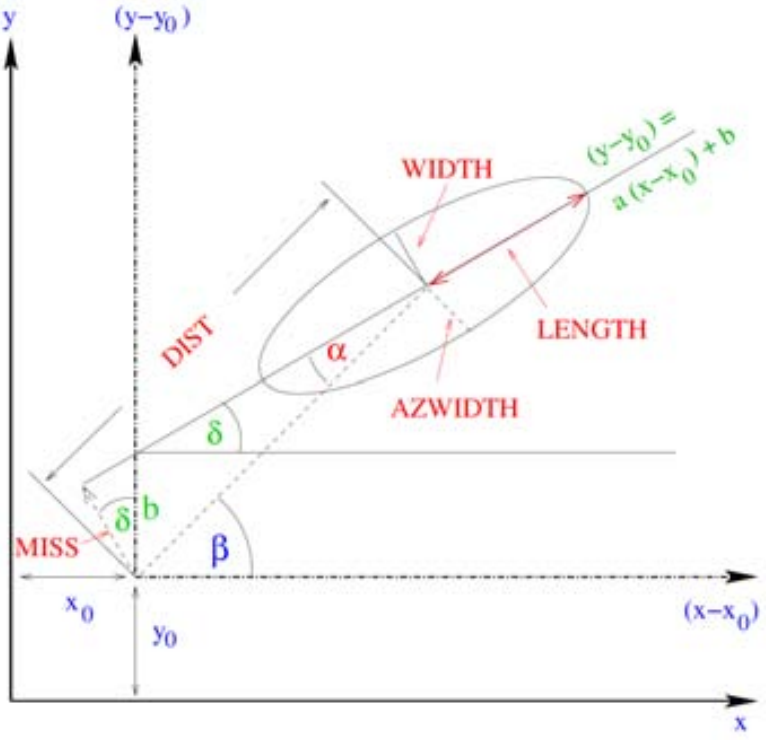

FIGURE 2.10: Graphical representation of the image parameters. The source is located in (x_0, y_0).

- **ALPHA** Angle between the major axis of the ellipse and the line joining the centroid and the source position.
- **CONC**[n] Fraction of the total amount of photoelectrons contained in the n brightest pixels.
- **LEAKAGE** Fraction of the light on the image contained in pixels that belong to the outermost ring of pixels of the camera. This parameter is useful to recognize images partially outside the camera.
- **M3LONG** Longitudinal third moment of the distribution of the charge along the major axis. It measures the asymmetry of the image, since it determines the side of the image with larger or lower charge.

The specific analysis for MAGIC, including the stereoscopic reconstruction, is described in section 2.4.

2.3 The MAGIC Telescopes

The Major Atmospheric Gamma-ray Imaging Cherenkov (MAGIC) "Florian Goebel" Telescopes are two IACTs located at the Observatorio del Roque de los Muchachos (ORM) in the Canary Island of La Palma, Spain, at an altitude of 2225 m above sea level. Both telescopes have a diameter of 17 m and a mirror surface of 236 m^2. The large reflector area of MAGIC was designed with the purpose to achieve low energy threshold to cover a then-uncharted energy region between ∼10 GeV and ∼ 200 GeV [Barrio, 1998a]. The cameras of both telescopes are

FIGURE 2.11: MAGIC Telescopes operating under moonlight. On the left is MAGIC-I and on the right MAGIC-II.

equipped PMTs with enhanced quantum efficiency. The MAGIC telescopes have a light-weight design: many elements in the structure are made of aluminum and reinforced carbon fiber, and the readout electronics is separated from the camera, reducing its weight. This design allows the telescope to move relatively fast in order to respond the fast as possible to alerts for transient events, such as Gamma-Ray Bursts (GRBs), that are flashes of gamma rays lasting a few tens of seconds. The MAGIC Collaboration comprises more than 150 members from several institutions in several countries, mainly from Germany, Spain and Italy.

Historically, MAGIC started operations with only one telescope, now called MAGIC-I, which was completed in 2003. For six years it operated in standalone mode until 2009, when MAGIC-II became operative. The structural design of MAGIC-II is the same as MAGIC-I. However, cameras and readout systems where different. MAGIC-I had a camera of 577 pixels of two different sizes and a readout system based on a Flash Analog-to-Digital Converters [Goebel et al., 2008]. MAGIC-II has a 1039 pixels camera and the read-out was based on the chip Domino Ring Sampler v2 [Pegna et al., 2007, Ritt, 2004]. In the summers of 2011 and 2012, the system underwent into an upgrade to make it more homogeneous. Both readouts were substituted by a solution base on the Domino Ring Sampler v4 [Ritt, 2008] and the MAGIC-I camera was exchanged for a camera with the same design as MAGIC-II.

MAGIC is what is called a "third generation" Cherenkov telescope. Other third generation Cherenkov telescopes are the High Energy Stereoscopic System (HESS.) and the Very Energetic Radiation Imaging Telescope Array System (VERITAS). HESS is located in the southern hemisphere in Namibia, whereas VERITAS is in the northern hemisphere, in Arizona, U.S.A.

2.3.1 Main components of the telescopes

2.3.1.1 Telescope structure and drive systems

The telescope structure supporting the mirrors is a three-layer frame of octagonal shape, based on a carbon fiber-epoxy tubes joined by aluminum knots (see Fig. 2.12 (a)). The maximum deformation of the structure, according to the specifications, is below 3.5 mm, for whatever position of the telescope. Apart of its rigidity, the structure has negligible thermal expansion and an excellent oscillation damping. Additionally, the carbon fiber-epoxy is also specially

resistant to the hard atmospheric condition of the site: strong solar radiation in summer, very low temperatures in winter, and occasional rain and even snow.

(a) (b)

FIGURE 2.12: Structure of MAGIC Telescopes: (a) aluminum knot joining the fiber-epoxy tubes, (b) general view of MAGIC-II structure, where the metallic arch holding the camera and the three-layer frame supporting the mirrors are clearly visible.

The camera is sustained by a metallic arch, stabilized by 10 pairs of steel cables tied to the main frame. Following a circular shape, the arch continues also over the back of the dish becoming a rail for the altitude drive and support for the counterweights (see Fig. 2.12 (b)). This allows the telescope to move $-90°$ to $+90°$ in zenith during normal observations, although it can be pointed slightly below the horizon ($> +90°$). The whole structure is connected to six bogeys resting on a circular rail, enabling a movement on azimuth from $-90°$ to $+318°$.

The movement on azimuth of each one of the MAGIC telescopes is provided by two 11 kW motors, mounted on two out the six bogeys close to the support towers, in diametrically opposite positions. A chain fixed to the rail forms a mechanical drive link to the motors, which are engaged by toothed wheels. The elevation axis has a single motor of also 11 kW installed in the arch base.

During regular observations, the telescopes are able to track a source with a precision of about $0.02°$, thanks to two absolute shaft-encoders that constantly monitor the position of the two telescope axes. The calibration between the shaft encoder values and real pointing coordinates is done with a star-guider camera, mounted on the center of the mirror dish. The star-guider camera points to the telescope camera but its field of view (FoV) is large enough to see also directly some of the stars in the FoV of the telescope. Then, it compares the position of the MAGIC camera, aided with a ring of LEDs placed at the camera edges, with the position of the background stars.

The drive system has a fast repositioning mode that can rotate the telescope $180°$ in azimuth in 20 s. This fast mode is used only in the case of a GRB alert.

2.3.1.2 Reflector and mirrors

The parabolic reflector has a diameter of 17 m as well as its focal distance f. The total surface area is a little over 236 m^2. The reflector is tessellated consisting in 247 facets. Each facet is a movable 1 m^2 mirror unit, which are adjusted by an *Active Mirror Control* (AMC) system depending on the orientation of the telescope. In MAGIC-I each unit consists of 4 individual spherical mirror tiles mounted in a panel (see Fig. 2.3.1.2 (a)). In MAGIC-II each unit is a single mirror of 1 m^2 (see Fig. 2.3.1.2 (b)).

(a) MAGIC-I mirrors, each 1 m^2 unit is composed of 4 mirrors

(b) MAGIC-II mirrors, each unit is a single mirror of 1 m^2

Three types of mirrors are installed in the MAGIC telescopes:

- **0.25 m^2 aluminum mirror.** They are composed by an aluminum box open on the upper side where a honeycomb aluminum structure is inserted to guarantee rigidity of the mirror. A thin aluminum plate is located on the top of the mirror and glued to the honeycomb. This layered setup is called the "sandwich" . The aluminum plate is polished with a special diamond milling machine which make the surface reflective. The reflecting surface is protected with a layer of quartz-based material which coats the mirror to prevent scratches and oxidation of the aluminum. MAGIC-I is composed almost entirely by these 0.25 m^2 aluminum mirrors. These mirrors are not directly mounted on the frame but in panels holding 4 mirrors each. The panel is mounted on the frame through the actuators of the AMC.
- **1 m^2 aluminum mirrors.** The structure of the 1 m^2 mirror is pretty similar to the 0.25 m^2 one, it is basically a scaled version of the same mirror. The main difference is the use of a mold to shape the whole mirror sandwich with a spherical curvature roughly similar to the final one before proceeding to polish the surface. In such a way the thickness of the aluminum plate can be maintained small since there is no need to create the whole curvature milling the center of a flat plate. Out of the 247 mirrors tiles of MAGIC-II, 143

are of 1 m^2 aluminum mirrors. These mirrors are directly mounted on the frame through the actuators of the AMC.

- **1 m^2 glass mirrors.** The remaining 104 mirrors tiles of MAGIC-II are produced as sandwich of glass plates around an aluminum honeycomb layer using a "cold slumping" technique. The frontal glass surface is coated with a reflecting aluminum layer and a protective quartz coating. This kind of mirror has a slightly better reflectivity with respect to the aluminum mirror, and has a lower production cost.

All mirror facets in both telescopes are spherical with a curvature radius varying from 34 m to 36.7 m, depending on their position in the dish. Their typical point spread function (PSF, defined as the 39% containment radius of the reflected spot of a point-like source on the focal plane of the mirror) is less than 10 mm wide, so most of the reflected light is contained inside a single PMT.

The parabolic reflector has the advantage of being an isochronous surface, that is, the relative arrival times of the photons are conserved on the camera plane. This allows to have a reduced level 1 trigger window (described in section 2.3.1.4) and consequently lower the contamination of the NSB. However, the reflector suffers from several aberrations: curvature of the field, astigmatism, finite quality aberration, tessellation aberration and coma aberration. The effective contribution of all is to smear the reflected image, making the PSF larger. This is mitigated by the AMC. Coma aberration, affects off-axis images only and cannot be corrected by the AMC.

2.3.1.3 Camera

The camera is one of the most critical systems of the telescope. The sensitivity, energy threshold and signal/background discrimination are highly dependent on the capability of the camera to generate good quality shower images. The MAGIC cameras are temperature stabilized cylindrical boxes with a diameter of 1.46 m and a thickness of 0.81 m.

(c) Front view of the MAGIC-II camera

(d) Back view of the MAGIC-II camera without its protective cover

FIGURE 2.13: MAGIC-II camera. The MAGIC-I camera, after the upgrade, has the same design of the MAGIC-II camera.

The camera host clusters of PMTs that convert the Cherenkov photons from the air showers into electrical signals. The PMTs from both cameras have a high Quantum Efficiency of around

20-30% depending on the wavelength. The photon entrance of each PMT is equipped with a hexagonal light collector (Winston cone), that increases the entry window for each pixel as well as the double-crossing probability of photons with a large incidence angles. The PMTs are protected from atmospheric agents and light by a plexiglass window and movable lids (see Fig. 2.13 (c)).

The pre-upgrade MAGIC-I camera was of hexagonal shape, and a FoV of $\sim 3.6°$. It was equipped with two types of PMTs: 397 in the inner section of the camera of 30 mm diameter and 180 PMTs in the outer region of 60 mm diameter. The trigger region of the camera was circumscribed by the inner section of the camera. The central pixel of the camera was specially designed to perform optical measurements (e.g. optical pulsations of the Crab Nebula pulsar) to check the time-stamp of the overall system. This camera was uninstalled in summer 2012.

The post-upgrade MAGIC-I camera and the MAGIC-II camera have the same design, with a roughly circular shape, 1.2 m diameter and a FoV of 3.5°. It is composed of 1039 PMTs of 30 mm ($\sim 0.1°$ FoV) . The trigger area covers the innermost 2.5° diameter region ($\sim 5\%$ larger than the pre-upgrade MAGIC I camera trigger region). The PMTs are grouped in a hexagonal configuration of 7 members to form a *cluster*. Each cluster is independent from the others, which allows easy exchange of faulty ones.

2.3.1.4 Data acquisition

The Cherenkov photons that arrive to the camera are converted into an electric signal by the PMTs. The electric signal is amplified and converted into optical pulses by the Vertical Cavity Surface Emitting Laser (VCSEL). The output of the VCSEL is coupled to 162 m optical fibers that transmit the signal from the camera (see Fig. 2.13 (d)) to the *Counting House*, a building hosting the rest of the electronics and the operations center. In the electronics room, inside the Counting House, the optical pulse is converted back to an electronic signal in the receiver boards through a photodiode and split in two branches. One branch is transmitted to the trigger system, while the other is amplified and passed to the Data Acquisition System (DAQ) (see Fig. 2.14).

The telescope *trigger* is a multiple level decisional system which determines the acquisition of an event in time coincidence with a EAS. The Cherenkov light from an EAS is typically much more intense that the NSB light and illuminates several neighboring pixels at the same time. The first three levels of trigger work over the individual telescope signal, while the fourth is shared by both the instruments (see Fig. 2.14).

- **Level zero (L0).** Hosted in the receiver boards, it evaluates every channel individually and issues a trigger only if the signal is above a certain discriminator threshold.
- **Level one (L1).** L0 signals are sent to L1, whose task is to determine if the channels have spatial and temporal correlation over the decomposition of the trigger region in 19 overlapping macrocells. This topology is based on the close compact next neighbor logic (CCNN), that is, if there is N neighboring pixels, and one of those pixels is remove, the N-1 remaining pixels has to be also neighbors (no pixels remains isolated). The CCNN can be setup with 2NN, 3NN, 4NN and 5NN configuration, being the 3NN the standard in regular observations.

- **Level two (L2).** It has the task of measuring the trigger rate and eventually imposing a scaling factor to the rate of events. This unit has no decisional power and merges L1 triggers with triggers generated by the calibration system and the stereo trigger.
- **Level three (L3).** Is a coincidence trigger, accepting only events that have triggered both telescopes within certain time interval. In order to minimize the coincidence gate in the level 3 trigger, the triggers produced by the individual telescopes are delayed by a time which depends on the pointing direction of the telescopes.

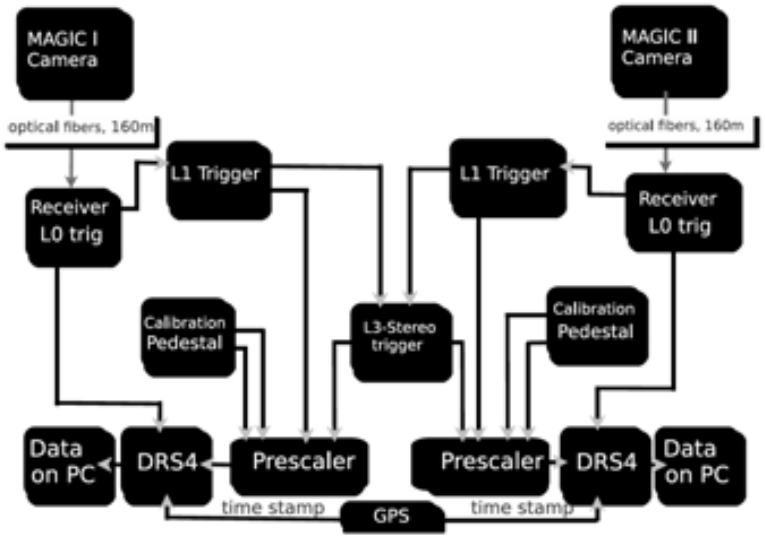

FIGURE 2.14: Electronic chain of the MAGIC telescopes (from [Sitarek et al., 2013]).

Before the upgrade, the two telescopes had different electronics to process the signals, but with the upgrade now both telescopes use the same system, based upon a analog sampler called *Domino Ring Sampler* version 4 (DRS4). The DRS4 is based on an array of 1024 capacitors for each channel. When running the system with a sampling speed of 2 GSample/s, the input signal is stored in analog form in the capacitors with a switching period of 500 ps, which results in a 512 ns deep buffer. After a trigger occurs, the sampling is stopped and the chargers of the capacitors are read out by an analog to digital converter of 14bit precision at a speed of 32 MHz [Sitarek et al., 2013].

2.3.1.5 Calibration

The signals recorded by the FADCs have to be calibrated in order to translate the information into incident light flux in the camera. This implies the calculation of the conversion factor between the number of recorded FADC counts and the number of photoelectrons in the PMT.

The calibration system is installed in the center of the telescope reflector. It consists of a frequency tripled passively Q-switched Nd-YAG laser, whose beam passes through two filter wheels with different attenuation factors, allowing for easy adjustment of the pulse intensity. After attenuation, the laser beam is diffused via an integrating (Ulbricht) sphere, providing a homogeneous illumination of the camera.

The calibration is done basically in two steps. First a relative calibration equalizes the response of different channels when exposed to the same input signal. Second, an absolute calibration

is computed using the method called *F-Factor*. This absolute calibration is needed for the conversion of the signal recorded by a pixel in FADC counts into physical quantities related to the flux of photons. The method is based on the fact that a PMT adds only a small excess noise to the intrinsic fluctuations of the photoelectron flux. This excess noise is linearly related to the initial number of photoelectrons that produce its output signal. The F-Factor is a numerical value that accounts for the additional noise introduced by the readout and amplification chain, assuming it is independent of the signal intensity. Knowing the F-Factor of the PMTs and the analysis of the pixel signals in a series of close-in-time calibration events, it is possible to derive the average number of photoelectrons impinging on the first dynode of each PMT.

2.3.2 Observation modes

The observation with MAGIC can be done either in on-source tracking mode, usually called just *tracking*, or in false-source tracking mode, also know as *wobble*. The observation mode affects the way the background signal is estimated.

In *tracking* mode, the telescopes are pointing directly to the source, which means that the nominal position of the target is located in the center of each camera. For the background estimation, in this observation mode, is necessary to additionally observe a sky region where no known gamma-ray sources is present with the same observational conditions. The latter cannot be guaranteed since atmosphere conditions can change. Moreover, since a time has to be dedicated to the off-source observations, this reduces the effective time available for the source observation.

Most of the observations with MAGIC are done in the *wobble* mode [Fomin et al., 1994]. In this mode, the telescope tracks alternatively two or four directions in the sky located at a defined offset of 0.4° from the source position. This has the advantage that there is no need to spend time to perform off observations because the background estimation is done using the same observation field. If the source is positioned far enough form the camera center, is possible to define *off regions* in the same field of view not affected by the gamma-ray source. If only two alternating, or "wobbling" directions are used, then the off region will be the "anti-source" position, located 180° around the camera center from the real source in the plane of the camera. In case of four wobbling directions, the positions are 0, 90, 180 and 270 degrees around the camera center. These directions sometimes are modified to avoid including a bright star or even another gamma-ray source in one of the off regions. The wobbling happens every ∼20 minutes, in this way, possible inhomogeneities in the acceptance of the field of view cancel out. A drawback of the wobble mode is loss in the gamma-ray efficiency due to the source being closer to the edge of the trigger region.

2.4 The MAGIC analysis pipeline

Once the data has been taken and stored, the process to differentiate the events initiated by gamma-rays from the ones initiated by hadrons, and the determination of the energy and direction of these primary gamma-rays is done via software.

The software for the analysis of MAGIC data is called MARS, acronym of MAGIC Analysis and Reconstruction Software [Moralejo et al., 2009]. MARS is written in C++ language and embedded in the framework of ROOT, which is a software developed at CERN [2].

The analysis of the MAGIC data is composed by several consecutive steps that will be described in the following sections.

2.4.0.1 Calibration

Before the actual *calibration* of data, the RAW files are converted into a format compatible with ROOT, and therefore with MARS. In this process, information regarding the observation conditions and performance from the subsystems are appended. This task is handled by an executable called `merpp`.

The *calibration* is performed by the executable name `sorcerer`. The Cherenkov photons flashes produce temporarily very short signal pulses on the PMTs. Each pulse is digitized with a sampling frequency of 2 GSample/s (see section 2.3.1.4). With the digitization system after the upgrade in MAGIC, 60 samples are recorded for each pulse. Every pulse is analyzed with the *signal extractor*. In the signal extraction, the amplitude of the signal and its arrival time is determined. The extraction is done following an algorithm called "sliding window": 60 recorded samples are scanned and the "window" is chosen for the 6 contiguous samples that give the maximum sum, the signal arrival time is the average of these 6 samples inside the window, weighted with the slice value and corrected for non-linearity of the sampling speed.

The signal intensity is calibrated, that is, converting the counts into number of photoelectrons (phe) arriving at the first dynode of the PMT. The conversion is performed using the *F-Factor* method [Mirzoyan, 1997]. Special data runs of pedestal and calibration events are taken for this purpose during the data taking. The pedestal events are obtained randomly triggering the telescope, so that no shower signal are recorded in the pixels and the data can be used to determined the baseline of the signals and its fluctuations. Calibration data events are generated by short ($\simeq$2 ns) light pulses of intensity comparable to the real Cherenkov signals. These events are digitally triggered and stored in special data runs called *calibration runs*. The number of phe produced in calibration runs are assumed to follow a Poisson distribution with mean N, and standard deviation $\sqrt{N}$. If the charge from calibration events measured in FADC counts has mean value $\langle Q \rangle$ and standard deviation σ_Q, the F-Factor is defined for each PMT as:

$$F = \frac{\sigma_Q \sqrt{N}}{\langle Q \rangle}. \tag{2.6}$$

The conversion factor C from a FADC counts to phe depends on F^2:

$$C = \frac{N}{\langle Q \rangle} = F^2 \frac{\langle Q \rangle}{\sigma_Q^2}. \tag{2.7}$$

During the data taking there can be variations in the transmission of the signal from the camera to the readout. To keep the conversion factors constantly updated, interleaved calibration events are also taken. See Gaug 2006 for a more detailed description of the calibration procedure.

[2] http://root.cern.ch/drupal/

2.4.0.2 Image cleaning and parameterization

With the information from each pixel property calibrated, the next step is the reconstruction of the Cherenkov images. This process is performed by the executable in MARS called `star`.

The charge and arrival time information from each pixel for each recorded event are used to identify noise generated by the NSB light and remove it from the shower image. This process is known as the *image cleaning*. In MAGIC two image cleaning algorithms are used: the *absolute* cleaning and the *sum* cleaning. In both methods, first, the pixels that actually form the shower image are identified and classified between *core* and *boundary*. Then, the remaining ones (the pixels containing noise) are removed (see Fig. 2.15). The difference between two cleaning methods is the way the image core is defined. The absolute cleaning was the standard for data analysis up to 2011, since the sum cleaning was developed later.

The absolute method uses a threshold phe value to select the core pixels. Only clusters with two or more contiguous pixels with charge above the threshold are considered to form the core. Then, a second threshold value is used to select the neighbors as boundary pixels. Apart of being above the boundary threshold, a pixel is selected as boundary at least one of its neighbors is a core pixel. The method is called absolute because the threshold values are set as absolute numbers of phe in the pixel (a common alternative is to set the threshold relative to the noise fluctuations in the pixel).

In the sum cleaning, the amplitudes of the signal are clipped and all possible 2NN, 3NN and 4NN combinations are summed up. If the sum is above certain charge threshold, then the pixels belonging to the group that gave that sum are accepted as core pixels. The clipping ensures that NSB fluctuations or PMT afterpulses do not dominate the summed signal. The signal of the core pixels should be within a given time window. For pulses just above the charge threshold, the coincidence probability for signals from showers falling within the time window is $\approx$ 80 - 90%. The charge thresholds on the sum of 2NN, 3NN and 4NN groups are 2×10.8 phe, 2×7.8 phe, 4×6 phe and the corresponding time windows: 0.5, 0.7 and 1.1 ns. The boundary pixels are selected doing a loop over al pixel neighboring a core pixel, and then are selected if the charge is above 3.5 phe and the signal arrived within 1.5 ns with respect to the core pixel.

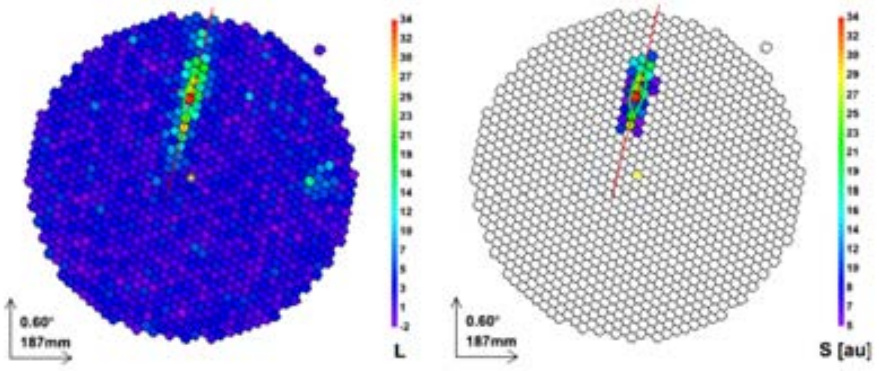

(a) Reconstruced charges (phe) (b) Cleaned image

FIGURE 2.15: Image cleaning: actual shower image in MAGIC-II camera. In the position of the shower is superimposed the Hillas ellipse parameterization.

Once the images are cleaned, then the parameters listed in section 2.2.1 are calculated. After this step only the image parameters values are kept. Information that is not relevant for higher analysis is dropped, for example, data from single pixels signal. This reduces significantly the size of the data.

Additionally, timing parameters, that exploit temporal properties of the shower, are computed. These are:

- **Time RMS**. Is a measure of the arrival time spread of all pixels that survived the image cleaning. It can be used as discriminator between gamma or hadron-iniciated showers.
- **Time gradient**. Is the linear coefficient of a fit to the arrival time of pixel signals vs their position along the major image axis. The sign of this parameter (positive or negative) is defined with respect to the point which correspond to he reconstructed event direction (i.e. roughly the intersection of the major axes of the two images).

Finally, to evaluate the quality of the cleaned images, the following parameters are computed:

- **LeakageN**. Fraction of the charge contained in the N outermost pixel rings of the camera. It serves as an estimator of the portion of the shower image that spills over the camera.
- **Number of islands**. Number of isolated groups of pixels that survive the image cleaning procedure. Gamma-ray showers are expected to generate a single-island image in most occasions, while the hadronic ones may produce several islands in a single event image. Also strong moonlight can generate islands from pure fluctuations of background light, which would require to increase the cleaning thresholds in order to get rid of such spurious islands.

2.4.0.3 Stereoscopic reconstruction

The events that survive the image cleaning, on standard observations, are around 80%, the rest are discarded. The surviving events are paired with the executable `superstar`. With this program, also stereo parameters are computed (see, e.g. Kohnle [1996]):

- **Shower axis**. The direction of the shower can be found by purely geometrical parameters by intersecting the major axes of the two elliptical images (these result is further enhanced using the *disp* parameters, to be described in the next section). Also, from this intersection and the knowledge of the telescope position and pointing direction, the impact point is calculated (see Fig. 2.16).
- **Impact parameter**. The perpendicular distance between the shower axis and the center of the telescope mirror.
- **Shower maximum height**. With the stereoscopic reconstruction is also possible to estimate the height at which the largest amount of Cherenkov light is coming from. This height will correspond approximately to the maximum of the shower.
- **Cherenkov radius**. The radius of the Cherenkov light pool on the ground, calculated assuming that the Cherenkov light is produced by a single electron with energy $E = 86$ MeV at the calculated shower maximum height.
- **Cherenkov photon density**. The density of Cherenkov photons on the ground, computed assuming the same conditions as the Cherenkov radius.

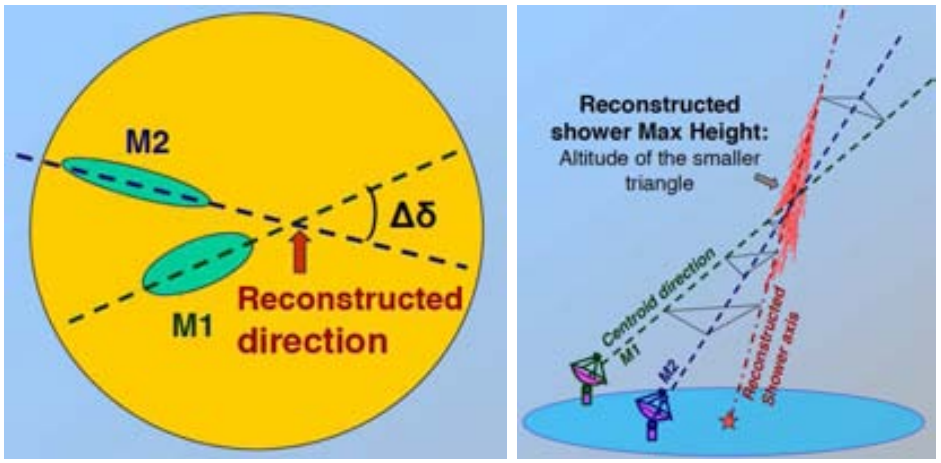

(a) Reconstruction of the shower direction

(b) Reconstruction of the shower maximum

FIGURE 2.16: Stereoscopic reconstruction of a shower maximum and the shower axis from the images on the camera and the position and pointing direction of the telescopes. Images credit, P. Colin.

2.4.0.4 gamma/hadron separation

The gamma/hadron separation in the MAGIC analysis is done using a flexible multivariate classification algorithm called *Random Forest* (RF) [Albert, 2008b, Breiman and Cutler]. This algorithm needs as inputs events of known nature, that is, images from electromagnetic and hadronic showers. The hadronic shower images are taken from real observations of regions of the sky where there is no know gamma-ray sources (called *off-data*). The gamma-ray events are taken from Monte Carlo (MC) simulations.

In the MC simulation, extensive air showers initiated by cosmic gamma rays are produced massively. The simulations include all the detection process with MAGIC: the air shower (simulated with CORSIKA [Heck et al., 1998]), the tracking of Cherenkov photons from the shower to the reflector and into the camera, the formation of shower images in the camera pixels, and the data acquisition. The simulations also include several aspect of the telescope that affect the detection of Cherenkov photons, for example, optical properties of the mirrors or the trigger thresholds. Therefore, the MC simulations have to be updated whenever there is a change in the telescopes hardware that may affect the detection process.

For the data analysis, the MC simulations are split into two samples: the so-called *training* sample, used in the production of the RF, and the other, the *test* sample, used for the evaluation of the instrument response functions (effective area, energy resolution, angular resolution, etc.). The training and test samples have to be independent, in order to avoid biased results.

The RF is based on *decision trees*. These trees are a set of consecutive cuts on the image parameters width and length (described in section 2.2.1) and the stereoscopic parameter for the shower maximum. A tree is built first taking a random sample from the training gammas (from the MC) and hadron events (from the off-data). A cut in one of the separation parameters is applied and the initial sample is split in two accordingly. These form the first two *branches*. These two branches most likely will still be a mix of gamma and hadron events. Therefore, the process is repeated iteratively. In each split, one of the separation parameters is chosen randomly, then a cut that better separates the samples applied. The optimizations of the cuts

is obtained minimizing the *Gini index* [Gini, 1921]. This index is expressed in terms of the number of gamma events, N_γ, the hadron events, N_{hadron}, and the total number of events in the tree, N:

$$Q_{Gini} = 4 \cdot \frac{N_\gamma}{N} \cdot \frac{N_{hadron}}{N}. \tag{2.8}$$

The process finish when a sub-sample composed only by gamma events or by hadronic events is reached. This final sample is called a *leaf*. The leaf is labeled as 0 if its made of gammas or 1 in the other case. The generation of the RF is done with the executable in MARS called `coach`.

Once the RF is produced, all the events from the actual data sample to be analyzed are passed through all the separating trees. Depending on the parameters values for each event, it will reach a leaf, scoring 1 or 0 depending on the leaf label. Averaging over all the results from the separations trees a mean score is computed, called *hadronness*. The gamma-like events will have a hadronness closer to 0, whereas an hadronic one will tend to 1. This classification is handled by the executable `melibea`.

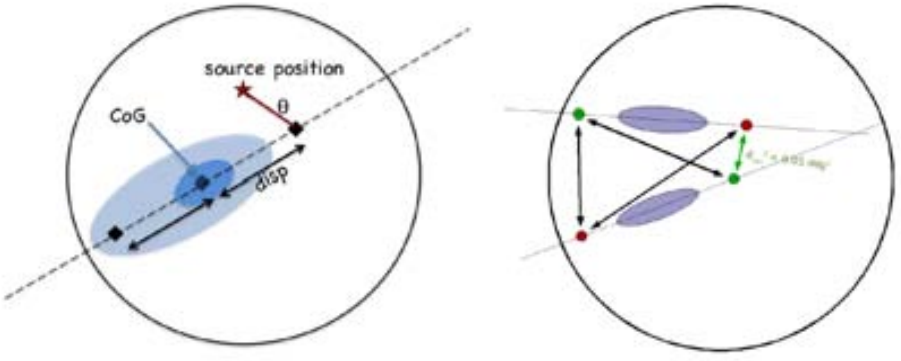

(a) *Disp* parameter. Image credit: R. Zanin

(b) Primary particle direction using *disp* from each telescope. Image credit: S. Klepser

FIGURE 2.17: Geometrical definition of *disp* parameter. Seen by a single telescope, the shower impact point has two possible degenerate solution. The degeneracy is broken in a stereoscopic shower reconstruction, by choosing the closest possible pair.

From the stereo parameters, listed in the previous section, it is possible to reconstruct the direction of the primary gamma-ray. However, more accuracy can be achieve including a parameter used for the direction determination with a single telescope. The *disp* parameter is the estimated distance between the image centroid and the source position, under the assumption that the source position is in the line containing the main axis of the Hillas ellipse. As shown in Fig. 2.17 (a), there is two possible solutions on either side of the image centroid. The ambiguity can be solved from the asymmetry along the main axis of the image. However, for events at high energy, the images can be truncated, whereas for event at low energies, the images consists of few pixels, making in either case difficult to resolve the asymmetry of the Hillas ellipse. Since the shower elongation-*disp* correlation invokes a multi-parameter space, a RF algorithm also has been implemented. This *Disp RF* is trained with a sample of gamma-ray events from MC and it grows the corresponding decisional trees to evaluate the correlation between the disp and the parameters that may influence the determination of disp value. The disp values are estimated

for events in each telescope separately. In each telescope there are two possible reconstructed source positions along the image major axis (see Fig. 2.17 (b)). When the events are merged, the distances between all possible position pairs combinations are computed. The closest pair is chosen as correct, and the arrival direction is determined as the weighted average of those positions plus the crossing point of the major axes of the images. The angular distance from this point to the nominal source position is called θ.

2.4.0.5 Statistical significance of a detection

The squared value of θ can be used to evaluate the *significance* of the detection of the observed source. The hadronic events are expected to have isotropic arrival directions, therefore the θ^2 distribution for this *background* should be flat. For point-like sources, the θ^2 allows us to check if the background around the source is consistent with the background computed in the *OFF* region. Then, the histogram of θ^2 calculated with respect to the nominal source position should peak close to zero for the gamma-ray events coming from the source. A region called *ON* is defined as a "cone" of directions around the nominal position of the source (a circle in the camera) (see Fig. 2.18). An independent region where gamma-ray signal is not expected is defined as the OFF region. From the measured number events in the *ON* region, N_{ON}, and *OFF* region, N_{OFF}, the number of excess events N_{ex} is:

$$N_{ex} = N_{ON} - \frac{N_{OFF}}{\tau} \tag{2.9}$$

where τ is the normalization factor between *ON* and *OFF* regions.

The statistical test used to evaluate the detection significance S of a source signal is from Li and Ma [1983]:

$$S = \sqrt{2}\left\{ N_{ON} \ln\left[(1+\tau)\left(\frac{N_{ON}}{\tau N_{ON} + N_{OFF}}\right)\right] + \frac{N_{OFF}}{\tau} \ln\left[(1+\tau)\left(\frac{N_{OFF}}{\tau N_{ON} + N_{OFF}}\right)\right]\right\}^{1/2} \tag{2.10}$$

Detection of a source is claimed when the significance is $S \geq 5\sigma$. A 5σ excess has a probability 3×10^{-7} of being produced by a purely statistical fluctuation of the background.

2.4.0.6 Energy estimation

The energy estimation for each event is estimated through the use of *look-up tables* (LUTs). The LUTs are built from the simulated gamma events. The LUTs relate the energy of the events with the impact parameter, the Cherenkov radius, r_C, and the Cherenkov density, ρ_C. The sample of simulated gamma-ray events is divided in bins of $size$ and in bins of $impact/r_C$ ratio. The energy of the primary gamma-ray is proportional to $size/\rho_C$, then each of the table bins contains the mean value of the distribution of $E_{true} \times \rho_C/size$, where E_{true} is the true energy, and the uncertainty is given by the RMS of the distribution. A bias from the dependence of the zenith angle Zd, is corrected using the empirical factor $0.4 \times \cos(Zd)$. A second correction is applied to account for a small azimuth dependence coming from the geomagnetic field effect. For each telescope, an estimated energy and its uncertainty is computed, then, the final estimated energy E_{est} is the weighted average of the two estimations.

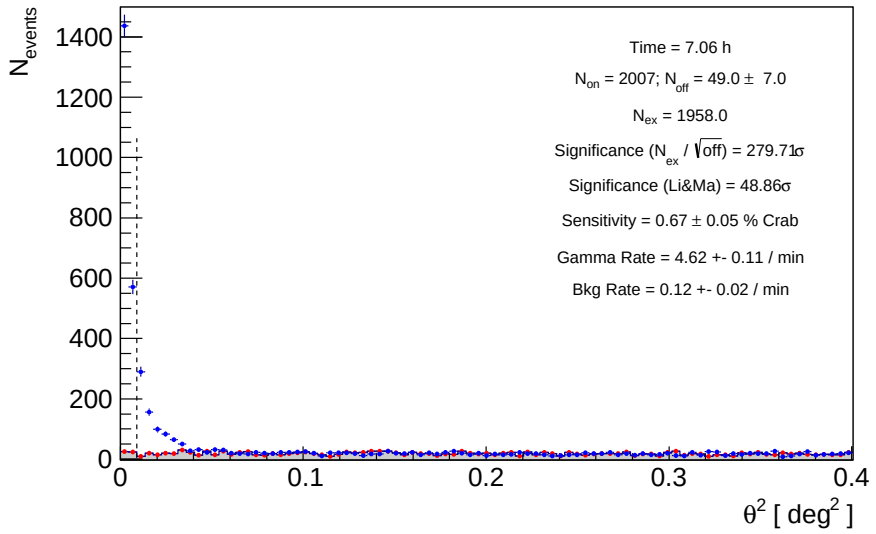

FIGURE 2.18: Example of a θ^2-plot from a 7-hours observation of Crab Nebula. The blue points represent the excess gamma-ray events, whereas the red points are the background estimation. The *ON* region is defined between $\theta^2 = 0$ and the vertical dashed line. The background control region is set (standard analysis) between 0.15 and 0.3 deg^2.

2.4.0.7 Reconstruction of the energy spectrum and light curve

One of the main objectives of the analysis is the calculation of the energy spectrum of the sources. The differential gamma-ray energy spectrum is given by:

$$\frac{d\phi(E)}{dE} = \frac{dN_\gamma}{dE \times dA_{eff} \times dt_{eff}} \quad , \tag{2.11}$$

where N_γ is the number of detected gamma rays, t_{eff}, the exposure time, corrected for the *dead time* of the readout electronics and A_{eff} is the *effective collection area*.

The A_{eff} is the geometrical area around the telescope where gamma-ray showers produces trigger events that survive the whole analysis process, A_{sim}, folded with the gamma-ray efficiency ε_γ for all the cuts applied in the analysis. It is computed from the MC simulations and depends on the true energy E of the primary gamma-ray:

$$A_{eff}(E) = A_{sim}\varepsilon_\gamma(E) = A_{sim}\frac{N_{\gamma\ \mathrm{AfterCuts}}(E)}{N_{\gamma\mathrm{Total}}} \quad , \tag{2.12}$$

where ε_γ has been defined as the fraction of simulated gamma-ray events that survive the trigger and the analysis cuts ($N_{\gamma\ \mathrm{AfterCuts}}(E)$) over the total number of produced events ($N_{\gamma\mathrm{Total}}$).

The differential spectrum is computed dividing the sensitive energy range in equal bins (in logarithm scale) and calculating the gamma-ray flux in each bin separately (analysis cuts can be set different in each bin in order to obtain an optimal result). However, for each gamma-ray event what we have is the estimated energy E_{est} (see section 2.4.0.6). An unfolding procedure is needed to calculate the true energy E, correcting the measured one from its natural distortions due to the finite resolution of the detector. The transformation from E_{est} to E is possible

through a detector response function $M(E, E_{est})$, know as the *migration matrix*. Then, the measured distribution $g(E_{est})$ can be written in terms of the true distribution $f(E)$:

$$g(E_{est}) = \int M(E, E_{est}) f(E) dE. \tag{2.13}$$

Ideally, to compute exactly how the events in a given true energy E are distributed in estimated energy E_{est}, a migration matrix with infinite statistics would be needed. Then, for a given value of true energy, the projection of the migration matrix over the estimated energy axis, normalized to 1, will be the probability density function (PDF) for the distribution of events in estimated energy (see Fig.2.19). The addition of each one of these "overlapping" distribution of events (weighted with the gamma-ray flux at energy E), for each value of true energy, will give the distribution of all the recorded gamma rays in estimated energy.

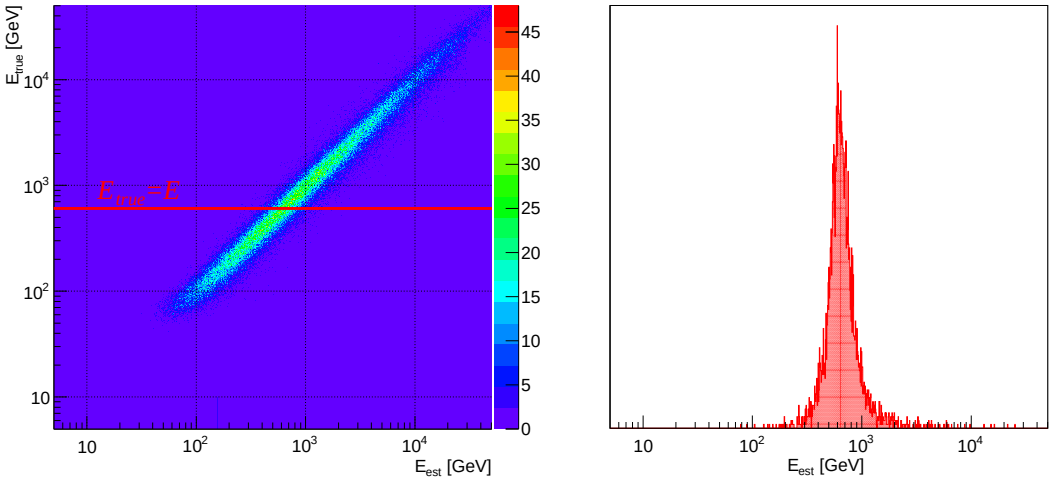

(a) Migration matrix with fine bins

(b) Projection to the E_{est} axis of the migration matrix

FIGURE 2.19: On the left, is an example of a migration matrix with ~ 1 million events distributed in fine bins. For a given value of true energy E (the dashed horizontal red line), the distribution of the migration matrix over the estimated energies is shown on the right panel. Normalized to 1(the shaded area under the curve), this distribution can be used as probability density function for the probability of an event in true energy to be reconstructed at a certain value of estimated energy.

However, in practice, the amount of MC simulations is finite, and hence only a binned version of the ideal matrix is available. Besides, the bins in estimated energy defined in the analysis of real data must be large enough to contain a sufficiently significant excess of gamma rays over the cosmic-ray background after all the applied cuts. The values in the binned migration matrix (unlike its ideal counterpart) will depend not only on the instrument performance, but also on the energy spectrum of the MC gamma rays used to build it (see Fig.2.20).

Being discretized, the expression 2.13 is reformulated as:

$$g_i = M_{i,j} f_j. \tag{2.14}$$

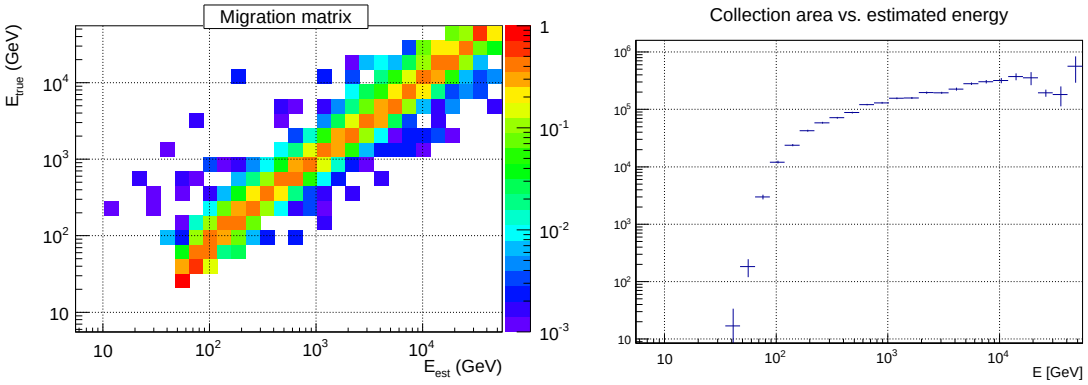

(a) Migration matrix

(b) Collection area vs E_{true}

FIGURE 2.20: Example of Migration matrix (left) and collection area (right) from a real observation. Notice the coarse binning in both plots. The generation of both plots depend on the assumed *tentative spectrum* in the iterative process to match the observed source spectrum.

Where g_i will be the events in the bin i of estimated energy after cuts. Therefore, to computed the spectrum in bins to true energy, the equation 2.14 is solved for f_j. The tentative spectrum used to produce the migration matrix and the effective collection area is modified during the analysis in an iterative process in order to match the observed source spectrum. In each iteration (although more than one iteration is seldom needed) the migration matrix is recalculated accordingly.

The light curve shows the integrated gamma-ray flux in a certain energy range $[E_a, E_b]$, as function of time. Thus, the integral flux in the time interval $[T_i, Tj]$ is computed integrating the expression eq:DiffEnerSpectrum:

$$\Phi(E_a, E_b) = \int_{T_i}^{T_j} \int_{E_a}^{E_b} \frac{d\phi(E)}{dE} dE dt \quad . \tag{2.15}$$

The calculation of the migration matrix, the effective collection area, differential energy spectrum and light curve is handled by the MARS executable `flute`.

2.4.1 Crab Nebula crosscheck

The analysis chain of MAGIC using the standard settings for all the steps (cleaning, stereo reconstruction, gamma-hadron separation, reconstruction of the spectrum) has been optimized to get the correct physical values out of the data. Nonetheless, is always convenient to crosscheck the analysis (direction and energy reconstruction, the produced RF, etc.) using data from the Crab Nebula.

The Crab Nebula is a pulsar wind nebula located at a distance of ~ 2 kpc and it was the first source detected in very-high energy γ-rays [Weekes, 1989]. This source is commonly known as the "standard candle" in very-high energy γ-ray astronomy since no significant variability (short- or long-term) has been observed at VHE. This enables us to compare observations of the Crab Nebula taken in any given period with historical data from MAGIC [Albert, 2008a] and HESS [Aharonian, 2006].

The usual procedure for doing the crosscheck is to take a data sample of Crab Nebula the closest in time to the observations dates of the source that is being analyzed. The proximity in time is to reduce the possibility that both observations (from the source and Crab Nebula) were taken with different hardware conditions of the telescope, weakening the validity of the crosscheck. Additionally, the Crab Nebula sample has to been taken with similar conditions of the data analyzed, that is, with similar zenith angles, light conditions and observation mode (wobble with same camera offset).

Since Crab Nebula is a strong source, the amount of exposure needed in order to have a reasonable crosscheck is of the order of few hours. The first thing to check is the achieved sensitivity using the so called "standard cuts". The significance of a signal with an excess of N_{excess} events over a well defined background of N_{bkgd} events can be computed with the simplified formula $N_{excess}/\sqrt{N_{bkgd}}$. This way, the sensitivity can be defined as the flux of a source giving $N_{excess}/\sqrt{N_{bkgd}} = 5$ after 50 hours of effective observation time [Aleksić et al., 2014b]. The sensitivity is usually given in a percentage of Crab nebula Units (C.U.). For the Crab Nebula, the sensitivity is calculated in what for historical reasons is called "full energy" range, which means that only events above 250 GeV are taken into account. The "standard cuts" are the lower limits in *size*, set in 300 photo-electrons for each telescope, and the upper limit in *hadronness*, set in 0.16. For the standard cuts and the full energy range the sensitivity is expected to be around 0.7 % C.U (see Fig. 2.18).

The next thing to compare is the obtained Crab Nebula spectrum with the historical spectrum. Fig. 3.25 shows a comparison for Crab Nebula data taken between February and March 2013 (6.38 hours of exposure) and the historical spectrum, in the representation of spectral energy distribution. The agreement between the observed spectrum and the historical Crab Nebula spectrum confirm the validity of the produced RF and the MC sample used for the test.

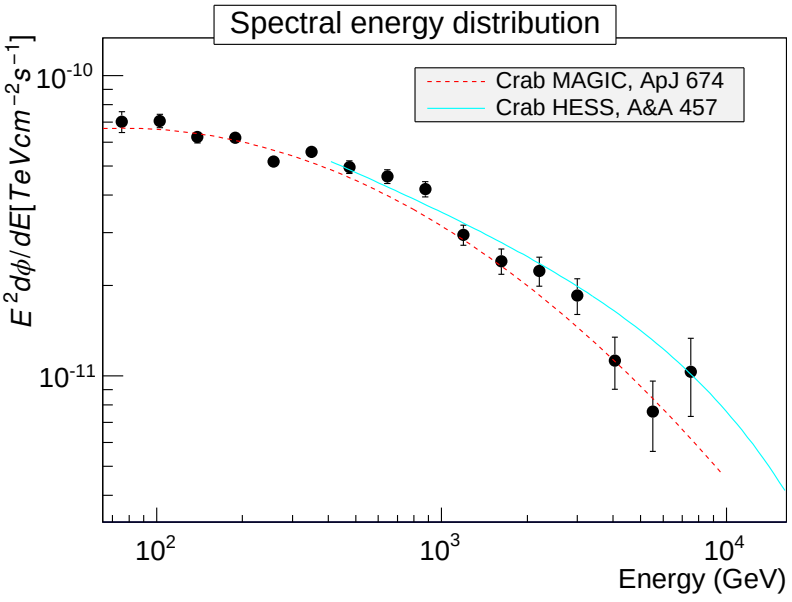

FIGURE 2.21: Spectral energy distribution of Crab nebula data selected for a crosscheck. The dashed red line is the Crab Nebula spectrum as published in [Albert, 2008a]. The blue line is the spectrum reported by H.E.S.S. in [Aharonian, 2006].

Chapter 3

The extraordinary flares of Markarian 421 and 1ES1011+496

The first chapter of the present work described some important properties of the Active Galactic Nuclei (AGN), as sources of very-high energy gamma rays. The study of these objects is one of the central purposes of the MAGIC collaboration. The observation of their gamma-ray fluxes at very-high energy (VHE) provides relevant information to understand the inner workings of these powerful sources. Several of these sources have been observed over extended periods of times, either to increase the number of detected gamma rays and reconstruct a more statistically significant energy spectrum (particularly for steady sources) or study long-term variability. However, and more often in the case of blazars (see section 1.2.1), an AGN can enter in a state of high activity, a *flare*, during which the flux rises significantly and exhibits rapid changes from night to night, and in some cases, the flux varies in timescales as short as minutes (though to probe such fast variability one needs very high flux levels).

In this chapter, the observations by the MAGIC telescopes and analysis results of the extraordinary flaring states from Markarian 421 and 1ES 1011+496 will be described. The sections dedicated to each source will begin with a summary of previous observations, followed by the analysis performed by the author. The study of the Extragalactic Background Light (EBL) using these data will be presented in the next chapter.

3.1 Markarian 421

One of the most intense, and therefore most studied sources in the gamma-ray sky, is Markarian 421 (Mrk421). It is an active galatic nucleus (AGN) hosted in the galaxy UGC 6132 (see Fig.3.1). It can be seen in all wavelengths across the electromagnetic spectrum, from radio to VHE gamma rays. Due to the rapid variability of it emission and the presence of compact features, Mrk421 is classified as a blazar. These observed properties can be explained as coming from the presence of a relativistic jet seen at small angle relative to our line of sight (see section 1.2.2). Mrk421 is the closest known blazar, with a redshift $z = 0.031$ (≈ 400 million light-years).

As for all AGNs, it is assumed that the central engine of this blazar is a supermassive black hole. From velocity dispersion measurements in the host galaxy, the mass of the black hole in the center of Mkr421 has been estimated to be $(1.9 \pm 0.5) \times 10^8\ M_\odot$ [Barth et al., 2003]. However, the host galaxy of Mrk421, being elliptical, can be the result of the merging of two galaxies

(a) Optical (b) X-ray

FIGURE 3.1: Markarian 421 seen in optical and in X-rays. In optical it can be seen its companion galaxy Markarian 421-5. Optical image from the Hubble Legacy Archive WFPC2. X-ray image from *Swift*/XRT.

(see e.g. Conselice [2014] and references therein). Therefore, instead of a single black hole, there could be a binary system powering Mrk421 [De Paolis et al., 2002]. In a recent study by Chen et al. [2014], they analyzed historical data in the B and V bands together with their own observations in those bands to build lightcurves, claiming a possible periodicity of 1.36 years. That periodicity could be explained with a binary system with a primary black hole with mass $1.7 \times 10^8\ M_\odot$ and a secondary $\sim (0.49 - 2.9) \times 10^7\ M_\odot$. Such periodicity has not been reported in any other wavelength.

3.1.1 Previous observations

Mrk421 is the first extragalactic source detected at VHE by an IACT [Punch, 1992]. This source has been the subject of several observations by MAGIC, either as a Target of Oportunity (ToO) observation in an outburst, or in planned-ahead campaigns. In both cases the source is usually observed by more than one instrument, gathering data in several wavelengths (optical, UV, X-ray, gamma-ray).

Noticeably are the multi-wavelength (MWL) campaigns done first with MAGIC I in standalone mode (since MAGIC II was not yet in operation) in April 2006 [Acciari, 2009a] [Aleksić, 2010], December 2007-June 2008 [Donnarumma and et al., 2009], and January-June 2009 [Abdo et al., 2011] and then with the stereoscopic system in March 2010 [Aleksić et al., 2014a].

The activity of the source was followed by MAGIC night by night between April 22 and 30, 2006, having a peak activity of approximately 2 times the Crab Nebula flux (Crab Units; C.U.). The activity of the source was strong enough to infer light curves in the MAGIC data with a resolution below one hour at VHE (see Fig.3.2). Of all the nights, only one showed evidence of intra-night variability.

The data from the MWL campaign of April 2006 was arranged in four (non-independent) data sets. One set was just the night of highest activity, April 27. The nights with flux higher than a C.U. form another set called "high-state" (April 24, 27 and 30). The nights with "low-state" (April 22, 25, 26, 28 and 29) formed the third set, and finally "all April" nights formed another set. The observed energy spectra for these data sets were fitted using three different functions:

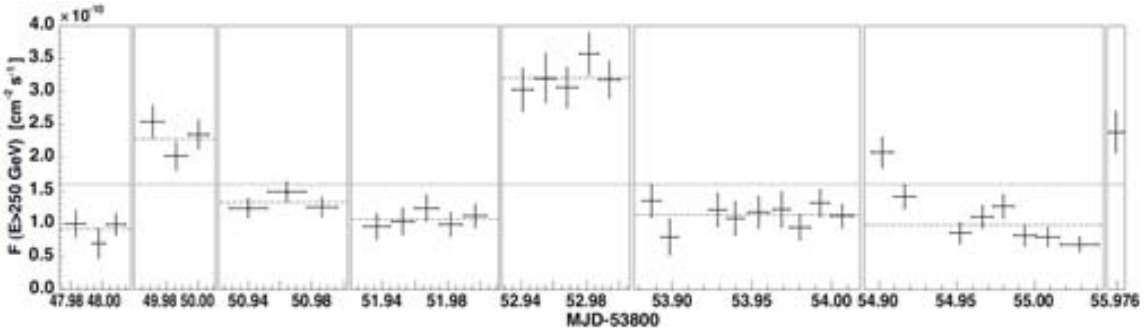

FIGURE 3.2: Light curve for $E > 250$ GeV for the MAGIC observations of Mrk421 in April, 2006. The solid line represent the Crab nebula flux, whereas the individual dashed lines show the average nightly flux of each night [Aleksić, 2010].

simple power-law, log-parabola and power-law with exponential cut-off. For the four data sets, the fits to the log-parabola and the power-law with exponential cut-off gave better χ^2 values than the fits to a simple power-law, indicating that the spectra had curvature and that curvature could be due to a cut-off energy. The position in energy of the synchrotron peak E_{peak} for the four data sets are shown in the Fig.3.3 together with other historical values. The cut-off energies E_{cut} where derived from the fits to the power-law function with exponential cut-off. The values are shown in the Table 3.1.

TABLE 3.1: Cut-off and peak energies derived from the four data sets from the April 2006 observation of Mrk421

Data set	E_{cut}[TeV]	E_{peak}[TeV]
April 27 2006	2.6 ± 1.3	1.2 ± 0.2
High-state	6.1 ± 4.0	1.1 ± 0.3
Low-state	2.9 ± 1.3	0.48 ± 0.12
All April 2006	3.6 ± 1.1	0.69 ± 0.06

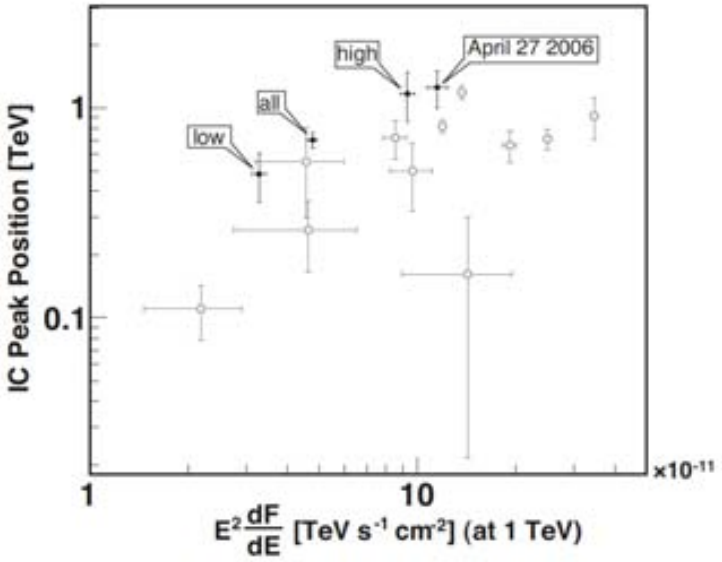

FIGURE 3.3: Peak energy position derived from fits to a log-parabola versus flux at 1 TeV for the data sets (April 27 2006, high, low, all). In gray is historical data. From [Aleksić, 2010].

The campaign of 2008 was complemented with optical data from the Kungliga Vetenskaplika Academy (KVA) telescope (operated by the Tuorla Observatory), *Swif*/UVOT [Roming, 2005], for the UV part of the spectrum, and for the X-rays, *Swift*/XRT [Burrows, 2005] and RXTE/ASM [Bradt et al., 1993]. The light curve at VHE from December 2007 to June 2008 showed a maximum activity of the source of ~ 3.6 C.U (see Fig.3.4). In high state, the evolution of the flux was investigated at sub-hour scale searching for rapid variability. In the night of February 6, 2008, where a 4 hour long observation was carried out, an episode of variability with doubling/halving times down to 16 min was observed for $E > 400$ GeV (see Fig. 3.5). This variability episode could not be complemented with MWL data. No firm conclusion could be drawn on the sub-hour flux variability of Mrk421 since the MWL data was either taken with very short observation windows or in nights where the flux was low. The MAGIC data used for the MWL SED modeling were fitted using log-parabola functions.

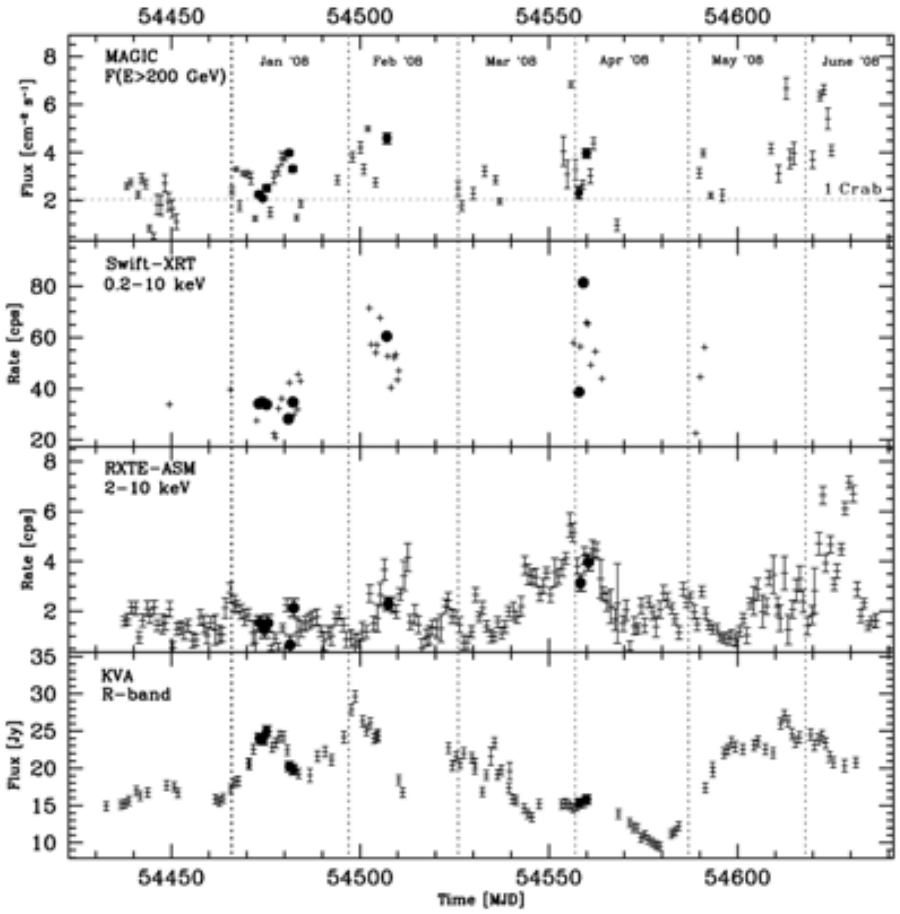

FIGURE 3.4: Multi-wavelenght light curves of Mrk421 during the observation period of MAGIC-I. The full circles mark the simultaneous observations of MAGIC-I and *Swift*/XRT. **Upper panel**: MAGIC-I VHE light curve above 200 GeV. The Crab nebula flux is represented by the dashed line. **Middle-upper panel**: soft X-ray counts measured by *Swift*/XRT. **Middle-lower pannel**: soft X-ray counts measured by RXTE/ASM. **Lower panel**: Johnson R-band optical light curve from the Tuorla Observatory (from [Donnarumma and et al., 2009]).

The simultaneous MWL data in states in which the flux of the source is changing in a relative short time-scale provides information to study the correlations between X-ray and VHE bands. For the observation of Mrk 421 in 2006 and 2008, the simultaneous MWL data were modeled using a simple one-zone synchrotron self-Compton (SSC) model [Acciari, 2009b]. Rapid X-ray and very-high energy (VHE) flares are often expected to be correlated, as all photons are

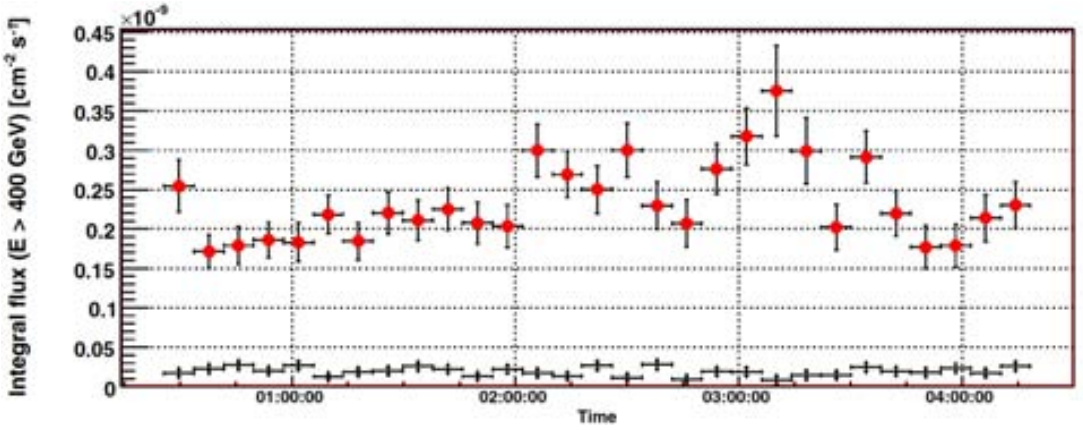

FIGURE 3.5: Mrk 421 light curve for $E > 400$ GeV and 8-min time bins from the observation taken on February 6, 2008 (red points). The black crosses show the evolution of the flux of gamma-like background events. (from [Donnarumma and et al., 2009]).

expected to originate from the same population of electrons [Maraschi and et al., 1999] (see Fig. 3.6).

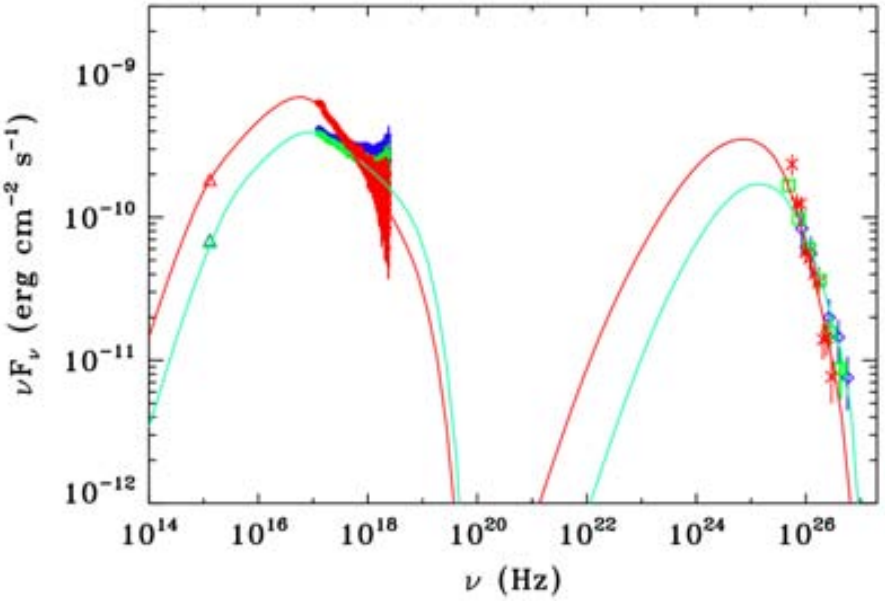

FIGURE 3.6: SED with the SSC model for the 2006 (teal blue) and 2008 (red) data. The data from *XMM-Newton* OM is shown in triangles, *XMM-Newton* EPN in filled circles, MAGIC in squares, Whipple in diamonds and VERITAS in crosses. The color code (green, blue and red) shows the simultaneous observations (from [Acciari, 2009b]).

The relevance of the January-June 2009 campaign [Abdo et al., 2011], is that for the first time, the SED of Mrk421 could be complemented with the HE data from the *Fermi* Large Area Telescope (*Fermi*-LAT) [Atwood et al., 2009]. For this campaign, the MAGIC observations were interrupted due to the shutdown for the scheduled hardware upgrade. Other instruments participating in this campaign were, in radio, the Very Long Baseline Array (VLBA), the Owens Valley Radio Observatory (OVRO) and the Metsähovi Radio Observatory. In optical and near-infrared the observations were performed by various telescopes within the GASP-WEBT program[1]. The

[1]http://www.to.astro.it/blazars/webt/

data in UV and soft X-ray was provided by *Swift*/UVOT [Roming, 2005], *Swift*/XRT [Burrows, 2005] and *Swift*/BAT [Barthelmy et al., 2005] together with data from the *Rossi X-Ray Timing Explorer* [RXTE Bradt et al., 1993]. For this campaign, the MAGIC data surviving the quality cuts amounted to almost 28 hours. The average observed differential VHE energy spectrum could be fitted with a log-parabola function $d\phi/dE = K \times (E/0.3TeV)^{-(\Gamma+\beta\cdot(E/0.3TeV))}$ with $K = (6.50 \pm 0.13) \times 10^{-10}$ photons cm^2 s^{-1} erg^{-1}, $\Gamma = 2.48 \pm 0.03$, and $\beta = 0.33 \pm 0.06$, with $\chi^2/NDF = 11/6$. During the campaign, the MAGIC observations registered an integral flux below the Crab Nebula, as shown in Fig. 3.7, with relatively mild (typically less than a factor of two) flux variations.

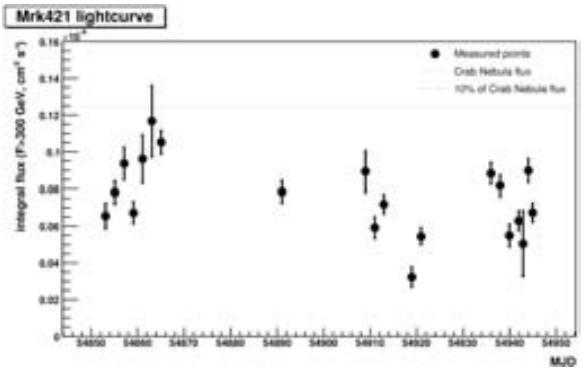

FIGURE 3.7: Light curve for the MAGIC data taken between 2009-01-22 and 2009-04-24 for energies above 300 GeV (from Tescaro [2010]).

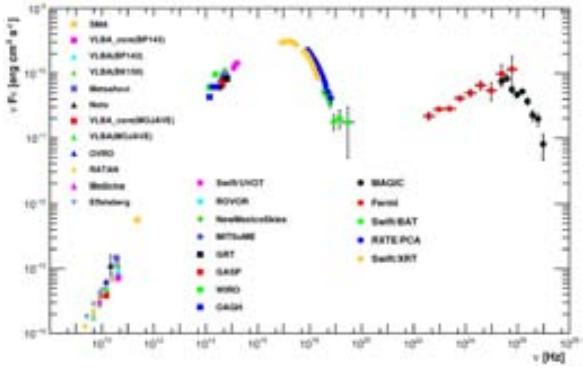

FIGURE 3.8: SED of Mrk421 averaged over all the observations taken during the multi-wavelength campaign from 2009-01-19 to 2009-06-01. The TeV data from MAGIC were EBL corrected using the EBL model by Franceschini et al. [2008] (from Abdo et al. [2011]).

The data from *Fermi*-LAT for the reconstruction of the SED of Mrk421 was collected from 2009-01-19 to 2009-06-01. The HE average spectrum could be fitted with a simple power-law function with index $\Gamma = 1.75 \pm 0.03$. The *Fermi*-LAT spectrum together with the MAGIC spectrum and the other participant instrument in the campaign can be seen in Fig. 3.8. An extensive study for the modeling of the broadband SED of Mrk421 for this campaign was presented by Abdo et al. [2011], where two different scenarios were considered: a leptonic (one-zone SSC) model and a hadronic synchrotron-proton blazar model. Both frameworks were able to describe reasonably well the average SED.

In March 2010 Mrk421 entered into a flaring state, which was observed for 13 consecutive days (from 2010-03-10 to 2010-03-22) in a MWL campaign from radio to VHE [Aleksić et al., 2014a]. The radio data was taken by OVRO, Metsähovi Radio Observatory, the University of Michigan Radio Astronomy Observatory (UMRAO) and the Sub-millimeter Array (SMA). Optical observations were conducted within the GASP-WEBT program. In UV the data was gathered by *Swift*/UVOT and in X-ray by *Swift*/XRT, RXTE and the Monitor off All-sky X-ray Image (MAXI) [Matsuoka et al., 2009]. Also data at HE was extracted from *Fermi*-LAT observations. The VHE data was complemented with data from VERITAS and Whipple telescopes. MAGIC participated in this campaign doing the observations in stereo mode, collecting 4.7 hours good-quality data.

Fig. 3.9 shows the light curve of the flaring episode for several bands, between 2010-03-10 and 2010-03-22, where it can be seen that the flux at VHE reached values of around 2 C.U., and then decreases roughly steadily with time. The data at HE from *Fermi*-LAT, however, does

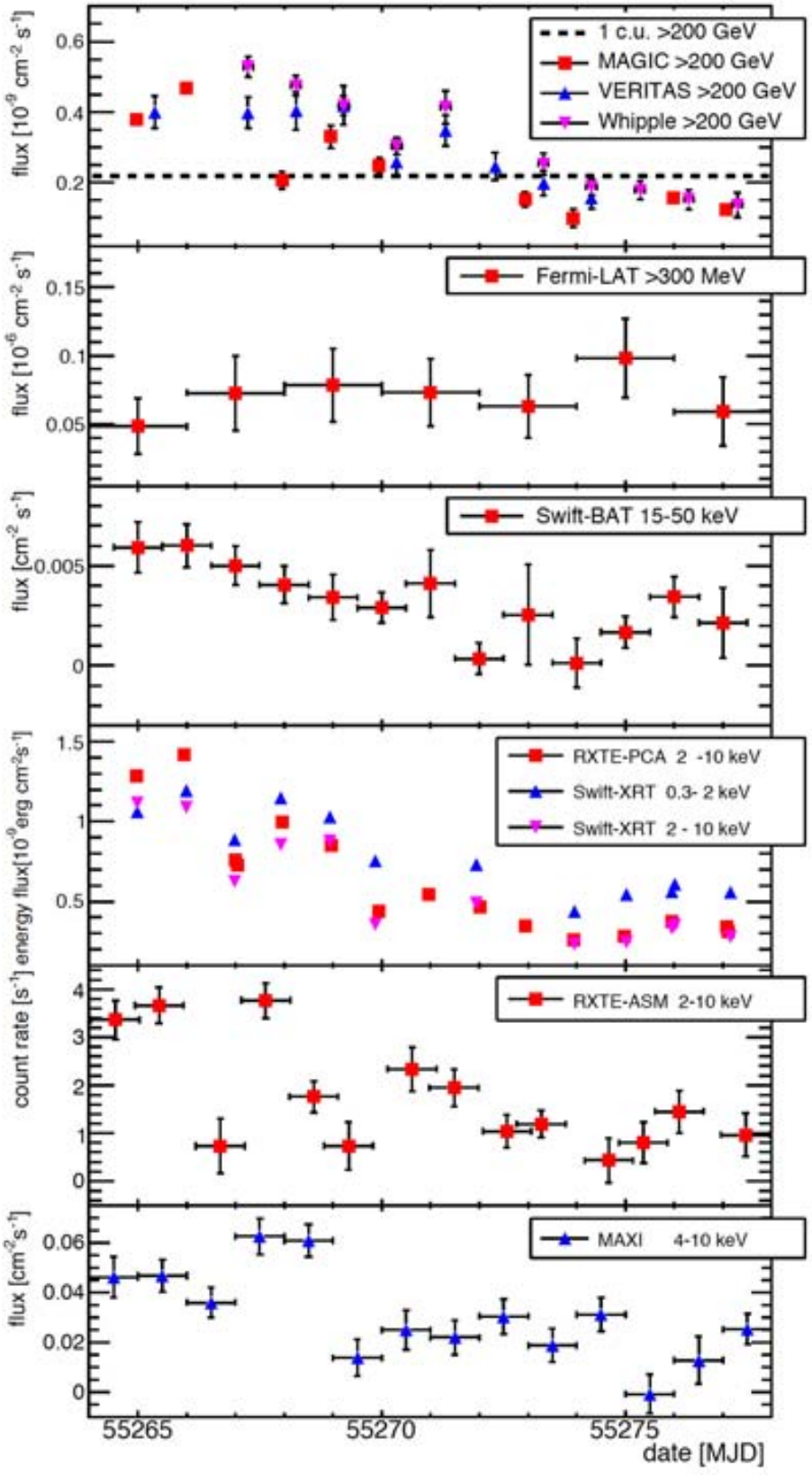

FIGURE 3.9: Light curves of Mrk421 for the flaring episode of March 2010, for different bands, from X-ray to VHE. The observations at VHE (MAGIC, VERITAS, Whipple) have a night-wise binning, whereas *Fermi*-LAT has a bin width of two days (from [Aleksić et al., 2014a]).

not show any significant variability. The X-ray band, clearly shows variability, more or less following the same pattern as the VHE band.

The MWL data collected in the flare of March 2010, was used for an extensive study of the broadband emission of Mrk421. The data was divided in 13 samples, from where 13 successive simultaneous SEDs for the 13 consecutive days were built. The SEDs were modeled using two leptonic scenarios: a one-zone SSC model, and a two-zone SSC model where one zone is responsible for the quiescent emission while the other (smaller, spatially separated) zone, contributes to the daily-variable emission occurring in X-rays and VHE gamma rays. It was found that the SED data at the peaks of the low- and high-energy bumps were better described with the two-zone SSC model [Aleksić et al., 2014a].

3.1.2 2013 observations

Between January and March 2013 Mrk421 was observed in a MWL campaign involving several instruments, from radio to VHE gamma rays [Baloković]. The OVRO and the Metsähovi Radio Observatory made the observations in radio. In optical, the observations were performed within the GASP-WEBT program. The observations in UV and soft X-ray were provided by *Swift*/UVOT [Roming, 2005] and *Swift*/XRT [Burrows, 2005]. In hard X-ray, observations were performed by *NuSTAR* [Harrison, 2013]. The HE gamma-ray data was collected with *Fermi*-LAT [Atwood et al., 2009]. Finally, at VHE, the observations were performed by the IACTs MAGIC and VERITAS [Rajotte, 2014].

Fig.3.10 shows the light curve (LC) of Mrk421 in all the wavelengths covered in the campaign [Baloković]. One thing that is evident from the LC is the correlated flux variability in the X-ray and VHE bands, both in the general 3-month upward trend, and the flux increase and decrease in particular coordinated observations. In the UV and *Fermi*-LAT bands, the general upward trend is also observable, although they do not show a short-term flux correlation. Fig. 3.11 (from Baloković) shows the results for the correlation analysis in the X-ray and VHE bands for strictly simultaneous observations, where a linear relationship was found. The observed correlation is expected in the one-zone SSC models. However, when the inverse-Compton scattering takes places only in the Thomson regime, the resulting flux follows a quadratic relationship, since the seed photons increase linearly with the population of scattering electrons. The fact that the correlation between the X-ray and VHE bands follows a linear relationship, could be an indication that the scattering cross-section is diminished, possibly because it takes place in the less efficient Klein-Nishina regime.

3.1.3 Extraordinary flare of April 2013

The 2013 observations briefly described in the previous section is a work that does not includes the flare of April 2013. Due to the extraordinary nature of this flare, it has given a separate treatment. The dates stated in this section follows the "date of the morning after" convention in MAGIC data: the specified date is that of the morning after the observation.

During the observations of Mrk421 in April 2013, the MAGIC OnLine Analysis (MOLA), in 2013-04-11 to 2013-04-13, reported a persistent hight flux of about 5 times the Crab Nebula flux (Crab Units, C.U.) above 300 GeV, with a maximum above 11 c.u [Cortina and Holder, 2013]. The source was observed for 10 nights, from 2013-04-10 to 2013-04-19, summing up a total exposure of 49 hrs. The observation after 2013-04-19 were stopped since the observed

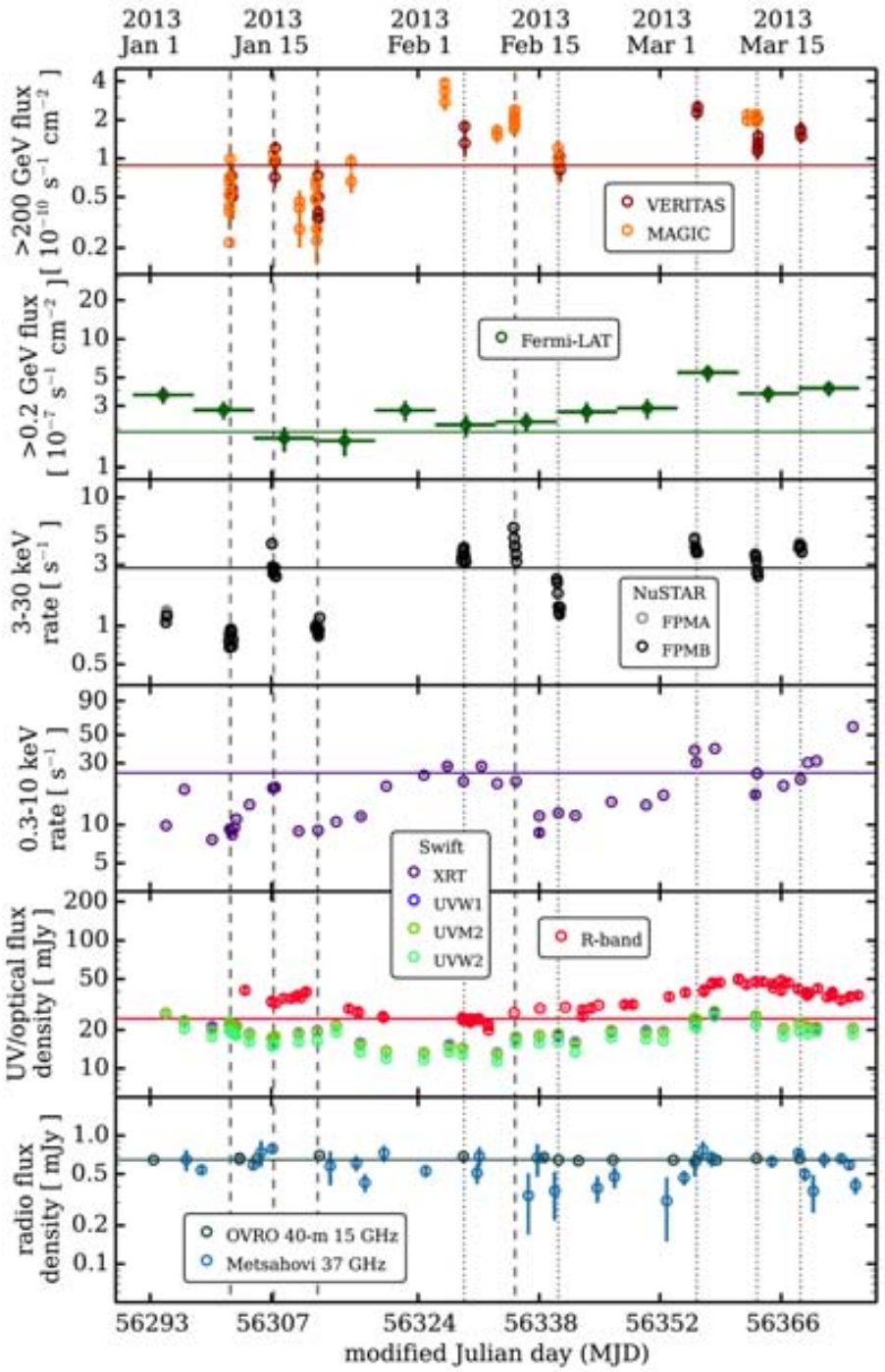

FIGURE 3.10: Mrk421 light curve from all the instruments participating in the MWL campaign: MAGIC, VERITAS ($E > 200$ GeV, ~ 30 min bins), *Fermi*-LAT (0.2-100 GeV, binned weekly), *NuSTAR* (3-30 keV, binned by orbit), *Swift*/XRT (0.3-10 keV, complete observations), *Swift*/UVOT (UVW1, UVW2 and UVW3 bands, complete observations), groud-based optical observatories (R-band, $\sim$ daily cadence), OVRO and Metsáhovi (15 and 37 GHz, 3-4 days cadence). The vertical lines mark midpoints of the coordinated *NuSTAR* observations (dashed and dotted lines). Horizontal lines are the long-term median flux for each band (from [Baloković]).

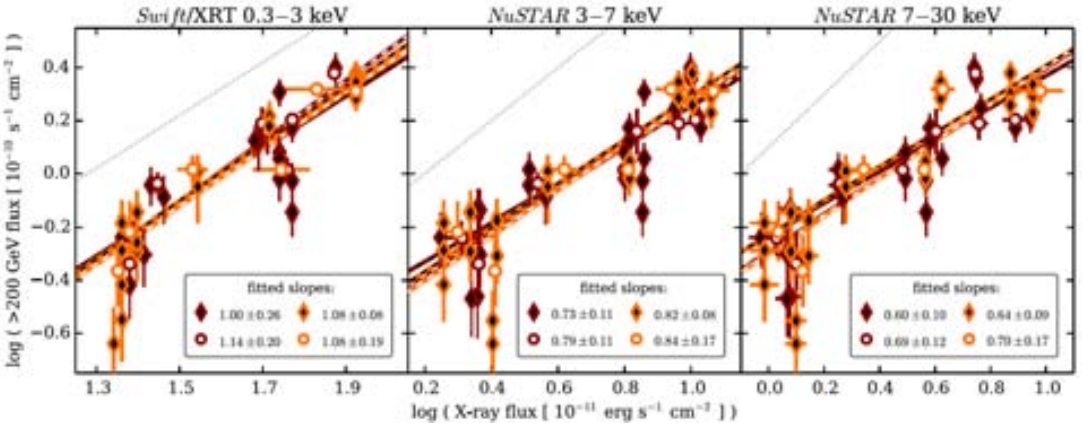

FIGURE 3.11: Flux-flux correlation between the X-ray flux in three different bands and VHE gamma-ray flux. The results based on MAGIC data are shown in orange, while those based in VERITAS are shown in red. Strictly simultaneous data are black-filled diamonds, while white-filled circles show nightly-averaged measurements. Best-fit lines match the inner and the outer color of the symbols used to plot the relevant data (from [Baloković]).

flux or Mrk421 return to a level below the Crab Nebula flux. According to the log entries by the observers, 70% of the data were taken on dark conditions and 30% with moonlight. The atmospheric conditions were good for observations except for 2013-04-12, 2013-04-17 and 2013-04-18, where some clouds were reported. Details are given in the Table 3.2.

TABLE 3.2: Observation dates, light conditions, exposure time in minutes and zenith angle coverage according to the reports logged in the runbook. The dates are following the "date of the morning after" convention.

Night	Twilight		Moonlight		Dark	
	Time (min.)	Zd (deg.)	Time (min.)	Zd (deg.)	Time (min.)	Zd (deg.)
2013-04-10	-	-	-	-	28	29-34
2013-04-11	7	27-28	-	-	353	9-65
2013-04-12	-	-	-	-	381	9 -64
2013-04-13	9	25-27	42	17-25	394	9-64
2013-04-14	8	25-26	94	10-24	280	9-63
2013-04-15	-	-	114	9-18	236	13-60
2013-04-16	-	-	102	9-18	144	21-51
2013-04-17	-	-	137	9-28	97	32-51
2013-04-18	-	-	177	9-40	55	41-51
2013-04-19	-	-	223	9-48	73	48-64

3.1.3.1 Data selection

The standard way to do the data selection is checking the data after the cleaning, that is, at `star` level (see section 2.4.0.2). The data at this level is organized in sub-runs. Each data sub-run has around 2 to 3 minutes of observations. Several sub-runs (> 10) form a data run, accounting for ≈ 20 minutes of data. The advantage of doing the data selection at `star` level (in contrast of doing the data selection at `superstar` level, where the data is already merged into files each which corresponds to one run) is that if a certain quantity in a sub-run does not

pass a quality criteria, the sub-run can be discarded without sacrificing a whole run. In the analysis presented here the data selection was therefore done at `star` level.

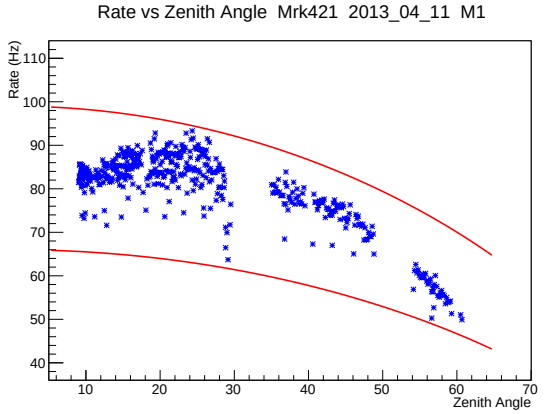

FIGURE 3.12: Rates for MAGIC 1 for a size cut of 100 photoelectrons, April 11th, 2013. Each point represents a subrun. The red lines in the figure are just guidelines showing the behavior that the rates are expected to follow depending on the zenith angle, positioned +20% and -20% of the median rate.

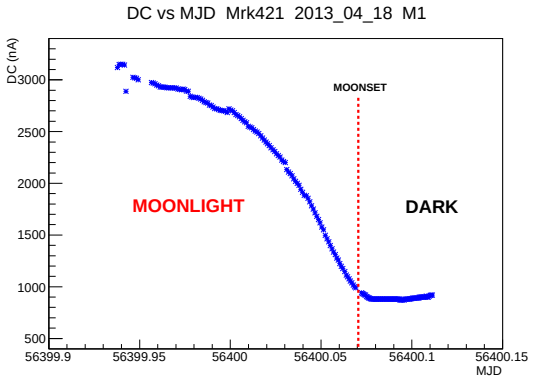

FIGURE 3.13: DC vs time in Modified Julian Date for MAGIC 1, April 18th, 2013. Each point represents a subrun. The DC changes accordingly to the light conditions in the sky: high DC means strong moonlight and decreases as the Moon moves to the horizon.

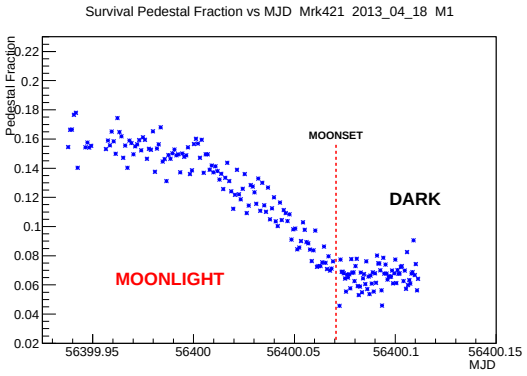

FIGURE 3.14: Fraction of interleaved pedestals surviving cleaning for MAGIC 1, April 18th, 2013. Each point represents a subrun. This quantity indicates if the level of cleaning applied to the images is appropriate for the light conditions.

The main quantity to check is the *event rates*. These rates are the events (cleaned images) within a sub-run, divided by the time interval of the sub-run. The rates are selected by the analyzer after a cut in *size*, which is the number of photoelectrons measured in one image. Since most of events come from hadronic cosmic rays, it is expected that in dark conditions (when there is no moonlight of twilight) the rates during data taking are more less constant for zenith angles below $\sim 35°$. For zenith angles above $35°$ the rates begin to steadily decrease (see Fig.3.12). Departures from this behavior are mainly due to the presence of clouds in the field of view and occasionally to technical problems, or to the lights of cars passing by near the MAGIC site. Sub-runs with rate values that are 20% above or below the reference value for optimal conditions, at the corresponding interval of zenith angle, are discarded. Twilight can be encountered at the beginning of the observations or at the end, however, the observations are planed to avoid as much as possible taking data under these light conditions. Moonlight, however, is harder to avoid and can have a great impact in the observations. This effect can

be clearly seen in the mean direct current (DC) of the camera. The DC is proportional to the light intensity measured by the photomultipliers in the camera. In dark conditions the DC has a approximately constant value, but it grows rapidly as moonlight increases (Fig. 3.13).

Another quantity useful to check the quality of the data is the fraction of *interleaved pedestal* events surviving cleaning. These pedestals are recorded at a rate of 25 Hz, interleaved with shower-triggered events and contain just light from the NSB and they should not contain light from atmospheric showers. However the cleaning is also applied over them to check how many of them survive. For dark conditions and standard cleaning, around 1 of 10 events from these pedestals produces an "island" that comes from noise (see Fig.3.14) (see section 2.4.0.2). If the fraction of surviving interleaved pedestal is higher than 10%, it means that the levels of cleaning applied to the data are not strong enough since the same fraction of triggered events would contain spurious pixels unrelated to the shower image.

For the study in the EBL presented in this work, the data from April 2013 taken only in dark conditions was selected, amounting to 33.46 hours of good quality data. The data taken with moonlight conditions needs a special image cleaning, a process that is not standardized and could lead to (more) systematic uncertainties. Just as will be explained later, our measurement of the gamma-ray opacity, caused by the EBL, relies in a particular imprint in the observed feature. Therefore, only with data taken in dark conditions the highest precision can be achieved.

3.1.3.2 Data reduction

Once the data is selected, following the analysis pipeline described in section 2.4, the data is passed through the stereo reconstruction and then the gamma/hadron separation, using the Random Forest algorithm. As stated in section 2.4.0.4, for this last step, a sample of OFF data (hadron-initiated showers) is needed, together with a set of Monte Carlo (MC) simulations (gamma-ray-initiated showers).

The OFF sample is taken preferentially from observations on dates that are close to the dates of the data to be analyzed, in order to avoid serious changes in the hardware conditions of the telescopes. Also the sample has to match the zenith angle range of the data. In the OFF sample for the analysis of the Mrk421 April 2013 flare listed in the Table 3.3 the are some potential gamma-ray sources. However, the selected sample does not contain any indication of signal.

TABLE 3.3: Source names and observation dates for the hadron sample used to training the Random Forest. The dates are following the "date of the morning after" convention.

Source	Date
1ES0927+500	2013-04-02
DarkPatch11	2013-02-08
DarkPatch28	2013-01-21
DarkPatch32	2013-02-11
DarkPatch33	2013-02-10, 2013-02-15
Geminga	2013-02-12
GRB130504	2013-05-04
SegueA	2013-01-15, 2013-01-16, 2013-01-17, 2013-01-18, 2013-01-19, 2013-01-20, 2013-01-21

There is no a unique set of MC simulations for all MAGIC observations. Since the beginning of stereo operations, the telescopes have gone through several modifications, being the main ones,

the upgrade in the readout electronics and the replacement of the MAGIC I camera. There are also non intentional changes in the hardware of the telescopes that affect the light collected by the cameras, like the aging of the mirrors or changes in the performance of the Active Mirror Control system (see section 2.3.1.2) resulting in a non-optimal optical point-spread function of the telescopes. The impact that the hardware changes has in the acquired data is periodically evaluated by the Software Board of the Collaboration (SoBo). If the data changes significantly with respect to the current MC in use, then a new set of MC simulations are produced, optimized to this changes. A MC sample that has not been optimized for the conditions of the telescopes in a given period will result in wrong reconstruction of the gamma-ray spectra of the observed sources.

3.1.3.3 Mismatch in the estimated energy from the telescopes

After the replacement of the MAGIC I camera in the summer of 2012, a new set of MC simulations (ST.03.01) were produced for the analysis of data taken with this new camera. In Table 3.4 the different MC simulations produced after the upgrade are listed. The data taken within each period of validity has to be analyzed with the corresponding MC production. The first analysis of the Mkr421 April flare was done using the MC labeled as "ST.03.01". With this MC a Random Forest was produced for the processing of the data with `melibea`.

TABLE 3.4: Labels for the stereo Monte Carlo simulations productions after the upgrade of the MAGIC telescopes

Label	Period of validity
ST.03.01	2012-11-01 - 2013-01-17
ST.03.02	2013-01-18 - 2013-07-26
ST.03.03	2013-07-27 - 2014-06-18
	2014-07-05 - 2014-08-05
ST.03.05	2014-08-31 - 2014-11-22

Right after the `melibea` files were produced, a comparison between the estimated energy from MAGIC-I and MAGIC-II revealed a mismatch. The April flare of Mrk421 was an extraordinary event that produced a record amount of gamma-rays showers observed by MAGIC. It is because of this high statistics that the mismatch was easily revealed. Fig. 3.15 show the logarithm of the ratio between the energies estimated for the same (gamma-like) events seen by MAGIC-I and MAGIC-II, for different energy cuts. The distributions do not peak at 1.0 as would be expected from a correct energy calibration between the two telescopes. A gaussian fit was made to each one of the histograms, and from the mean values the mismatch was estimated to be around 7-8%.

In order to check if the mismatch was a feature affecting equally the 10 days of observation, the ratio between the estimated energy of the two telescopes was calculated night-wise. The mean value of the gaussian fit for each observation night is shown in Fig. 3.16. The fit to a line shows that the mismatch is present in all days with more or less the same value except in the last two days, in which is about 1.3% higher. The efficiency of the telescope in collecting the Cherenkov light may unexpectedly change due to a minor maladjustment in one (or more) of the panels by the AMC (Each panel accounts for $\sim$0.4% of the total surface of the mirror). These minor changes are included within the reported systematic uncertainty of the instrument [Aleksić et al., 2014b].

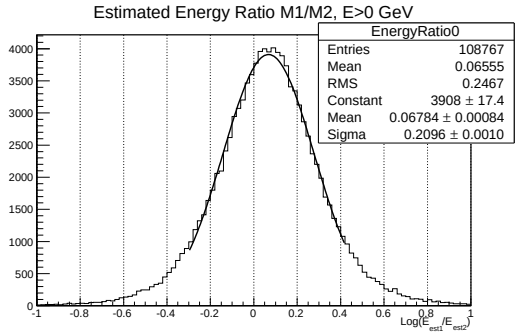

(a) Events with no cut in estimated energy.

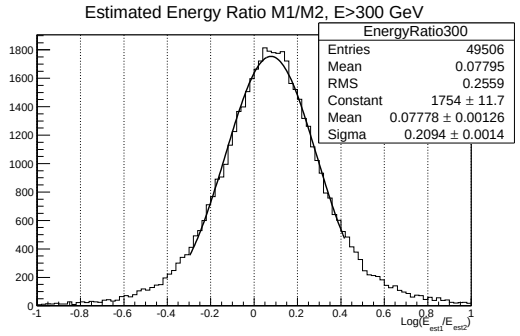

(b) Events with estimated energy above 300 GeV.

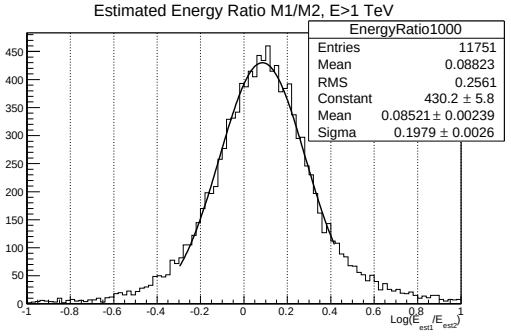

(c) Events with estimated energy above 1 TeV.

FIGURE 3.15: Logarithm of the ratio between the estimated energy of MAGIC I and MAGIC II for events with different energy cuts and zenith angle below 35°, for the 10 days of observation of the April flare. The solid lines in the three plots are fits to a gaussian function. The mean of these functions reveal the mismatch.

The main suspect for the origin of the problem was a mismatch between the simulated performance of the telescopes and the actual one. The SoBo made a deeper analysis of the problem and a new, improved, version of MC went into production. Any production of new MC simulations take a considerable amount of time, since all the parameters have to be carefully tuned. While the MC was in production, to continue with the analysis we decided to test an alternative solution.

The ratio between the estimated energy of the two telescopes showed that there was a mismatch among them, but it was not clear which one had the incorrect calibration, or even if both telescopes were wrongly calibrated. A solution was to apply scaling factors before the image cleaning (at `star` level), which means that the light on each one of the pixels was scaled by a given factor. There was no particular reason to apply the scaling factor to only one of the telescopes. Arbitrarily we decided to test the scaling of the light recorded by MAGIC-II only with a reduced data sample (only the night of highest activity, 2013-04-13). We tried first 6 scaling factors: 1.04, 1.05, 1.07, 1.08, 1.10 and 1.12. The values were chosen under the assumption that if the mismatch in the reconstructed energy was around 7-8%, the scaling factor in the telescope light collection efficiency should more less correspond to that percentage. In that first run we found that applying the scaling factor of 1.08 we obtained the best result. The mismatch was drastically reduced, in this particular case, with data from only one night,

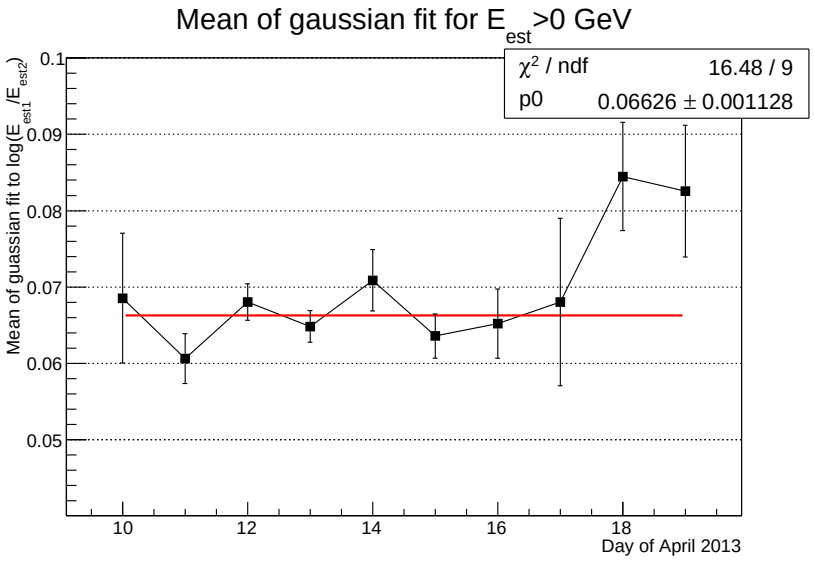

FIGURE 3.16: Mean values for the gaussian fits of the ratio between the estimated energy of MAGIC I and MAGIC II for each day of the observation. The red line is a fit to a line with constant value.

to less than 0.5%. In the next step, we apply the scaling factor of 1.08 to all the data sample (10 nights) from MAGIC-II (see Fig. 3.17 (a)). We also test scaling down the signal from MAGIC-I only by a factor of 0.92 (Fig. 3.17 (b)). Then we test scaling down the signal from MAGIC-I and scaling up the signal from MAGIC-II at the same time, by the factors 0.96 and 1.04, respectively (Fig. 3.17 (c)). In all three cases, we made a gaussian fit to the histograms, to find that the mismatch was effectively reduced. The biggest shift from the mean of the fits is of 0.23%.

Applying the scaling factor to either of the telescopes, or to both, effectively fixes the mismatch in the estimated energy, but obviously the three options result in a slightly different absolute energy scale (up- or down-shifted with respect of the original one). This will in turn affect the reconstruction of the observed spectrum of the source. Fig. 3.18 shows the comparison between the spectral energy distributions (SEDs) obtained taking all the data from the 10 days of observation with zenith angles below 35°. The SEDs were computed using the MARS executable `flute` (see section 2.4.0.7). To have a closer look of how different are the calculated SEDs among them, Fig. 3.19 shows the ratio of the SEDs using the scalings 0.92 in MAGIC I and 1.00 in MAGIC II, and scalings 1.00 in MAGIC I and 1.08 in MAGIC II, with respect to the case with scalings 0.96 in MAGIC I and 1.04 in MAGIC II, that is used as a reference. The agreement between SEDs is good for energies between 100 GeV and 1 TeV. Between $\sim$ 1 and $\sim$ 6 TeV, there is a clear and systematic departure between SED points, with a maximum ratio difference between them of 0.47. Since there is not possible to tell which one give the closes description to the real SED, this uncertainty has to be taken into account, as we will show in the next chapter.

Coming back to the SEDs shown in Fig. 3.18, one thing that immediately catches the attention is the "pile up" in the first points for the 3 scaling cases. For the case of scaling factors of 1.0 in MAGIC I and 1.08 in MAGIC II there is even an extra point at lower energies with a higher pile up. The energy threshold of the telescopes is defined as the peak in a differential rate plot using MC simulations for a hypothetical source with a certain spectral index. For a Crab-like source with an index of -2.6, the energy threshold is $\sim$ 70 GeV [Aleksić et al., 2014b] (see Fig. 3.20). In the case of the April 2013 flare of Mrk421, the energy threshold is $\sim$ 71 GeV. Below

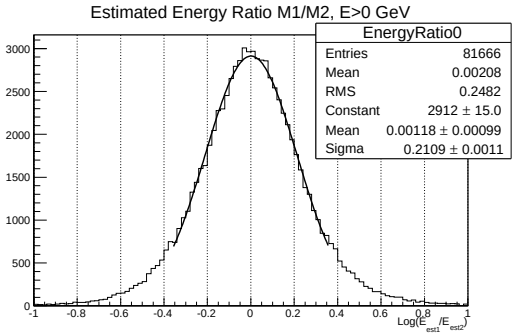

(a) Scaling factor of 1.08 applied to MAGIC II data only.

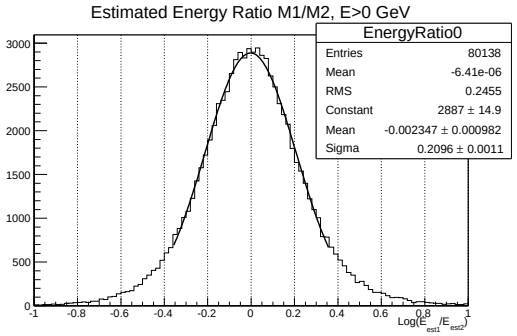

(b) Scaling factor of 0.92 applied to MAGIC I data only.

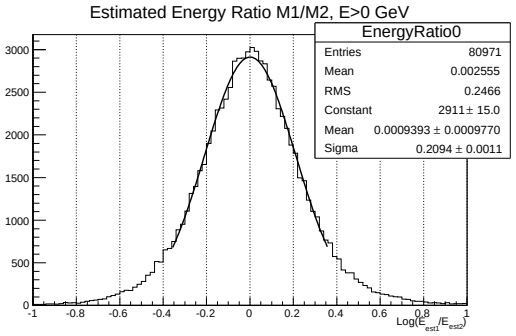

(c) Scaling factor of 0.96 and 1.04 applied to MAGIC I and MAGIC II respectively.

FIGURE 3.17: Logarithm of the ratio between the estimated energy of MAGIC I and MAGIC II for events without a cut in energy and zenith angle below 35° for the 10 days of observation of the Mrk421 April 2013 flare, where different combinations of scaling factors were applied to the data from MAGIC Telescopes. The solid line is a fit to a gaussian function. The mean of these fits reveal that the mismatch has been considerably reduced.

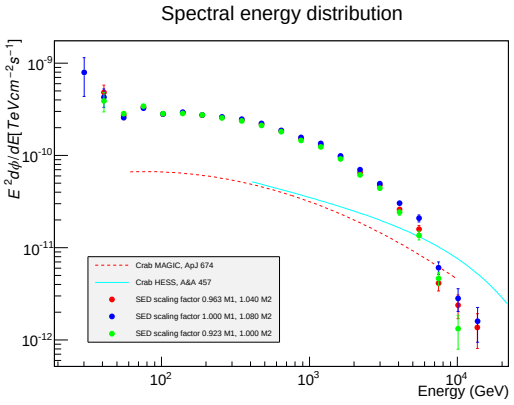

FIGURE 3.18: Comparison of the estimated SEDs for the 3 cases of applied scalings detailed in the legend.

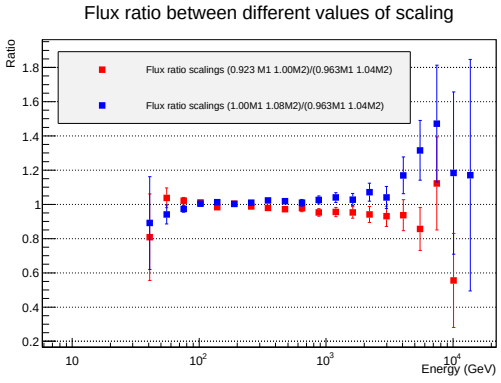

FIGURE 3.19: Ratio of the SEDs for the 3 cases of applied scalings detailed in the legend.

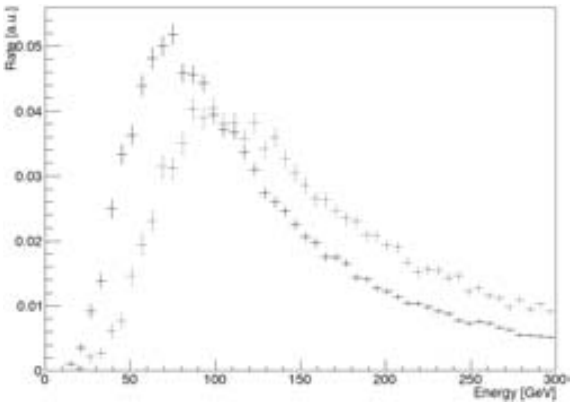

FIGURE 3.20: Rate of γ-ray events (in arbitrary units) surviving the image cleaning with at least 50 phe for a source with a spectral index of -2.6. Solid line: zenith angle below 30°, dotted line: zenith angle between 30° and 45°. From [Aleksić et al., 2014b]

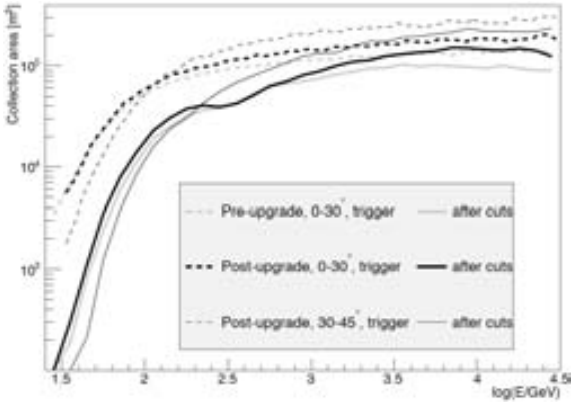

FIGURE 3.21: Collection area of the MAGIC telescopes after the upgrade at the trigger level (dashed lines) and after all cuts (solid lines). Thick lines show the collection area for low zenith observations, while thin lines correspond to medium zenith angle. From [Aleksić et al., 2014b]

the energy threshold the collection area falls rapidly (see Fig. 3.21), and only events with a significant upward fluctuation in their light yield can trigger the telescope. The presence of the pile-ups pointed out that the MC simulations were not perfectly tuned. Apart of the error in the absolute energy calibration of the telescopes, a plausible explanation is that the settings for the trigger were slightly too high. This causes that the number of recorded events in the simulations is smaller compared with actual number in the real data. In consequence, the effective area at low energies (< 100 GeV) is underestimated. Then, in the calculation of the spectrum and the SED if this area is lower than the real one, in the step where the excess events are divided by the effective area the resulting spectral point suffers a pile-up.

3.1.3.4 Analysis with corrected MC simulations

As a result of our findings in the preliminary analysis of Mrk421 April 2013 flare, new MC simulations were properly tuned for the correct absolute calibration of the telescopes and the trigger settings were optimized using data from observation of the Crab Nebula. This new MC production was labeled as "ST.03.02" (see table 3.4).

The very first thing to check with the MC ST.03.02 was the ratio between the estimated energy from the telescopes. Fig. 3.22 show the logarithm of the ratio between the estimated energy of MAGIC I and MAGIC II for different energy cuts. The mismatch found using the MC ST.03.01 is no longer there. The mean of the gaussian fits to the histograms reveal that the estimated energy mismatch between telescopes is down to $\sim 1\%$. The data for the Fig. 3.22 has no scaled signal in any of the telescopes.

The average SED for the whole selected data sample is in the Fig. 3.23. In this plot it can be seen that the pile-up appears in only one point, the very first one. The difference with the situation with the previous MC production, is that in this case the pile-up appears to be reduced and is not very significant, that is, in the Fig. 3.18 more that one point has the pile-up, whereas in the Fig. 3.23 only one point has it.

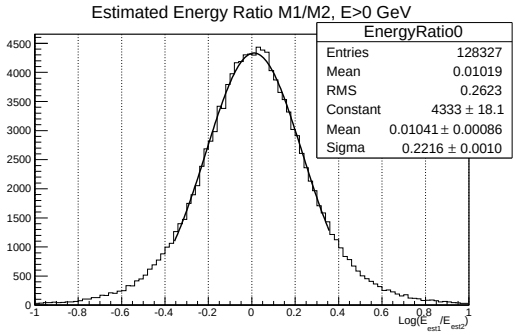

(a) Events with no cut in estimated energy.

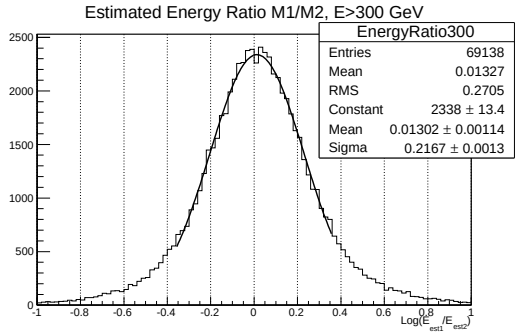

(b) Events with estimated energy above 300 GeV.

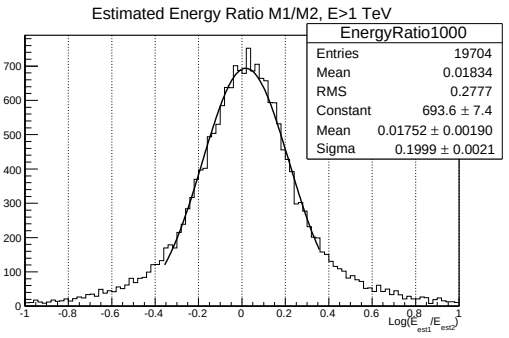

(c) Events with estimated energy above 1 TeV.

FIGURE 3.22: Logarithm of the ratio between the estimated energy of MAGIC I and MAGIC II for events with different energy cuts and all zenith angles for the 10 days of observation of the April flare. The solid lines in the three plots are fits to a gaussian function.

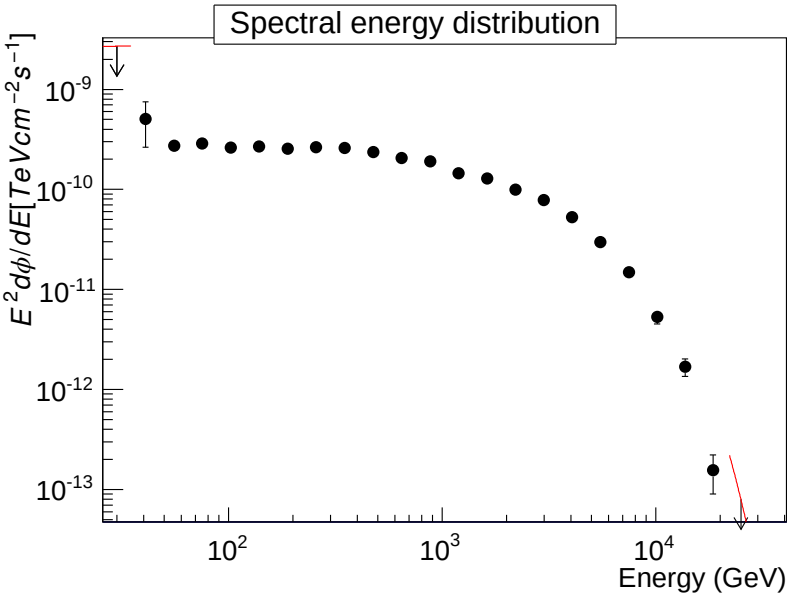

FIGURE 3.23: Average spectral energy distribution of the 10 days of observation of the April flare for all zenith angles.

3.1.3.5 Crab Nebula crosscheck

For the crosscheck of the telescope performance and the validity of the analysis (detailed in section 2.4.1), 6.38 hours of good quality data were collected. The observation dates are 2013-02-10, 2013-03-12, 2013-03-15. The dates are more than a month before the April 2013 Mkr421 flare since is not possible to observe the Crab Nebula at low zenith angle in the month of April. The data is still within the period valid for the MC ST.03.02 (therefore with no significant changes in hardware performance in between).

The sensitivity is expected to be around 0.7 % C.U. [Aleksić et al., 2014b]. For the data selected from Crab Nebula using the RF produced for the analysis of Mrk421, the sensitivity is 0.75±0.06 % C.U..

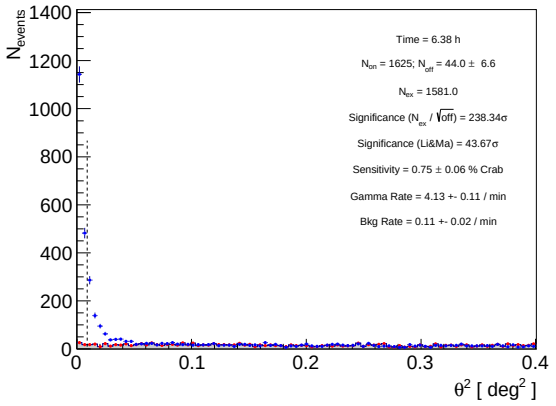

FIGURE 3.24: Θ^2 plot for the Crab Nebula data selected for the crosscheck. In blue are the excess events and in red the background (OFF) events. The vertical dashed line indicates the cut in Θ^2 for the calculation of the significance of the signal and the sensitivity.

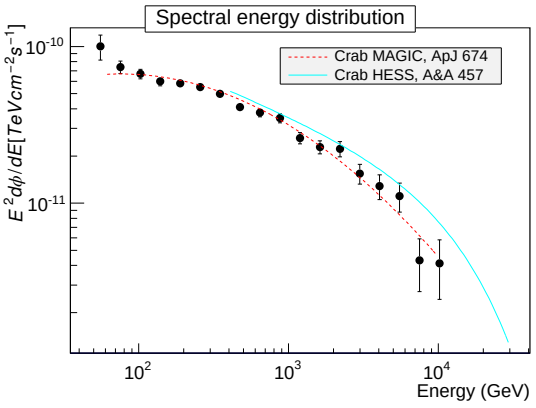

FIGURE 3.25: Spectral energy distribution Crab Nebula data selected for the crosscheck. The dashed red line is the Crab Nebula spectrum as published in [Albert, 2008a]. The blue line is the spectrum reported by H.E.S.S. in [Aharonian, 2006].

In Fig. 3.24 the significance of the signal is given by the formula developed by Li and Ma [1983] (see eq. 2.10 in section 2.4.0.5).

The fact that the value of the sensitivity is around the expected value indicates that the data analysis has been done in the proper way. The next thing to compare is the obtained spectrum with the Crab Nebula from historical records. In Fig.3.25 the spectrum is shown in the SED representation. It can be seen that the observed spectrum matches fairly well with the spectrum of Crab Nebula reported in [Albert, 2008a].

3.1.3.6 Results

The April 2013 flare of Mrk421 produced a record amount of gamma-ray events observed by MAGIC. The average gamma-ray event rate for the day of highest activity, 2013-04-13, was of $\sim$ 32 events per minute after cuts ($E_{est} > 250$ GeV, *hadronness*< 0.16, $size_1$ and $size_2 > 300$ photoelectrons and $\theta^2 < 0.009$). In comparison, the gamma-ray event rate for a Crab Nebula observation is $\sim$ 5 events per minute (after the same cuts).

The significance of the signal after cuts ($E_{est} > 250$ GeV, *hadronness*< 0.16, $size_1$ and $size_2 > 300$ photoelectrons and $\theta^2 < 0.009$) is shown in Fig. 3.26.

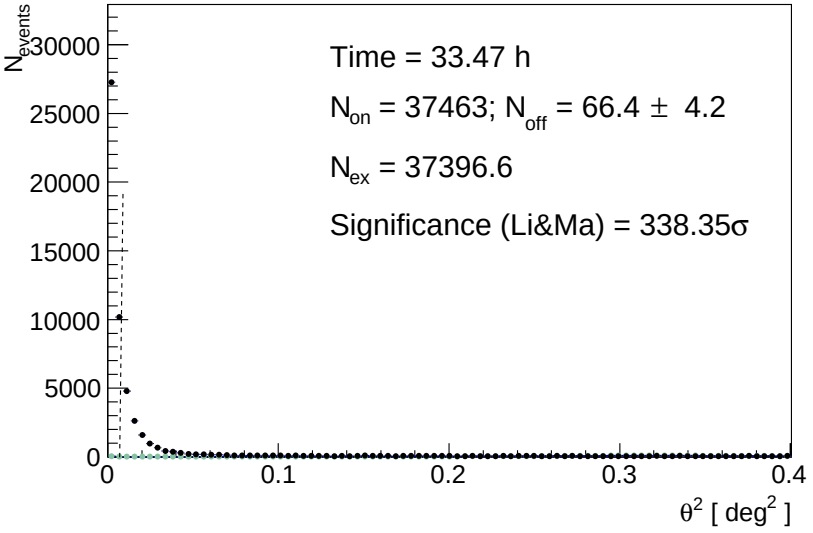

FIGURE 3.26: Θ^2 event distribution for the observation of the April 2013 flare of Mrk421 after cuts.

Due to the extraordinary nature of this flare, Mrk421 was granted long observation times (the source was visible for most part of the night), and since the flux was high, this gave the opportunity to explore the intra-night variability. Fig. 3.27 shows the light curve (LC) for gamma rays with energy above 300 GeV. We chose this energy since is closer to the plateau in the dependence of the collection effective area with the energy, where the acceptance of the instrument is more stable against the change in the zenith angle and changes in the transparency of the atmosphere. The red line in the LC shows the Crab Nebula flux as reported in [Albert, 2008a]. The comparison reveals the enormous increase in the flux from Mrk421, reaching more than 12 times the flux of Crab Nebula. The LC in Fig. 3.28 also reveals that also within one night, particularly the dates of 2013-04-13 and 2013-04-15, the flux changed up to a factor 2, although the increase in the flux happened in a timescale of hours. There is no evidence of a rapid variability in any of the analyzed dates of this flare.

In order to study the changes in the energy spectrum of Mrk421 during this flaring episode, we decided to make a somewhat arbitrary classification of the data according to the flux level. Fig.3.30 shows how the data runs are distributed according to the observed flux, for energies higher than 300 GeV. Taking advantage of the gaps that appear in the histogram, we divided the data between "low" ($F(E > 300) < 0.45 \times 10^{-9}$ cm^{-2}s^{-1}), "medium" ($0.45 \times 10^{-9} < F(E > 300) < 1.1 \times 10^{-9}$ cm^{-2}s^{-1}) and "high" ($F(E > 300) > 1.1 \times 10^{-9}$ cm^{-2}s^{-1}) activity levels.

We calculated the spectra separately for each night, and within a night, the data were further divided to produce high-, medium- and low-level spectra according to the flux ranges defined above. For most of the nights only one spectrum was produced, whereas for the night of 2013-04-13, two spectra were produced, for medium and high activity. In the case of 2013-04-15, the changes in the flux produced three data samples, from medium to high activity and then again medium (see Fig.3.31). Each spectrum was corrected for the EBL absorption using the EBL model by Domínguez et al. [2011].

The evolution of the observed and the de-absorbed SED at VHE of Mrk421 for the April 2013 flare is shown in Fig.3.32 and 3.33. The long exposure time and the intensity of the flux allowed the reconstruction of the SED, in some cases, up to three decades in energy. The first thing to notice is how much the "shape" of the spectra (both observed and de-absorbed) changes

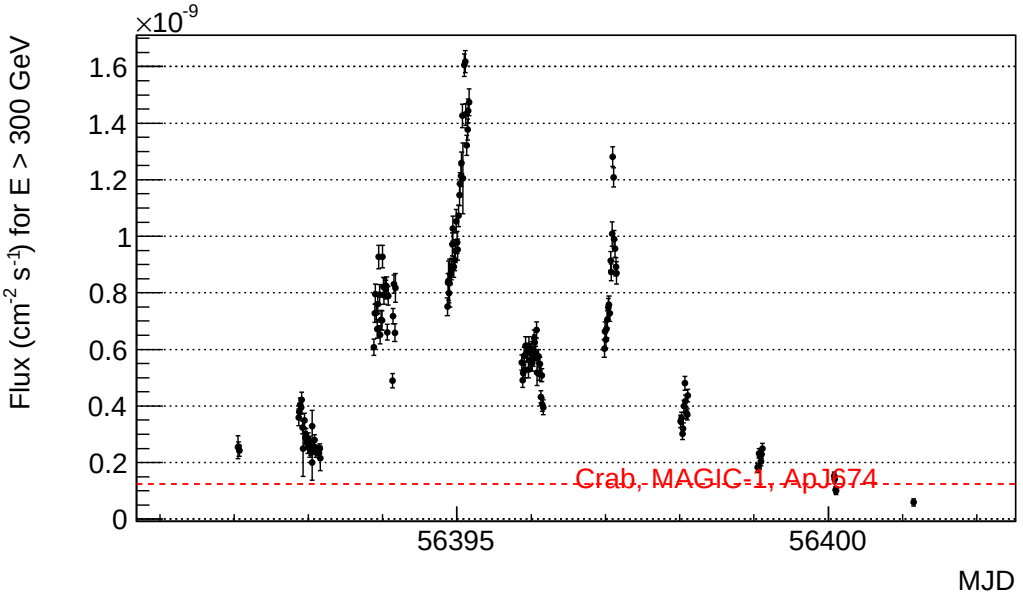

FIGURE 3.27: Light curve for all the data from the April 2013 flare of Mrk421 taken in dark conditions with energy above 300 GeV. Each point represent one run of data (∼ 20 min) and the dates are given in Modified Julian Date. The dashed horizontal red line represents the Crab Nebula flux as published in [Albert, 2008a].

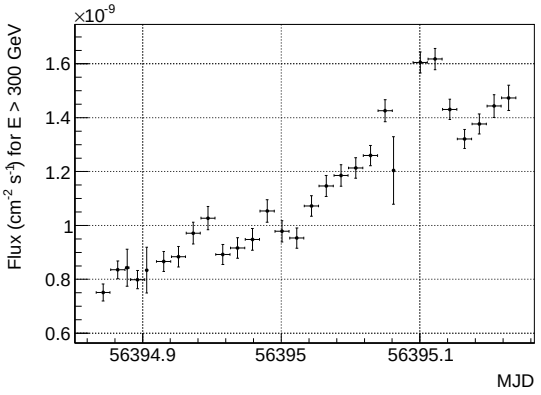

FIGURE 3.28: Light curve of the night of 2013-04-13 from Mrk421 taken in dark conditions with energy above 300 GeV. Each point represent one run of data (∼ 20 min) and the dates are given in Modified Julian Date.

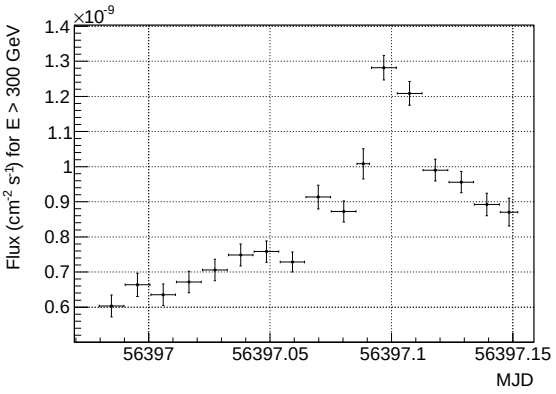

FIGURE 3.29: Light curve of the night of 2013-04-15 from Mrk421 taken in dark conditions with energy above 300 GeV. Each point represent one run of data (∼ 20 min) and the dates are given in Modified Julian Date.

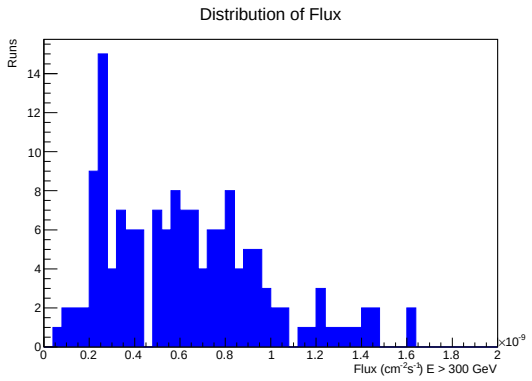

FIGURE 3.30: Distribution of data runs according to their flux from the light curve in the Fig. 3.27.

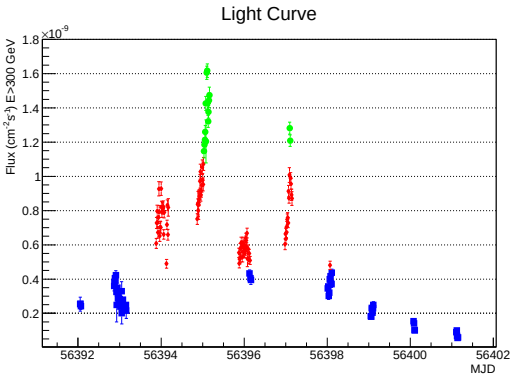

FIGURE 3.31: Light curve for all the data from the April 2013 flare of Mrk421 taken in dark conditions with energy above 300 GeV, classified according to its flux level: blue points are "low" flux, red points are "medium" flux and green points, "high" flux.

TABLE 3.5: Functions tested for modeling the observed spectra from the April 2013 flare of Mrk421.

Name	Abbreviation	Formula
Power law	PWL	$\phi_0(E/E_0)^{-\Gamma}$
Log-parabola	LP	$\phi_0(E/E_0)^{-\Gamma-\beta\log(E/E_0)}$
Exponential cut-off power law	EPWL	$\phi_0(E/E_0)^{-\Gamma}\exp(-E/E_{cut})$
Exponential cut-off log-parabola	ELP	$\phi_0(E/E_0)^{-\Gamma-\beta\log(E/E_0)}\exp(-E/E_{cut})$
Super exponential cut-off power law	SEPWL	$\phi_0(E/E_0)^{-\Gamma}\exp(-(E/E_{cut})^{\gamma})$

from one sample to the other. These changes are visible doing the comparison with the average observed SED from the whole data sample (gray points in Fig.3.32 and 3.33). In order to characterized the de-absorbed spectra, we test fitting the spectral points to each sample to five different functions listed in Table 3.5. The function chosen for fitting each one of the samples was the one which gave the best χ^2-probability. The functions and the parameters for each fit to the de-absorbed spectra are listed in Table 3.6.

In Fig. 3.32 (c, d, e, f, g, h and i) it can be seen that the flux, at energies close to the energy threshold of MAGIC, seems to change very little between the "medium" and "high" states. Around the MAGIC threshold and below is the energy range covered by *Fermi*-LAT. In Fig. 3.34 it can be seen that the fluxes observed by *Fermi*-LAT, around the same dates where the "medium" and "high" states were measured by MAGIC, also have little variability. Also in Fig. 3.32 it can be seen how the maximum of the de-absorbed SEDs (which could be the inverse Compton peak) shifts to the right as the integrated flux increases. This kind of behavior in the emission from Mrk421 has been observed in Aleksić et al. [2014a]. Another feature to be notice is how the E_{cut} in the fits for the spectra shown in Fig. 3.32 (f), (g) and (h) (after the highest state) seems to increase. Subsequent spectra were best fitted by LP functions (except the very last two), that is, the spectra in those sample became flatter. The full characterization of the spectral evolution of the April 2013 flare of Mrk421 is beyond the scope of this work. However a study is underway and will be published elsewhere.

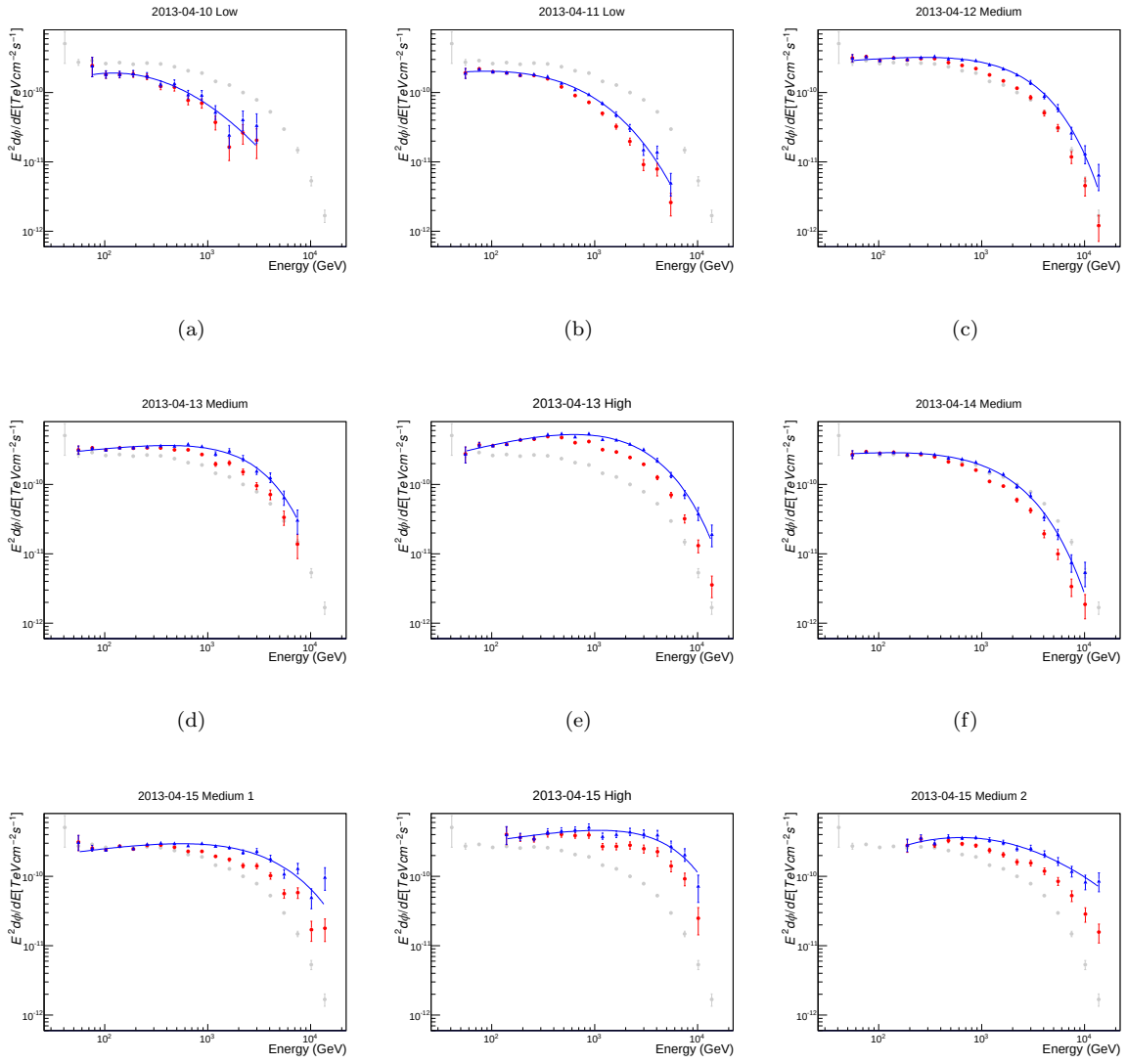

(a) (b) (c)

(d) (e) (f)

(g) (h) (i)

FIGURE 3.32: Evolution of the observed (black markers) and de-absorbed (blue markers) SED at VHE from the April 2013 flare of Mrk421. The EBL de-absorption was done using the EBL model by Domínguez et al. [2011]. The histograms titles indicate the observation date and the level of flux according to the classification shown in Fig.3.31. The gray points are the observed average spectrum for the whole data set, drawn as a reference. The blue line in each de-absorbed spectrum is the fit to a function as described in Table 3.6.

TABLE 3.6: Functions and parameters used to characterized the observed spectra of the April 2013 flare of Mrk421, with $E_0 = 300$ GeV. All uncertainties are statistical

Date	Flux level	Function	χ^2/NDF	Fitting parameters				
				f_0 ($\times 10^{-10}$ Tev^{-1}cm^{-2}s^{-1})	Γ	β	E_{cut} (TeV)	γ
2013-04-10	Low	LP	9.7/10	1.6 ± 0.1	2.4 ± 0.1	0.54 ± 0.14	-	-
2013-04-11	Low	SEPWL	14.0/12	7.4 ± 15.0	1.6 ± 0.6	-	0.1 ± 0.5	0.5 ± 0.3
2013-04-12	Medium	SEPWL	14.0/15	3.9 ± 0.3	1.9 ± 0.1	-	2.1 ± 0.4	0.9 ± 0.1
2013-04-13	Medium	EPWL	12.2/14	4.1 ± 0.1	1.8 ± 0.1	-	2.4 ± 0.2	-
2013-04-13	High	SEPWL	26.0/15	6.9 ± 1.0	1.6 ± 0.1	-	1.3 ± 0.5	0.7 ± 0.1
2013-04-14	Medium	SEPWL	17.8/14	3.8 ± 0.1	1.9 ± 0.1	-	1.2 ± 0.4	0.8 ± 0.1
2013-04-15	Medium	SEPWL	22.1/15	3.6 ± 0.1	1.8 ± 0.1	-	2.5 ± 1.7	0.7 ± 0.2
2013-04-15	High	EPWL	12.7/12	4.3 ± 0.2	1.8 ± 0.1	-	4.6 ± 0.7	-
2013-04-15	Medium	LP	7.8/12	3.3 ± 0.2	1.7 ± 0.1	0.63 ± 0.04	-	-
2013-04-16	Low	LP	12.5/13	2.0 ± 0.0	2.2 ± 0.0	0.37 ± 0.04	-	-
2013-04-17	Low	LP	15.4/13	1.1 ± 0.0	2.3 ± 0.0	0.30 ± 0.07	-	-
2013-04-18	Low	PWL	10.8/8	0.8 ± 0.0	2.7 ± 0.1	-	-	-
2013-04-19	Low	EPWL	9.7/5	1.5 ± 0.5	1.6 ± 0.6	-	0.4 ± 0.2	-

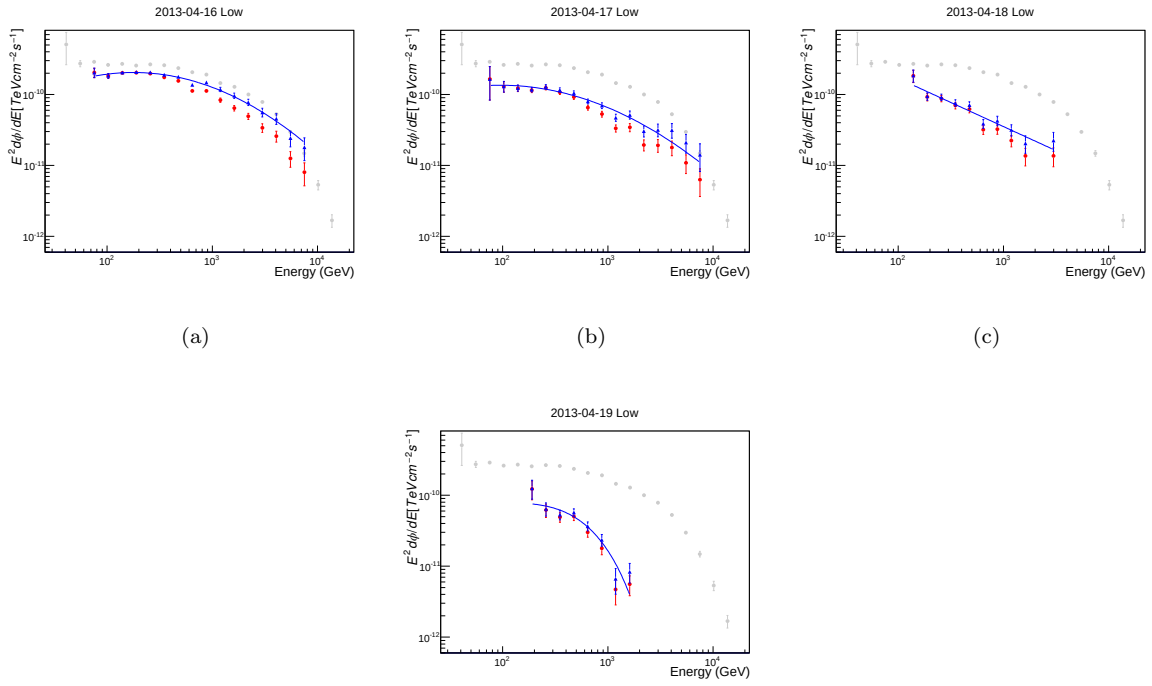

(a) (b) (c)

(d)

FIGURE 3.33: Evolution of the observed (black markers) and de-absorbed (blue markers) SED at VHE from the April 2013 flare of Mrk421. The EBL de-absorption was done using the EBL model by Domínguez et al. [2011]. The histograms titles indicate the observation date and the level of flux according to the classification shown in Fig.3.31. The gray points are the observed average spectrum for the whole data set, drawn as a reference. The blue line in each de-absorbed spectrum is the fit to a function as described in Table 3.6.

3.1.4 Observations of the April 2013 flare by space instruments

The April 2013 flare of Mrk421 was also observed by detectors onboard satelites. The high-energy gamma-ray detector *Fermi*-LAT [Atwood et al., 2009] followed the evolution of the flare measuring the flux on a daily basis. Observation were also executed by *Swift*/XRT [Burrows, 2005] and *NuSTAR* [Balokovic et al., 2013, Harrison, 2013] on the soft and hard X-ray bands, respectively. Fig.3.34 shows the LC for the three instruments together with MAGIC, between April 9th and April 19th, 2013. With the exception of *Fermi*-LAT, all instruments represented in Fig. 3.34 were able to follow the flare at the scale of tens of minutes.

From the comparison between LCs, it can be seen that the variations in flux in the X-ray band are correlated with the variations in the VHE band. The increase in activity between April 12th and 13th (56394 and 56395 MJD) was well followed by *NuSTAR* and with less "snapshots" by *Swift*/XRT. MAGIC observations are interrupted due to its duty cycle, but the increase at VHE is clearly visible reaching its peak in 2013-04-13. The second peak of activity on 2013-s04-15 (56397 MJD) in the VHE band is also clearly visible in the X-ray band, followed by the decrease towards the end of the period shown. The LC from *Fermi*-LAT does not shows these peaks of activity seen in the other bands, although roughly follows the trend of activity decrease of the source towards the period. It catches the attention the peak seen by *Fermi*-LAT between 2013-04-11 and 2013-04-12, which is not observed by the other instruments. This peak coincides

with the gap in MAGIC observations but in the X-ray band the source appears to be decreasing in activity.

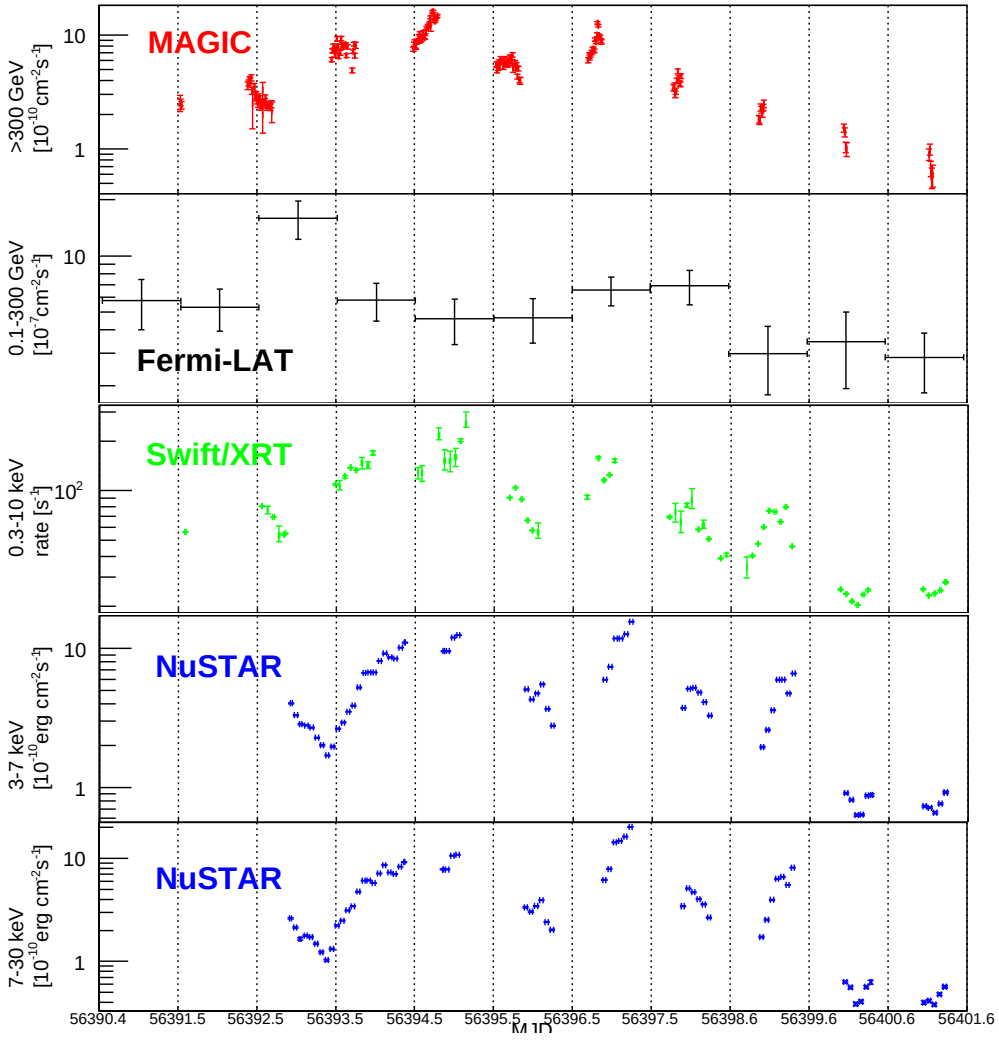

FIGURE 3.34: Light curve for MWL observations of the flare of Mrk421 between April 9th and April 19th, 2013. The red points are the MAGIC observations, for energies above 300 GeV binned by "runs" ($\sim$ 20 minutes). *Fermi*-LAT points are in black, for energies between 0.1 and 100, binned daily. The green points represent the observations by *Swift*/XRT for energies between 0.3 and 10 keV, binned by "snapshots" (20-30 minutes). *NuSTAR* observations are in blue, for energies between 3 to 7 keV and 7 to 30 keV, binned by "snapshots". *Swift*/XRT data ware supplied by the UK Swift Science Data Centre at the University of Leicester [Evans, 2007, 2009]. The *Fermi*-LAT analysis is from public data [Longo et al.]. All uncertainties in the fluxes are statistical.

The observed correlation between the X-ray and the VHE bands during the April 2013 flare provides more evidence in favor of a synchrotron self-Compton (SSC) model for the broad-band emission of Mrk421, since similar levels of variability in both bands points to a common source of radiation, e.g. the same electron population. In the LCs shown in Fig. 3.34 it can be seen that several snapshots from *Swift*/XRT and *NuSTAR* are coincident in time with MAGIC runs. From this strictly simultaneous data, for different epochs of the flare, various broad-band SED could be built. The characterization and the study of the correlation between energy bands and the broad-band SED is a work still in progress and, as pointed out before, it will be published elsewhere.

3.2 1ES 1011+496

3.2.1 Previous observations with MAGIC

1ES 1011+496 is a high-frequency BL Lac (see section 1.2.1) located at redshift =0.212 [Albert and al., 2007]. It was discovered at VHE by the MAGIC Collaboration in 2007 following an optical high state reported by the Tuorla Blazar Monitoring Programme [Albert and al., 2007]. MAGIC members of the Tuorla Observatory made the measurement of the redshift. The flux of the source for the 2007 observations showed no evidence of variability with an emission level of F(>200 GeV)=(1.58±0.32)×10^{-11} $cm^{-2}s^{-1}$. The observed spectrum at the time of discovery could be approximated by a power-law function with index $\Gamma = 4.0 \pm 0.5_{stat} \pm 0.2_{sys}$ and normalization $f_0 = (2.0 \pm 0.1) \times 10^{-10}$ TeV^{-1} cm^{-2} s^{-1} at 200 GeV. The systematic uncertainty for the absolute flux level was estimated to be 75%. The estimated intrinsic spectrum assuming the Kneiske et al. [2002] model for the EBL absorption, was a power-law with photon index $\Gamma_{int} = 3.3 \pm 0.7_{stat}$. Following the discovery, a MWL campaign was organized by MAGIC [Reinthal et al., 2012], centered around common observation windows of the AGILE satellite [Tavani, 2008]. The data in the optical band was taken by KVA telescope. The Metsähovi Radio Observatory made the observations in radio and *Swift*/XRT [Burrows, 2005] did measurements in X-rays. For that campaign the source was observed by MAGIC in 25 nights between March and May 2008. The mean integral flux showed a level similar to the one measured during the discovery in 2007 of F(>200 GeV)=(1.57±0.30)×10^{-11} photons $cm^{-2}s^{-1}$. The observed γ-ray spectrum could also be fitted with a simple power-law with index $\Gamma = 3.2 \pm 0.6_{stat}$ and normalization $f_0 = (1.6 \pm 0.1) \times 10^{-10}$ TeV^{-1} cm^{-2} s^{-1} at 200 GeV.

A second MWL campaign, also led by MAGIC, observed 1ES 1011+496 in two periods, from March to April, 2011 and from January to May, 2012 [Aleksić]. The MWL data included observations from *Fermi*-LAT, *Swift*/UVOT and *Swift*/XRT, the KVA telescope and the radio-telescopes Owens Valley Radio Observatory (OVRO) and Metsähovi. No significant variability at VHE was measured within the periods of these observations, and the mean integral flux F(>200 GeV)=$(0.79 \pm 0.12_{stat} \pm 0.05_{sys})\times10^{-11}$ photons $cm^{-2}s^{-1}$ was lower than in previous observations by MAGIC. The observed spectrum at VHE could be fitted with a simple power law with index $\Gamma = 3.66 \pm 0.22_{stat} \pm 0.15_{sys}$ and normalization $f_0 = (1.33 \pm 0.06_{stat} \pm 0.20_{sys}) \times 10^{-10}$ TeV^{-1} cm^{-2} s^{-1} at 200 GeV. Using the EBL model by Domínguez et al. [2011], the de-absorbed differential energy spectrum showed a good agreement with a simple power law function with index $\Gamma = 2.95 \pm 0.25_{stat}$ and normalization $f_0 = (1.87 \pm 0.08_{stat}) \times 10^{-10}$ TeV^{-1} cm^{-2} s^{-1} at 200 GeV.

Although MAGIC did not measure a significant variability in the 2007, 2008 and 2011/2012 observations, 1ES 1011+496 was still a good candidate to be observed in flaring state.

3.2.2 MAGIC February 2014 observation

On February 5th 2014, VERITAS issued and alert for the flaring state of 1ES 1011+496. MAGIC performed target of opportunity (ToO) observations for 17 nights during February-March 2014. All nights presented good weather conditions, except the night of March 7th, were some cloudiness affected the data. Most of the data ware taken under dark conditions, except the night of February 7th, where part of the observations were done under moonlight. Details are given in the Table 3.7.

TABLE 3.7: Observation dates, light conditions, exposure time in minutes and zenith angle coverage according to the reports logged in the runbook.

Night	Dark		Moonlight	
	Time (min.)	Zd (deg.)	Time (min.)	Zd (deg.)
2014-02-06	36	22-26	-	-
2014-02-07	39	21-24	101	22-36
2014-02-08	118	21-37	-	-
2014-02-09	79	27-39	-	-
2014-02-10	40	39-45	-	-
2014-02-11	30	41-46	-	-
2014-02-12	40	50-56	-	-
2014-02-22	36	26-32	-	-
2014-02-23	39	30-36	-	-
2014-02-25	30	20-21	-	-
2014-02-26	38	24-29	-	-
2014-02-27	28	20-23	-	-
2014-03-01	28	24-28	-	-
2014-03-02	29	24-28	-	-
2014-03-03	30	24-28	-	-
2014-03-05	37	24-29	-	-
2014-03-07	28	21-21	-	-

3.2.2.1 Data selection

The data selection, as with Mrk421, was done based in the stability of the rates and the light conditions (see section 3.1.3.1) . For this analysis again only dark data was selected. Rates were stable over almost all the observations in dark conditions, so only few subruns were discarded. At the end, 11.8 hours of exposure were collected.

3.2.2.2 Data reduction

The data from 1ES 1011+496 ware analyzed using the standard MAGIC analysis pipeline (see section 2.4). The MC simulations used to generate the Random Forest and the Look-Up tables for the analysis are those labeled ST.03.03 (see Table 3.4). The data used as the hadron sample (OFF signal) is listed in Table 3.8.

TABLE 3.8: Source names and observation dates for the data samples used to training the Random Forest.

Source	Date
TXS2320+343	2013-08-08, 2013-08-10, 2013-08-14, 2013-10-02, 2013-10-06, 2013-10-07
W44-SRC1	2013-09-24, 2013-09-27
3c58	2013-10-07
LSI+61	2013-10-11, 2013-10-12

3.2.2.3 Crosscheck with Crab Nebula data

For the crosscheck (detailed in section 2.4.1), 7.06 hours of good quality Crab data were collected. The observation dates are February 22nd, 25th, 27th, and March 1st, and 2nd, 2014. The dates are within the period valid for the MC ST.03.03.

The sensitivity is expected to be around 0.7 % C.U. [Aleksić et al., 2014b]. For the data selected from Crab Nebula using the RF produced for the analysis of 1ES 1011+496, the sensitivity is 0.67 ± 0.05 % C.U. (see Fig. 3.35).

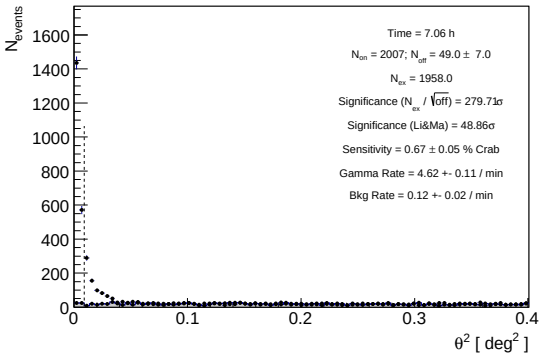

FIGURE 3.35: Θ^2*plot* for the Crab Nebula data selected for the crosscheck. The vertical dashed line indicated the cut in Θ for the calculation of the significance of the signal and the sensitivity.

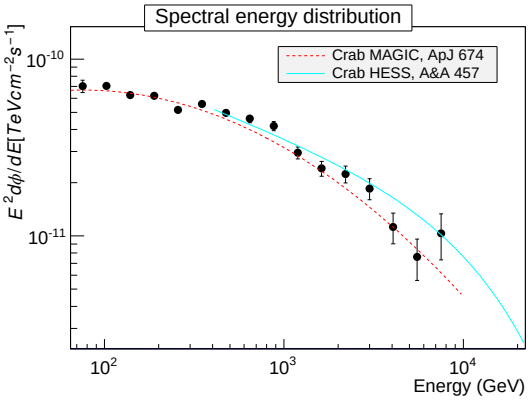

FIGURE 3.36: Spectral energy distribution Crab Nebula data selected for the crosscheck. The dashed red line is the Crab Nebula spectrum as published in [Albert, 2008a]. The cyan line is the spectrum reported by H.E.S.S. in [Aharonian, 2006].

3.2.2.4 Results

Fig. 3.38 shows the night-wise gamma-ray light curve for energies E > 200 GeV between February 6th and March 7th 2014. The source was detected with a significance of $\sim 41\sigma$ (see Fig. 3.37) after the following cuts in the events: $E > 250$ GeV, *hadronness*< 0.16 and $size_1$ and $size_2 > 300$ photoelectrons and $\theta^2 < 0.009$. The emission in this period had a high night-to-night variability, reaching a maximum of $(2.32 \pm 0.14) \times 10^{-10}$ cm^{-2}s^{-1}, ∼14 times the mean integral flux measured by MAGIC in 2007 and 2008 for 1ES 1011+496 [Albert and al., 2007, Reinthal et al., 2012] and ∼29 times the mean integral flux from the observation in 2011-2012 [Aleksić]. For most of the nights the exposure time was ∼40 minutes, only for two nights (February 8th and 9th) the observations were extended to ∼2 hours. No significant intra-night variability was observed at any time scale.

The averaged observed spectrum for the whole data set was fitted to a log-parabola function (see Fig. 3.39):

$$\frac{dF}{dE} = f_0 \left(\frac{E}{E_0} \right)^{-\Gamma - \beta \log(E/E_0)} \tag{3.1}$$

with a probability of 0.002 and $\chi^2 = 30.7/12$. The photon index is $\Gamma = 2.84 \pm 0.03_{stat}$, curvature index $\beta = 0.99 \pm 0.05_{stat}$ and normalization factor at $E_0 = 250$ GeV $f_0 = (3.58 \pm 0.10_{stat}) \times 10^{-11}$

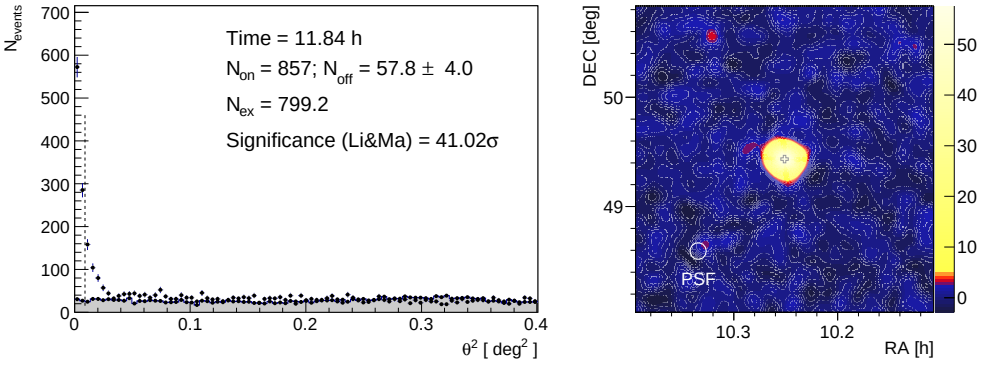

(a) θ^2 event distribution.

(b) Skymap.

FIGURE 3.37: Detection significance from the θ^2 distribution of events from 1ES 1011 (left) and the test statistic (TS) value map (right). The significance and the TS are calculated following the formula developed by Li and Ma 1983 (see eq. 2.10 in section 2.4.0.5) .

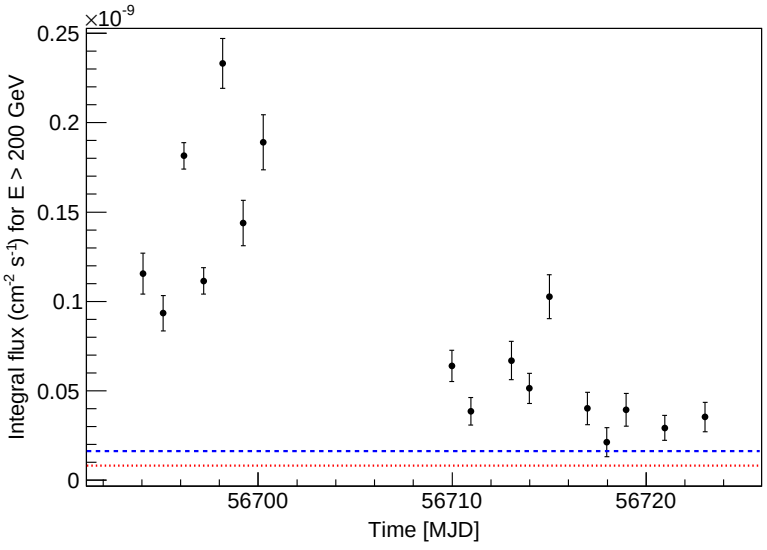

FIGURE 3.38: 1ES 1011+496 light curve between February 6th and March 7th 2014 above an energy threshold of 200 GeV with a night-wise binning. The blue dashed line indicates the mean integral for the MAGIC observations of 2007 and the blue dotted line the MWL campaign between 2011 and 2012.

$\mathrm{cm}^{-2}\mathrm{s}^{-1}\mathrm{TeV}^{-1}$. The de-absorbed spectrum using the EBL model by Domínguez et al. [2011] can be fitted with a simple power-law function with a photon index $\Gamma = 2.05 \pm 0.03_{stat}$ and normalization factor at 250 GeV $f_0 = (5.42 \pm 0.10_{stat}) \times 10^{-11}$ $\mathrm{cm}^{-2}\mathrm{s}^{-1}\mathrm{TeV}^{-1}$.

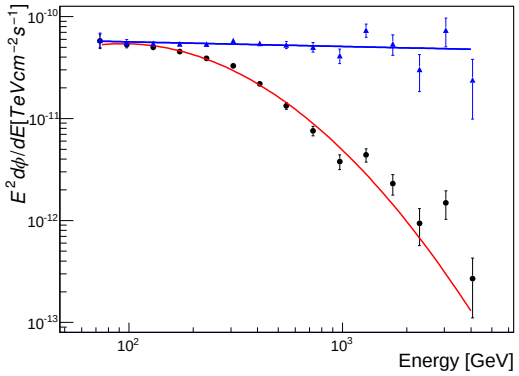

FIGURE 3.39: Average spectral energy distribution (SED) of 1ES 1011+496 for the 17 nights of observations between February 6th and March 7th 2014. The black dots are the observed data and the blue triangles are the data after EBL de-absorption. The red line indicate the fit to a log-parabola function of the observed SED whereas the blue line indicate the fit to a power-law function of the de-absorbed SED.

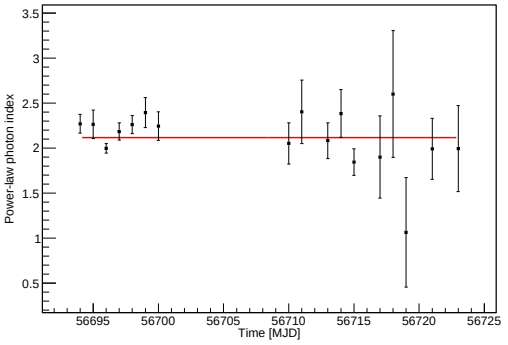

FIGURE 3.40: Evolution of the photon index from power-law fits to the de-absorbed night-wise spectra of 1ES 1011+496 between February 6th and March 7th 2014. The error bars are the parameter uncertainties from the fits. The red line represents the fit to a simple line, for which the probability is 10%. If the night of February 8th (third point from the left) is not included in the fit, the probability is almos 50%.

From the light curve is clear that the flux was changing significantly from night to night. For the description of the night-wise spectra we de-absorbed the spectrum of each night with the EBL model by Domínguez et al. 2011. These de-absorbed spectra could be fitted with simple power-law functions. The evolution of the photon index of the fits can be seen in Fig. 3.40. For each power-law fit, the de-correlation energy[2] was used as normalization energy. For the first seven nights of the observed period all photon indexes are compatible with each other within errors, with the index of 2013-02-08 having the biggest departure. In the latter part of the observed period, the activity of the source was lower resulting in bigger uncertainties for the fits.

[2]Normalization energy at which two adjusted parameters are more independent of each other.

Chapter 4

EBL measurement using observations of Markarian 421 and 1ES 1011+496

4.1 Previous EBL measurements using cosmic gamma-rays

The setting of constrains to the EBL intensity using galaxy counts was briefly described in section 1.3. These measurements set lower limits to the EBL mostly in the optical band. However, the near infrared (NIR) region of the EBL is more difficult to measure due to the intense foreground light from interplanetary dust. Indirect measurements of the EBL in the NIR region are possible observing very-high energy (VHE) gamma rays from extragalactic sources.

The observed differential energy spectra from AGNs are modified by the interaction of the gamma rays with the EBL (section 1.3.1) However, it is not possible to distinguish source-intrinsic spectral features from those induced by the EBL. Therefore, in order to attempt a measurement of the EBL itself, some assumptions about the intrinsic source spectrum have to be made. The most basic assumption is related to the limited hardness of the intrinsic spectra of AGNs at VHE. It is well-accepted that the relativistic electrons involved in the synchrotron self-Compton (SSC) models are Fermi-accelerated, that is, accelerated in shock fronts. These electrons will have a power-law energy spectrum, $dN/dE \propto E^{-\Gamma_e}$, with index $\Gamma_e \sim 2$. The synchrotron photons emitted by the relativistic electrons will have a power-law spectrum with index $\Gamma_{syn} = \frac{\alpha+1}{2} = 1.5$. These synchrotron photons are scattered by the same electron population via inverse-Compton. If the process occurs in the Thomson regime, the resulting spectrum will be approximately the same as that of the synchrotron photons. If the scattering process takes place in the Klein-Nishina regime, the spectral index will be larger (i.e. steeper spectrum). A too high EBL density may result in a de-absorbed spectrum which violates this limit, therefore this method allows to set upper limits to the EBL density [e.g. Aharonian et al., 2006, Mazin and Raue, 2007, Stecker and de Jager, 1996].

Gamma rays observed by *Fermi*-LAT are emitted in the optically-thin regime of the EBL ($E < 25$ GeV). Therefore, the measured spectrum is the actual intrinsic spectrum of the source. Based in the fact that models for gamma-ray emission from AGNs predict convex spectra, it can be assumed that the measured spectrum of a given source can be extrapolated to higher energies. Then, the extrapolated spectrum can be compared with the spectrum of the same source

observed by Cherenkov telescopes, setting upper limits to the EBL intensity [Georganopoulos et al., 2010, Meyer et al., 2012, Orr et al., 2011].

The Fermi collaboration employed an alternative technique to actually measure the EBL density using a likelihood ratio test on LAT data from a number of extragalactic sources Ackermann et al. [2012]. Spectral energy distributions from 150 BL Lacs in the redshift range 0.03 - 1.6 were modeled as log parabolae in the optical-thin regime (E< 25 GeV), then extrapolated to higher energies and compared with the actually observed photon fluxes. A likelihood ratio test was used to determine the best-fit scaling factor for the optical depth $\tau(E, z)$ according to a given EBL model, hence providing a measurement of the EBL density relative to the model prediction. Several EBL models were tested using this technique [e.g. Finke et al., 2010, Stecker and Scully, 2006], including the most widely and recently used by IACTs by Franceschini et al. [2008] and Domínguez et al. [2011]. They obtained a measurement of the UV component of the EBL of 3 ± 1 nW m^{-2} sr^{-1} at $z \approx 1$.

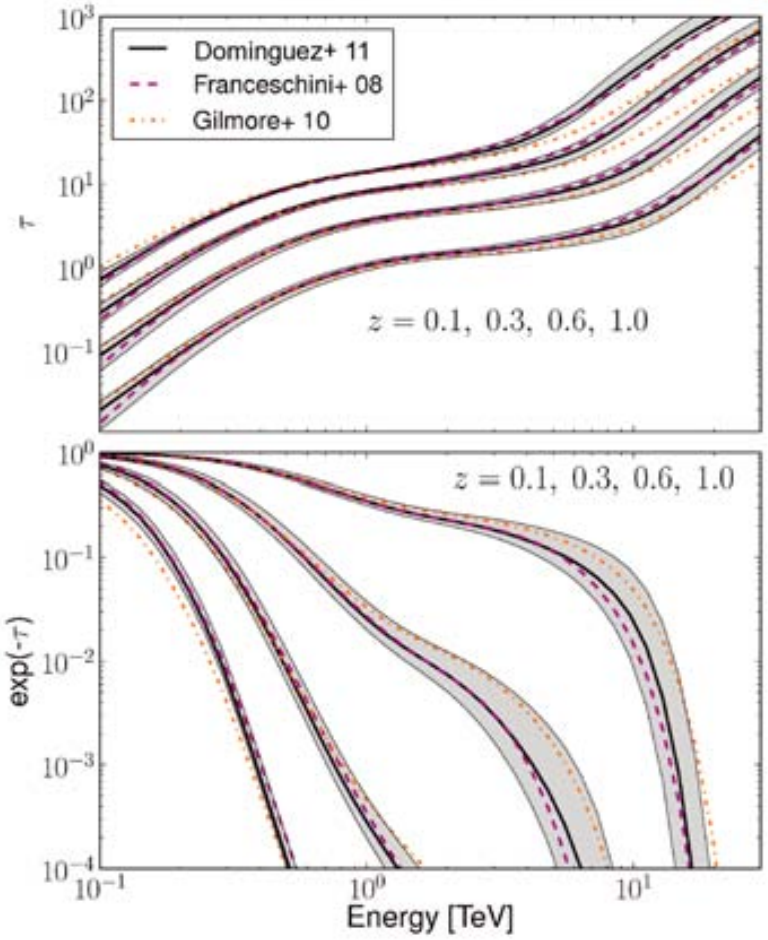

FIGURE 4.1: **Upper panel**: Optical depth versus observed energy of gamma rays for sources at different redshifts for three EBL models: black solid line is Domínguez et al. 2011, dashed magenta line is Franceschini et al. [2008] and dot-dashed orange line is Gilmore et al. [2012]. **Lower panel**: flux attenuation versus observed energy of gamma rays for fictitious sources at different redshifts. The EBL uncertainties for the EBL model of Domínguez et al. are represented by the shadowed area.

Fig.4.1 shows the optical depth τ versus the energy of the observed gamma rays. An initial rise of the EBL intensity at UV-optical wavelengths (see Fig.1.7) causes an increase in the optical depth between 10 and 500 GeV. The decline in the EBL intensity between $\sim$ 1 and 15 μm causes τ to rise less rapidly between 1 and 10 TeV. Then the rise in the EBL intensity towards

the peak of the dust emission at $\sim 100 - 200$ μm causes τ to resume its rising beyond 10 TeV reflects. These inflection points of τ versus logarithm of energy, seen more less in the same energy range at all redshifts, is greatly accentuated in the flux attenuation of the observed gamma rays, due to the exponential dependence with τ. Therefore is expected that this EBL feature leaves an imprint in the observed differential energy spectra of blazars at VHE. With this idea as starting point, the H.E.S.S. collaboration used a likelihood ratio test to measure the EBL taking advantage of their observations of distant sources at VHE [Abramowski et al., 2013]. They modeled the intrinsic spectra of several AGNs using simple functions (up to 4 parameters), then applied a flux suppression factor $\exp(-\alpha \times \tau(E, z))$, where τ is the optical depth according to a given EBL model and α a scaling factor. A scan over α was performed to achieve the best fit to the observed VHE spectra Abramowski et al. [2013]. The no-EBL hypothesis, $\alpha = 0$, was excluded at the 8.8σ level, and the EBL flux density was constrained in the wavelength range between 0.30 μm and 17 μm with a peak value of $15 \pm 2_{stat} \pm 3_{sys}$ nW m^{-2} sr^{-1} at 1.4 μm. Their sample consisted of 17 observations of different flux states of seven blazars: Mrk421, PKS 2005-489, PKS 2155-304, 1ES 0229+200, H 2356-309, 1ES 1101-232 and 1ES 0347-121. The redshifts of these sources are between 0.031 and 0.188. Statistically, the HESS measurement was dominated by the observation of PKS 2155-304, at redshift $z = 0.116$, which was observed in a spectacular flux outburst in July 2006 [Aharonian et al., 2007b]. The data for Mrk421 that they used was from 2004 H.E.S.S. observations, taken at large zenith angle, yielding a high energy threshold around 1 TeV but also leading to the detection of photons up to ~ 40 TeV [Aharonian et al., 2005], well inside the optically-thick region of the EBL, even for a source as nearby as Mrk421. However, the Mrk421 data alone did not gave a positive result for the likelihood ratio test (see Fig.4.2).

Using data from multi-wavelength (MWL) observations of PKS 2155-304, Mankuzhiyil et al. [2010] tested another approach for measuring indirectly the EBL. In this approach, the spectral energy distribution (SED) of the source, from the optical band to high-energy gamma rays ($\sim 0.1 - 100$ GeV) was fitted with a SSC model, and this was taken as the intrinsic emission of the source since it is in the optical-thin regime of the EBL. Then, the model was extrapolated to VHE and compared with the actual measurements at those energies, where the EBL absorption can be evaluated. With a similar approach, Domínguez et al. [2013] modeled the SED of 15 blazars to measure the gamma-ray horizon (CGRH). The CGRH is, by definition, the energy at which the optical depth of the photon-photon pair production becomes unity as function of redshift. 1ES 1011+496 was part of the blazar sample. For that study, Domínguez et al. modeled the SED of each source, doing a prediction for the VHE band, and then made a comparison with the observed VHE data. In the case of 1ES 1011+496, they compared their modeled SED with the VHE data taken in 2007 by MAGIC. Their prediction was below the observed VHE data, which led to no optical-depth information. A caveat in Domínguez et al. approach is that the SED modeling of 1ES 1011+496 2007 observations was done using non simultaneous data between the measurements at different wavelengths. The lack of simultaneity in MWL data could lead to an inaccurate SED modeling and therefore a incorrect prediction at VHE. That is why MWL observations of AGNs (or any astrophysical object) with high variability have to be done as simultaneous as possible. Using only VHE data from IACTs to measure the EBL (as HESS did) has the advantage that avoids the additional complication of collecting strictly simultaneous MWL data.

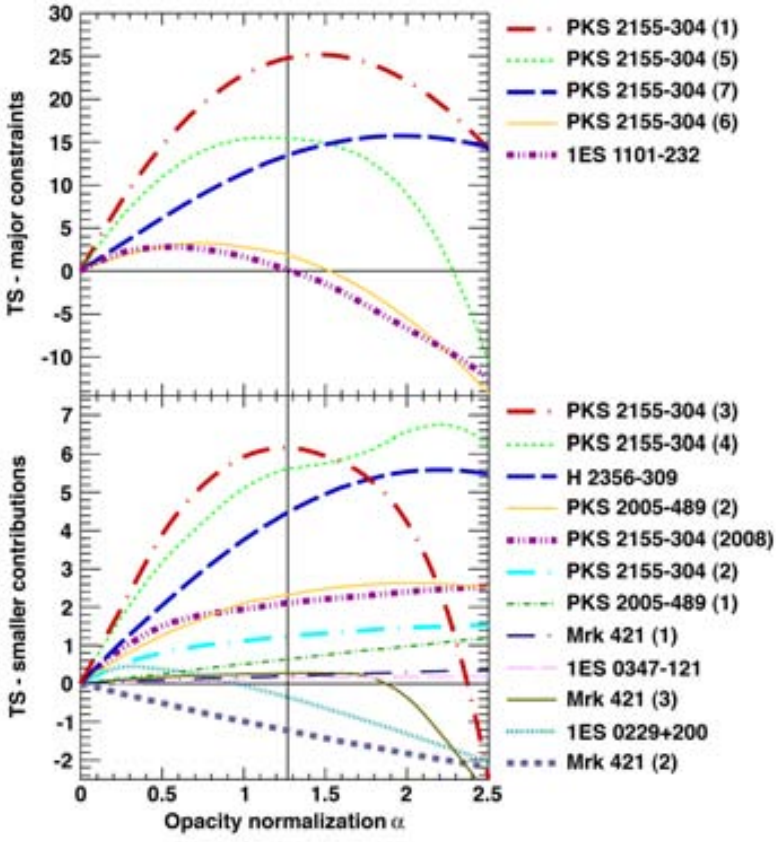

FIGURE 4.2: Test Statistics (TS) as a function of the opacity normalization α for the best fit intrinsic models for each spectrum in the sample of H.E.S.S.. The TS profiles are sorted by contribution to the combined TS. The top panel shows the most constraining data sets, while the bottom panel shows the less constraining contributions. The vertical line indicates the best fit value from all contributions. From Abramowski et al. 2013.

4.2 The likelihood maximization method

The method for measuring the EBL optical depth normalization followed in the present work basically follows the approach by Abramowski et al. [2013]. In the following lines the general method will be described and the application to the observations of 1ES 1011+496 and Mrk421 will be given in the next sections.

Based in what is expected from the SSC models (on previous observations of blazars in the optically thin regime at HE and VHE), the intrinsic differential energy spectrum of the photon flux, $d\phi/dE$ (photons per unit of area, time and energy) from a blazar can be modeled with a smooth and convex function. The simplest approximation to a non-thermal spectrum is a power-law (PWL). If the measurements are precise enough, and span a sufficiently wide energy range, then a power-law may provide a poor fit. The next-order polynomial, in a log-log scale, is the log-parabola function (LP). A blazar may have a cut-off at VHE, which can be modeled with an exponential cut-off. This can be added as a multiplicative factor to the functions above, resulting in two new parameterizations: power-law with exponential cut-off (EPWL) and log-parabola with exponential cut-off (ELP). The cut-off in the EPWL can be smoother or sharper, which can be modeled by a power-law with super exponential cut-off (SEPWL). The functions are detailed in Table 4.1.

TABLE 4.1: Functions tested for modeling the intrinsic spectrum

Name	Abbreviation	Formula
Power law	PWL	$\phi_0(E/E_0)^{-\Gamma}$
Log-parabola	LP	$\phi_0(E/E_0)^{-\Gamma-\beta\log(E/E_0)}$
Exponential cut-off power law	EPWL	$\phi_0(E/E_0)^{-\Gamma}\exp(-E/E_{cut})$
Exponential cut-off log-parabola	ELP	$\phi_0(E/E_0)^{-\Gamma-\beta\log(E/E_0)}\exp(-E/E_{cut})$
Super exponential cut-off power law	SEPWL	$\phi_0(E/E_0)^{-\Gamma}\exp(-(E/E_{cut})^{\gamma})$

We choose one of the functions as model for the intrinsic spectrum and each one of the parameters are set free in the likelihood maximization process. The set of parameters will be represented as Θ. Then, the effect of the scaled EBL is applied to obtain the observed spectrum:

$$\frac{d\phi_{obs}(E)}{dE} = \frac{d\phi_{int}(E)}{dE} \times \exp(-\alpha \times \tau(E,z)) \tag{4.1}$$

where $\tau(E,z)$ is the EBL-induced optical depth, for photons of energy E, between a source at redshift z and the Earth. The value of τ is obtained from a model of the EBL (taking into account its evolution), and α is a scaling factor.

The observed spectrum then is *folded* with the response of the telescope to obtain the expected number of gamma-ray events g_j in a given bin j of energy $E_{low} < E < E_{high}$. Mathematically this is expressed as:

$$g_j = t_{eff} \int_{E_{low}}^{E_{high}} \frac{d\phi_{obs}(E)}{dE} A_{eff}(E) dE \tag{4.2}$$

where A_{eff} is the effective collection area of the telescope, t_{eff} the effective observation time and the integration is between the edges $[E_{low}, E_{high}]$ of the energy bin. By construcion, the resulting expected number of gamma-ray events g_j are in bins of *true* energy. We now have to simulate the energy reconstruction as it takes place during the analysis of the real data (see section 2.4.0.7). For this purpose, we use the migration matrix (E_{est} vs E_{true}). Then, the expected number of gamma-ray events in a bin i of estimated energy is:

$$g_i = t_{eff} \int_{E_{low}}^{E_{high}} \int_{E=0}^{E=\infty} \frac{d\phi_{obs}(E)}{dE} A_{eff} M(E, E_{est}) dE dE_{est} \tag{4.3}$$

As explained in section 2.4.0.7, what we have in reality is a discretized transformation, where the migration matrix $M(E, E_{est})$ is computed in bins of estimated energy large enough to contain sufficiently significant excess of gamma rays over the cosmic-ray background after cuts (in energy, θ^2, $size_1$ and $size_2$, hadroness, etc.). Then, with the assumed spectrum $d\phi/dE$ and for a given observation time, we compute the expected event distribution g_i in bins of E_{est}, to be compared with the real observation, where the gamma-ray events are combined with the cosmic-ray background. The real number of observed events from the ON region, $N_{on,i}$ and from the OFF region, $N_{off,i}$, are taken from the actual data (see section 2.4.0.5 for definitions

of ON and OFF regions). From this data, a background parameter μ_i will be computed. Also, it is assumed that the Poisson parameter of the background μ_i is the same for the ON and OFF regions, normalized by ν, the ON/OFF exposure ratio. Depending on the value of $N_{on,i}$ and $N_{off,i}$, there are two limiting cases:

Gaussian approximation If $N_{on,i}$ and $N_{off,i}$ have high enough number of events (we set as limiting case 20) for a given bin i, the best estimator of the gamma-ray excess is then $N_{exc,i} = N_{on,i} - \nu \cdot N_{off}$. Propagating the Poissonian uncertainties, we get $\Delta N_{exc,i} = \sqrt{(N_{on,i} + \nu^2 \cdot N_{off,i}}$. Now we calculate the χ^2 contribution of this bin with respect to the model which predicts $g_i \pm \Delta g_i$:

$$\chi^2_i = \frac{(N_{exc,i} - g_i)^2}{(\Delta N_{exc,i})^2 + (\Delta g_i)^2}. \tag{4.4}$$

Poissonian regime If $N_{off,i}$ is too low or even zero (see Fig.4.3), we can no longer approximate the Poissonian distributions by Gaussians, and a full Poissonian calculation of the likelihood is needed.

The contribution to the total likelihood of the bin i will be the product of the probability of observing N_{on} events in the ON region, times the probability of observing N_{off} events in the OFF region:

$$L(N_{on,i}, N_{off,i}|\Theta, \mu_i) = P(N_{on,i}|\Theta, \mu_i) \times P(N_{off,i}|\mu_i/\nu_i) \tag{4.5}$$

where Θ are the parameters of the spectral model $d\phi_{int}(E)/dE$. The OFF probability is given by:

$$P(N_{off,i}|\mu_i/\nu_i) = Poisson(N_{off,i}|\mu_i/\nu_i) = \frac{\exp(-\mu_i/\nu_i)(\mu_i/\nu_i)^{N_{off},i}}{N_{off,i}!} \tag{4.6}$$

and the ON probability is reformulated in terms of the Poisson parameter $g_i(\Theta)$ of the number of expected gamma events $N_{\gamma,i}$.

$$P(N_{on,i}|\Theta, \mu_i) = Poisson(N_{on,i}|\mu_i + g_i) = \frac{\exp(-(\mu_i + g_i))(\mu_i + g_i)^{N_{on},i}}{N_{on,i}!} \quad . \tag{4.7}$$

The next step is find the μ_i that maximizes the likelihood L_i given the set of parameters Θ. In the limiting case where there is no expected gammas ($g_i = 0$), the likelihood is maximized for:

$$\mu_i = \frac{\nu_i}{1 + \nu_i}(N_{on,i} + N_{off,i}) \tag{4.8}$$

which is the expression used by Li and Ma [1983] (eq. 7) for the computation of the Poisson parameter of the background, under the assumption that there is no gamma-ray signal.

For the case $g_i \neq 0$, the equation to solve looking for the maximum of $\log Li$ vs the free parameter μ_i is, from eq. 4.5 to 4.7:

$$\frac{\mathrm{d}}{\mathrm{d}\mu_i}(\log L_i) = -\left(1 + \frac{1}{\nu_i}\right) + \frac{N_{on,i}}{\mu_i + g_i} + \frac{N_{off,i}}{\mu_i} = 0 \tag{4.9}$$

which is a second degree equation in μ_i. Solving for μ_i and feeding the result in formula 4.5 we obtain the contribution of bin i to the joint likelihood.

The joint likelihood for all n estimated energy bins is the product of the likelihood of each bin $L = \prod_{i=1}^{n} L_i$. This last expression has to be maximized in the space of the spectral parameters Θ. For this operation, we decided to used the dedicated software `Minuit2` [1] which is implemented within the ROOT framework. `Minuit2` has several algorithms for the maximization procedure. For our computations we used `MIGRAD`. This algorithm is based in the variable metric method with inexact line search. The variable metric method is used for determining numerically local minima of differentiable functions of several variables. In the process of locating each minimum, a matrix which characterized the behavior of the function about the minimum is determined. In the line search, the code computes the direction along which the function is reduced and then the step size is estimated to determine how far the set of parameters should move along that direction.

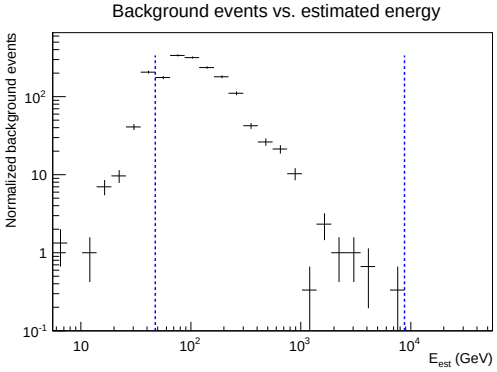

FIGURE 4.3: Background events in bins if *estimated* energy normalized to the ON region for the observation of Mrk421 on 2014-04-16. Notice that some bins at very-high energies ($E_{est} > 1TeV$) does contain only few or none events. The vertical dashed lines mark the limits of the energy range taken into account for the calculation of the likelihood where there is a clear photon excess.

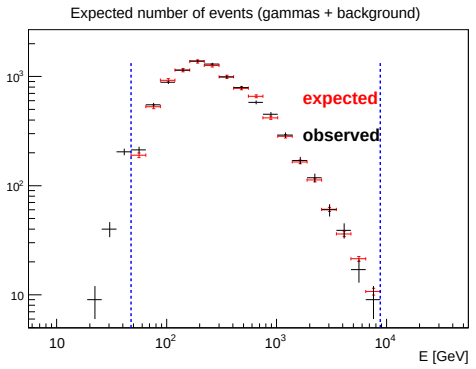

FIGURE 4.4: Observed events (black) compared with the expected events (red) in bins of estimated energy after the likelihood maximization process. The vertical dashed lines mark the limits of the energy range taken into account for the calculation.

The likelihood maximization described above is carried out to find the best-fitting parameters Θ of the intrinsic spectrum, for a given assumption on the level of the EBL (e.g. no EBL, or nominal EBL from a certain model).

We required to make a scan over different values of the scaling factor α to find the one which give the maximum likelihood. However, the function for modeling the intrinsic spectrum $d\phi/dE$ is not fixed a priori and can be any of the functions proposed in Table 4.1. In order to make the comparison for the case with the maximum likelihood at $\alpha = \alpha_0$ with the case for $\alpha = 0$, the function $d\phi/dE$ used for the evaluation at $\alpha = 0$ has to be the same evaluated at $\alpha = \alpha_0$. In this way, the condition for the likelihood ratio test in which the models to be compared have to be nested, is fulfilled. In case the assumed model is correct, then, according to Wilks' theorem, $-2\log(L(\alpha = \alpha_0)/L(\alpha = 0))$ will follow asymptotically a χ^2 distribution with the number of degrees of freedom that have been left free in the maximization of L leading to $L(\alpha = \alpha_0)$. In this expression, $L(\alpha = 0)$ is the "absolute maximum" likelihood, that of a model which predicted *exactly* the number of observed events in each bin (i.e. as many parameters as bins, hence 0 degrees of freedom). Therefore, following what was proposed by Abramowski et al. [2013], a scan over α is done with each one of the functions in Table 4.1. Through the relation $\chi^2 = -2\log L$, χ^2 probabilities profiles are produced for each one of the tested functions. In the

[1] http://seal.web.cern.ch/seal/snapshot/work-packages/mathlibs/minuit/

case of Abramowski et al., they selected the one that gave the highest χ^2 probability, regardless of the value of α. Although our selection criteria is based also in the χ^2 probabilities, other considerations, detailed in the next section, were taken into account.

Once a function has been selected as a model of the intrinsic spectrum, the maximum in the likelihood profile at $\alpha = \alpha_0$ will indicate the EBL opacity scaling which achieves a best fit to the data. A likelihood ratio test is then performed to compare the no-EBL hypothesis ($\alpha = 0$) with the best-fit EBL hypothesis ($\alpha = \alpha_0$). The test statistics $TS = 2\log(L(\alpha = \alpha_0/L(\alpha = 0))$ will asymptotically follow a χ^2 distribution with one degree of freedom, since the two hypothesis differ by just one free parameter: α.

4.3 Measurement of the opacity normalization using data from the February 2014 flare of 1ES1011+496

The unprecedented flare of 1ES 1011+496 in February 2014 provided enough data to reconstruct the average differential energy spectrum from ~ 70 GeV up to ~ 4 TeV. Due to the redshift of the source ($z = 0.212$), the observed spectra is well inside the optically thick regime of the EBL and includes the range in which the EBL absorption has the distinctive feature that motivated the H.E.S.S. measurement of the EBL (see Fig. 4.5).

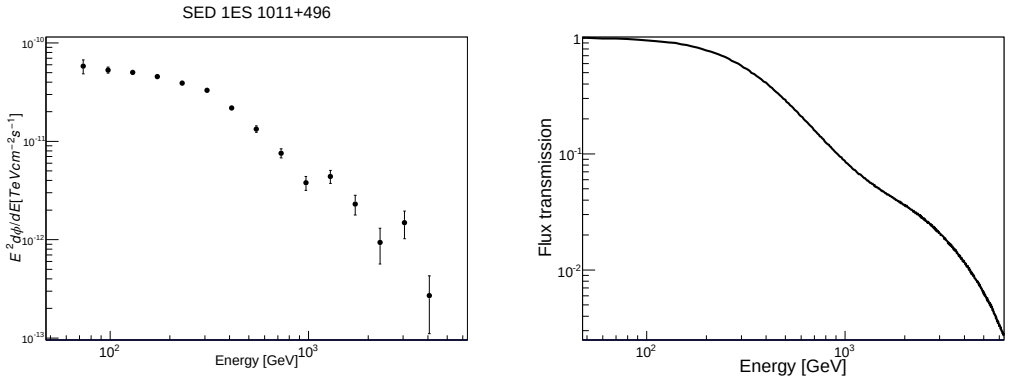

(a) Average observed SED of 1ES 1011+412

(b) Effect of the EBL-induced absorption as function of gamma-ray energy for a source at $z = 0.212$

FIGURE 4.5: **Left**: reconstructed SED of 1ES 1011+496 for the MAGIC observations of the February flare of 2014. **Right**: EBL gamma-ray flux transmission for a source located at redshift as 1ES 1011+496. Notice the same energy range for both plots.

To apply the likelihood maximization method we decided to use the average spectrum, so the event statistics are large and the Poissonian likelihood behaves close to its asymptotic limits. Despite changing the flux level, the EBL determination method should work properly as long as the average intrinsic spectrum in the observation period can be described with one of the tested parameterizations. This would of course be the case if the spectral *shape* is stable, or changes moderately. A varying spectral shape would in any case need quite some fine tuning to reproduce, in the average spectrum, a feature like the one expected to be induced by the EBL. A simple way to check the stability of the spectral shape is fitting the points on the Fig. 3.40 (section 3.2.2.4) to a simple line. The χ^2 of this fit is 23.5/16 and the probability is

10%, therefore there is no significant evidence for variation of the spectral shape through the observation period.

For modeling the intrinsic differential energy spectrum of 1ES 1011+496, the five functions listed in Table 4.1 were tested, but with a relevant modification: we have added the constraint that the shapes cannot be concave, i.e. the hardness of the spectrum cannot increase with energy, as this is not expected in emission models, nor has it been observed in any BL Lac in the optically-thin regime. In the LP and ELP the curvature β can take only positive values and the cut-off energies in the functions with exponential cut-offs can only be positive. Fig. 4.6 shows the $-2\log L$ probability profiles for the five tested models, following the procedure described in section 4.2. The model that gives the highest probability in the scanned range of α is the PWL. However, the selection of a PWL as model for the intrinsic spectrum, following the approach of Abramowski et al. 2013 is rather questionable, since would not allow any intrinsic spectral curvature, meaning that all curvature in the observed spectrum must come from the EBL absorption. Such strong and unrealistic assumption would result in an EBL "detection" at the ~ 13 sigma level, not based on the characteristic EBL feature that cannot be reproduce by any of the models tried for the intrinsic spectrum, but on the rather bold assumption that the intrinsic spectrum is a pure power-law. We prefer to adopt a more conservative approach, choosing the second-best function, the log-parabola, which is the one providing the best fit for the no-EBL hypothesis.

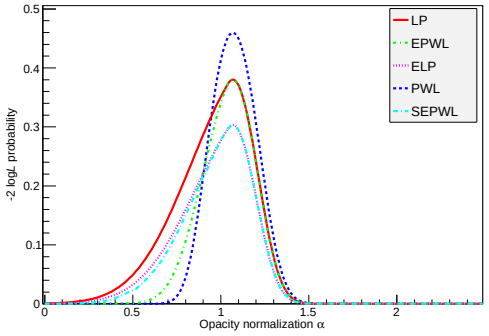

FIGURE 4.6: $-2\log L$ probabilities profiles for the average spectrum of the Feb-March flare of 1ES 1011+496 for the 4 models tested. PWL in blue (dashed line), LP in red (solid line), EPWL in green (dash-dot line), ELP in pink (dotted line) and SEPWL in light blue (long dash-dot line).

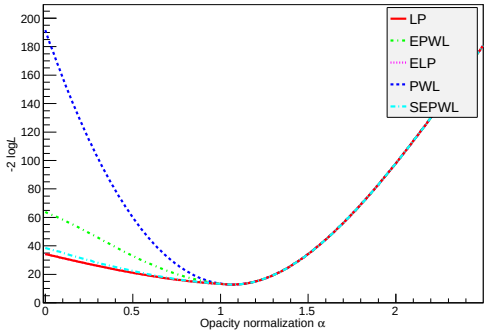

FIGURE 4.7: $-2\log L$ profiles for the average spectrum of the Feb-March flare of 1ES 1011+496 for the 5 models tested. PWL in blue (dashed line), LP in red (solid line), EPWL in green (dot-dash line) and ELP in pink (dotted line) and SEPWL in light blue (long dash-dot line). Notice how all curves converge after reaching the minimum.

Note in the Fig. 4.7 that after reaching the minimum, the $-2\log L$ are identical for all models, that is, all the tested functions become simple power-laws, hence the fit probabilities at the peak depend only on the number of free parameters. This happens because of the convexity restriction imposed to the functions. After reaching the point where the EBL de-absorption result in a straight power-law intrinsic specrum, EPWL, EPL and SEPWL functions converge, and the de-absorbed spectra become more and more concave as α increases. The shape of the spectrum observed by MAGIC is thus very convenient for setting upper bounds to the EBL density, under the adopted assumption that concave spectra are "unphysical". Given these arguments, we take the LP as our model for the intrinsic spectrum. For the data sample from the February 2014 flare of 1ES 1011+496, the test statistics has a maximum of TS = 21.5 at $\alpha_0 = 1.07^{+0.09}_{-0.13}$ (see Fig.4.8). This means that the EBL optical depth from the model of

Domínguez et al. [2011] scaled by the normalization factor α_0 is preferred over the null EBL hypothesis with a significance of 4.6σ. For the EBL model by Franceschini et al. [2008] (which was used in the study by Abramowski et al. [2013]), the test statistic using the LP as model for the intrinsic spectrum has a maximum of TS=20.6 at $\alpha_0 = 1.14^{+0.09}_{-0.14}$, which is compatible with our result.

Fig.4.9 shows the ratio between the observed events and the expected events from the model for two cases: the left pad shows the residuals for the null EBL hypothesis $\alpha = 0$, while the right pad shows the same plot for the cases of the best-fit EBL scaling $\alpha = 1.07$. The comparison reveals how the LP plus the imprint of the EBL (including the feature introduced by the change in the slope) fits the data better that the LP alone.

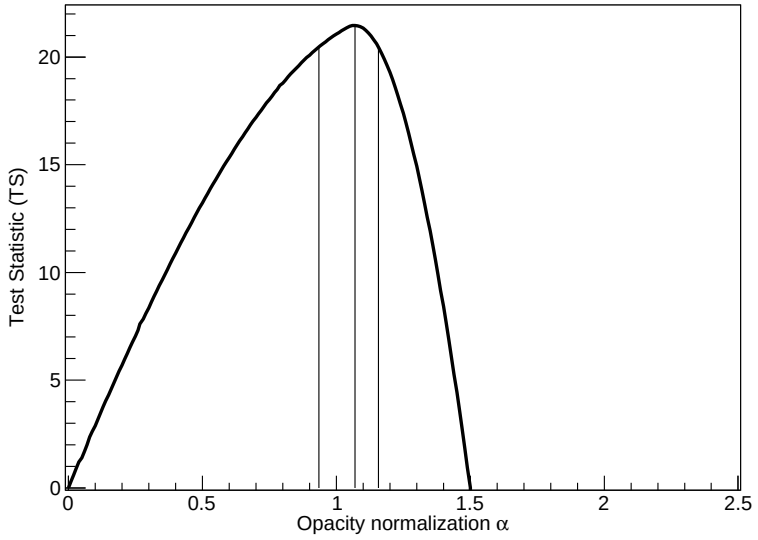

FIGURE 4.8: Test Statistics (TS) distribution for the data sample for the February 2014 flare of 1ES 1011+496. The vertical lines mark the maximum and the uncertainty corresponding to 1σ.

4.3.1 Systematic uncertainties

The MAGIC telescopes have a systematic uncertainty in the absolute energy scale of 15% [Aleksić et al., 2014b]. The main source of this uncertainty is the imprecise knowledge of the atmospheric transmission, mirror reflectivity, properties of the photomultipliers, etc.. In order to assess how the systematic uncertainty in the energy scale affects the EBL measurement, the calibration constants used to convert the pixel-wise digitized signals into photoelectrons (see section 2.4.0.2) were multiplied by scaling factors $\vartheta = 0.80$, 0.85, 0.90, 0.95, 1.05, 1.10, 1.15 and 1.20 (the same for both telescopes). This is equivalent to modifying the energy scale by -20% to +20% in steps of 5% (see Fig.4.10). For each of the ϑ factors the data were processed in an identical manner through the full analysis chain, starting from the image cleaning, and using in all cases the same MC simulations sample for this observation period. In this way we try to asses the effect of a potential miscalibration between the data and the MC simulation.

For all the data samples scaled by ϑ, we compute $-2 \log L$ profiles for α between 0 and 2.5. which are shown in Fig. 4.11. Fig. 4.12 contains the same information as Fig. 4.11 although taking the ϑ as an additional dimension. If the EBL imprint in the observed data from 1ES1011+496

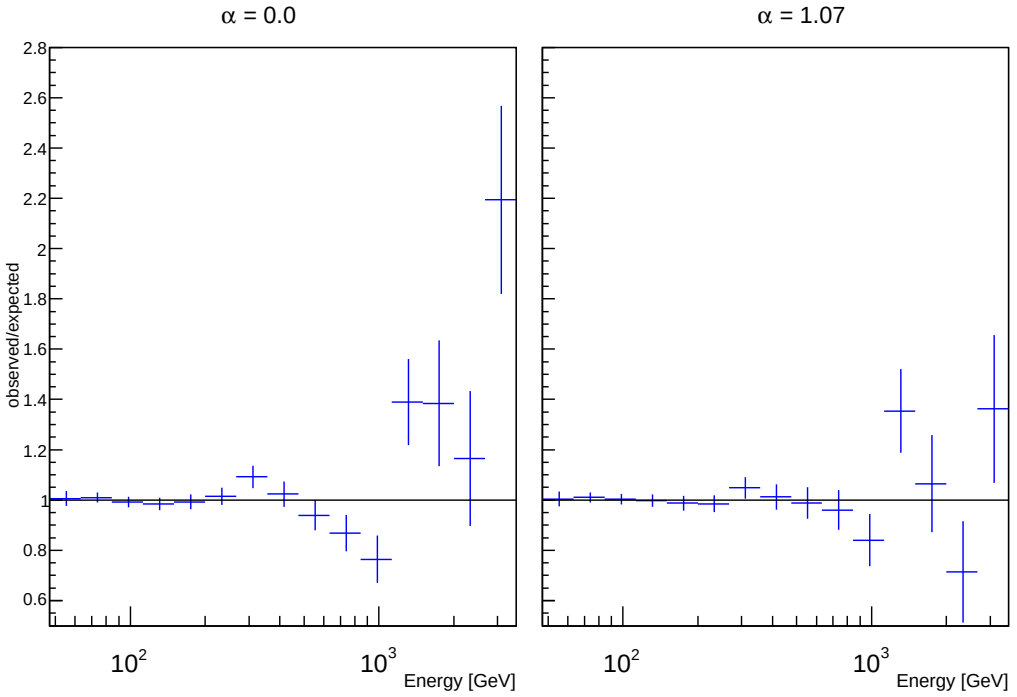

FIGURE 4.9: Ratio between the observed events and the expected events from the model of the intrinsic spectrum of the February flare 2014 of 1ES 1011+496 for two normalization values of the EBL optical depth, $\alpha = 0$ to the left and $\alpha = 1.07$ to the right, which corresponds to the normalization where the maximum TS was found. The error bars have been calculated to represent accurately the contribution of each point to the global likelihood. In both plots the line corresponding to a ratio=1 is shown.

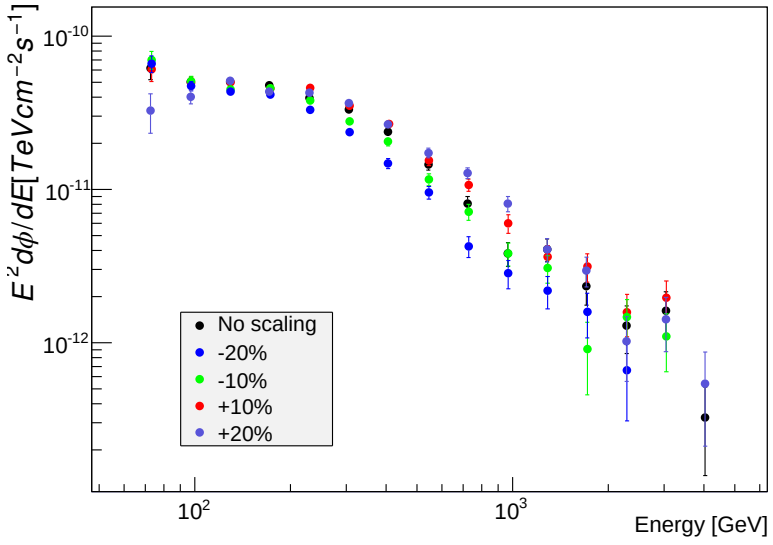

FIGURE 4.10: Spectral energy distributions of 1ES 1011+496 for different levels of signal scaling indicated in the legend, including the case without scaling.

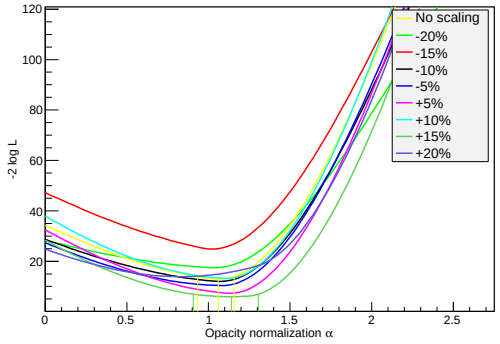

FIGURE 4.11: $-2\log L$ profiles for the average spectrum of the Feb-March flare of 1ES 1011+496 for the different scaling factors applied to the data as indicated in the legend. Notice that the profile corresponding to a signal scaling of +15% has the minimum $-2\log L$ value.

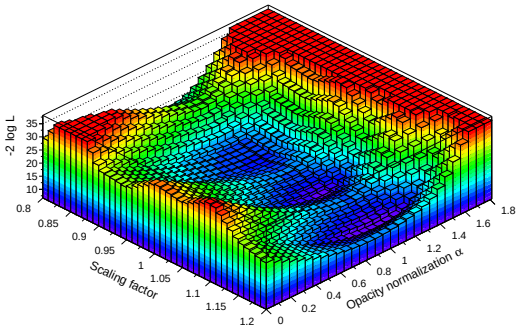

FIGURE 4.12: $-2\log L$ vs opacity normalization α vs scaling factors. The absolute minimum is visible for $\vartheta = 1.5$ (corresponding to an increase of +15% in the signal) and $\alpha = 1.14$.

was more pronounce, or the statistics of the data higher, there was the possibility that the plot in Fig. 4.12 showed a clear minimum, where constrains could be impose not only to the EBL intensity but to the absolute energy scale of the MAGIC telescopes (assuming that the EBL template from Domínguez et al. [2011] is an accurate model for the actual EBL). However, the statistics of our data is limited and such measurement in the energy scale of the telescopes cannot be performed. As seen in Fig. 4.12, the plot shows three local minima. The uncertainty in the energy scale of 15% from the MAGIC telescopes is an approximated (although conservative) estimation. Taking the minimum at $\vartheta = 1.15$, which is what Figs. 4.11 and 4.12 reveal, would have been maybe too pessimistic, in the sense that, although we cannot quantify it from our data, is less likely that the scale corresponds to $\vartheta = 1.15$ instead of $\vartheta = 1.00$. If we had a probability density function (PDF) for the systematic uncertainty in the energy scale and not just the maximum, we could include it as an additional factor in the computation of the likelihood and then, instead of having just discrete values corresponding to different values of ϑ, we could have a continuous curve (or at least finer binning in ϑ) where a clear and absolute minimum could be found. in the absence of such PDF, we have opted for taking the limits in the uncertainty of α form those corresponding to the widest minimum in the range $\pm 15\%$ in the energy scale. It can be seen that the curve corresponding to $\vartheta = 1.15$ has the widest statistical uncertainty with $\alpha_\vartheta = 1.14^{+0.16}_{-0.23}$. Then, the opacity normalization found using the data of the February 2014 flare of 1ES 1011+496 is $\alpha_0 = 1.07$ (-0.13,+0.09)$_{stat}$ (-0.10, +0.7)$_{syst}$.

Abramowski et al. [2013] found an opacity normalization of $\alpha_{0,HESS} = 1.27$ (-0.15,+0.18)$_{stat} \pm 0.25_{syst}$ using as a template the EBL model of Franceschini et al. [2008]. With this opacity normalization, they discarded the null EBL hypothesis with a significance of 8.8σ. Although the HESS measurement has higher significance than our measurement, it should be noted that ours was performed using data from only one source. Moreover, 1ES 1011+496 is farther away than any of the sources used by HESS. As mentioned before, the HESS measurement is statistically dominated by the data from PKS 2155-304, which is at redshift $z = 0.116$, while the redshift of 1ES 1011+496 is $z = 0.212$. Abramowski et al. made the exercise of calculate the opacity normalization depending on the redshift. They divided their data sample in three groups. For the two closest sources, with an average redshift of $z_1 = 0.051$, the TS is maximum at $\alpha_{z1,HESS} = 1.6$ (-1.1,+0.5). From the data of PKS 2155-304 alone, they measured an opacity normalization of $\alpha_{z2,HESS} = 1.36 \pm 17$ and for the sample of sources farther than PKS 2155-304,

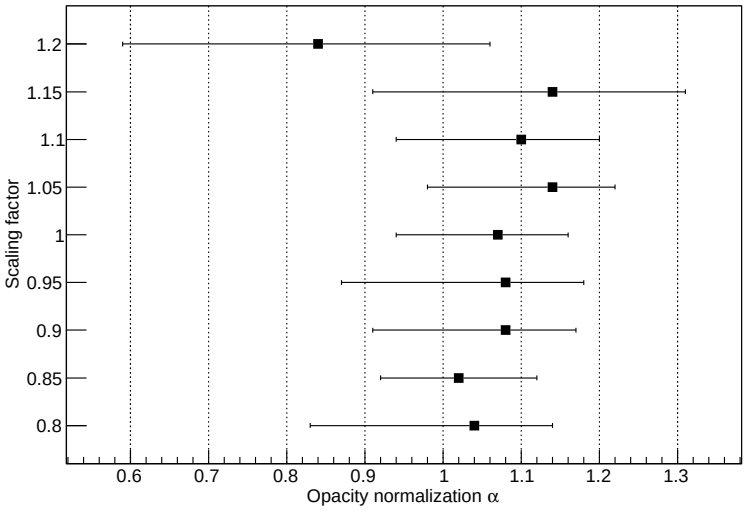

FIGURE 4.13: Values of α corresponding to the minima in the $-2\log L$ profiles in Fig. 4.11 with their 1σ uncertainty, for the different scaling factors.

with a mean redshift of $z_3 = 0.170$, the opacity normalization is $\alpha_{z3,HESS} = 0.71$ (-0.29,+0.46) (see Fig. 4.14).

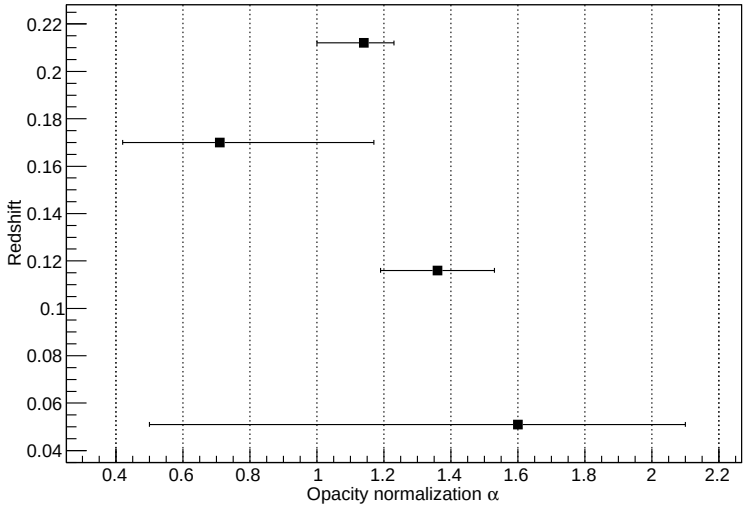

FIGURE 4.14: Opacity normalizations α vs redshift. The point with the higher redshift corresponds to 1ES 1011+496 (this work) and the other 3 are from Abramowski et al. [2013]. In all cases the EBL template is from Franceschini et al. [2008].

The measurement of the opacity normalization α from only one source, as presented in this work so far, opens the possibility that the EBL could be measured in different directions, revealing possible inhomogeneities in the spatial distribution of EBL photons. This kind of measurements could be hard to achieve by the current generation of IACTs, but it should be within the capabilities of the future Cherenkov Telescope Array [Acharya et al., 2013].

4.3.2 Measurement of the EBL intensity

The relation of the γ-ray of energy E_γ from the source and the EBL wavelength at the peak of the cross section for the photon-photon interaction is given by:

$$\lambda_{EBL}(\mu\text{m}) = 1.187 \times E_\gamma(\text{TeV}) \times (1+z)^2 \tag{4.10}$$

Where z is equal or less than the redshift of the source. The energy range used for our calculations was between 0.06 and 3.5 TeV. However, the measurement of the EBL following the method from Abramowski et al. [2013] is based in the fact that after de-absorbing the EBL effect, with the right normalization, the feature between $\sim$ 100 GeV and $\sim$5-10 TeV is suppressed. It can be seen in Fig.4.9 that the differences between the residuals start to become evident after 200 GeV, a region where the EBL introduces a feature (an inflection point) that cannot be fitted by the log-parabola. Since it is the feature what drives the TS value on which the EBL measurement is based we decided to take the energy range between 0.2 to 3.5 TeV to calculate the corresponding EBL wavelength range for which our measurement is valid.

The energy range has to take into account the redshift dependency in Eq.4.10 since the interaction of the γ-ray and the EBL photon can happen in any point between the Earth and the source. The range is between $[(1+z)^2 E_{min}, E_{max}]$, corresponding to a wavelength range of the EBL where the interaction with the γ-ray can take place along the entire path between the source and the Earth. Fig. 4.15 shows the contours from the statistical + systematic uncertainty of the EBL flux density, derived scaling up the EBL template model by Domínguez et al. [2011] at redshift $z = 0$. The wavelength coverage is in the so-called cosmic optical background (COB) part of the EBL, where we found the peak flux density $\lambda F_\lambda = 12.27^{+2.75}_{-1.83}$ nW m^{-2} sr^{-1} at 1.4 μm, systematics included.

4.4 Measurement of the opacity normalization using data from the April 2013 flare of Markarian 421

Mrk421 is the closest known blazar, with redshift $z = 0.031$, therefore, the EBL absorption suffered by the VHE gamma rays is not as pronounced as in the case of 1ES 1011+496. Fig. 4.16 shows the observed VHE SED of Mrk421 for the observation in 2013-04-12, where the gamma-ray flux was measured at energies greater than 10 TeV, next to the EBL gamma-ray flux transmission suffered by a source located at $z = 0.031$. The comparison shows the necessity of measuring the flux of Mrk421 at energies around $\sim$ 10 TeV, not only to have spectral points with sizable EBL absorption, but to also to fully cover the energy range where the EBL absorption has the feature characterized by a change in the slope of τ vs observed gamma-ray energy (see 4.1).

We apply the same method described in section 4.2 for measuring the EBL imprint in the spectra collected during the April flare 2013 of Mrk421. Since the flare presented high variability and high statistics for most of the dates, we divided the data sample as described in section 3.1.3.6 and listed in Table 3.6, excluding only the spectrum from 2014-04-19, since the statistics of this sample is poor and the asymptotic limit of the Poissonian likelihood could not be ensured.

For modeling the intrinsic energy spectra of Mrk421, in the different dates and activity levels of the flare, we used the functions listed in Table 4.1. Following the method proposed in

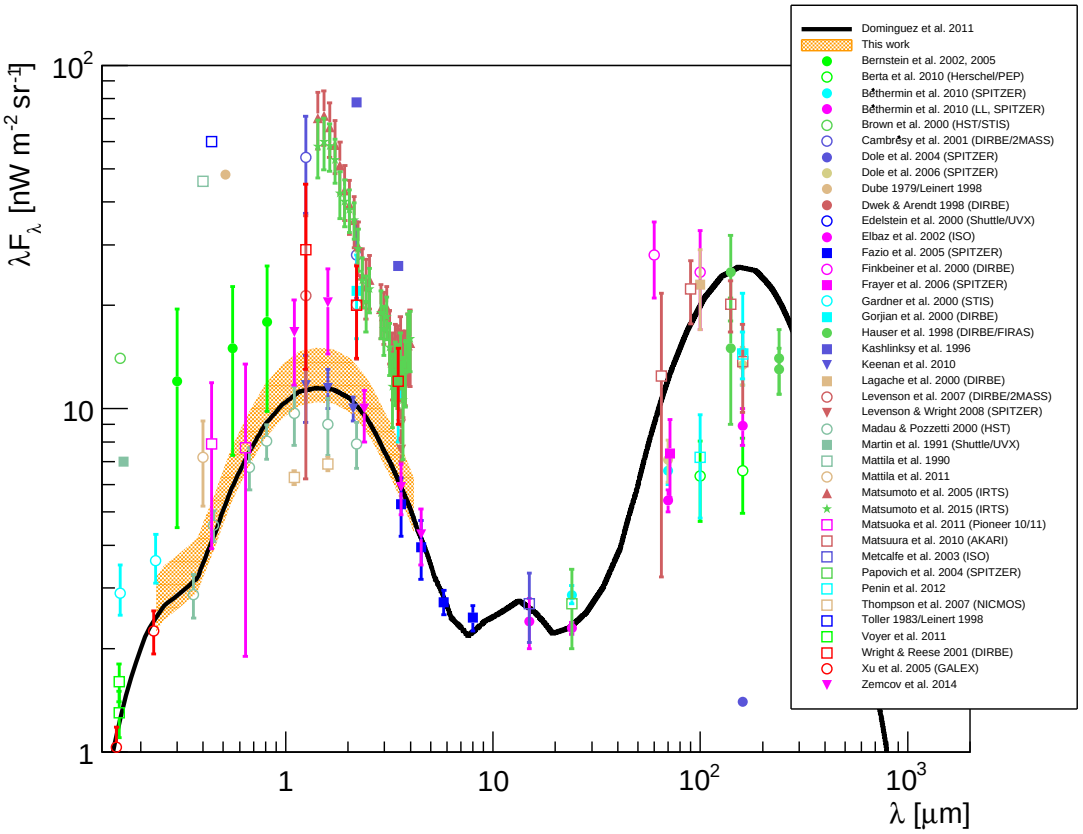

FIGURE 4.15: Extragalactic background light intensity versus wavelength at $z = 0$. The solid black line is the EBL template model [Domínguez et al., 2011] that we used for our calculations. The orange shaded area spans the wavelength range for which our measurement is valid, scaled from the EBL template. The width of the shaded area includes the statistical and systematic uncertainties. As a comparison we include EBL measurements by Berta et al. [2010], Béthermin et al. [2010], Brown et al. [2000], Cambrésy et al. [2001], Dole et al. [2004], Dwek and Arendt [1998], Elbaz et al. [2002], Finkbeiner et al. [2000], Frayer et al. [2006], Gardner et al. [2000], Gorjian et al. [2000], Hauser et al. [1998], Kashlinsky et al. [1996], Keenan et al. [2010], Lagache et al. [2000], Levenson et al. [2007], Levenson and Wright [2008], Matsumoto et al. [2005], Matsumoto et al. [2015], Matsuoka et al. [2011], Metcalfe et al. [2003], Papovich et al. [2004], Pénin et al. [2012], Thompson et al. [2007], Voyer et al. [2011] and Xu et al. [2005].

Abramowski et al. [2013], for each one of the spectra derived from the sub-samples, we compute $-2\log L$ probability profiles for the 5 functions (see Fig.4.17 for some examples). The function that had the highest $-2\log L$ probability for each sub-sample was chosen as listed in the Table 4.2. Unlike 1ES 1011+496, none of the sub-samples was best-fitted with a PWL, therefore, there was no risk of asserting that all the curvature in the observed spectrum came from the EBL absorption. Something to be notice is the relatively low values of the $-2\log L$ probabilities (for the samples of 2013-04-13 High and 2013-04-15 Medium the maxima are around 0.1 or less). This can be expected from measurements of flaring episodes with very high fluxes, where the high statistics of the points in differential energy spectra start to reveal features that cannot be fitted with simple smooth functions. These features are most likely systematic effects from the instrument.

Fig.4.18 (a) shows the TS profiles for each one of the sub-samples using the best-fitting functions listed in Table 4.2. It can be seen that the most constraining data is from the sub-sample for

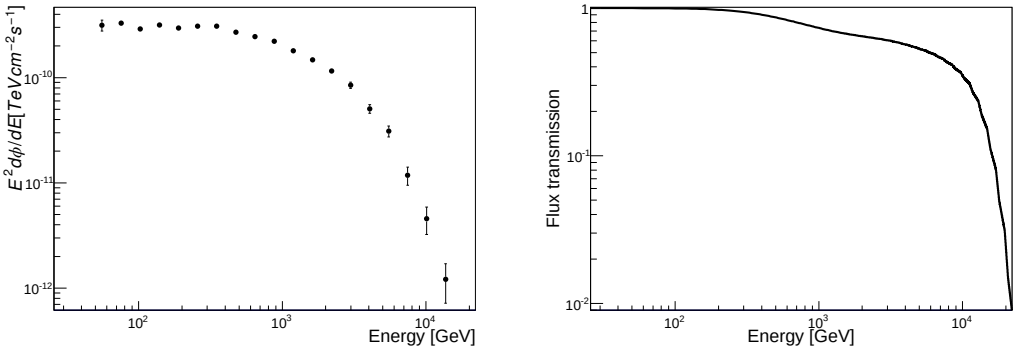

(a) Observed SED of Mrk421 on 2013-04-12

(b) Effect of the EBL-induced absorption as function of gamma-ray energy for a source at $z = 0.212$

FIGURE 4.16: **Left**: reconstructed SED of Mrk421 for the MAGIC observation on 2013-04-12. **Right**: EBL gamma-ray flux transmission for a source located at redshift as Mrk421 according to the model by Domínguez et al. [2011]. Notice the same energy range for both plots.

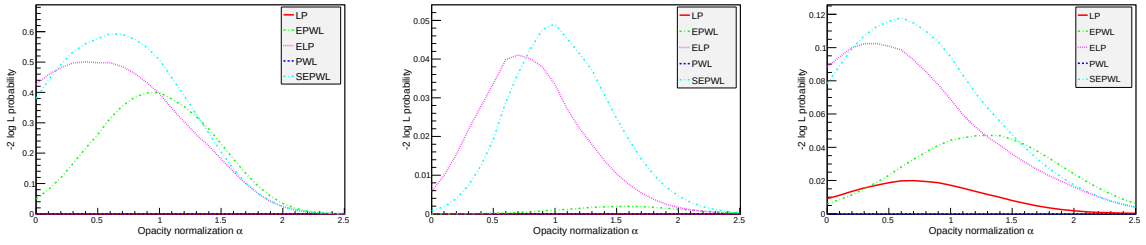

(a) 2013-04-12 - Medium

(b) 2013-04-13 - High

(c) 2013-04-15 - Medium

FIGURE 4.17: Examples of the $-2 \log L$ probability profiles used for the selection of the model for the intrinsic differential energy spectrum of Mrk421 for 3 sub-samples of the April flare 2013. The legends indicate the functions used as listed in Table 4.1. The selected function is the one that give the highest probability.

2013-04-13 High, which is when Mrk421 reached the highest activity observed by MAGIC (see Fig.3.31). Fig.4.18 (b) shows the combined TS from the addition of all the individual ones presented in Fig.4.18 (a) for the April 2013 flare of Mrk421. The test statistics has maximum of TS= 33.2 at $\alpha_0 = 0.90^{+0.11}_{-0.17}$, indicating that the EBL model of Domínguez et al. [2011] scaled by the normalization factor α_0, for this data sample, is preferred over the null EBL hypothesis with a significance of 5.8σ.

Fig.4.19 shows the ratio between the observed events and the expected events combined from all the sub-samples for two cases: the left pad shows the residuals for the null EBL hypothesis $\alpha = 0$, while the right pad shows the same plot for the cases of the best-fit EBL scaling $\alpha = 0.90$. Each spectrum for each subsample was fitted with the corresponding selected function as listed in Table 4.2. Although the TS reached a higher value than in the case of 1ES 1011+496, visually the EBL imprint suppression is not as clear (see Fig.4.9). In the residuals it can be seen spectral features characterized by deviations of spectral points going up and below the line that mark the fitted function, in a oscillating pattern. This pattern has already been observed in spectra

TABLE 4.2: Functions selected for modeling the intrinsic spectrum of Mrk421 for the April 2013 flare sub-samples.

Date - activity level	Function
2013-04-10 - Low	LP
2013-04-11 - Low	SEPWL
2013-04-12 - Medium	SEPWL
2013-04-13 - Medium	EPWL
2013-04-13 - High	SEPWL
2013-04-14 - Medium	SEPWL
2013-04-15 - Medium	SEPWL
2013-04-15 - High	EPWL
2013-04-15 - Medium	LP
2013-04-16 - Low	LP
2013-04-17 - Low	LP
2013-04-18 - Low	LP

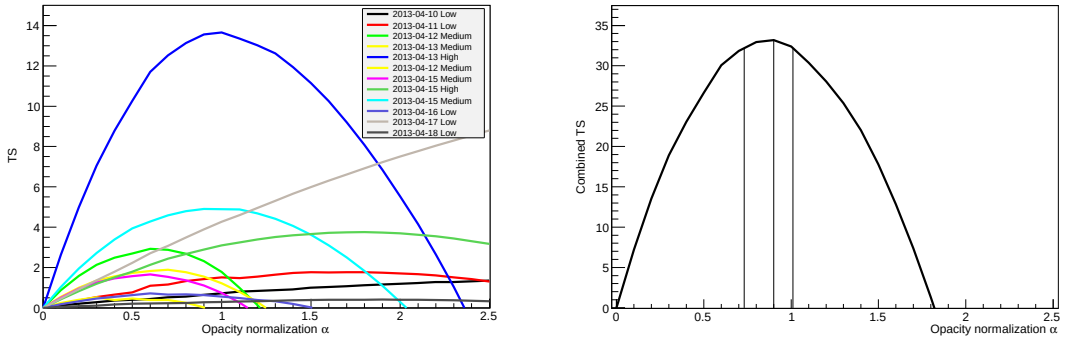

(a) TS of each sub-sample

(b) Combined TS

FIGURE 4.18: **Left**: Individual TS of each sub-sample as indicated in the legend. Notice the sizable contribution of the subsample of 2013-04-13 - High. **Right**: combined TS for all the sample of the April 2013 flare of Mrk421. The vertical lines indicate the best fit value and the statistical uncertainty corresponding to 1σ

from Crab nebula for observations with high statistics. In a test presented in the Ph. D thesis by Zanin [2011, section 5.3.2], the observed Crab Nebula spectrum, which could be fitted with a LP, was compared with the observations of Mrk421 done by MAGIC in January 2010, which also had high statistics. From the January 2010 Mrk421 data, a correction factor was computed in each energy bin as the ratio between the value of the fitted function (in that case, a EPWL) and the measured differential spectrum. These correction factors were then applied to the Crab Nebula spectrum improving the fit to a LP. The result of that test was an indication of the systematic nature of the wiggles in the MAGIC high-precision measurements from two different sources.

Fig. 4.20 and 4.21 shows the residuals comparison for the null EBL hypothesis and the best-fit EBL, for the samples of the April 2013 flare of Mrk421 characterized for their high statistics. As expected, it can be seen that the wiggles are not so pronounce as in the global residuals, but there is still a significant scatter of spectral points around the fit. A visual inspection over the

points reveals that some of them get closer to the line (ratio=1) after the EBL de-absorption in the energy range where the observed spectrum would be more affected by the EBL imprint. The TS profiles for these samples in Fig. 4.18 (a) reveal that the likelihood of the fit including the EBL effect for $\alpha = 0.90$ is preferred over the likelihood of the fit for the null EBL, although, statistically speaking, the difference is significant only for the sub-sample 2013-04-13 - High.

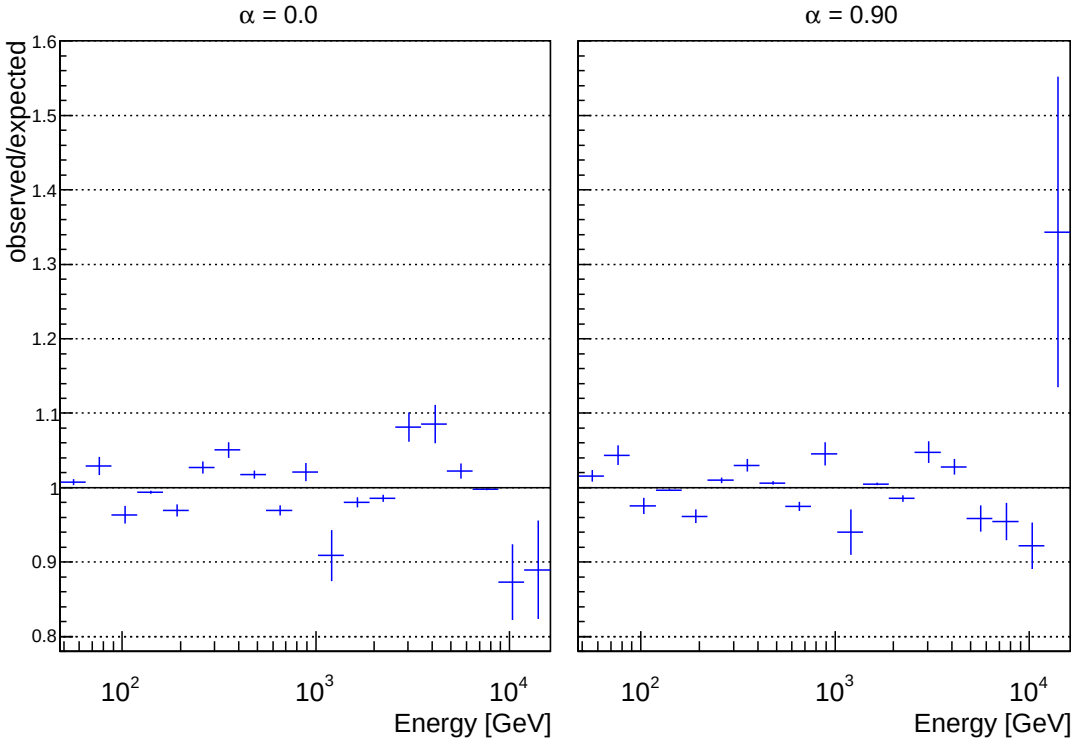

FIGURE 4.19: Ratio between the observed events and the expected events combined from the different models of the intrinsic spectrum of each sub-sample of the April 2013 flare of Mrk421 for two normalization values of the EBL optical depth, $\alpha = 0$ to the left and $\alpha = 0.90$ to the right, which corresponds to the normalization where the maximum TS was found. In both plots the line corresponding to a ratio=1 is shown.

Having features in the differential energy spectrum (like the wiggles) is a challenge to the measurement of the EBL imprint, since these could, in the worst case scenario, mimic the effect of the EBL in the observed spectra. Then, upon applying the EBL de-absortion, we will be "correcting" wiggles instead of the EBL imprint. However, it also can be argued that the EBL imprint is an additional spectral feature *on top* of the wiggles. Then, in that case, the TS will be effectively measuring the EBL imprint. The origin of these, apparently systematic, features (observed in differential energy spectra from observations with high statistics) has to be understood before having a conclusive result regarding the measurement of the EBL with Mrk421 data.

4.4.1 Systematic uncertainties

The systematic uncertainties arising from the uncertainty in the absolute energy scale of the telescopes were studied in an analog way as in section 4.3.1. The signal in each pixel was scaled by the factors $\vartheta = 0.80$, 0.85, 0.90, 0.95, 1.05, 1.10, 1.15 and 1.20 (the same for both telescopes). For each of the ϑ factors the data were processed in an identical manner through the full analysis

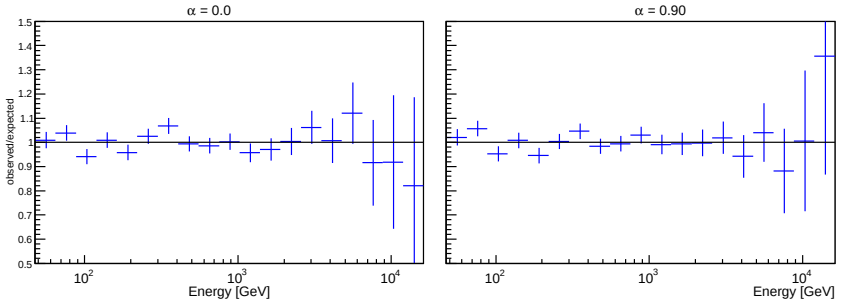

(a) 2013-04-12 - Medium

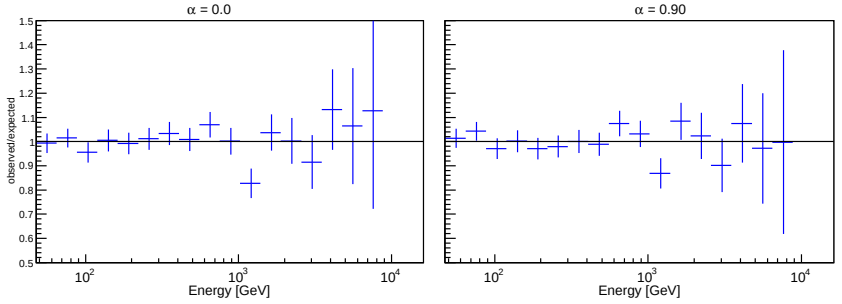

(b) 2013-04-13 - Medium

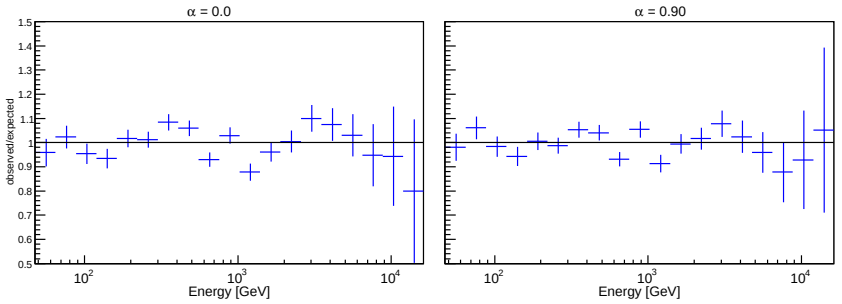

(c) 2013-04-13 - High

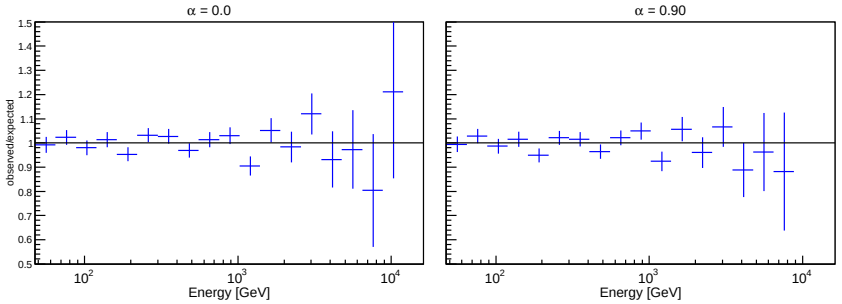

(d) 2013-04-14 - Medium

FIGURE 4.20: Ratio between the observed events and the expected events for sub-samples with high statistics of the April 2013 flare of Mrk421 for two normalization values of the EBL optical depth, $\alpha = 0$ to the left and $\alpha = 0.90$ to the right, which corresponds to the normalization where the maximum TS was found. In all plots the line corresponding to a ratio=1 is shown.

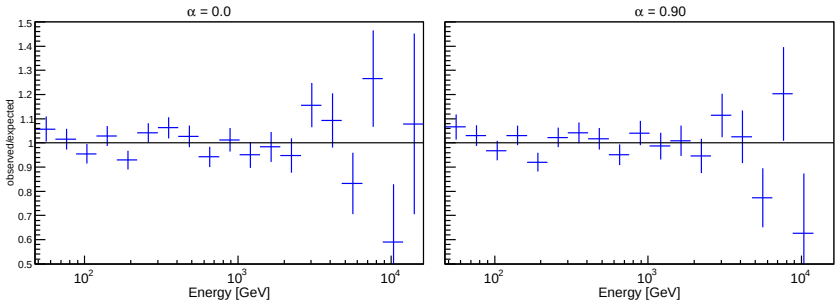

(a) 2013-04-15 - Medium 1

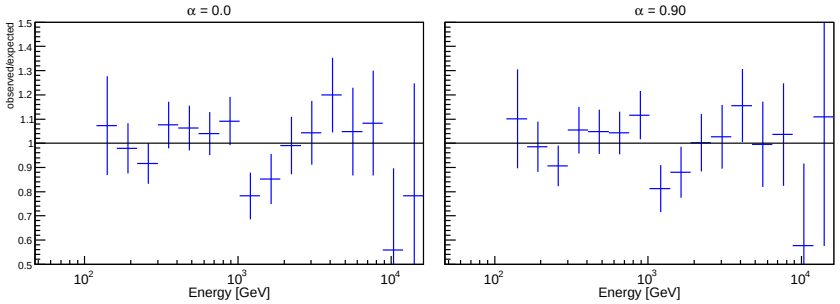

(b) 2013-04-15 - High

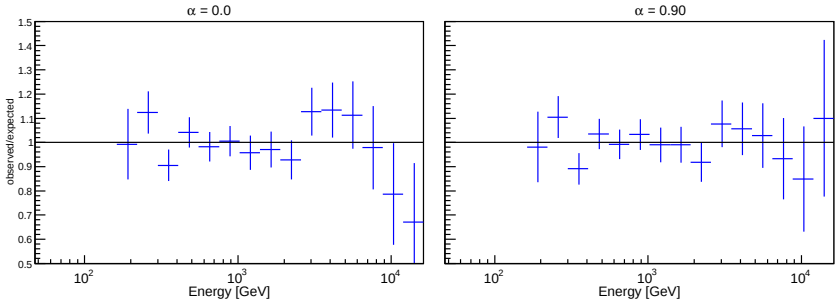

(c) 2013-04-15 - Medium 2

FIGURE 4.21: Ratio between the observed events and the expected events for sub-samples with high statistics of the April 2013 flare of Mrk421 for two normalization values of the EBL optical depth, $\alpha = 0$ to the left and $\alpha = 0.90$ to the right, which corresponds to the normalization where the maximum TS was found. In all plots the line corresponding to a ratio=1 is shown.

chain, starting from the image cleaning, and using in all cases the same MC simulations sample for this observation period.

In this case, the operation was more extended with respect to 1ES 1011+496, since instead of a single spectrum, we were dealing with 12 different spectra. Fig.4.22 shows two examples of how the energy spectrum is affected when the scaling factor ϑ is applied. The change in the energy scale is noticeable.

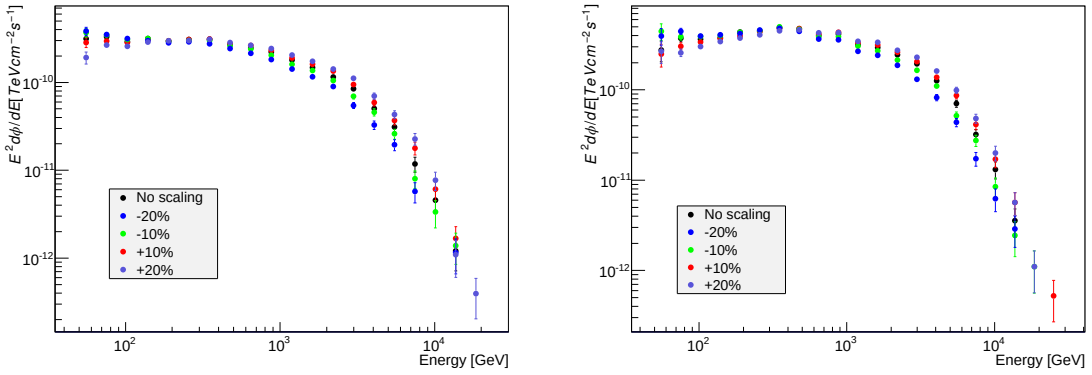

(a) 2013-04-12 - Medium

(b) 2013-04-13 - High

FIGURE 4.22: Examples of the changes in the spectral energy distributions for two randomly selected sub-samples of the April 2013 flare or Mrk421 in different levels of activity, where the scaling in the signal is indicated in the legends. **Left**: SEDs for the observation on 2013-04-12, when the source was in "medium" activity. **Right**: reconstruced SEDs for the observations on 2013-04-13, when the source was in "high" activity.

Since we were looking for the maximum likelihood (or minimum $-2\log L$) in the parameter space with the addition of ϑ, we produced again $-2\log L$ probability profiles (for α between 0 and 2.5) for each scaling factor ϑ and each one of the sub-samples testing the functions listed in Table 4.1 in order to confirm if the already selected function for modeling the intrinsic energy spectrum provides the best fit (as listed in Table 4.2) or another function has to be selected. In several cases, another function provide the best fit to the data (see Fig. 4.23 and compare with Fig. 4.17).

Once the functions for modeling the intrinsic differential energy spectra of each one of the sub-samples were selected, for each scaling factor ϑ, the joint likelihood of all sub-samples was computed, that is, for the analyzed period of the April 2013 flare. Fig.4.24 shows the joint $-2\log L$ for the sub-samples of the April 2013 flare or Mrk421 for each one of the scaling factors. Fig. 4.26 shows the values of α for each curve with its statistical uncertainty. It can be seen that there is not a single curve with 1σ statistical uncertainty wide enough to cover the α_0 ($\vartheta = 1.0$) and its statistical uncertainty (as in the case for 1ES1011+496). As noticed at the end of the previous section, the observation of Mrk421 is a particular case due to the high statistics (unprecedented in MAGIC) and the presence of the spectral features (the so-called wiggles). The origin of these wiggles is not yet fully understood and is reasonable to think that the outcome of computing the $-2\log L$ profiles, when changing the energy scale, will be influenced by these.

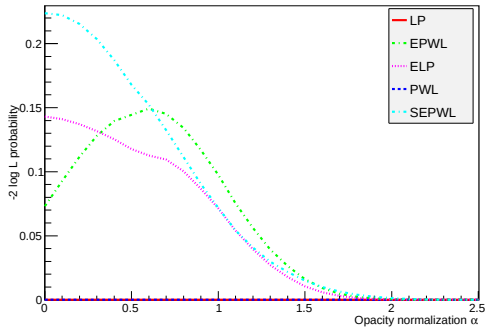

(a) 2013-04-12 - Medium, $\vartheta = 0.8$

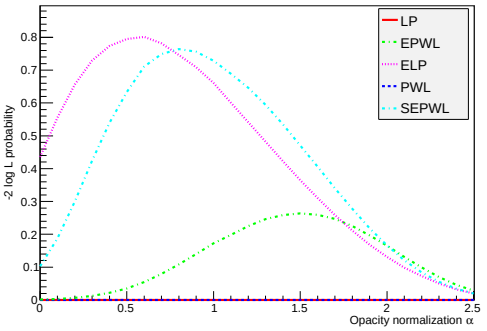

(b) 2013-04-12 - Medium, $\vartheta = 1.2$

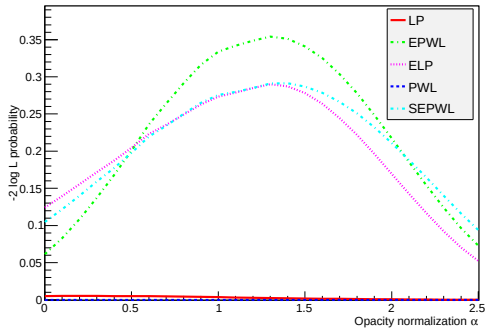

(c) 2013-04-15 - Medium, $\vartheta = 0.8$

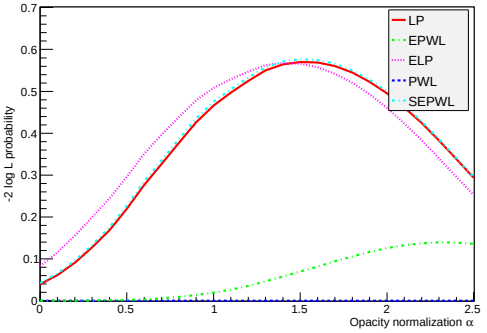

(d) 2013-04-15 - Medium, $\vartheta = 1.2$

FIGURE 4.23: Examples of how the $-2 \log L$ probability profiles for two sub-samples changes with the application of the scaling factor ϑ. On the left are the profiles for $\vartheta = 0.8$ and on the right for $\vartheta = 1.2$. The legends indicate the functions used as listed in Table 4.1. The selected functions is the one that give the highest probability in each case.

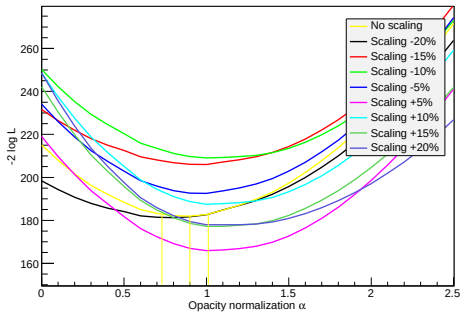

FIGURE 4.24: $-2 \log L$ profiles for the different scaling factors applied to the data as indicated in the legend.

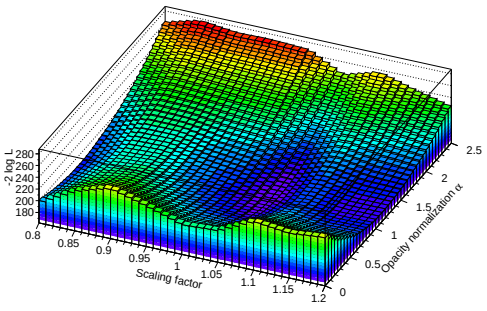

FIGURE 4.25: $-2 \log L$ vs opacity normalization α vs scaling factors. The absolute minimum is visible for $\vartheta = 1.05$ (corresponding to an increase of +5% in the signal) and $\alpha = 1.02$.

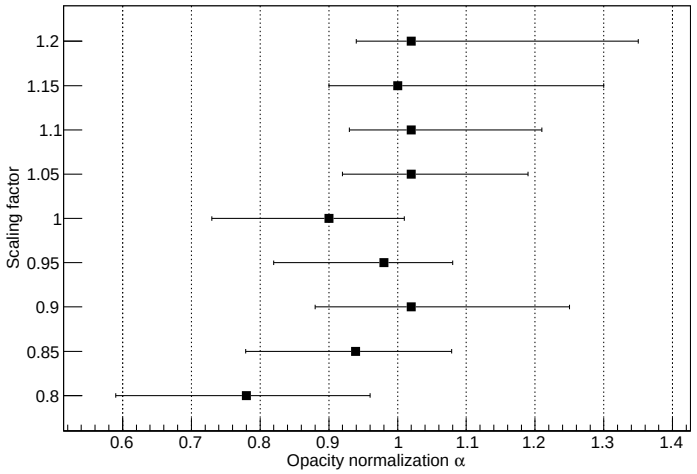

FIGURE 4.26: Values of α corresponding to the minima in the $-2\log L$ profiles in Fig. 4.24 with their 1σ uncertainty, for the different scaling factors.

Considering the widest statistical variation arising from changing the energy scale (the lower limit of α for $\vartheta = 1.00$ and the upper limit of α for $\vartheta = 1.15$), the opacity normalization measured from the April 2013 of Mrk421 data is $\alpha_0 = 0.90(-0.17, +0.11)_{stat}(-0.0, +0.29)_{syst}$.

As a final exercise, we can combine the TS profile from the February 2014 observations of 1ES 1011+496 (Fig. 4.8) and the TS profile from the April 2013 observations of Mrk421 (Fig. 4.18 (b)). The combined test statistics has a maximum of TS=53.5 at $\alpha_{comb} = 1.00^{+0.07}_{-0.15}$, indicating that, with the combined TS from the data samples of 1ES 1011+496 and Mrk421, the EBL model of Domínguez et al. [2011] scaled by the normalization factor α_{comb}, is preferred over the null EBL hypothesis with a significance of 7.3σ.

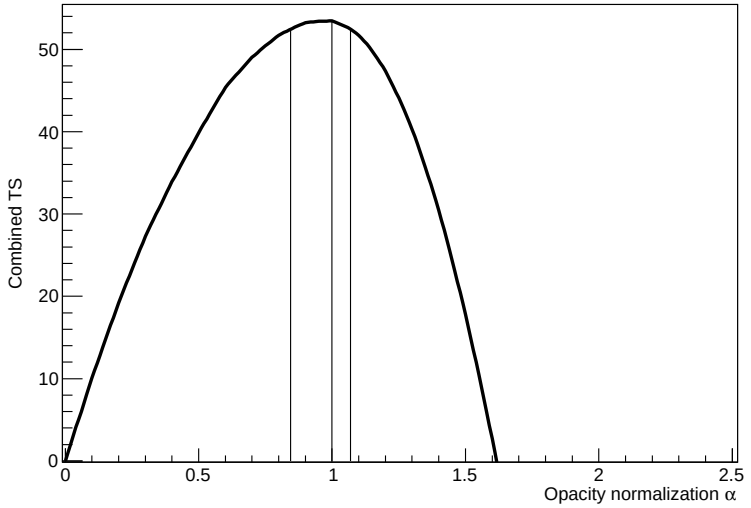

FIGURE 4.27: Combined Test Statistics (TS) from the February 2014 observations of 1ES 1011+496 and the April 2013 observations of Mrk421. The vertical lines indicate the best-fit value and the statistical uncertainty corresponding to 1σ.

Chapter 5

Additional analyses

The measurement of the extragalactic background light (EBL) observing very-high energy (VHE) gamma rays depends strongly on the quality of the observed differential energy spectrum and the distance of the source (redshift). This interplay between demanding a good quality spectrum and a large enough distance makes difficult to select a source and plan the observations. Sources with relatively high redshift can be observed by MAGIC mainly when they are in flaring state, therefore, planning long observations does not guarantee that spectra with high statistics will be obtained. That is why the program for measuring the EBL of the MAGIC Collaboration relies mostly on *target of opportunity* (ToO) observations. These observations are triggered by alerts issued by other instruments (ground or space based), or are extended if the online analysis of the MAGIC telescopes measure an activity increase in a monitored source.

The sources to be monitored by MAGIC are selected based in the type (mainly blazars, since these are more prone to have outbursts), the redshift, and the previously observed energy spectrum measured at VHE (by MAGIC itself or other IACT), or at HE (by *Fermi*-LAT). Markarian 421 and 1ES 1011+496 are part of that list . This list also includes 1ES 0229+200, which has been monitored since November 2012. In the following sections the observations up to October 2014 will be described.

The analysis and detection of another source, 1ES 0547+250 will also be described. The analysis of this source was of interest due to its high redshift ($z = 0.45$), having the potential that reconstructed spectral points were affected by strong EBL absorption.

Additionally, a study of prospects for detection of axion-like particles, for a particular model and using a simulated performance of the Cherenkov Telescope Array, will be included at the end of this chapter.

5.1 1ES 0229+200

1ES 0229+200 is an AGN classified as high-frequency peaked BL Lac, located at redshift $z = 0.14$ [Woo et al., 2005]. It was discovered at VHE by the H.E.S.S. Collaboration in an extended campaign between 2005 and 2006 where 70.2 h of data were collected [Aharonian et al., 2007a]. The differential energy spectrum from that observation could be fitted with a simple power-law function with index $\Gamma = 2.50 \pm 0.19_{stat} \pm 0.10_{syst}$ 5.1. No evidence of a break or cutoff was

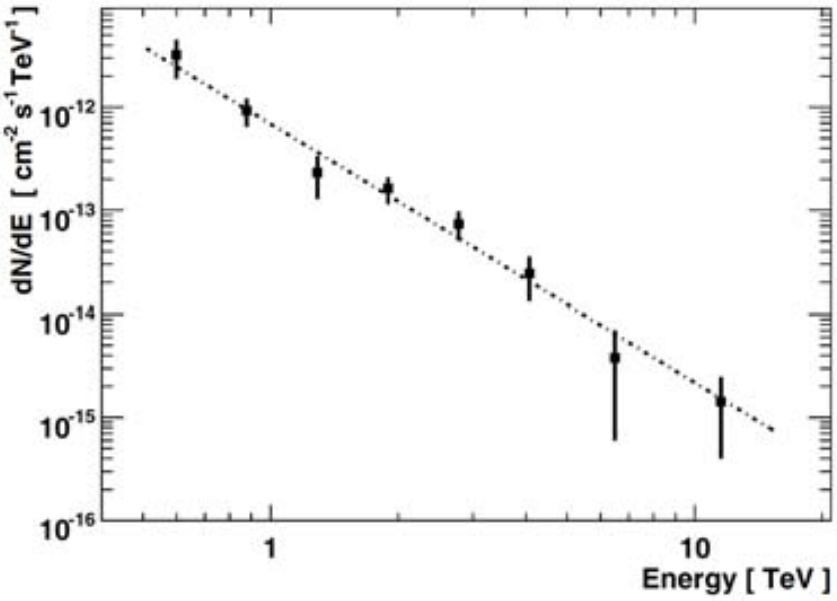

FIGURE 5.1: Observed differential energy spectrum from 1ES0229+200. The line represents a fit to a power-law function (from Aharonian et al. [2007a]).

found. Also they did not find evidence of variability on any time scale within the observation period.

The observed spectrum of 1ES 0229+200 was reconstructed up to ~ 10 TeV, probing the EBL in the near and mid-infrared band. Using the hypothesis of the limited hardness of the intrinsic energy spectrum of the source at VHE ($\Gamma_{int} > 1.5$), upper limits where set to the EBL intensity, of around 60% above the EBL level in the model by Primack et al. [2005].

Apart from the interest of measuring the EBL intensity with data from 1ES 0229+200, this source has been widely studied to set limits to the extragalactic magnetic field (EGMF), mainly due to its hard intrinsic energy spectrum. The studies are centered in the fact that the pairs electron-positron created by the interaction of gamma rays with the EBL, will interact with the cosmic microwave background, producing secondary gamma rays via inverse Compton interactions. If the EGMF is strong enough, the pairs will be deflected significantly from their initial direction, causing that the secondary GeV photons will have low probability of reaching the observer. With this approach, limits have been set to the EGMF [e.g. Dermer et al., 2011, Dolag et al., 2011, Neronov and Vovk, 2010, Tavecchio et al., 2010a, Taylor et al., 2011, Vovk et al., 2012]. Another approach is based in the imaging capabilities of the IACTs and *Fermi*-LAT. For a certain range of EGMF ($10^{-7} - 10^{-12}$ G), the gamma-ray emission from the electron-positron pairs will produce a "halo" around the observed direction of the primary gamma rays. For weaker magnetic field values ($< 10^{-14}$ G), no pair halo is formed, but the particle cascade propagation along the initial beam directions causes a broadening of the beam width. In a extensive study by Abramowski et al. [2014], where data from 1ES 0229+200 was analyzed among other sources, they concluded that no pair emission was found in their data, setting limits to the EGMF strength (a similar study by Aleksić et al. [2010] also set constrains to the EGMF although using observations of Mrk421). This kind of analysis requires a good understanding of the point spread function of the instrument (see section 2.3.1.2).

5.1.1 MAGIC observations

The MAGIC telescopes have been collecting data from 1ES 0229+200 since 2012-11-13. The data have been collected for the study of the secondary emission (the halo) but also for monitoring the activity of the source. Catching the source in an outburst has the potential of provide spectral points in the optically-thick regime of the EBL. The dates of the observations analyzed up to now are listed in the Table 5.1.

TABLE 5.1: Observations dates of 1ES 0229+200. The dates follow the "day after" convention.

Year	Month	Days
2012	November	13, 16
	December	16, 17
2013	January	6, 8, 11, 13
	February	7, 8, 9, 11, 12, 13
	September	3, 8, 10, 28, 29, 30
	October	1, 2, 5, 6, 7, 8, 10, 11, 12
	November	2, 5, 7, 24, 25, 29
	December	4, 5, 24, 26, 28
2014	January	1, 4
	September	2, 3, 4, 20, 22, 23, 24
		25, 27, 28, 29, 30
	October	1, 2, 3

The data was analyzed following the standard analysis chain, doing the selection based on rates and light conditions. Only data taken in dark conditions have been included in the analysis. After data selection, 49 hours of data were gathered. Due to the extension in time of the observations, for the analysis of the data, samples from all the Monte Carlo simulations available after the upgrade of the MAGIC telescopes were used (listed in Table 3.4 in section 3.1.3.3). The OFF data to produce the random forest (see section 2.4.0.4) ware taken from several sources, listed in Table 5.2.

TABLE 5.2: Source names for the background sample used to training the Random Forest.

MC version	Source	
ST.03.01	NGC1275	2012-12-15, 2013-01-11, 2013-01-13
	SegueA	2012-12-22, 2012-12-23, 2013-01-09
ST.03.02	SegueA	2013-02-11, 2013-02-13, 2013-02-15, 2013-02-16
	DarkPath11	2013-02-08
	2FGLJ1410+74	2013-03-15, 2013-03-20
ST.03.03	B1957+20	2013-08-31, 2013-09-02
	DarkPatch15	2013-12-21
	DarkPatch22	2013-12-21
	DarkPatch40	2013-09-09
	LSI+61	2013-11-06, 2013-12-31
ST.03.05	1ES0120+340	2014-09-20, 2014-09-22, 2014-09-23, 2014-09-24
	Cyg-X1	2014-09-17, 2014-09-18, 2014-09-20, 2014-09-23

5.1.2 Results

Fig. 5.2 shows the θ^2 distributions for the collected data up to 2014-09-03 accounting for 49 hours of observations. The source is detected with a significance of 9.40σ after "full range" MAGIC standard cuts (used to evaluate the significance of the signal above ∼200 GeV): $E > 200$ GeV, *hadronness*< 0.28, $size_1$ and $size_2 > 55$ and $\theta^2 < 0.009$ (for definitions about *hadroness*, *size* and θ see section 2.4).

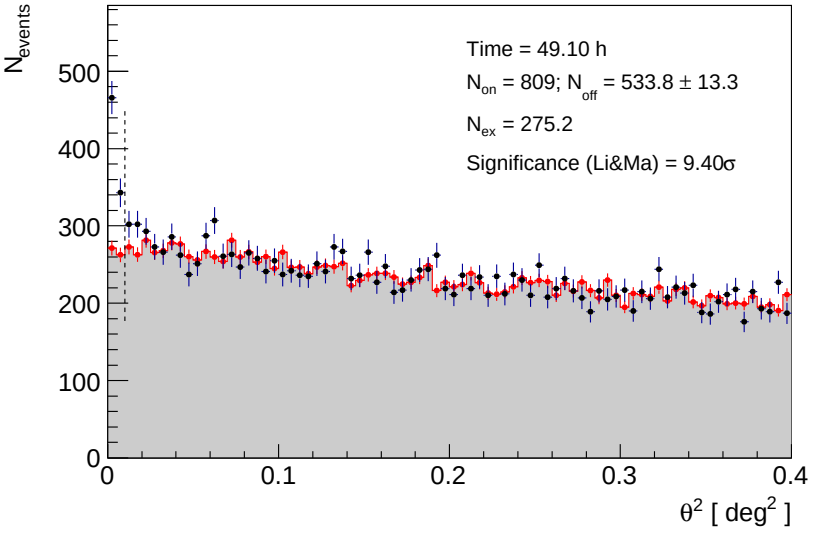

FIGURE 5.2: Θ^2 event distribution for the observations of 1ES 0229+200 listed in Table 5.1. The cuts are detailed in the text.

From the light curve shown in Fig. 5.3 it can be seen that 1ES 0229+200 in all MAGIC observations never enter into a clear flaring state. There is a small increase of activity in the dates of 2013-11-24 and 2013-11-25, but the flux was still quite weak. In several nights no significant detection was achieved. From the point of view of EBL studies, this is unfortunate, because even after the long exposure, not enough VHE gamma rays have been detected in order to have a good enough reconstruction of the observed energy spectrum in the range in which the characteristic EBL imprint could be measured. Fig. 5.4 shows the average differential energy spectrum the analyzed data of 1ES 0229+200. The observed data could be fitted to a simple power-law function with photon index $\Gamma_{obs} = 2.72 \pm 0.15_{stat}$, with a probability of 32% ($\chi^2/ndf = 5.87/5$). The de-absorbed spectrum (using the EBL model by Domínguez et al. [2011]) also could be fitted with a power-law, with index $\Gamma_{int} = 1.52 \pm 0.24$, with probability of 4% ($\chi^2/ndf = 11.81/5$)

In a extended study performed by VERITAS [Aliu et al., 2014], where MWL data taken over three years from 1ES 0229+200 was analyzed, they found evidence of possible variability in the flux above 300 GeV. Fig. 5.5 shows the light curve from VERITAS observations with a yearly binning together with previous data from HESS [Aharonian et al., 2007a]. A fit to a constant flux ($(22.9 \pm 2.8) \times 10^{-9} m^{-2} s^{-1}$) yield a probability of 1.6% ($\chi^2/ndf = 8.32/2$). Based on VERITAS result, we divided our sample in observing seasons coincident with validity periods of the MC simulations (periods shown in table 3.4) to produce the light curve shown in Fig. 5.6. A fit to a constant flux yield a probability of 9.9% ($\chi^2/ndf = 6.27/3$). A qualitative evaluation of the light curve observed by MAGIC shows a decreasing trend in the emission at VHE of 1ES 0229+200. Doing the comparison between the light curves shown in Fig. 5.5 and

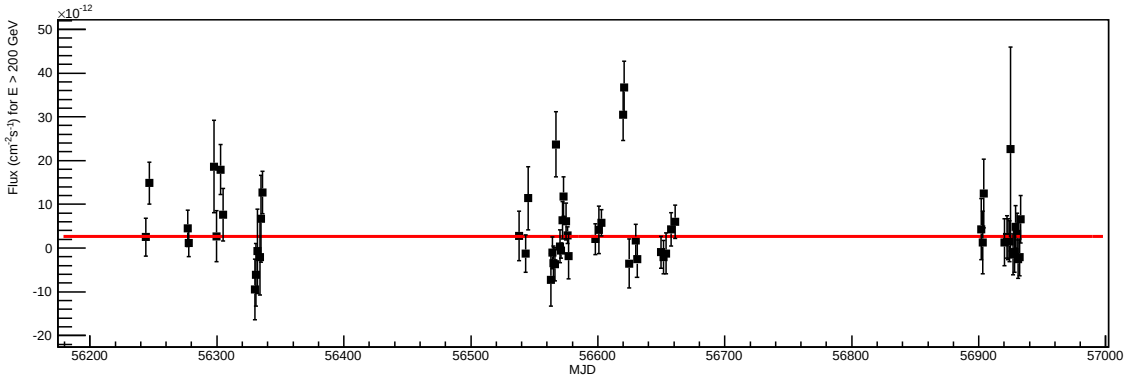

FIGURE 5.3: Light curve for all the analyzed observation dates of 1ES 0229+200 for $E > 200$ GeV. In red is a fit to a constant flux with a probability of 2.7×10^{-7}.

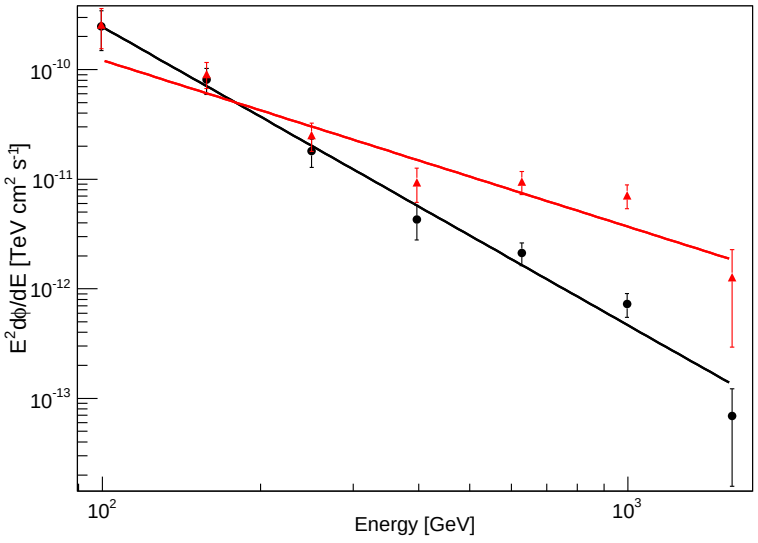

FIGURE 5.4: Reconstructed differential energy spectrum of 1ES 0229+200. In black are the observed spectral points, fitted with a simple power-law (solid black line). The red triangles are the same points after EBL de-absorption, fitted also with a power-law.

Fig. 5.6 reveals that the measured flux in the first point by MAGIC is at the same level as the flux measured by VERITAS in the period labeled as 2009-2010, whereas the flux in the period 2011-2012 is compatible with the last point in the MAGIC light curve. A more detailed analysis is forthcoming and will be published elsewhere. The source is still being observed under the monitoring program.

5.2 1ES 0647+250

1ES 0647+250 is an AGN classified as a high-frequency peaked BL Lac. One characteristic of the BL Lacs is their absence of emission lines, making difficult to measure their redshift. Initially, the distance of 1ES 0647+250 had been estimated to be $z = 0.203$, however, recent

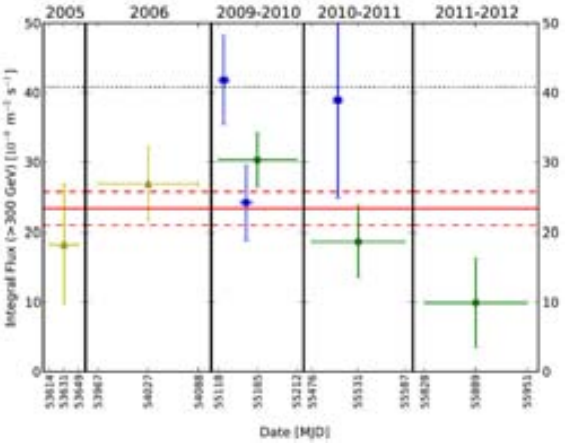

FIGURE 5.5: Integral flux above 300 GeV for 1ES 0229+200, binned by observing season (green circle). Previous HESS measurements are shown in yellow triangles. The blue squares are data binned by observing period. The horizontal red lines (solid is the value and dashed is the statistical error range) are the fit to the green circles (from [Aliu et al., 2014]).

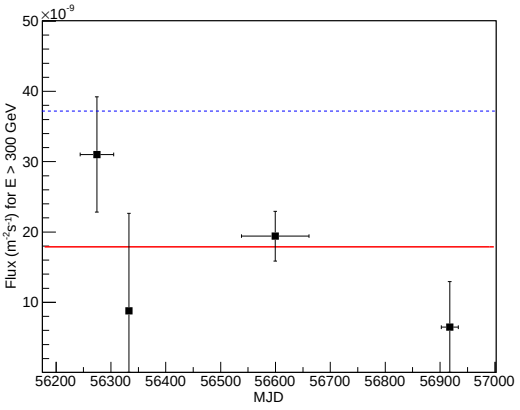

FIGURE 5.6: Integral flux above 300 GeV for 1ES 0229+200, binned by observing seasons. The solid red line is a fit to a constant flux. The dashed blue line shows a 3% Crab Nebula flux [Albert, 2008a].

measurements placed the redshift of the source at $z = 0.45$ [Kotilainen et al., 2011, Meisner and Romani, 2010].

In a survey of 28 blazars with X-ray flux larger than 2 μJy at 1 keV, 1ES 0647+250 was observed by the MAGIC I between February and March, 2008, collecting almost 30 hours of good quality data, although it was no detected [Aleksić et al., 2011].

5.2.1 MAGIC 2010-2011 observations

1ES 0647+250 was observed again in stereoscopic mode by the MAGIC Telescopes in 22 nights between 2010-01-19 and 2011-03-01. The observations dates are listed in the Table 5.3.

TABLE 5.3: Observations dates of 1ES 0647+250. The dates follow the "day after" convention.

Year	Month	Days
2010	January	19, 22, 23
	October	13, 17
	November	6, 11, 16
	December	13, 14
2011	January	3, 8, 9, 10, 11, 12, 29
	February	6, 7, 8, 23
	March	1

The data was analyzed following the standard analysis chain, selecting the data based on rates and light conditions. Only dark data was selected in order to achieve a low energy threshold. The Monte Carlo simulations used were the pre-upgrade standard ones (ST.01.02). The OFF data was taken from the sources and dates listed in Table 5.4.

TABLE 5.4: Source names and observation dates for the background sample used to training the Random Forest. The dates are following the "day after" convention.

Source	Date
CygnusLoop	2010-07-14, 2010-07-17, 2010-07-22
Cygnus X1	2010-03-26
GRB100117-2106	2010-01-18
GRB101231-0136	2010-12-31

The crosscheck with 12 hours of Crab Nebula data indicates a sensitivity of $0.74 \pm 0.06\%$ C.U. Fig. 5.7 shows the θ^2-plot and the reconstructed differential energy spectrum, where it can be seen that the observed spectrum reproduces the expected Crab Nebula spectrum.

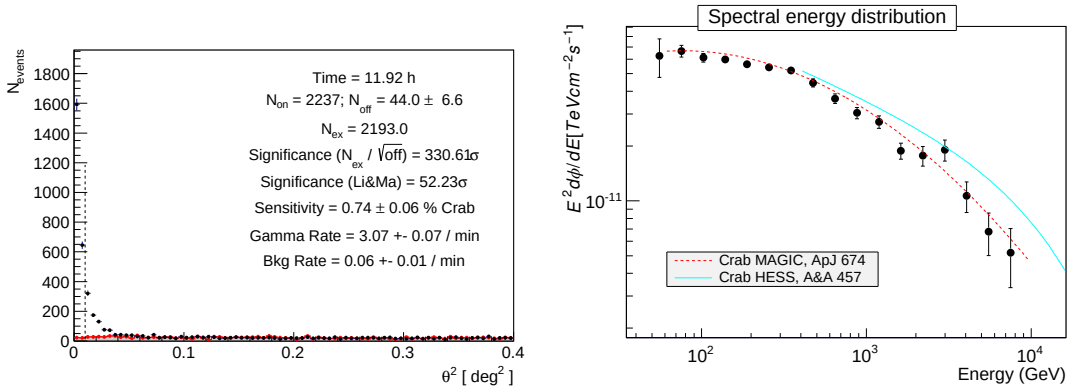

(a) (b)

FIGURE 5.7: **Left**: θ^2 plot for the Crab Nebula data selected for the crosscheck. In black are the excess events and in red the background (OFF) events. **Right**: the spectral energy distribution of the Crab Nebula, the blue line and the green dashed line are the Crab nebula spectrum from [Aharonian, 2006] and [Albert, 2008a], respectively.

5.2.2 Results

Fig. 5.8 shows the θ^2 distribution of events for the collected data from 1ES 0647+250 for 25.5 hours of observations. The significance of 6.32σ was achieved after "low energy range" MAGIC standard cuts (used to evaluate the significance of the signal above ~100 GeV) : $E > 100$ GeV, *hadronness*< 0.28, $size_1$ and $size_2 > 55$ and $\theta^2 < 0.009$ (for definitions about *hadroness*, *size* and θ see section 2.4). Fig. 5.9 shows the so-called skymap, where the significance of the signal is shown, computed trough a test statistics (TS), which is the eq. 17 from Li and Ma [1983], applied on a smoothed and modeled background estimation. Its null hypothesis distribution mostly resembles a Gaussian function. The applied cuts are the same as for the θ^2 plot. The observed distributions in the θ^2 and the skymap confirm the positive detection of the source with a significance larger than 5σ.

Fig. 5.10 shows the light curve for the observations of 1ES 0647+250 between 2010-01-19 and 2011-03-01, with a monthly binning. It can be seen that the flux is quite weak, for observations within any particular month. Fig. 5.11 shows the observed differential energy spectrum, together with the spectrum after EBL de-absorption (using Domínguez et al. [2011] EBL model). The

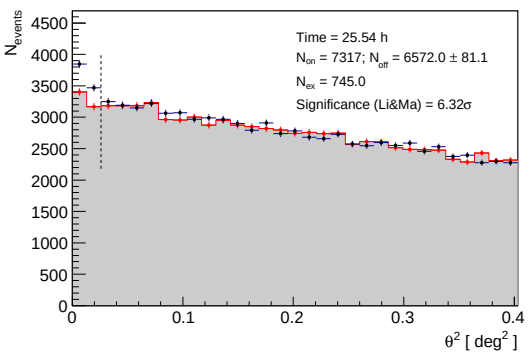

FIGURE 5.8: Θ^2 event distribution for the observation of 1ES 0647+250 after cuts detailed in the text.

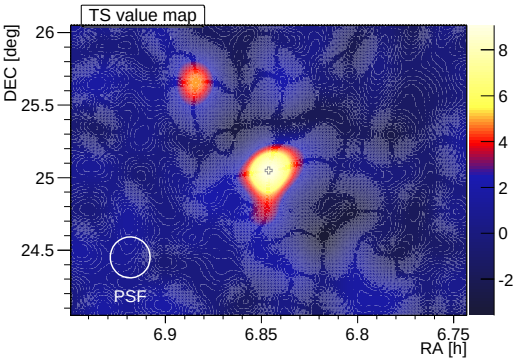

FIGURE 5.9: TS value map for the selected data of 1ES 0647+250. The cross indicates the center of the camera and the color code is the significance.

observed spectrum can be fitted with a simple power-law with photon index $\Gamma_{obs} = 3.49 \pm 0.37_{stat}$, with a probability of 74% ($\chi^2/ndf = 1.27/3$). The de-absorbed spectrum also could be fitted with a power-law, with index $\Gamma_{int} = 2.77 \pm 0.49$, with probability of 44% ($\chi^2/ndf = 2.71/3$). The intrinsic energy spectrum of the source seems to be soft, therefore making difficult to have spectral points in the optically thick regime of the EBL. Is clear that from this data set is not possible to obtain a measurement of the EBL applying the method described in section 4.2.

It should be noted that the discovery of 1ES 0647+250 at VHE was performed by MAGIC.

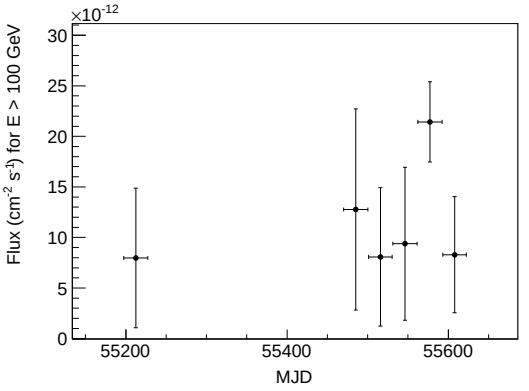

FIGURE 5.10: Light curve for the observations of 1ES 0647+250 with a monthly binning for $E > 100$ GeV.

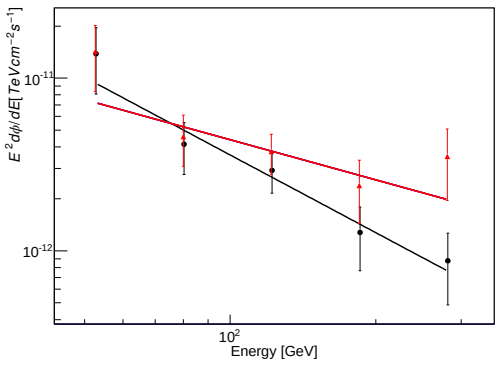

FIGURE 5.11: The reconstructed spectral energy distribution of 1ES 0647+250. In black are the observed spectral points, fitted with a simple power-law (solid black line). The red triangles are the same points after EBL de-absorption, fitted also with a power-law.

5.3 Possibilities of detection of anomalies in the propagation of gamma-rays: axion-like particles

5.3.1 Prospect for detection of axion-like particles with CTA for a test case.

This study of prospects for detection of axion-like particles (ALPs) was published as part of an special issue dedicated to the physics prospects for the future Cherenkov Telescope Array (CTA) [Doro et al., 2013]. CTA will be a new observatory for very high-energy gamma rays [Acharya et al., 2013], programed to start operations between 2016 and 2017. The telescopes of this array will work under the same principles of the IACTs that will described in section 2.2.

In our study, in order to quantitatively study the effect of photon-axion conversion over the cosmological distances of AGN, we consider the total photon intensity. It becomes then useful to define the *axion boost factor* as the difference between the predicted arriving photon intensity (after the absorption due to the interactions with the EBL) without including ALPs and that obtained when including the photon/ALP conversions. Qualitatively speaking, it is found that the more attenuating the EBL model considered, the more relevant the effect of photon/ALP conversions in the IGMF (since any ALP to photon reconversion might substantially enhance the intensity arriving at Earth). Furthermore, higher B values do not necessarily translate into higher photon flux enhancements. There is always a B value that maximizes the axion boost factors; this value is sensitive to the source distance, the considered energy and the adopted EBL model.

In the approach by Sánchez-Conde et al. [2009], they predict the existence of a universal feature in the spectrum of the sources due to the intergalactic mixing, that is completely independent on the sources themselves and only depends on the ALP and IGMF properties. This feature should be present at the same critical energy E_{crit} for all sources, and would show up in the spectra as a drop in the flux (whenever E_{crit} is in the range where the EBL effect is negligible) or even as a sudden flux increase, if the EBL absorption is strong for $E = E_{crit}$. However, it has been pointed out that because of the random nature of the intergalactic magnetic fields, the effect of photon/ALP mixing should be very different from one source to another [Burrage et al., 2009, Mirizzi and Montanino, 2009].

To test the scenario predicted by Sánchez-Conde et al. [2009], we took as a test source the flat spectrum radio quasar 4C +21.35 (PKS 1222+21), at redshift $z = 0.432$, which was detected by MAGIC above 70 GeV [Aleksić, 2011] in June 2010, during a *target of opportunity* observation triggered by the high state of the source in the Fermi-LAT energy band. This source is the second most distant object detected by ground-based gamma-ray telescopes, and hence an ideal candidate for the study of propagation effects. The observed energy spectrum of 4C +21.35 during the 0.5 hour flare recorded by MAGIC was well described by a power law of index $\Gamma = 3.75 \pm 0.27_{stat} \pm 0.20_{syst}$. The intrinsic spectrum, assuming the EBL model of Domínguez et al. 2011 was estimated to be a power law of index $\Gamma = 2.72 \pm 0.34$, which extrapolated down to an energy of about 5 GeV, connects smoothly with the harder spectrum ($\Gamma = 1.95 \pm 0.21$) measured by Fermi-LAT (see section XX for description of the instrument) between 0.2 and 2 GeV in a 2.5 h period encompassing the MAGIC observation.

We simulated observations, with the expected performance parameters of CTA, of 4C +21.35 assuming an intrinsic unbroken power-law spectrum, in the relevant energy range, like the one determined by MAGIC for 4C +21.35 during the flare, i.e. $dF/dE = F_0 \times [E/(0.2\ \text{TeV})]^{-2.72}$. Keeping the spectral shape unchanged, we have tried different absolute flux normalizations,

taking as a reference the flux observed by MAGIC, $F_0 = 1.78 \times 10^{-5}$ m^{-2} s^{-1} TeV^{-1}. We have also tested different observation times: the actual duration of the VHE flare observed by MAGIC is unknown, since the observation was interrupted while the flare was still going on, but the flares observed by Fermi-LAT above 100 MeV show rise and decay time scales of the order of a day [Tanaka, 2011], so it is reasonable to expect that the source may stay several hours in flux states as high as that observed by MAGIC. For the detector simulation we have used a CTA candidate array called *E* (see Acharya et al. [2013] Fig. 6). The EBL model by Domínguez et al. 2011 has been used to account for the effect of the EBL, and the conversion of photons into ALPs and *vice versa* has been simulated following the formalism detailed in Sánchez-Conde et al. 2009 as outlined above. Only conversions in the IGMF have been considered (in this case, mixing in the source typically leads to only a few percent of flux attenuation, so we neglected it in order to avoid extra uncertainties).

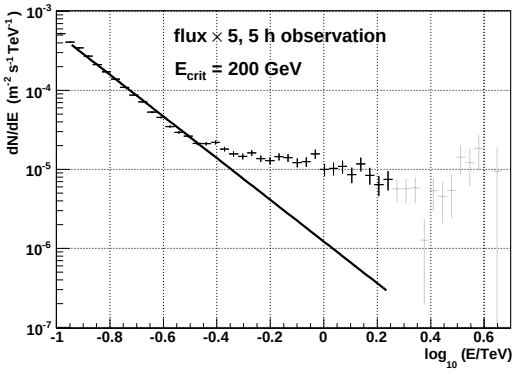

FIGURE 5.12: Simulation of a 5 h CTA observation of a 4C +21.35 flare 5 times more intense than the one recorded by MAGIC [Aleksić, 2011]. In black, energy bins used for the fit (those with a signal exceeding three times the RMS of the background, and a minimum of 10 excess events). Excluded points are displayed in grey. The estimated intrinsic differential energy spectrum (after correcting for the EBL effect) shows a *boost* at high energies due to photon/ALP mixing. The IGMF strength is assumed to be 0.1 nG, and ALP parameters result in E_{crit} = 200 GeV.

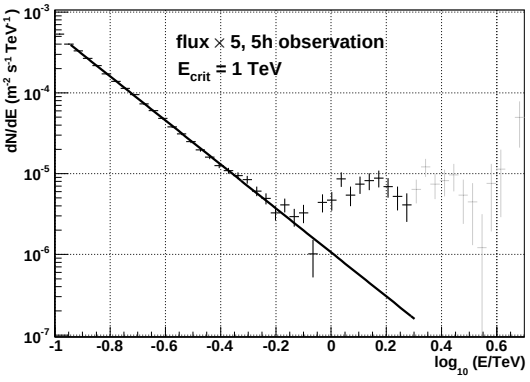

FIGURE 5.13: Same as in Fig. 5.12, but with E_{crit} = 1 TeV. Note that in scenarios like this, where E_{crit} is within the energy range in which the EBL absorption is already large, the *boost* in the flux shows up as a sudden rise (smeared out by the spectral resolution of the instrument) which would even allow to determine E_{crit} accurately.

We assumed the same parameters for the IGMF as those in the fiducial model in Sánchez-Conde et al. 2009: 0.1 nG is the (constant) modulus of the IGMF. This value is just one order of magnitude below the current upper limits [de Angelis et al., 2008], and lower limits lie many orders of magnitude below [Neronov and Vovk, 2010, Tavecchio et al., 2010b]. The IGMF is assumed to have fixed orientation within domains of size 1 Mpc. The orientation of the IGMF varies randomly from one domain to the next. The ALP parameters, mass and coupling constant, enter via E_{crit}, below which the conversion probability is negligible. We have scanned E_{crit} in the range 0.1 to 10 TeV in steps of 0.1 TeV.

Using the performance parameters of the candidate array *E*, we obtain the expected gamma-ray and cosmic-ray background rates in bins of estimated energy, and from them the reconstructed differential energy spectrum. After this, we correct the observed spectrum by the energy-dependent attenuation factors expected from the EBL in order to get an estimate of the intrinsic

source spectrum. Each simulated spectrum is fitted to a power-law with variable index of the form $dF/dE \propto E^{-\alpha-\beta\ log(E/0.1\mathrm{TeV})}$, in which we constrain the β parameter so that the spectrum cannot become harder with increasing energy (such behavior is not expected from emission models in this energy range). Only energy bins with a signal exceeding three times the RMS of the background, and a minimum of 10 excess events, are considered in the fit.

In the absence of any significant photon/ALP mixing, the resulting fits will all match the spectral points within the experimental uncertainties, resulting in *good* χ^2 values. But, as shown in Sánchez-Conde et al. 2009, certain combinations of ALP parameters and values of the IGMF may result in significant modifications of the observed VHE spectra. The most striking feature is a *boost* of the expected flux at high energies, which is particularly prominent in the estimated intrinsic (i.e. EBL-de-absorbed) spectrum. Such a feature may result in a low value of the χ^2-probability of the spectral fit. In Figs. 5.12 and 5.13 we show two such cases, in which the observed spectra, after de-absorption of the EBL effect, show a clear hardening of the spectral index. The effect is particularly striking in the cases in which the EBL absorption at $E = E_{crit}$ is already strong (e.g. Fig. 5.13), because then the boost sets in very fast, resulting in dN/dE rising with energy at around E_{crit}. The rise is actually very sharp, but it is smoothed by the energy resolution of the instrument. An improvement in the energy resolution would increase the significance of the feature and improve the determination of E_{crit}. In contrast, if E_{crit} is in the range in which the EBL absorption is small or negligible (Fig. 5.12), the feature at E_{crit} would just be a flux drop of at most $\simeq 30\%$, also washed out by the instrumental energy resolution. In those cases, though a high-energy boost may still be clearly detected, it would be hard to determine the exact value of E_{crit}. This is because, in the formalism described in Sánchez-Conde et al. 2009, similar ALP boost factors are always achieved at energies $E > E_{crit}$, independently of the particular value of E_{crit} in each case.

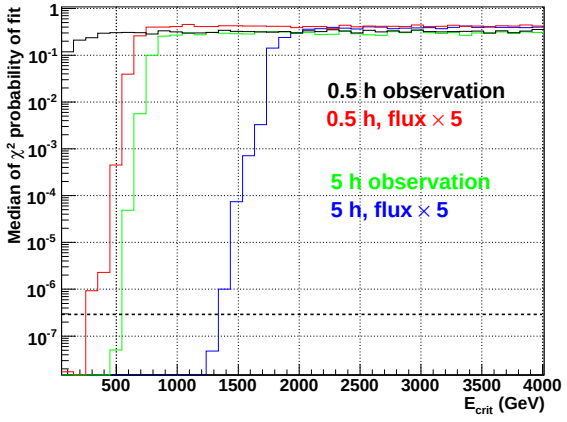

FIGURE 5.14: Median of the χ^2-probabilities of the fits to the de-absorbed differential energy spectra of 4C+21.35 measured by CTA, assuming photon/ALP mixing, for different values of E_{crit}. We simulated observations of flares of two different durations: 0.5 and 5 hours, and with intensities equal to 1 and 5 times that of the flare reported in Aleksić [2011]. The dashed horizontal line marks the probability that corresponds to 5 standard deviations.

For each of the E_{crit} values scanned, we performed 10^3 simulations of a CTA observation, all with the same source flux and observation time. We considered that a given value of E_{crit} is within the reach of CTA whenever the median of the χ^2-probability distribution is below 2.9×10^{-7}, which corresponds to 5 standard deviations. In Fig. 5.14 we show the median of the χ^2 probability versus E_{crit}, for two different assumptions on the source flux and two different observation times. The range of E_{crit} which can be probed with CTA for the different scenarios

is the one for which the curves in Fig. 5.14 are below the dashed horizontal line. As expected, the range becomes larger as we increase the observation time and/or the flux of the source. A 0.5 h duration flare like the one reported in Aleksić 2011 would not be enough for CTA to detect a significant effect in any of the tested ALP scenarios, i.e. the solid black line never goes below the dashed line for any value of E_{crit}. A flare of similar intensity, but lasting 5 hours (green line) would already be enough to see the boost due to ALPs for those scenarios with $E_{crit} \leq 500$ GeV. In Fig. 5.14 we can also see that for a hypothetical flare with an intensity 5 times larger, lasting 5 hours, the accessible range of E_{crit} would extend up to 1.3 TeV.

5.3.2 Hints of detection of axion-like particles with current IACTs

Following the framework proposed by [Burrage et al., 2009, Mirizzi and Montanino, 2009], a study was conducted by Horns and Meyer 2012 (and updated in [Horns et al., 2013]), where they took a sample of 50 VHE gamma-ray spectra from IACTs observations. Under some reasonable assumptions on the EBL density and on the intrinsic spectral shape of the gamma-ray emission, they compared the scatter of the spectral measurements, around the extrapolation of a power-law functions fitted to the optically this part of the spectrum, between well-defined samples covering ranges in optical depth of $1 \leq \tau < 2$ and $2 \leq \tau$. The two samples show significant differences, which leads the author to claim the existence of an anomaly in the transparency of the Universe (see Fig. 5.15).

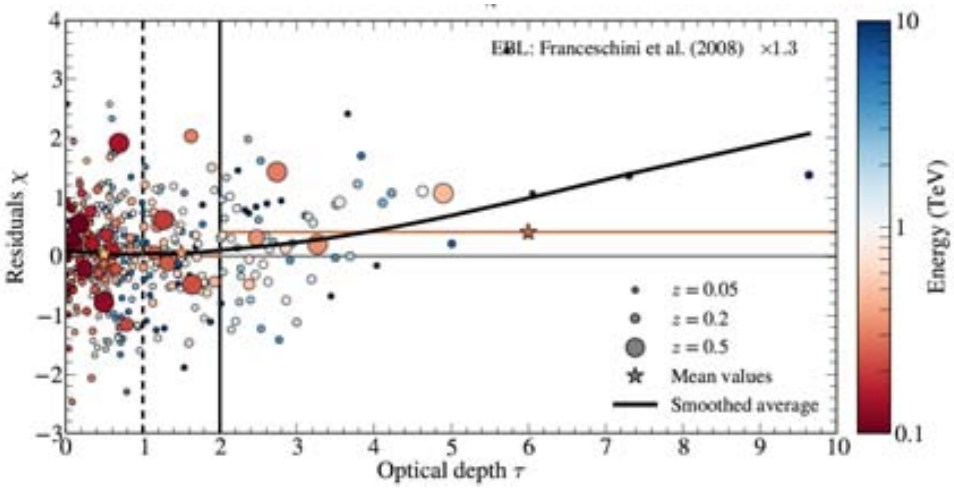

FIGURE 5.15: Scatter of the residuals after fitting power-law functions to the optically-thin region of the spectra, as a function of the optical depth. The marker sizes correspond to the redshift of the objects and the color coding represents the energy of each data point. The black solid line shows a smoothed average and the stars mark the mean of the distributions. The claimed anomaly is the deviation of the solid black line from the line marking zero residuals. (from Horns et al. 2013).

It the work by Wouters and Brun 2012, is pointed out that the sharp drop in the gamma-ray flux due to the photon/ALP mixing above the E_{crit} is not a robust observable and is not what should be searched for. Due to the unpredictable nature of the different domains of magnetic field that the photon/ALP has to cross, according to their calculation, the probability amplitude for the photon/ALP conversion above and around certain threshold (dependent on the magnetic field and the properties of the ALP) becomes unpredictable. However, the noise level (fluctuations in the probability of a photon to be converted into an ALP as function of the observed gamma-ray energy, eq. 5.1 in section 1.4) is a prediction of the model. This prediction significantly differs

from what was presented in the formalism by Sánchez-Conde et al. 2009 and, consequently, in the simulations for CTA presented in the previous lines. In Fig. 5.16 is represented, as an example, the survival probability of a photon from a source at redshift $z = 0.1$ traveling through a single realization of a 1 nG IGMF with coherent domains of size $s = 1$ Mpc. One can see that the prediction of the model including ALPs has a significant level of fluctuations in the energy spectrum. In Grossman et al. 2002 it has been shown that averaging over a large number of realization of N domains in each of which the conversion probability is P_0 (see eq. 5.1) yields an overall probability

$$P_{\gamma\to a} = \frac{1}{3}(1 - e^{-3NP_0}) \quad , \tag{5.1}$$

which is what is followed in Sánchez-Conde et al. 2009. In the case of the observation of one source only, if N is very large and the energy spectrum is binned, then the smooth behavior can be retrieved in principle. Nevertheless, according to Wouters and Brun 2012, N in reality is not large enough, therefore the smooth behavior is not recovered leaving an imprint that could be measured. The detection approach proposed by Wouters and Brun 2012 is based in choosing the best fit for an observed spectrum and then measure the variance of the residuals. An anomalous dispersion could be interpreted as a signature of photon/ALP mixing.

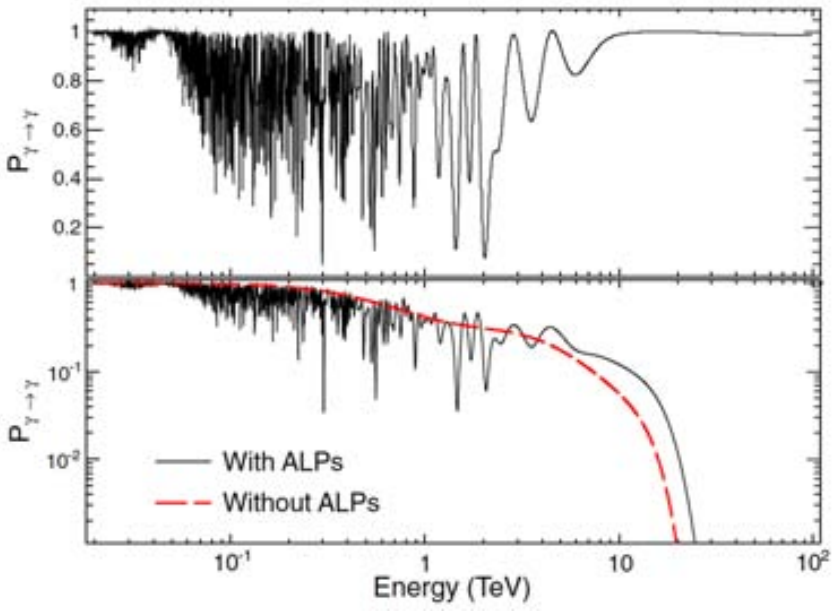

FIGURE 5.16: Photon survival probability as a function of the energy for a realization of a source at $z = 0.1$ using $B = 1$ nG, $s = 1$ Mpc, coupling constant $g = 8 \times 10^{-11}$ GeV^{-1} and $m_a = 2$ neV without absorption (upper panel) and with EBL absorption (lower panel) (from Wouters and Brun 2012).

Chapter 6

Conclusions

In this work we have presented the results of the data analysis from four AGNs observed at very-high energies by the MAGIC telescopes: Mrk421, 1ES 1011+496, 1ES 0229+200 and 1ES 0647+200. We have made emphasis in two of them: Mrk421 and 1ES 1011+496. The flaring episodes of April 2013, from Mrk421, and February 2013, from 1ES 1011+496, were by themselves of great interest and a comprehensive description of the spectral aspects of the VHE emissions were presented. The redshift of 1ES 1011+496 is $z = 0.212$, therefore, was natural to attempt an EBL measurement for these observations. In the case of Mrk421, its proximity (redshift $z = 0.031$) causes that the EBL effect over its observed flux is perceptible only at energies of several TeV. However, the extraordinary nature of the April 2013 flare provided observations with good statistics at TeV energies, which opened the possibility to also attempt an EBL measurement.

The observed emission of 1ES 1011+496 from the February 2014 flare could be represented with an average energy spectrum after showing that the spectral shape (after EBL de-absorption) did not changed significantly, even when the flux did. This average spectrum covered an energy range where the EBL absorption leaves a distinctive imprint in the observed differential energy spectrum. Then, the hypothesis to test was that, assuming that the intrinsic source spectrum can be modeled with a smooth, concave function, the best fit to the observed spectrum can be achieved only after the EBL effect is applied scaled by an opacity normalization factor α. Using a likelihood maximization method, a scan was made over α to find the maximum likelihood to the observed spectra. Then, this likelihood was compared with the likelihood of the null-EBL hypothesis ($\alpha = 0$) with a test statistics. To assess the effect of the systematic uncertainty from the energy scale of the MAGIC telescopes (reported to be 15%) over our result, the light collected in each of the pixels of the MAGIC cameras was scaled up and down from -20% to +20% in steps of 5%. Then for each reconstructed spectra corresponding to each light scaling, the same likelihood maximization method was applied to find the opacity normalization factor for each case. From those results, the effect of the systematic uncertainty was estimated. At the end, from the observations of the February 2014 flare of 1ES 1011+496, it was concluded that the EBL model scaled by an opacity normalization factor of $\alpha_0 = 1.07$ $(-0.13,+0.09)_{stat}$ $(-0.10, +0.7)_{syst}$ was preferred over the null-EBL hypothesis with a significance of 4.6σ.

The approach using the data from the April 2013 flare of Mrk421 was slightly different. The measured light curve showed high night-wise and intra-night variability, therefore a single average spectrum would have not been suitable to describe the emission of the whole flaring episode. The sample was divided in 12 subsamples, following a somewhat arbitrary classification based in the intensity of the flux with respect to time. For each one of the subsamples,

the likelihood maximization method was applied to produce test statistics profiles as function of the opacity normalization α. Then, this profiles were combined to find the value of α at which the combined test statistics was maximum. As done for 1ES 1011+496, to evaluate the effect of the systematic uncertainty in the energy scale of the telescopes, the collected light was scaled up and down from -20% to +20% in steps of 5%. From the analysis of the April 2013 of Mrk421, it was found that the EBL model scaled by an opacity normalization factor of $\alpha_0 = 0.90(-0.17, +0.11)_{stat}(-0.0, +0.29)_{syst}$ was preferred over the null-EBL hypothesis with a significance of 5.8σ. The analysis of the data from the April 2013 flare of Mrk421 revealed the necessity of a deeper understanding of spectral features, the so-called wiggles, that appear in differential energy spectra with high statistics. If the origin of these spectral features could be identified an a possible correction implemented, this could increase the sensitivity to measure spectral features that are source-intrinsic or a imprint in the propagation of the gamma rays from the source to the Earth.

1ES 0229+200, located at a redshift of $z = 0.14$ has been monitored over the last two years, on the expectative that it could enter into a flaring state. Up to October 2014, such flare has not happened. From the collected data no EBL measurement was attempted. However, the light curve, binned over sizable periods of time, reveal a possible variability of the emission at VHE. This could motivate a deeper study on the already collected data and the forthcoming observations.

The redshift of 1ES 0647+250 was initially estimated to be $z = 0.203$, however, more precise measurements placed the redshift at $z = 0.45$, which prompted our interest in a possible EBL measurement. The intrinsic differential energy spectrum of this source, after the analysis and the EBL correction, revealed to be quite soft, which makes difficult the measurements of spectral points in the optically-thick regime of the EBL. This analysis was also performed to confirm the discovery of 1ES 0457+250 at VHE by the MAGIC telescopes.

Finally, we also include a study about a possible measurable effect of the interaction of the hypothetical axion-like particles with the gamma rays from a distant source, using a very particular model. Such study was published as part of a special publication of physics prospects with the future Cherenkov Telescope Array.

Our measurements of the EBL imprint on the observed spectra from individual sources, with a reasonable significance value, opens the possibility of measure the EBL intensity in different directions in the sky searching for a possible angular distribution of the EBL. The observations of a source with relatively high redshift, by a current IACT, are performed in most cases if the source is in a flaring state. However, with an instrument with high sensitivity as expected from the Cherenkov Array Telescope, it should be possible to produce good quality spectra from sources with relatively high redshift, independently if they are in a flaring state or not. Moreover, for sources with low redshift (as Mrk421), it will be possible to measure the differential energy spectrum in the optically-thick regime of the EBL. The measurement of the EBL with high accuracy will not only bring knowledge about the history and evolution of the mechanisms that produced it, but also, since all the spectra from extragalactic sources have to be corrected for the EBL absorption, will increase the precision in which the intrinsic spectra from those sources is determined, ultimately increasing our understanding of the extreme processes responsible of the emission of very-high energy gamma rays.

Bibliography

A. A. Abdo, M. Ackermann, M. Ajello, L. Baldini, J. Ballet, and et al. Fermi Large Area Telescope Observations of Markarian 421: The Missing Piece of its Spectral Energy Distribution. *ApJ*, 736:131, 2011.

A. Abramowski, F. Acero, and et al. Measurement of the extragalactic background light imprint on the spectra of the brightest blazars observed with H.E.S.S. *Astronomy and Astrophysics*, 550:A4, February 2013.

A. Abramowski, F. Aharonian, F. Ait Benkhali, and et al. Search for extended γ-ray emission around AGN with H.E.S.S. and Fermi-LAT. *A&A*, 562:A145, 2014.

V. A. et al. Acciari. Simultaneous Multiwavelength Observations of Markarian 421 During Outburst. *Astrophysical Journal*, 703:169, 2009a.

V. A. et al. Acciari. Simultaneous Multiwavelength Observations of Markarian 421 During Outburst. *The Astrophysical Journal*, 703:169, 2009b.

B. S. Acharya, M. Actis, T. Aghajani, G. Agnetta, J. Aguilar, F. Aharonian, M. Ajello, A. Akhperjanian, M. Alcubierre, J. Aleksić, and et al. Introducing the CTA concept. *Astroparticle Physics*, 43:3–18, 2013.

M. Ackermann, M. Ajello, A. Allafort, P. Schady, and et al. The Imprint of the Extragalactic Background Light in the Gamma-Ray Spectra of Blazars. *Science*, 338:1190, 2012.

F. Aharonian and A. M. Taylor. Limitations on the photo-disintegration process as a source of VHE photons. *Astroparticle Physics*, 34:258, 2010.

F. Aharonian, A. G. Akhperjanian, K.-M. Aye, and et al. Observations of Mkn 421 in 2004 with HESS at large zenith angles. *Astronomy and Astrophysics*, 437:95, 2005.

F. Aharonian, A. G. Akhperjanian, A. R. Bazer-Bachi, and et al. A low level of extragalactic background light as revealed by γ-rays from blazars. *Nature*, 440:1018, 2006.

F. Aharonian, A. G. Akhperjanian, U. Barres de Almeida, and et al. New constraints on the mid-IR EBL from the HESS discovery of VHE γ-rays from 1ES 0229+200. *A&A*, 475:L9, 2007a.

F. Aharonian, A. G. Akhperjanian, A. R. Bazer-Bachi, and et al. An Exceptional Very High Energy Gamma-Ray Flare of PKS 2155-304. *Astrophysical Journal*, 664:L71, 2007b.

F. A. Aharonian. *Very high cosmic gamma radiation: a crucial window on the extreme universe*. 2004.

F. et al. Aharonian. Observations of the Crab nebula with HESS. *Astronomy and Astrophysics*, page 899, 2006.

J. Albert and al. Discovery of Very High Energy γ-Rays from 1ES 1011+496 at z = 0.212. *Astrophysical Journal*, 667:L21, 2007.

J. el al. Albert. VHE γ-Ray Observation of the Crab Nebula and its Pulsar with the MAGIC Telescope. *The Astrophysical Journal*, 674:1037, 2008a.

J. et al. Albert. Implementation of the Random Forest method for the Imaging Atmospheric Cherenkov Telescope MAGIC. *Nuclear Instruments and Methods in Physics Research A*, 588: 424, 2008b.

J. Aleksić, L. A. Antonelli, P. Antoranz, and et al. Search for an extended VHE γ-ray emission from Mrk 421 and Mrk 501 with the MAGIC Telescope. *A&A*, 524:A77, 2010.

J. Aleksić, L. A. Antonelli, P. Antoranz, and et al. Gamma-ray Excess from a Stacked Sample of High- and Intermediate-frequency Peaked Blazars Observed with the MAGIC Telescope. *ApJ*, 729:115, 2011.

J. Aleksić, S. Ansoldi, L. A. Antonelli, and et al. Unprecedented study of the broadband emission of Mrk 421 during flaring activity in March 2010. *ArXiv e-prints*, 2014a.

J. Aleksić, S. Ansoldi, and et al. The major upgrade of the MAGIC telescopes, Part II: The achieved physics performance using the Crab Nebula observations. *ArXiv e-prints*, 2014b.

J. et al. Aleksić. Unprecedent insights in the blazar 1ES 1011+496 via MAGIC observations in 2011 and 2012 in combination with simultaneous MWL observations and polarimetry data. *In preparation.*

J. et al. Aleksić. MAGIC TeV gamma-ray observations of Markarian 421 during multiwavelength campaigns in 2006. *Astronomy and Astrophysics*, 519(A32), 2010.

J. et al. Aleksić. MAGIC Discovery of Very High Energy Emission from the FSRQ PKS 1222+21. *Astrophysical Journal*, 730:L8, 2011.

E. Aliu, S. Archambault, T. Arlen, T. Aune, and et al. A Three-year Multi-wavelength Study of the Very-high-energy γ-Ray Blazar 1ES 0229+200. *ApJ*, 782:13, 2014.

M. Arik, S. Aune, K. Barth, and et al. Search for Sub-eV Mass Solar Axions by the CERN Axion Solar Telescope with He3 Buffer Gas. *Physical Review Letters*, 107(26):261302, 2011.

W. B. Atwood, A. A. Abdo, M. Ackermann, W. Althouse, B. Anderson, M. Axelsson, L. Baldini, J. Ballet, D. L. Band, G. Barbiellini, and et al. The Large Area Telescope on the Fermi Gamma-Ray Space Telescope Mission. *Astrophysical Journal*, 697:1071, 2009.

M. Balokovic, A. Furniss, G. Madejski, and F. Harrison. NuSTAR detects extreme X-ray flaring of Mrk 421. *The Astronomer's Telegram*, 4974:1, April 2013.

M. et al. Baloković. Multi-wavelength study of quiescent states of Mrk421 with unprecedented hard X-ray coverage provided by *NuSTAR* in 2013. *In preparation.*

J. A. et al. Barrio. The magic telescope: Design study for the construction of a 17 m cherenkov telescope for gamma-astronomy above 10 gev. *Technical report, MAGIC Collaboration*, 1998a.

J. et al. Barrio. MAGIC telescope design report. *Technical report, MAGIC Collaboration*, 1998b.

A. J. Barth, L. C. Ho, and W. L. W. Sargent. The Black Hole Masses and Host Galaxies of BL Lacertae Objects. *Astrophysical Journal*, 583, January 2003.

S. D. Barthelmy, L. M. Barbier, J. R. Cummings, and et al. The Burst Alert Telescope (BAT) on the SWIFT Midex Mission. *Space Sci. Rev.*, 120:143, 2005.

J. F. Beacom. The Diffuse Supernova Neutrino Background. *Annual Review of Nuclear and Particle Science*, 60:439, 2010.

J. Beringer, J.-F. Arguin, R. M. Barnett, and et al. Review of Particle Physics. *Phys. Rev. D*, 86:010001, 2012.

J. et. al. Beringer. Review of Particle Physics. *Phys. Rev. D*, 86(1), 2012.

K. Bernlöhr. Impact of atmospheric parameters on the atmospheric Cherenkov technique. *Astroparticle Physics*, 12:255, 2000.

S. Berta, B. Magnelli, D. Lutz, B. Altieri, and et al. Dissecting the cosmic infra-red background with Herschel/PEP. *A&A*, 518:L30, July 2010.

M. Béthermin, H. Dole, A. Beelen, and H. Aussel. Spitzer deep and wide legacy mid- and far-infrared number counts and lower limits of cosmic infrared background. *A&A*, 512:A78, March 2010.

P. M. S. Blackett. A possible contribution to the night sky from the Cherenkov radiation emitted by cosmic rays. *The Emission Spectra of the Night Sky and Aurorae*, page 34, 1948.

H. V. Bradt, R. E. Rothschild, and J. H. Swank. X-ray timing explorer mission. *AAS*, 97:355, 1993.

L. Breiman and A. Cutler. Random forests. URL `https://www.stat.berkeley.edu/~breiman/RandomForests/cc_home.htm`.

T. M. Brown, R. A. Kimble, H. C. Ferguson, J. P. Gardner, N. R. Collins, and R. S. Hill. Measurements of the Diffuse Ultraviolet Background and the Terrestrial Airglow with the Space Telescope Imaging Spectrograph. *AJ*, 120:1153, August 2000.

C. Burrage, A.-C. Davis, and D. J. Shaw. Active Galactic Nuclei Shed Light on Axionlike Particles. *Physical Review Letters*, 102(20):201101, 2009.

D. N. et al. Burrows. The Swift X-Ray Telescope. *Space Science Reviews*, 120:165, 2005.

L. Cambrésy, W. T. Reach, C. A. Beichman, and T. H. Jarrett. The Cosmic Infrared Background at 1.25 and 2.2 Microns Using DIRBE and 2MASS: A Contribution Not Due to Galaxies? *ApJ*, 555:563, July 2001.

X. Chen, S. M. Hu, D. F. Guo, and J. J. Du. Optical variability of Mrk 421. *Astrophysics and Space Science*, 349:909, 2014.

ADMX Collaboration. SQUID-Based Microwave Cavity Search for Dark-Matter Axions. *Physical Review Letters*, 104(4):041301, 2010.

CAST Collaboration. An improved limit on the axion photon coupling from the CAST experiment. *JCAP*, 4:10, 2007.

C. J. Conselice. The Evolution of Galaxy Structure Over Cosmic Time. *ARAA*, 52:291, 2014.

J. Cortina and J. Holder. MAGIC and VERITAS detect an unprecedented flaring activity from Mrk 421 in very high energy gamma-rays. *The Astronomer's Telegram*, 4976:1, April 2013.

A. de Angelis, M. Roncadelli, and O. Mansutti. Evidence for a new light spin-zero boson from cosmological gamma-ray propagation? *Physical Review D*, 76(12):121301, 2007.

A. de Angelis, M. Persic, and M. Roncadelli. Constraints on Large-Scale Magnetic Fields from the Auger Results. *Modern Physics Letters A*, 23:315–317, 2008.

F. De Paolis, G. Ingrosso, and A. A. Nucita. Astrophysical implications of binary black holes in BL Lacertae objects. *Astronomy and Astrophysics*, 388:470, 2002.

C. D. Dermer, M. Cavadini, S. Razzaque, J. D. Finke, J. Chiang, and B. Lott. Time Delay of Cascade Radiation for TeV Blazars and the Measurement of the Intergalactic Magnetic Field. *ApJ*, 733:L21, 2011.

K. Dolag, M. Kachelriess, S. Ostapchenko, and R. Tomàs. Lower Limit on the Strength and Filling Factor of Extragalactic Magnetic Fields. *ApJ*, 727:L4, 2011.

H. Dole, G. H. Rieke, G. Lagache, J.-L. Puget, and et al. Confusion of Extragalactic Sources in the Mid- and Far-Infrared: Spitzer and Beyond. *ApJS*, 154:93, September 2004.

H. Dole, G. Lagache, J.-L. Puget, K. I. Caputi, N. Fernández-Conde, E. Le Floc'h, C. Papovich, P. G. Pérez-González, G. H. Rieke, and M. Blaylock. The cosmic infrared background resolved by Spitzer. Contributions of mid-infrared galaxies to the far-infrared background. *Astronomy and Astrophysics*, 451:417, May 2006.

A. Domínguez, J. R. Primack, D. J. Rosario, F. Prada, R. C. Gilmore, S. M. Faber, D. C. Koo, R. S. Somerville, M. A. Pérez-Torres, P. Pérez-González, J.-S. Huang, M. Davis, P. Guhathakurta, P. Barmby, C. J. Conselice, M. Lozano, J. A. Newman, and M. C. Cooper. Extragalactic background light inferred from AEGIS galaxy-SED-type fractions. *MNRAS*, 410:2556, 2011.

A. Domínguez, J. D. Finke, F. Prada, J. R. Primack, F. S. Kitaura, B. Siana, and D. Paneque. Detection of the Cosmic γ-Ray Horizon from Multiwavelength Observations of Blazars. *Astrophysical Journal*, 770:77, 2013.

I. Donnarumma and et al. The June 2008 Flare of Markarian 421 from Optical to TeV Energies. *Astrophysical Journal*, 691:L13, 2009.

M. Doro, J. Conrad, D. Emmanoulopoulos, M. A. Sànchez-Conde, J. A. Barrio, and et al. Dark matter and fundamental physics with the Cherenkov Telescope Array. *Astroparticle Physics*, 43:201, 2013.

E. Dwek and R. G. Arendt. A Tentative Detection of the Cosmic Infrared Background at 3.5 μm from COBE/DIRBE Observations. *ApJ*, 508:L9, November 1998.

E. Dwek and F. Krennrich. Simultaneous Constraints on the Spectrum of the Extragalactic Background Light and the Intrinsic TeV Spectra of Markarian 421, Markarian 501, and H1426+428. *Astrophysicial Journal*, 618:657, January 2005.

E. Dwek and F. Krennrich. The extragalactic background light and the gamma-ray opacity of the universe. *Astroparticle Physics*, 43:112, 2013.

D. Elbaz, H. Flores, P. Chanial, I. F. Mirabel, D. Sanders, P.-A. Duc, C. J. Cesarsky, and H. Aussel. ISOCAM mid-infrared detection of HR 10: A distant clone of Arp 220 at z = 1.44. *A&A*, 381:L1, January 2002.

P. A. et al. Evans. An online repository of Swift/XRT light curves of γ-ray bursts. *Astronomy and Astroparticles*, 469:379, 2007.

P. A. et al. Evans. Methods and results of an automatic analysis of a complete sample of Swift-XRT observations of GRBs. *MNRAS*, 397:1177, 2009.

D. P. Finkbeiner, M. Davis, and D. J. Schlegel. Detection of a Far-Infrared Excess with DIRBE at 60 and 100 Microns. *ApJ*, 544:81, November 2000.

J. D. Finke, S. Razzaque, and C. D. Dermer. Modeling the Extragalactic Background Light from Stars and Dust. *Astrophysical Journal*, 712:238, March 2010.

V. P. Fomin, A. A. Stepanian, R. C. Lamb, D. A. Lewis, M. Punch, and T. C. Weekes. New methods of atmospheric Cherenkov imaging for gamma-ray astronomy. I. The false source method. *Astroparticle Physics*, 2:137, 1994.

G. Fossati, L. Maraschi, A. Celotti, A. Comastri, and G. Ghisellini. A unifying view of the spectral energy distributions of blazars. *MNRAS*, 299, 1998.

A. Franceschini, G. Rodighiero, and M. Vaccari. Extragalactic optical-infrared background radiation, its time evolution and the cosmic photon-photon opacity. *Astronomy and Astrophysics*, 837(487), 2008.

D. T. Frayer, M. T. Huynh, R. Chary, M. Dickinson, D. Elbaz, D. Fadda, J. A. Surace, H. I. Teplitz, L. Yan, and B. Mobasher. Spitzer 70 Micron Source Counts in GOODS-North. *ApJ*, 647:L9, August 2006.

W. Galbraith and J. V. Jelley. Light Pulses from the Night Sky associated with Cosmic Rays. *Nature*, 171:349, 1953.

J. P. Gardner, T. M. Brown, and H. C. Ferguson. Ultraviolet Galaxy Counts from Space Telescope Imaging Spectrograph Observations of the Hubble Deep Fields. *ApJ*, 542:L79, October 2000.

M. Gaug. *Calibration of the MAGIC telescope and observation of gamma-ray bursts.* PhD Thesis, UAB, 2006.

M. Georganopoulos, J. D. Finke, and L. C. Reyes. A Method for Setting Upper Limits to the Extragalactic Background Light with Fermi-lat and TeV Observations of Blazars. *Astrophysical Journal Letters*, 714:L157, 2010.

G. Ghisellini. Radiative Processes in High Energy Astrophysics. *arXiv:1202.5949*, 2012.

G. Ghisellini and F. Tavecchio. The blazar sequence: a new perspective. *MNRAS*, 387, 2008.

G. Giavitto. *Observing the VHE Gamma-ray Sky with the MAGIC Telescopes: the Blazar B3 2247+381 and the Crab Pulsar.* PhD Thesis, UAB, 2013.

R. C. Gilmore, R. S. Somerville, J. R. Primack, and A. Domínguez. Semi-analytic modelling of the extragalactic background light and consequences for extragalactic gamma-ray spectra. *MNRAS*, 422:3189, June 2012.

C. Gini. Measurement of inequality of income. *Economic Journal*, 31:22, 1921.

F. Goebel, H. Bartko, E. Carmona, and et al. Upgrade of the MAGIC Telescope with a Multiplexed Fiber-Optic 2GSamples/s FADC Data Acquisition System system. *International Cosmic Ray Conference*, 3:1481, 2008.

V. Gorjian, E. L. Wright, and R. R. Chary. Tentative Detection of the Cosmic Infrared Background at 2.2 and 3.5 Microns Using Ground-based and Space-based Observations. *ApJ*, 536: 550, June 2000.

Y. Grossman, S. Roy, and J. Zupan. Effects of initial axion production and photon-axion oscillation on type Ia supernova dimming [rapid communication]. *Physics Letters B*, 543:23, 2002.

Claus Grupen. *Astroparticle Physics*. 2005.

F. A. et al. Harrison. The Nuclear Spectroscopic Telescope Array (NuSTAR) High-energy X-Ray Mission. *Astrophysical Journal*, 770:103, 2013.

M. G. Hauser, R. G. Arendt, T. Kelsall, E. Dwek, and et al. The COBE Diffuse Infrared Background Experiment Search for the Cosmic Infrared Background. I. Limits and Detections. *ApJ*, 508:25, November 1998.

D. Heck, J. Knapp, J. N. Capdevielle, G. Schatz, and T. Thouw. *CORSIKA: a Monte Carlo code to simulate extensive air showers.* 1998.

A. M. Hillas. Cerenkov light images of EAS produced by primary gamma. *International Cosmic Ray Conference*, 3:445, 1985.

D. Hooper and P. D. Serpico. Detecting Axionlike Particles with Gamma Ray Telescopes. *Physical Review Letters*, 99(23):231102, 2007.

D. Horns and M. Meyer. Indications for a pair-production anomaly from the propagation of VHE gamma-rays. *JCAP*, 2:33, 2012.

D. Horns, M. Meyer, and M. Raue. "revisiting the indication for a low opacity universe for very high energy gamma-rays". *arXiv:1211.6405*, 2013.

John D. Jackson. *Classical Electrodynamics: Second Edition*. 1975.

A. Kashlinsky, J. C. Mather, S. Odenwald, and M. G. Hauser. Clustering of the Diffuse Infrared Light from the COBE DIRBE Maps. I. C(0) and Limits on the Near-Infrared Background. *ApJ*, 470:681, October 1996.

R. C. Keenan, A. J. Barger, L. L. Cowie, and W.-H. Wang. The Resolved Near-infrared Extragalactic Background. *ApJ*, 723:40, November 2010.

T. M. Kneiske, K. Mannheim, and D. H. Hartmann. Implications of cosmological gamma-ray absorption. I. Evolution of the metagalactic radiation field. *Astronomy and Astrophysics*, 386: 1, 2002.

A. et al. Kohnle. Stereoscopic imaging of air showers with the first two HEGRA Cherenkov telescopes. *Astroparticle Physics*, 5:119, 1996.

J. K. Kotilainen, T. Hyvönen, R. Falomo, A. Treves, and M. Uslenghi. The host galaxy of the BL Lacertae object 1ES 0647+250 and its imaging redshift. *A&A*, 534:L2, 2011.

Julian H. Krolik. *Active galactic nuclei: from the central black hole to the galactic environment.* 1999.

G. Lagache, L. M. Haffner, R. J. Reynolds, and S. L. Tufte. Evidence for dust emission in the Warm Ionised Medium sing WHAM data. *A&A*, 354:247, February 2000.

L. R. Levenson and E. L. Wright. Probing the 3.6 μm CIRB with Spitzer in Three DIRBE Dark Spots. *ApJ*, 683:585, August 2008.

L. R. Levenson, E. L. Wright, and B. D. Johnson. DIRBE Minus 2MASS: Confirming the CIRB in 40 New Regions at 2.2 and 3.5 μm. *ApJ*, 666:34, September 2007.

T.-P. Li and Y.-Q. Ma. Analysis methods for results in gamma-ray astronomy. *The Astrophysical Journal*, 272:317, 1983.

Malcom S. Longair. *High Energy Astrophysics: Volume 1*. 1999.

F. Longo, S. Ansoldi, M. Palatiello, and B. Biasuzzi. Fermi analysis. URL `http://fermi.gsfc.nasa.gov/ssc/data/`.

E. Lorenz and R. Wagner. Very-high energy gamma-ray astronomy. A 23-year success story in high-energy astroparticle physics. *European Physical Journal H*, 37:459, 2012.

P. Madau and L. Pozzetti. Deep galaxy counts, extragalactic background light and the stellar baryon budget. *MNRAS*, 312:L9, February 2000.

N. Mankuzhiyil, M. Persic, and F. Tavecchio. High-frequency-peaked BL Lacertae Objects as Spectral Candles to Measure the Extragalactic Background Light in the Fermi and Air Cherenkov Telescopes Era. *Astrophysical Journal Letters*, 715:L16, 2010.

K. Mannheim. The proton blazar. *Astronomy and Astrophysics*, 269:67, March 1993.

K. Mannheim, P. L. Biermann, and W. M. Kruells. A novel mechanism for nonthermal X-ray emission. *Astrophysics and Astroparticles*, 251:723, November 1991.

L. Maraschi and et al. Correlated variability of MKN 421 at X-ray and TeV wavelengths on time scales of hours. *Astroparticle Physics*, 11(2), 1999.

T. Matsumoto, S. Matsuura, H. Murakami, M. Tanaka, M. Freund, M. Lim, M. Cohen, M. Kawada, and M. Noda. Infrared Telescope in Space Observations of the Near-Infrared Extragalactic Background Light. *ApJ*, 626:31, June 2005.

T. Matsumoto, M. G. Kim, J. Pyo, and K. Tsumura. Reanalysis of near-infrared extragalactic background light based on the IRTS observation. *ArXiv e-prints*, 2015.

M. Matsuoka, K. Kawasaki, S. Ueno, H. Tomida, and et al. The MAXI Mission on the ISS: Science and Instruments for Monitoring All-Sky X-Ray Images. *PASJ*, 61:999, 2009.

Y. Matsuoka, N. Ienaka, K. Kawara, and S. Oyabu. Cosmic Optical Background: The View from Pioneer 10/11. *ApJ*, 736:119, August 2011.

I. Matute, F. La Franca, F. Pozzi, C. Gruppioni, C. Lari, and G. Zamorani. Active galactic nuclei in the mid-IR. Evolution and contribution to the cosmic infrared background. *Astronomy and Astrophysics*, 451:443, 2006.

D. Mazin and M. Raue. New limits on the density of the extragalactic background light in the optical to the far infrared from the spectra of all known TeV blazars. *Astronomy and Astrophysics*, 471:439, August 2007.

A. M. Meisner and R. W. Romani. Imaging Redshift Estimates for BL Lacertae Objects. *ApJ*, 712:14–25, 2010.

L. Metcalfe, J.-P. Kneib, B. McBreen, B. Altieri, A. Biviano, M. Delaney, D. Elbaz, M. F. Kessler, K. Leech, K. Okumura, S. Ott, R. Perez-Martinez, C. Sanchez-Fernandez, and B. Schulz. An ISOCAM survey through gravitationally lensing galaxy clusters. I. Source lists and source counts for A370, A2218 and A2390. *A&A*, 407:791, September 2003.

M. Meyer, M. Raue, D. Mazin, and D. Horns. Limits on the extragalactic background light in the Fermi era. *Astronomy and Astrophysics*, 542:A59, 2012.

A. Mirizzi and D. Montanino. Stochastic conversions of TeV photons into axion-like particles in extragalactic magnetic fields. *JCAP*, 12:4, 2009.

A. Mirizzi, G. G. Raffelt, and P. D. Serpico. Signatures of axionlike particles in the spectra of TeV gamma-ray sources. *Physical Review D*, 76:023001, 2007.

R. Mirzoyan. On the Calibration Accuracy of Light Sensors in Atmospheric Cherenkov Fluorescence and Neutrino Experiments. *International Cosmic Ray Conference*, 7:265, 1997.

A. Moralejo, M. Gaug, E. Carmona, P. Colin, C. Delgado, S. Lombardi, D. Mazin, V. Scalzotto, J. Sitarek, D. Tescaro, and for the MAGIC collaboration. MARS, the MAGIC Analysis and Reconstruction Software. *ArXiv e-prints*, 2009.

A. Neronov and I. Vovk. Evidence for Strong Extragalactic Magnetic Fields from Fermi Observations of TeV Blazars. *Science*, 328:73–, 2010.

E. Nieppola, E. Valtaoja, M. Tornikoski, T. Hovatta, and M. Kotiranta. Blazar sequence - an artefact of Doppler boosting. *Astronomy and Astrophysics*, 488, 2008.

M. R. Orr, F. Krennrich, and E. Dwek. Strong New Constraints on the Extragalactic Background Light in the Near- to Mid-infrared. *Astrophysical Journal*, 733:77, 2011.

P. Padovani. The blazar sequence: validity and predictions. *Astrophysics and Space Science*, 309, 2007.

C. Papovich, H. Dole, E. Egami, E. Le Floc'h, and et al. The 24 Micron Source Counts in Deep Spitzer Space Telescope Surveys. *ApJS*, 154:70, September 2004.

R. D. Peccei and H. R. Quinn. CP conservation in the presence of pseudoparticles. *Physical Review Letters*, 38:1440, 1977.

R. Pegna, M. Barceló, M. Bitossi, R. Cecchi, M. Fagiolini, R. Paoletti, A. Piccioli, and N. Turini. A GHz sampling DAQ system for the MAGIC-II telescope. *Nuclear Instruments and Methods in Physics Research A*, 572:382, 2007.

A. Pénin, G. Lagache, A. Noriega-Crespo, J. Grain, M.-A. Miville-Deschênes, N. Ponthieu, P. Martin, K. Blagrave, and F. J. Lockman. An accurate measurement of the anisotropies and mean level of the cosmic infrared background at 100 μm and 160 μm. *A&A*, 543:A123, July 2012.

J. R. Primack, J. S. Bullock, and R. S. Somerville. Observational Gamma-ray Cosmology. 745: 23, 2005.

M. et al. Punch. Detection of TeV photons from the active galaxy Markarian 421. *Nature*, 477 (358), 1992.

J.-F. Rajotte. Upgrade and performance of the VERITAS telescope array. *Nuclear Instruments and Methods in Physics Research A*, 766:61, 2014.

R. Reinthal, S. Rügamer, E. J. Lindfors, and et al. Multi-wavelength Observations of the HBL 1ES 1011+496 in Spring 2008. *Journal of Physics Conference Series*, 355(1):012017, March 2012.

S. Ritt. The DRS chip: cheap waveform digitizing in the GHz range. *Nuclear Instruments and Methods in Physics Research A*, 518:470, 2004.

S. Ritt. Design and performance of the 6 GHz waveform digitizing chip DRS4. *Nuclear Science Symposium Conference Record, 2008. NSS '08. IEEE*, page 1512, 2008.

P. W. A. et al. Roming. The Swift Ultra-Violet/Optical Telescope. *Space Science Reviews*, 120: 95, 2005.

M. A. Sánchez-Conde, D. Paneque, E. Bloom, F. Prada, and A. Domínguez. Hints of the existence of axionlike particles from the gamma-ray spectra of cosmological sources. *Physical Review D*, 79(12):123511, 2009.

F. Schmidt. Corsika shower images. URL `http://www.ast.leeds.ac.uk/~fs/showerimages.html`.

J. Sitarek, M. Gaug, D. Mazin, R. Paoletti, and D. Tescaro. Analysis techniques and performance of the Domino Ring Sampler version 4 based readout for the MAGIC telescopes. *Nuclear Instruments and Methods in Physics Research A*, 723:109, 2013.

F. W. Stecker and O. C. de Jager. Absorption of high energy gamma-rays by low energy intergalactic photons. *Space Science Reviews*, 75:401–412, 1996.

F. W. Stecker and S. T. Scully. A Simple Analytic Treatment of the Intergalactic Absorption Effect in Blazar Gamma-Ray Spectra. *Astrophysical Journal*, 652:L9, 2006.

H. Takami. γ-rays as a diagnostic of the origin of core radiation in low-luminosity active galactic nuclei. *MNRAS*, 413:1845, May 2011.

Y. T. et al. Tanaka. Fermi Large Area Telescope Detection of Bright γ-Ray Outbursts from the Peculiar Quasar 4C +21.35. *Astrophysical Journal*, 733:19, May 2011.

M. et al. Tavani. The AGILE space mission. *Nuclear Instruments and Methods in Physics Research A*, 588:52, 2008.

F. Tavecchio, L. Maraschi, and G. Ghisellini. General constraints on the physical parameters of TeV blazar. *Memorie della Societa Astronomica Italiana*, 70:189, 1999.

F. Tavecchio, G. Ghisellini, L. Foschini, G. Bonnoli, G. Ghirlanda, and P. Coppi. The intergalactic magnetic field constrained by Fermi/Large Area Telescope observations of the TeV blazar 1ES0229+200. *MNRAS*, 406:L70, 2010a.

F. Tavecchio, G. Ghisellini, L. Foschini, G. Bonnoli, G. Ghirlanda, and P. Coppi. The intergalactic magnetic field constrained by Fermi/Large Area Telescope observations of the TeV blazar 1ES0229+200. *MNRAS*, 406:L70, 2010b.

A. M. Taylor, I. Vovk, and A. Neronov. Extragalactic magnetic fields constraints from simultaneous GeV-TeV observations of blazars. *A&A*, 529:A144, 2011.

D. Tescaro. *TeV γ-ray observation of nearby Active Galactic Nuclei with the MAGIC telescope: exploring the high energy region of the multi-wavelength picture.* PhD Thesis, UAB, 2010.

R. I. Thompson, D. Eisenstein, X. Fan, M. Rieke, and R. C. Kennicutt. Constraints on the Cosmic Near-Infrared Background Excess from NICMOS Deep Field Observations. *ApJ*, 657: 669, March 2007.

C. M. Urry and P. Padovani. Unified schemes for radio-loud active galactic nuclei. *PASP*, 803 (107), 1995. URL `http://arxiv.org/abs/astro-ph/9506063v2`.

H. J. Völk and K. Bernlöhr. Imaging very high energy gamma-ray telescopes. *Experimental Astronomy*, 25:173, 2009.

I. Vovk, A. M. Taylor, D. Semikoz, and A. Neronov. Fermi/LAT Observations of 1ES 0229+200: Implications for Extragalactic Magnetic Fields and Background Light. *ApJ*, 747:L14, 2012.

E. N. Voyer, J. P. Gardner, H. I. Teplitz, B. D. Siana, and D. F. de Mello. Far-ultraviolet Number Counts of Field Galaxies. *ApJ*, 736:80, August 2011.

T. C. Weekes and K. E. Turver. Gamma-ray astronomy from 10-100 GeV: A new approach. In R. D. Wills and B. Battrick, editors, *Recent Advances in Gamma-Ray Astronomy*, volume 124 of *ESA Special Publication*, pages 279–286, 1977.

T. C. Weekes, M. F. Cawley, D. J. Fegan, K. G. Gibbs, A. M. Hillas, P. W. Kowk, R. C. Lamb, D. A. Lewis, D. Macomb, N. A. Porter, P. T. Reynolds, and G. Vacanti. Observation of TeV gamma rays from the Crab nebula using the atmospheric Cerenkov imaging technique. *Astrophysical Journal*, 342:379, 1989.

T. C. et al. Weekes. Observation of TeV gamma rays from the Crab nebula using the atmospheric Cerenkov imaging technique. *The Astrophysical Journal*, 342:379, 1989.

J.-H. Woo, C. M. Urry, R. P. van der Marel, P. Lira, and J. Maza. Black Hole Masses and Host Galaxy Evolution of Radio-Loud Active Galactic Nuclei. *ApJ*, 631:762, 2005.

D. Wouters and P. Brun. Irregularity in gamma ray source spectra as a signature of axionlike particles. *Physical Review D*, 86(4), 2012.

C. K. Xu, J. Donas, S. Arnouts, T. K. Wyder, and et al. Number Counts of GALEX Sources in Far-Ultraviolet (1530 Å) and Near-Ultraviolet (2310 Å) Bands. *ApJ*, 619:L11, January 2005.

R. Zanin. *Observation of the Crab pulsar wind nebula and microquasar candidates with MAGIC*. PhD thesis, Universitat Autonoma de Barcelona, 2011.